AFCRL 72-0266

ELECTRO DYNAMICS LABORATORIES

Electron-Beam-Induced Luminescence Studies of Thermospheric Temperatures and Molecular Concentrations: Instrumentation for Aerobees AO 3.006-1 and AO 3.910-1

by

William R. Pendleton, Jr.
L. Carl Howlett
Larry L. Jensen

FINAL REPORT

Period Covered: 6 May 1969 to
31 December 1971

21 April 1972

Contract No. F19628-69-C-0242
Project No. 8692

Prepared for Air Force Cambridge Research Laboratories
Air Force Systems Command, United States Air Force
Bedford, Massachusetts 01730

Contract Monitor: Robert R. O'Neil
Optical Physics Laboratory

This research was sponsored by the
Advanced Research Projects Agency

UTAH STATE UNIVERSITY

LOGAN, UTAH 84322

191

Program code No.	9E50
Effective date of contract	6 May 1969
Contract expiration date	31 December 1971
Principal investigator and phone No.	Dr. Doran J. Baker 801 752-4100 ext 7800
Project scientist and phone No	Robert R. O'Neil 617 861-4904

~~Qualified requesters may obtain additional copies from the Defense Documentation Center. All others should apply to the National Technical Information Service.~~

AFCRL-72-0266

ELECTRON-BEAM-INDUCED LUMINESCENCE STUDIES OF THERMOSPHERIC TEMPERATURES AND MOLECULAR CONCENTRATIONS: INSTRUMENTATION FOR AEROBEES AO 3.006-1 AND AO 3.910-1

William R. Pendleton, Jr.
Larry L. Jensen
L. Carl Howlett,
Space Science Laboratory

Electro-Dynamics Laboratories
UTAH STATE UNIVERSITY
Logan, Utah 84322

Contract No. F19628-69-C-0242

FINAL REPORT

6 May 1969 - 31 December 1971
Date of Report: 21 April 1972

Contract Monitor: Robert R. O'Neil
Optical Physics Laboratory

Approved for public release; distribution unlimited.

Sponsored by
Advanced Research Projects Agency
ARPA Order No. 1366

Prepared for

Air Force Cambridge Research Laboratories
Air Force Systems Command
UNITED STATES AIR FORCE
Bedford, Massachusetts 01730

10

UNCLASSIFIED
Security Classification

DOCUMENT CONTROL DATA - R&D

(Security classification of title, body of abstract and indexing annotation must be entered when the overall report is classified)

1. ORIGINATING ACTIVITY (Corporate author)
Utah State University
Electro-Dynamics Laboratories
Logan, Utah 84322

2a. REPORT SECURITY CLASSIFICATION
UNCLASSIFIED

2b. GROUP

3. REPORT TITLE
ELECTRON-BEAM-INDUCED STUDIES OF THERMOSPHERIC TEMPERATURES AND MOLECULAR CONCENTRATIONS: INSTRUMENTATION FOR AEROBEES AO 3.006-1 AND AO 3.910.1

4. DESCRIPTIVE NOTES (Type of report and inclusive dates)
Scientific Final 6 May 1969--31 December 1971 Approved 9 June 1972

5. AUTHOR(S) (Last name, first name, initial)
William R. Pendleton, Jr.
L. Carl Howlett
Larry L. Jensen

6. REPORT DATE
21 April 1972

7a. TOTAL NO. OF PAGES
175

7b. NO. OF REFS
56

8a. CONTRACT OR GRANT NO.
F19628-69-C-0242/ARPA Order No. 1366

b. PROJECT NO., Task, Work Unit Nos.
8692 n/a n/a

c. DoD Element 62301D

d. DoD Subelement n/a

9a. ORIGINATOR'S REPORT NUMBER(S)

9b. OTHER REPORT NO(S) (Any other numbers that may be assigned this report)
AFCRL-72-0266

10. AVAILABILITY/LIMITATION NOTICES
A-Approved for public release; distribution unlimited

11. SUPPLEMENTARY NOTES
This research was sponsored by the Advanced Research Projects Agency

12. SPONSORING MILITARY ACTIVITY
Air Force Cambridge Research Laboratories(OP)
L. G. Hanscom Field
Bedford, Massachusetts 01730

13. ABSTRACT

Two Aerobee 150 rockets, No's AO 3.006-1 and AO 3.910-1, were instrumented for investigating thermospheric temperatures and particle densities. Electron-beam-induced luminescence was used as a diagonistic technique to investigate the rotational and vibrational distributions of thermospheric $N_2(X^1\Sigma_g^+)$ and to determine absolute number densities of N_2 and O_2. The first flight was made under disturbed (auroral) atmospheric conditions, whereas the second was made under quiescent conditions. Support instrumentation was included in the first payload to aid in defining auroral conditions. In addition, a possible correlation of elevated E-region electron temperatures with $N_2(X^1\Sigma_g^+)$ vibrational temperature prompted the inclusion of a Langmuir probe in each of the payloads. The present report provides background information on the technical problem and on the investigative technique which was adopted, documents the development of instrumentation for the two payloads, and briefly summarizes available results from the two flights

iA

Details of illustrations in this document may be better studied on microfiche

DD FORM 1 JAN 64 1473

UNCLASSIFIED
Security Classification

14 KEY WORDS	LINK A		LINK B		LINK C	
	ROLE	WT	ROLE	WT	ROLE	WT
Thermospheric Measurements						
Rocket Instrumentation						
Electron Beam Induced Luminescence						
N_2^+ First Negative System						
$N_2(X^1\Sigma_g^+)$ Vibrational Temperature						
$N_2(X^1\Sigma_g^+)$ Rotational Temperature						
N_2 Number Density						
O_2 Number Density						
Electron Temperature						

INSTRUCTIONS

1. **ORIGINATING ACTIVITY:** Enter the name and address of the contractor, subcontractor, grantee, Department of Defense activity or other organization *(corporate author)* issuing the report.

2a. **REPORT SECURITY CLASSIFICATION:** Enter the overall security classification of the report. Indicate whether "Restricted Data" is included. Marking is to be in accordance with appropriate security regulations.

2b. **GROUP:** Automatic downgrading is specified in DoD Directive 5200.10 and Armed Forces Industrial Manual. Enter the group number. Also, when applicable, show that optional markings have been used for Group 3 and Group 4 as authorized.

3. **REPORT TITLE:** Enter the complete report title in all capital letters. Titles in all cases should be unclassified. If a meaningful title cannot be selected without classification, show title classification in all capitals in parenthesis immediately following the title.

4. **DESCRIPTIVE NOTES:** If appropriate, enter the type of report, e.g., interim, progress, summary, annual, or final. Give the inclusive dates when a specific reporting period is covered.

5. **AUTHOR(S):** Enter the name(s) of author(s) as shown on or in the report. Enter last name, first name, middle initial. If military, show rank and branch of service. The name of the principal author is an absolute minimum requirement.

6. **REPORT DATE:** Enter the date of the report as day, month, year; or month, year. If more than one date appears on the report, use date of publication.

7a. **TOTAL NUMBER OF PAGES:** The total page count should follow normal pagination procedures, i.e., enter the number of pages containing information.

7b. **NUMBER OF REFERENCES:** Enter the total number of references cited in the report.

8a. **CONTRACT OR GRANT NUMBER:** If appropriate, enter the applicable number of the contract or grant under which the report was written.

8b, 8c, & 8d. **PROJECT NUMBER:** Enter the appropriate military department identification, such as project number, subproject number, system numbers, task number, etc.

9a. **ORIGINATOR'S REPORT NUMBER(S):** Enter the official report number by which the document will be identified and controlled by the originating activity. This number must be unique to this report.

9b. **OTHER REPORT NUMBER(S):** If the report has been assigned any other report numbers *(either by the originator or by the sponsor)*, also enter this number(s).

10. **AVAILABILITY/LIMITATION NOTICES:** Enter any limitations on further dissemination of the report, other than those imposed by security classification, using standard statements such as:

(1) "Qualified requesters may obtain copies of this report from DDC."

(2) "Foreign announcement and dissemination of this report by DDC is not authorized."

(3) "U. S. Government agencies may obtain copies of this report directly from DDC. Other qualified DDC users shall request through
____."

(4) "U. S. military agencies may obtain copies of this report directly from DDC. Other qualified users shall request through
____."

(5) "All distribution of this report is controlled. Qualified DDC users shall request through
____."

If the report has been furnished to the Office of Technical Services, Department of Commerce, for sale to the public, indicate this fact and enter the price, if known.

11. **SUPPLEMENTARY NOTES:** Use for additional explanatory notes.

12. **SPONSORING MILITARY ACTIVITY:** Enter the name of the departmental project office or laboratory sponsoring *(paying for)* the research and development. Include address.

13. **ABSTRACT:** Enter an abstract giving a brief and factual summary of the document indicative of the report, even though it may also appear elsewhere in the body of the technical report. If additional space is required, a continuation sheet shall be attached.

It is highly desirable that the abstract of classified reports be unclassified. Each paragraph of the abstract shall end with an indication of the military security classification of the information in the paragraph, represented as *(TS)*, *(S)*, *(C)*, or *(U)*.

There is no limitation on the length of the abstract. However, the suggested length is from 150 to 225 words.

14. **KEY WORDS:** Key words are technically meaningful terms or short phrases that characterize a report and may be used as index entries for cataloging the report. Key words must be selected so that no security classification is required. Identifiers, such as equipment model designation, trade name, military project code name, geographic location, may be used as key words but will be followed by an indication of technical context. The assignment of links, rules, and weights is optional.

i D

ABSTRACT

Two Aerobee 150 rockets, No's. AO 3.006-1 and AO 3.910-1, were instrumented for investigating thermospheric temperatures and particle densities. Electron-beam-induced luminescence was used as a diagnostic technique to investigate the rotational and vibrational distributions of thermospheric $N_2(X^1\Sigma_g^+)$ and to determine absolute number densities of N_2 and O_2. The first flight was made under disturbed (auroral) atmospheric conditions, whereas the second was made under quiescent conditions. Support instrumentation was included in the first payload to aid in defining auroral conditions. In addition a possible correlation of elevated E-region electron temperatures with $N_2(X^1\Sigma_g^+)$ vibrational temperature prompted the inclusion of a Langmuir probe in each of the payloads. The present report provides background information on the technical problem and on the investigative technique which was adopted, documents the development of instrumentation for the two payloads, and briefly summarizes available results from the two flights.

LIST OF CONTRIBUTORS

The list of contributors which follows has been restricted to include only scientists and engineers associated with either the Electro-Dynamics Laboratories (EDL) or the Space Science Laboratories (SSL).

D. J. Baker	Director of EDL
K. D. Baker	Director of SSL
R. D. Briscoe	Research Physicist
D. A. Burt	Senior Research Engineer
D. G. Frodsham	Research Engineer
L. C. Howlett	Project Engineer
L. L. Jensen	Research Engineer
W. R. Pendleton, Jr.	Project Engineer
E. F. Pound	Senior Research Engineer
K. G. Seljaas	Research Engineer

TABLE OF CONTENTS

Table of Contents (Cont.)

LIST OF FIGURES

Figure   Page

Figure | Page

LIST OF TABLES

INTRODUCTION

The developmental work described in this report was initiated for Air Force Cambridge Research Laboratories under Contract No. F19628-69-C-0242 to Utah State University (USU). The original objective of the work was to design and fabricate two rocket-based instruments for investigation of the number density, rotational temperature (T_r), and vibrational temperature (T_v) of atmospheric $N_2(X^1\Sigma_g^+)$. The diagonistic technique to be employed was electron-beam-induced luminescence [Muntz, 1962 and 1968]. A possible correlation of elevated E-region electron temperatures (T_e) with a plausible heat source involving vibrationally excited ground-state nitrogen ($N_2^{\dagger}$)[Walker, 1968] led to the inclusion of electron temperature (T_e) and number density (N_e) measurements as additional objectives. Also, since the first instrument was to be launched into an auroral event, it was decided that additional instrumentation for defining auroral conditions should be included in the payload.

The USU Space Science Laboratory, formerly Upper Air Research Laboratory of the University of Utah, integrated each of the payloads for launch on board Aerobee 150 rockets. The Space Science Laboratory (SSL) also provided a Langmuir probe for N_e and T_e measurements, as well as other instrumentation for defining auroral conditions. The USU Electro-Dynamics Laboratories (EDL) assumed primary responsibility for developing the electron-beam-induced luminescence system. However, able assistance was obtained from SSL personnel during certain phases of the work.

The first "vibrational temperature apparatus" (VTA) was launched aboard Aerobee No. AO 3.006-1 from Fort Churchill, Manitoba, Canada on March 13, 1970. The second VTA was flown on board Aerobee No. AO 3.910-1 from White Sands Missile Range, White Sands, New Mexico on October 15, 1971.

The primary purpose of this report is to document the development of instrumentation for the two payloads. Emphasis is placed on describing the development of the VTA since the major thrust of the work was in this direction. Also, much of the detail relating to the ancillary apparatus has previously been reported, and pertinent references are cited at appropriate points in this report. Background information pertaining to the general problem of $N_2^{\neq}$ in the thermosphere is presented together with a description of the experimental technique which was adopted for investigating the molecular nitrogen properties of interest. Following a consideration of the design of the VTA and documentation of payload instrumentation, attention is turned to the preflight calibration of the VTA. Finally, the performance of the flight instrumentation is discussed, and available results from the two flights are briefly considered.

A preliminary report of the $N_2^{\neq}$ results obtained from the Churchill flight has appeared elsewhere (O'Neil, Hart, and Pendleton; 1971). A more refined treatment of the data was subsequently carried out, and some of the results were communicated at the 1971 COSPAR meeting (O'Neil, Pendleton, Hart, and Stair; 1971). A complete description of the results is currently being prepared for submission to one of the aeronomy-related journals. In addition, a short communication relating to the theory of the N_2 vibrational temperature measurements has recently been submitted (Pendleton and O'Neil, 1972).

BACKGROUND INFORMATION

The Role of Metastable Species in Atmospheric Processes

In recent years the potentially important role of metastable atoms, ions, and molecules in the physics and chemistry of the upper atmosphere has received increasingly wide-spread attention. It has often proven difficult experimentally to recognize and completely separate the effects of excited state reactions, and, as a result, the zeroth-order approximation has been to assume that the contribution of excited-state reactions could be ignored. However, it is now generally recognized that relatively small concentrations of excited particles can sometimes produce large effects on total reaction rates and upon equilibrium conditions. Hence, a quantitative understanding of the quiescent and disturbed atmospheres requires a knowledge of excitation and de-excitation rates for binary encounters of atmospheric metastables with other atmospheric species.

The deposition of solar energy in the upper atmosphere results in a multitude of phenomena, including the production of metastable species. The metastables relax through a combination of radiative decay and collisional de-excitation, the importance of each process being determined by the relative probabilities for occurrence under given atmospheric conditions. The collisional de-excitation rate depends on the collision frequency and on the probability per collision that de-excitation will occur. Hence, for a particular species, collisional de-excitation may dominate at low altitudes where the collision frequency is relatively large, whereas radiative decay may dominate at high altitudes.

The concept of energy storage in metastable states may assume considerable importance in certain atmospheric phenomena since the internal energy of the metastables could, in principle, provide an energy source for "driving" certain atmospheric processes for a period of time even if the source of the metastables were suddenly turned off. The relaxation rate of the metastables would, of course, depend on the effective lifetime under given conditions.

Akin to the electronic metastability alluded to in the discussion above is the "vibrational metastability" of homonuclear diatomic molecules such as ${}^{14}_{7}N_2$ and ${}^{16}_{8}O_2$. Such molecules do not possess a permanent electric dipole moment in their electronic ground states. Hence, they are infrared inactive, and when vibrationally excited, the excess internal energy is normally dissipated through inelastic collisional processes.

The potentially important role of $N_2^{\neq}$ in the following atmospheric processes:

$$N_2^{\neq}(\upsilon>0) + e \longrightarrow N_2(\upsilon'<\upsilon) + e + K.E. \ , \tag{1}$$

$$O^+ + N_2^{\neq} \longrightarrow NO^+ + N \ , \tag{2}$$

and

$$N_2^{\neq}(\upsilon=1) + CO_2(00^\circ 0) \longrightarrow N_2(\upsilon=0) + CO_2^{\neq}(00^\circ 1) \tag{3a}$$

followed by

$$CO_2^{\neq}(00^01) \longrightarrow CO_2(00^00) + h\nu \qquad (3b)$$

has stimulated a great deal of speculation in recent years. Consideration will be given to these processes in the next subsection which deals with $N_2^{\neq}$ in the thermosphere. It should be noted that a knowledge of the concentration of $N_2^{\neq}$ is necessary in order to evaluate the potential importance of the processes.

$N_2^{\neq}$ in the Thermosphere

The thermal structure of the neutral atmosphere appears to be well established. However, a consideration of available atmospheric data relating to concentrations of atomic, molecular, ionic, and electronically excited species leads one to the conclusion that local thermodynamic equilibrium (LTE) does not exist in the upper atmosphere at altitudes $\gtrsim$ 100 km [Bauer, Kummler, and Bortner; 1971].

Under conditions of LTE, all energy states of particles within a given volume element are populated according to the equilibrium statistical-mechanical distributions with a *common temperature* characterizing the distributions. However, in the *non*-LTE region, the population distributions for translational, rotational, vibrational, and electronic degrees of freedom are frequently characterized by *individual temperatures* [Bond, Watson, and Welch; 1965]. As a result, under non-LTE conditions, a knowledge of the gas-kinetic temperature is of little value in predicting the concentration of vibrationally excited molecules such as $N_2^{\neq}$.

The definition of individual temperatures for the various degrees of freedom is based on the premise that the distribution of energy over each degree of freedom is Boltzmann-like. The rapidity of energy transfer within each degree of freedom and between degrees of freedom will usually determine the usefulness of the concept. If the *coupling* between degrees of freedom is weak, whereas rapid energy distribution occurs within each degree of freedom, the multitemperature concept should be useful. It is important to note that the concept is one of convenience and should not be interpreted too strictly, as the distribution functions describing each degree of freedom will be perturbed from their true equilibrium form by transitions between degrees of freedom.

The general theoretical problem of $N_2^{\neq}$ in the thermosphere has recently received a great deal of attention [Walker, 1968· Walker, Stolarski, and Nagy, 1969; Bortner and Kummler, 1971; Bauer, Kummler, and Bortner, 1971; Schunk and Hays, 1971]. Much of the interest has developed in connection with the role of $N_2^{\neq}$ in thermospheric processes. Walker (1968) suggested that $N_2^{\neq}$ might selectively heat the ambient *E*-region electrons through process (1) (pg. 3). The suggestion was prompted by the need for an additional heat source to explain reported Langmuir-probe measurements of T_e in the *E*-region. The Langmuir-probe results have consistently yielded $T_e > T_g$ by factors of two-to-three in this region. Although questions have arisen regarding the validity of the probe results [See Willimore (1970) for a review of the problem, including results available up to January, 1970.], there appears little doubt that *non*-LTE conditions do occur in the ionosphere. Walker found that an N_2 vibrational temperature of $\approx 3100^{\circ}$K, nearly independent of altitude in the altitude range 110-140 km, was required to explain the T_e results of Spencer *et al.* (1965).

Walker, Stolarski, and Nagy (1969) have calculated N_2 vibrational temperatures for the *E*- and *F*-regions by identifying significant sources and sinks of N_2 vibrational energy and then solving the continuity equation for vibrational quanta. The general problem is illustrated in Fig. 1 which identifies potential sources and sinks of N_2 vibrational energy. The solar input leads to the formation of a number of excited atmospheric species which subsequently contribute to the formation of $N_2^{\neq}$. Each of the sources indicated in the figure will be considered briefly.

Electronically excited molecular nitrogen (N_2^{*}) is formed primarily through electron-impact excitation involving photoelectrons and/or precipitating energetic particles. Both the Vegard-Kaplan (*VK*)$[A^3\Sigma_u^+ - X^1\Sigma_g^+]$ [Broadfoot and Hunten, 1964; Shemansky and Vallance Jones, 1968; Sharp, 1971] and the Lyman-Birge-Hopfield (LBH) $[a^1\pi_g - X^1\Sigma_g^+]$ [Fastie *et al.*, 1961; Isler and Fastie, 1965; Peek, 1970; Opal *et al.*, 1970] band systems have been observed in emissions from the upper atmosphere. A knowledge of the volume emission rates of quanta in these two systems under given atmospheric conditions would help to clarify the potential importance of the cascade source. The yield of vibrational quanta in the N_2 ground state will, of course, depend on the population distribution resulting from the

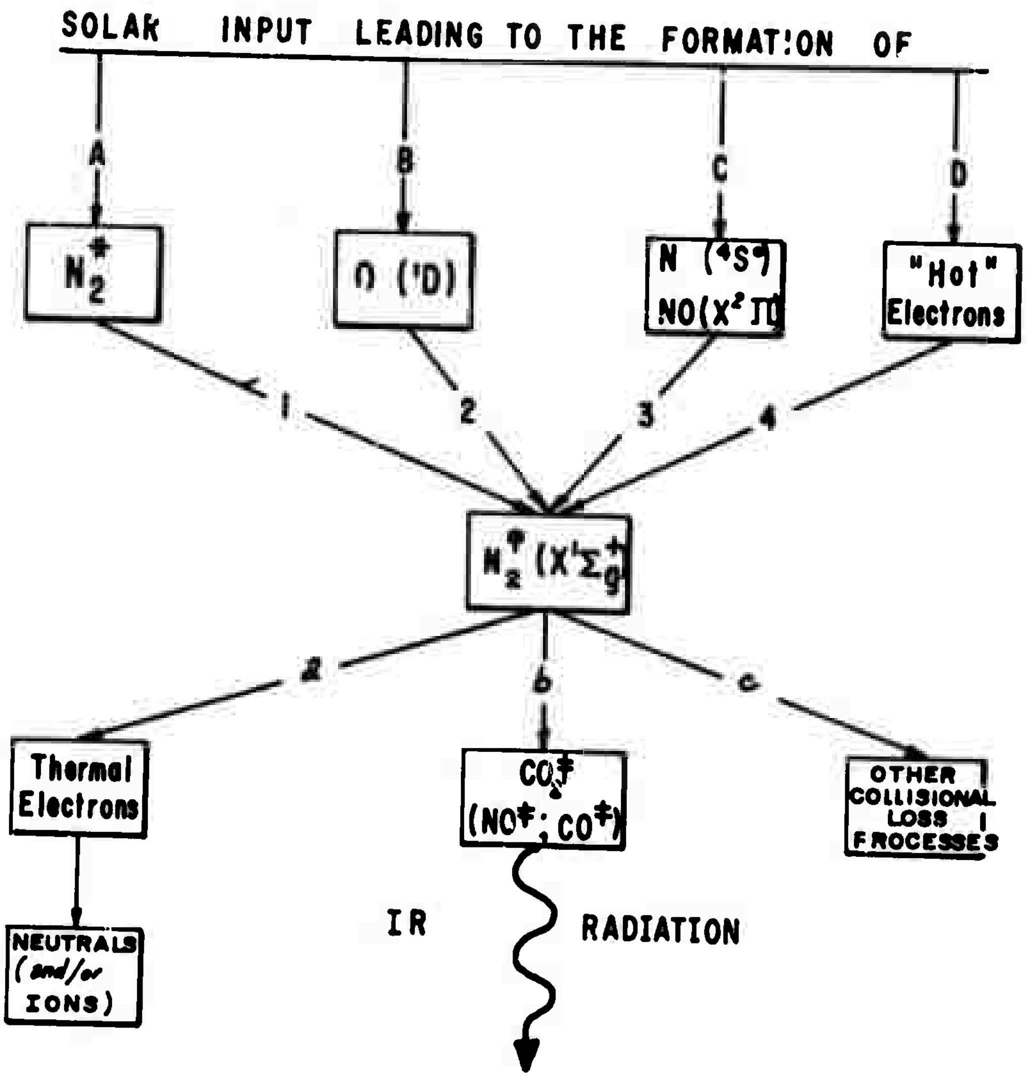

Figure 1. Thermospheric sources and sinks of $N_2(X^1\Sigma_g^+)$ vibrational energy.

cascading. It does not appear that this source has been included in previous treatments of the $N_2^{\neq}$ problem. However, a cursory examination of available data suggests that the contribution from the cascade source may be significant under certain atmospheric conditions.

A second potentially important source of $N_2^{\neq}$ is the reaction

$$O(^1D) + N_2(X,\ v=0) \longrightarrow O(^3P) + N_2^{\neq}(v>0) + \Delta E\ , \qquad (4)$$

which involves an interconversion of a portion of the electronic energy of the $O(^1D)$ atom to N_2 vibrational energy. The quenching of $O(^1D)$ by N_2 is known to be rapid [Young, Black, and Slanger, 1968; Noxon, 1970]; however, the average amount of available energy [1.96 eV/$O(^1D)$] which appears in N_2 vibration is not presently known. Walker *et al.* (1969) have considered the two extreme cases in their computations. They found that the inclusion of the maximum possible vibrational yield from process (4) [7 vibrational quanta per reaction] resulted in values of T_v which exceeded the lower limit values [no contribution from process (4)] by approximately a factor of two at high altitudes. Recent theoretical and experimental studies of process (4) [Black, Lorents, and Eckstrom, 1970; Peterson, 1972] suggest that the lower-limit assumption is more nearly correct.

The third source of thermospheric $N_2^{\neq}$ depicted in Fig. 1 is the reaction

$$N(^4S^o) + NO(X^2\pi) \longrightarrow N_2^{\neq} + O(^3P)\ , \qquad (5)$$

where an average of four vibrational quanta are produced per reaction [Morgan, Phillips, and Schiff, 1962; Phillips and Schiff, 1962]. The treatment of this source is complicated by its dependence on N_2 vibrational temperature [Walker *et al.*, 1969]. The dependence on T_v arises from process (2) [Schmeltekopf, Ferguson, and Feshenfeld; 1968] since [N] is determined in part from this process. It is interesting to note that large NO densities in the E-region have been reported under disturbed atmospheric conditions [Zipf, Borst, and Donahue, 1970]. Hence, it is possible that the $N_2^{\neq}$ source represented by process (5) may assume special significance under disturbed conditions provided the atomic nitrogen density is not significantly decreased.

The last source illustrated in Fig. 1 is the contribution from "hot electrons" which in the present context means electrons with kinetic energies $\gtrsim 0.3$ eV. These electrons contribute to N_2 vibration through the process

$$e + N_2(X,v=0) \longrightarrow N_2^{-}(X^2\pi_g) \longrightarrow N_2^{\neq}(v>0) + e \ , \tag{6}$$

which occurs with a high probability for low energies [Schulz, 1964]. The "hot electrons" will normally be photoelectrons or precipitating (auroral) electrons since the contribution of ambient thermal electrons is expected to be negligible in comparison [Dalgarno, McElroy, Rees, and Walker, 1968]. Several additional sources of $N_2^{\neq}$ have been considered by Walker *et al.*(1969) and were found to be much smaller than those mentioned above.

The N_2 vibrational energy resulting from the aforementioned processes is efficiently redistributed through vibrational exchange (V-V) collisions, and for altitudes less than about 250 km, the characteristic exchange time for vibrational quanta is somewhat less than the characteristic loss time [Walker, 1968]. At altitudes above 260 km, the diffusion time becomes less than the exchange time [Walker *et al.*, 1969]. Hence, a departure of the N_2 vibrational distribution from the Boltzmann form may occur at high altitudes, particularly for the higher vibrational levels.

The loss of $N_2^{\neq}$ occurs through channels such as those depicted in Fig. 1. Superelastic collisions between $N_2^{\neq}$ and thermal electrons [process (1), pg. 3] occur with a high probability [Walker, 1968]. Hence, as proposed by Walker (1968), the $N_2^{\neq}$ is potentially important as a heat source for the ambient electrons. The electrons then cool to the neutrals and/or ions depending on the altitude region. Walker *et al.* (1969) have shown that quenching of $N_2^{\neq}$ by vibrational exchange collisions with CO_2 [process (3a), pg. 3] should be the dominant loss process at altitudes below about 125 km. The vibrationally excited CO_2 subsequently looses the excess energy by the emission of infrared radiation. Walker *et al.* have also considered other potential loss mechanisms and deemed them negligible in comparison to the electron and CO_2 quenching. Diffusion should become important above 125 km [Walker *et al.*, 1969]. The diffusion process results in the transport of $N_2^{\neq}$ to lower altitudes where loss of vibrational energy occurs at a much greater rate.

The results of Walker *et al.* are summarized in Fig. 2 which presents N_2 vibrational temperature as a function of altitude. The curve labeled T_v^{max} is based on the use of the maximum possible $O(^1D)$ contribution in the computations, while the T_v^{min} curve results from assuming no contribution from $O(^1D)$. The curve labeled "gas kinetic" is a kinetic temperature profile for an exospheric temperature of 1000°K. The temperatures apply to noontime conditions.

The behavior of $N_2^{\neq}$ expected during auroral conditions has been considered by Walker *et al.* and more recently by Schunk and Hays (1971). As input data, both groups have used the observations of Belon, Romick, and Rees (1966) relating to a particular IBC II^+ (or III^-) aurora.

Rotational and Vibrational Temperatures

The concepts of rotational and vibrational temperatures are derived from analyses of the rotational and vibrational population distributions of natural (ground state) or excited molecules (or molecular ions). Under LTE conditions, the population N_i of a level having an energy E_i above the ground state of the molecule is given by the Maxwell-Boltzmann expression

$$N_i = \frac{N g_i \exp\,(-E_i/kT)}{Z} , \qquad (7)$$

where N is the total number of molecules in the volume element under consideration, g_i is the statistical weight of the level of energy E_i, and Z is the partition function, or sum over states. The partition function is given by $Z = \sum_i g_i \exp(-E_i/kT)$, where the summation is over all the allowed energy levels.

If one adopts Hund's case (b) to describe the coupling of angular momenta for $N_2(X^1\Sigma_g^+)$, the population distribution of the rotational energy states associated with the zeroth vibrational level is given by

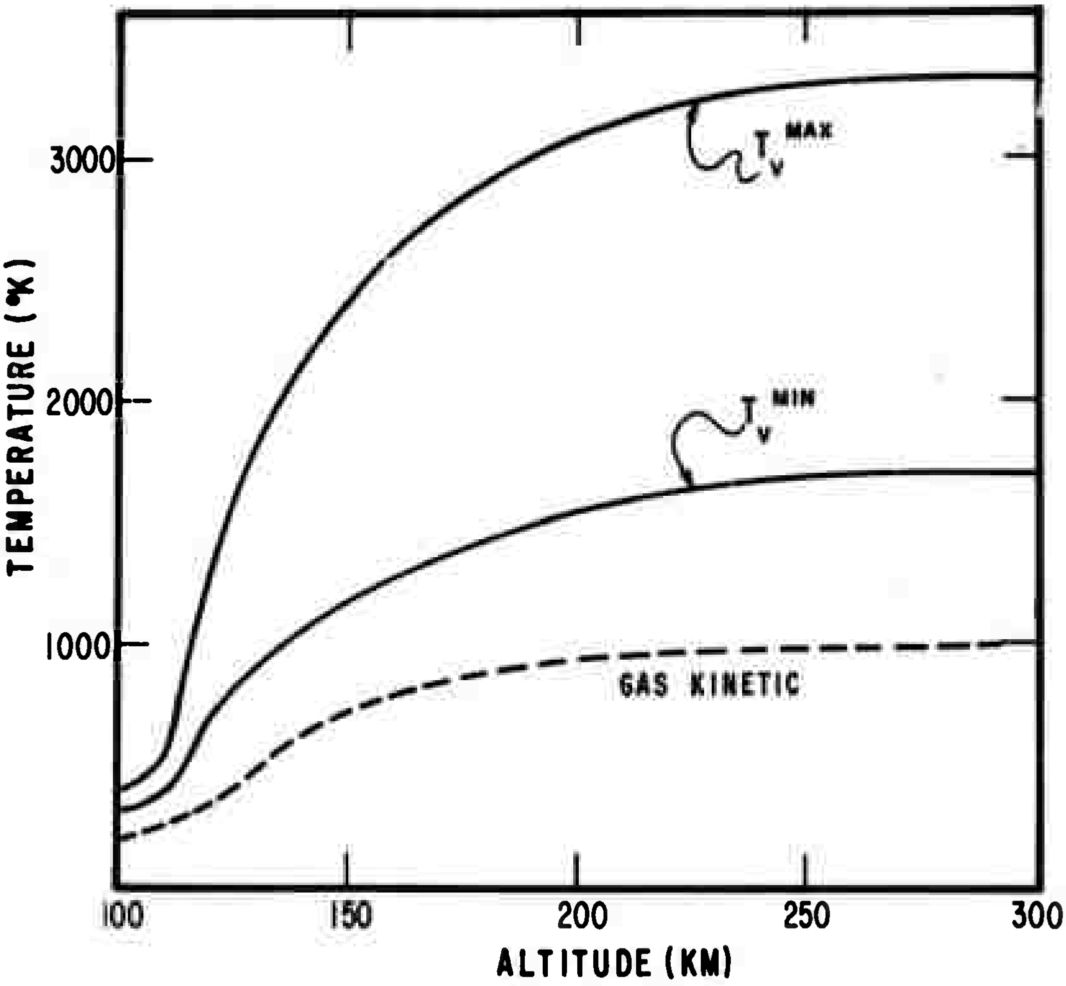

Figure 2. Results of theoretical T_υ calculations (Walker *et al.*, 1969) for thermospheric N_2.

$$N_{oK} = \frac{N\, g_{ok} \exp\,[-(E_o + E_k)/kT]}{Z_v Z_r} \,, \tag{8}$$

where

$$g_{ok} = \begin{cases} 3(2K+1), & K \text{ odd} \\ 6(2K+1), & K \text{ even} \end{cases}$$

$$E_o = hc[(\omega_e/2) - (\omega_e x_e/4) + \ldots] \,,$$

$$E_k = hc\; K(K+1)[B_e - (a_e/2) + \ldots] \,,$$

$$Z_v = \sum_{v=0}^{\infty} e^{-E_v/kT} \cong e^{\frac{-hc\omega_e}{kT}}(1-e^{\frac{-hc\omega_e}{kT}})^{-1} \,,$$

$$Z_r \cong \frac{kT}{hcB_e} \quad (\text{for } kT>>hcB_e) \,,$$

and $K = 0, 1, 2, \cdots$. The pertinent vibrational and rotational constants for $N_2(X^1\Sigma_g^+)$ are tabulated in Herzberg's volume on diatomic molecules (Herzberg, 1950). The relative populations expected for levels $K = 0$-20 are shown in Fig. 3 for rotational temperatures of 300°K and 800°K. For each temperature, the population of the level corresponding to the maximum in the distribution has been normalized to unity. In a similar manner, the population distribution over the vibrational levels of $N_2(X^1\Sigma_g^+)$ is given by

$$N_v = \frac{N \exp\,(-E_v/kT)}{Z} \,, \tag{9}$$

where

$$E_v = hc[\omega_e(v+\tfrac{1}{2}) - \omega_e x_e(v+\tfrac{1}{2})^2 + \cdots] \,,$$

$$Z = \sum_{v=0}^{\infty} \exp\,(-E_v/kT), \text{ and}$$

$v = 0, 1, 2, \cdots$. The relative population distributions expected at temperatures of 750, 1000, 2000 and 5000°K are shown in Fig. 4. It

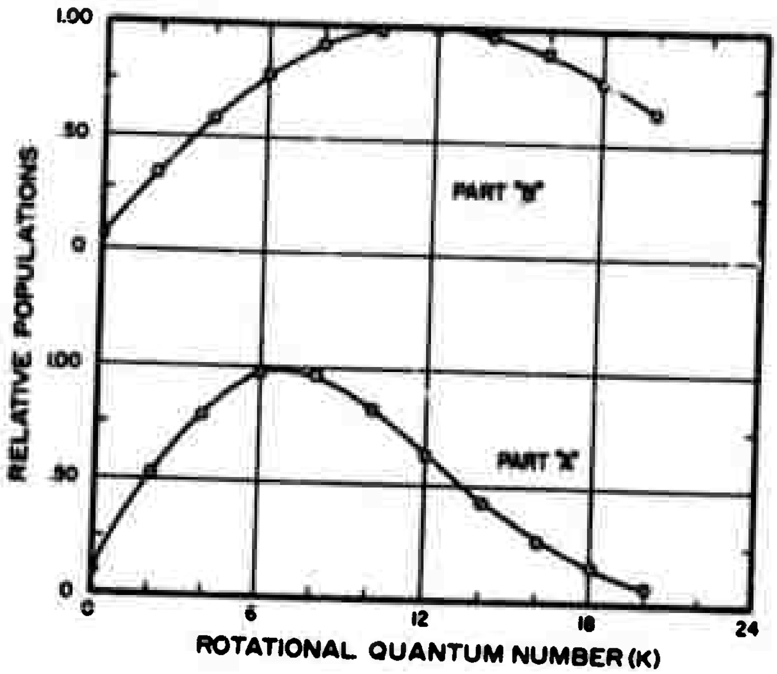

Figure 3. Relative populations of even-K rotational levels for $N_2(X^1\Sigma_g^+, v = 0)$ at temperatures of 300°K (A) and 800°K (B).

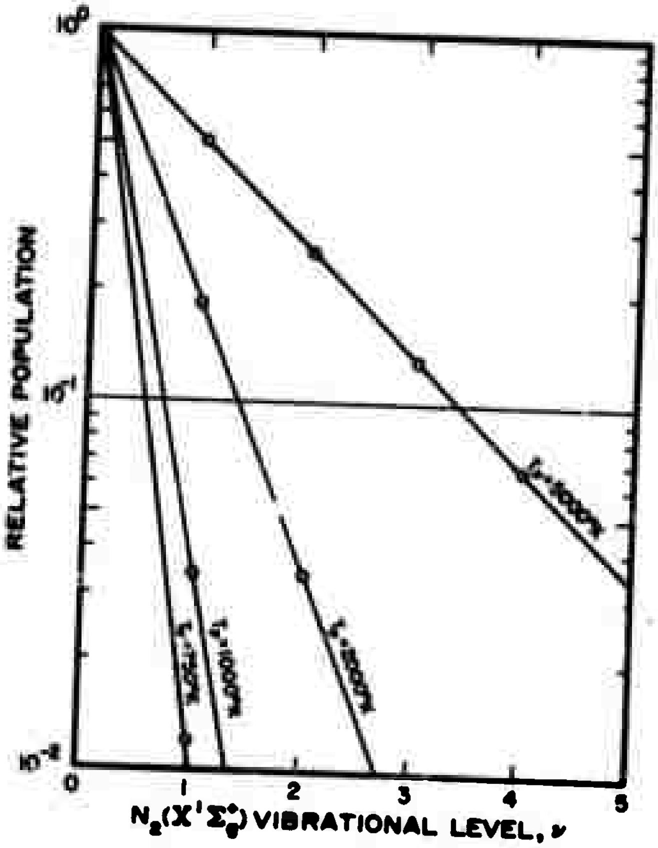

Figure 4. Relative populations of $N_2(X^1\Sigma_g^+)$ vibrational levels at several vibrational temperatures.

follows from expression (9) that the fractional change in the ratio $R_{10} \equiv (N_1/N_0)$ is related to the fractional change in temperature through the expression

$$\frac{dR_{10}}{R_{10}} = \frac{(3380^\circ\mathrm{K})}{T} \quad \frac{dT}{T} \,. \tag{10}$$

The quantities R_{10}, $\frac{dR_{10}}{dT}$, and the logarithmic derivative of R_{10} are displayed as functions of temperature in Fig. 5. It is seen that the optimum sensitivity to temperature change occurs at $T \simeq 1690^\circ$K where $\frac{dR_{10}}{dT}$ assumes its maximum value of about $1.58 \times 10^{-4}/^\circ$K. We shall see shortly that the vibrational development of an electronic band system of N_2 (or N_2^+) may in principle (and in practice) be more sensitive to changes in the N_2 ground-state vibrational temperature than would be expected on the basis of the above discussion.

The concept of "spectroscopic vibrational and rotational temperatures" is of primary interest to the present study. Such temperatures are derived from spectroscopic studies of the intensity distribution of vibrational bands within an electronic band system and from the intensity distribution of the rotational lines within a selected vibrational band. The details of the concept will be presented in the next subsection which deals with the electron-beam-induced luminescence technique of measuring vibrational and rotational temperatures. The usefulness of such "temperatures" depends on an understanding of the excitation and de-excitation processes affecting the excited levels. *We shall see that under certain conditions of excitation and de-excitation the excited-state distributions may reflect those in the ground state of the neutral molecule.*

Electron-Beam-Induced Luminescence Technique

An excellent introduction to the electron-beam-induced luminescence technique of studying basic physical properties of rarefied gas flows may be found in the review of the technique by Muntz (1968). Basic studies by Muntz (1962), Hunter (1967), and Hoppe (1968) relating to the validity of the technique are of special interest to this study. The present coverage

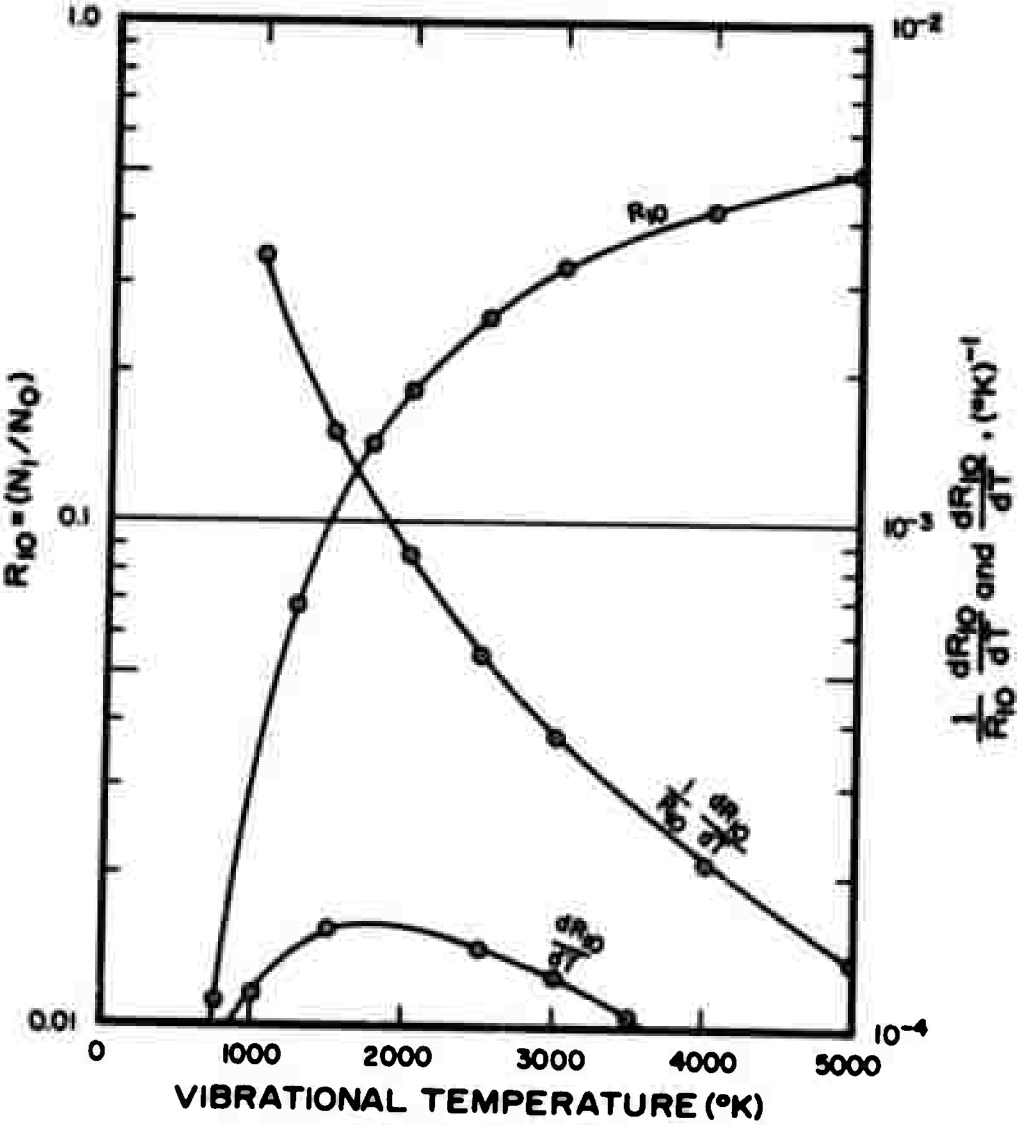

Figure 5. The quantities R_{10} ($\equiv N_1/N_0$), (dR_{10}/dT), and the logarithmic derivative of R_{10} versus $N_2(X^1\Sigma_g^+)$ vibrational temperature.

of the technique will be limited to its essential features as they apply to the study herein described.

Consider the passage of well-defined beam of nearly monenergetic electrons into a low-pressure target of N_2. Assume that the N_2 in in thermal equilibrium at temperature T. The beam will be attenuated as it passes through the gas; however, for sufficiently high energy or low pressure, the mean free path of the beam electrons will become great enough to permit measurement of the intensity under essentially single-collision conditions. The desired condition is most easily realized by examining the emissions from a small section of beam close to the point where the beam impinges on the target.

It is reasonable to assume that for an energetic electron beam (energy ~ 1 keV) impinging on a gaseous target the only significant energy-loss mechanisms are excitation and ionization of the target molecules. (For beam energies of somewhat less than $m_0c^2 \doteq 0.51$ MeV, bremsstrahlung production may be ignored.) The production and loss of excited target particles along the beam path may be described by a rate equation

$$\frac{dN_j}{dt} = P_j - L_j \ , \tag{11}$$

where N_j is the concentration of species j, P_j is the volume production rate of the species, and L_j is the volume loss rate.

Numerous optical excitation studies of the B-state of N_2^+ have shown that the emission intensities of vibrational bands belonging to the v'' progressions with $v' = 0$ and 1 of the N_2^+ first negative ($1N$) system $[B^2\Sigma_u^+ - X^2\Sigma_g^+]$ are directly porportional to both beam current and pressure over a relatively wide range of both variables. The emission intensity per unit volume of the (v',v'') band is given by

$$I_{v'v''} = E_{v'v''} \, A_{v'v''} \, N_{v'} \ , \tag{12}$$

where $E_{v'v''} = hc\lambda_{v'v''}^{-1}$ is the average energy per photon, $A_{v'v''}$ is the Einstein A coefficient for the (v',v'') transition, and $N_{v'}$ is the concentration of ions in the v' vibrational level of the N_2^+ B-state.

The proportionality of $I_{v'v''}$ to the product NI, where N is the target concentration and I the beam current, thus implies that $N_{v'}$ is proportional to the product. It is easily shown from Eq. (11) that under steady-state conditions $N_{v'}$ is given by the expression

$$N_{v'} = \left(\frac{\sigma_{v'}}{A_{v'}}\right) \left(\frac{JN}{e}\right) \tag{13}$$

where $\sigma_{v'}$ is the total direct excitation cross section for level v', $A_{v'} = \sum A_{v'v''}$ is the total transition probability from v' to lower optically accessible levels, and (J/e) is the flux density of electrons. Expression (13) is valid provided simultaneous ionization-excitation of $N_2(X^1\Sigma_g^+, v)$ to $N_2^+(B^2\Sigma_u^+, v')$ is the only population mechanism, and spontaneous decay is the only depopulation mechanism. Thus, the expression for $I_{v'v''}$ may be written

$$I_{v'v''} = E_{v'v''} \left(\frac{A_{v'v''}}{A_{v'}}\right) \sigma_{v'} \left(\frac{JN}{e}\right) . \tag{14}$$

It is seen from Fig. 4 that for vibrational temperatures of less than about 500°K a negligible fraction ($\leq 10^{-3}$) of the target molecules is in excited vibrational levels. The "critical temperature" above which excitation from vibrational levels of $N_2(X^1\Sigma_g^+)$ with $v \geq 1$ must be considered depends on the $N_2^+(B^2\Sigma_u^+)$ vibrational level under consideration and the criterion used. For example, if one accepts a one percent contribution as satisfactorily defining the critical temperature, then the critical temperatures for the $v' = 0$, 1, and 2 B-state vibrational levels are *expected* to be about 1360, 530 and 370°K, respectively.

When the direct contribution to the excitation of the v' level of the B-state from N_2 ground-state levels with $v \neq 0$ can not be ignored, one must write Eq. (14) in the form

$$I_{v'v''} = E_{v'v''} \left(\frac{A_{v'v''}}{A_{v'}}\right) \left(\frac{J}{e}\right) \sum_{v} \sigma_{vv'} N_v . \tag{15}$$

Equation (14) forms the basis for both number density and ground-state vibrational temperature measurements by means of electron-beam-induced luminescence. At a given temperature and beam current density, $I_{v'v''}$

is proportional to the total ground-state concentration since $N_v \propto N$. Hence, an instrument which provides a measure of $I_{v'v''}$, or a proportional quantity, can readily be calibrated to yield N.

The usefulness of Eq. (15) in determining $N_2(X^1\Sigma_g^+)$ vibrational temperatures, or ground-state vibrational temperatures of other molecules, depends on the applicability of certain assumptions. In addition to the assumptions which were made in deriving Eq. (15), one must also assume that the ground-state vibrational population can be represented by Eq. (9). With this assumption, equation (15) takes the form

$$I_{v'v''} = E_{v'v''} \left(\frac{A_{v'v''}}{A_{v'}}\right) \left(\frac{JN}{eZ}\right) \sum_v \sigma_{vv'} \exp\left(-E_v/kT\right) . \qquad (16)$$

The vibrational development of the N_2^+ 1N system for various N_2 ground-state vibrational temperatures should be described by Eq. (16) provided the pertinent assumptions are satisfied.

From the point of view of the experimentalist, it is convenient to examine the ratio of $I_{v'v''}$'s for two bands for which v' differs. For example, consider the ratio of $I_{v'v''}$'s for the (0,1) and (1,2) bands of the N_2^+ 1N $\Delta v = -1$ sequence. Denote the ratio by $R_0^1(T)$ to write

$$R_0^1(T) = \frac{E_{(1,2)}}{E_{(0,1)}} \frac{A_{(1,2)}}{A_1} \frac{A_0}{A_{(0,1)}} F_0^1(T) , \qquad (17)$$

where

$$F_0^1(T) = \sum_v \sigma_{v1} \, e^{-E_v/kT} \Big/ \sum_v \sigma_{v0} \, e^{-E_v/kT} . \qquad (18)$$

Experimental values of $\sigma_{0v'}$ are available for $v' = 0$, 1, 2, and 3 [Stanton and St. John, 1969]; however, it does not appear that experimental information is available regarding the other $\sigma_{vv'}$. Consequently, in order to complete the model, it is necessary to theoretically estimate the values of the unknown excitation cross sections.

Nicholls (1962) has shown that the application of the familiar Born and Born-Oppenheimer approximations to the quantum-mechanical treatment of the excitation problem yields the approximate formula

$$\sigma_{vv'} = \sigma_0(\bar{r}_{vv'})\, q_{vv'} , \qquad (19)$$

where $\sigma_0(\bar{r}_{vv'})$ is the excitation cross section calculated for a vertical (Franck-Condon) excitation at an internuclear distance $\bar{r}_{vv'}$, and $q_{vv'}$ is the Franck-Condon factor for the excitation transition. *Nicholls suggests that* $\sigma_0(\bar{r}_{vv'})$ *is probably relatively slowly varying with* $\bar{r}_{vv'}$. However, this point, although sound theoretically, has not received a great deal of experimental verification.

In previous attempts to determine ground-state vibrational temperatures through the use of electron-beam-induced luminescence, $\sigma_0(\bar{r}_{vv'})$ has been treated as a constant, independent of the *r*-centroid of the excitation transition. Hence, the σ's in Eq. (18) are replaced by the appropriate Franck-Condon factors. Two of the resulting functions, $F_0^1(T)$ and $F_0^2(T)$, are shown in Fig. 6 for vibrational temperatures extending to 2500°K. RKR Franck-Condon factors (Cartwright, 1971) were used.

The theoretical model developed above has been tested by Hunter (1967) and Hoppe (1968). They examined the vibrational development of the N_2^+ 1*N* system excited by 28-keV electron impact on a "static", temperature-controlled $N_2(X^1\Sigma_g^+)$ target. Intensity ratios of $v' = 0$ and 1 bands in the $\Delta v =$ -2 and -1 sequences were studied over a range of gas temperatures between 300 and about 1000°K. The residence time of the N_2 molecules in the heated collision chamber is estimated to be $\sim 10^4$ sec, a value which should be long enough to ensure *V-T* equilibration.

The results of their study of $I_{(0,1)}/I_{(1,2)}$ are shown in Fig. 7. It is seen that the experimental points lie close to but systematically above the theoretical curve based on Eq. (18). The major source of uncertainty in $I_{(0,1)}/I_{(1,2)}$ at temperatures above 400°K was attributed to the necessity of unfolding the blend of the rotational structure of the (0,1) band (*R*-branch) with that of the (1,2) band. It was estimated that the overall uncertainty in the vibrational temperature determination was approximately ±15%.

The basis for $N_2(X^1\Sigma_g^+)$ rotational temperature measurements using the electron-beam-induced luminescence technique is illustrated in Fig. 8 which presents spectral scans of the *R*-branch rotational structure of the N_2^+ 1*N* (0,0) band at gas temperatures of 300°K (part a) and 800°K (part b). The data were obtained by Hunter (1967) using the special test facility mentioned

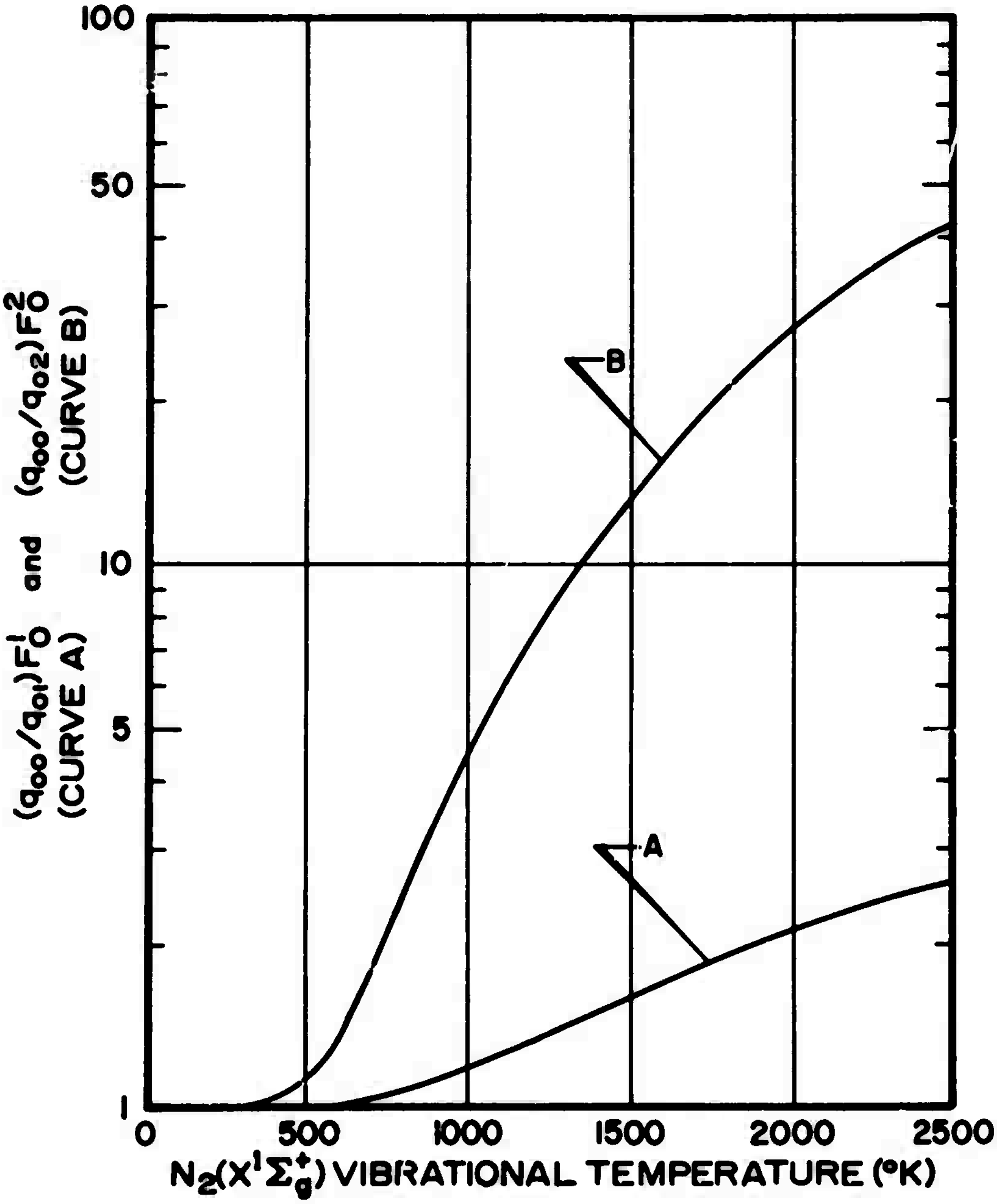

Figure 6. Normalized values of $F_0^1(T)$ Eq. (18) and $F_0^2(T)$ versus $N_2(X^1\Sigma_g^+)$ vibrational temperature.

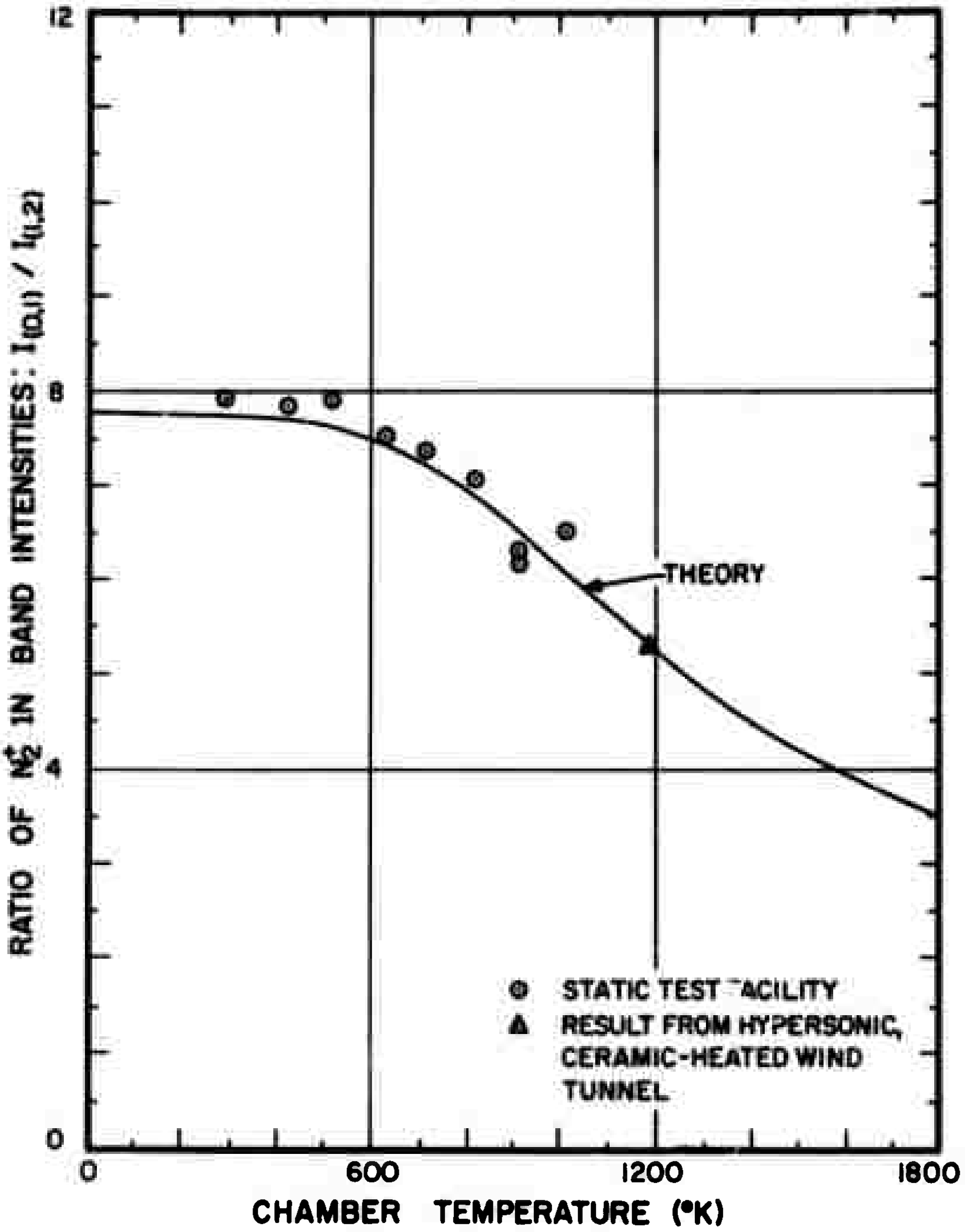

COMPARISON OF EXPERIMENTAL VIBRATIONAL TEMPERATURES WITH PREDICTIONS OF THE THEORETICAL MODEL.

Figure 7. Comparison of experimental N_2^+ 1N band intensity ratios at various gas temperatures with predictions of the theoretical model (Adapted from Hoppe, 1968).

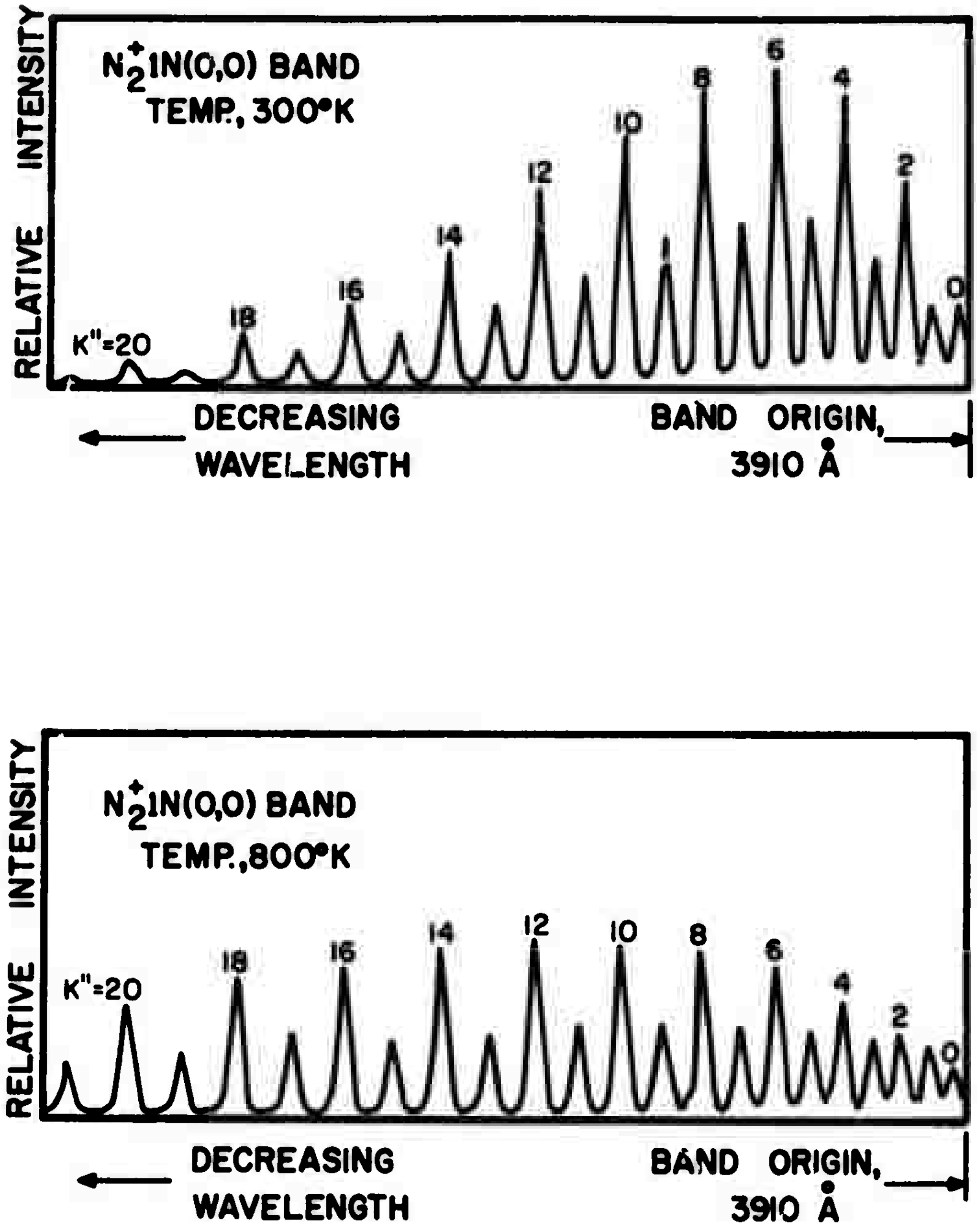

Figure 8. Spectral scans of N_2^+ 1N (0,0) R-branch rotational structure at gas temperature of 300°K (upper scan) and 800°K (lower scan) [after Hunter, 1967].

above. It is seen that the intensity distribution among the R-branch rotational lines changes markedly between 300 and 800°K. The intensity maximum shifts from the $K'' = 6$ line to the $K'' = 12$ line, and a pronounced spreading of the distribution occurs. Hence, a quantitative measure of the change in the distribution can in principle be used as a measure of the rotational temperature of $N_2(X^1\Sigma_g^+)$.

Muntz (1962) has predicted theoretically the dependence of the N_2^+ 1N rotational structure on the $N_2(X^1\Sigma_g^+)$ rotational temperature to be expected under single-collision conditions. He assumed that simultaneous ionization-excitation was the only significant N_2^+ B-state population mechanism and that no collisional redistribution of rotational energy occurred in the excited state. The optical selection rules for Hund's case (b) [Herzberg, 1950] were applied to the excitation transitions, i.e. it was assumed that both the $X^1\Sigma_g^+$ and $B^2\Sigma_u^+$ states belong to Hund's case (b) and consequently that $\Delta K = \pm 1$ are the only allowed excitation transitions. Muntz's rather lengthy treatment will not be presented here.

Muntz (1962) tested his rotational-temperature model at known gas temperatures of 298 and 373°K and found satisfactory agreement between theory and experiment. Hunter (1967) extended the range of investigation to about 1000°K. Hunter's results are shown in Fig. 9 where the difference between the spectroscopically inferred temperature T_r and the measured gas temperature T, expressed as percent difference, is plotted versus the gas temperature. The small but systematic difference in the two temperatures was discussed by Hunter (1967), but no definitive conclusion was reached.

The electron-beam-induced luminescence (EBIL) technique has previously been applied to atmospheric $N_2(X^1\Sigma_g^+)$ rotational temperature measurements by DeLeeuw and Davies (1969). A two-channel photometer was used to monitor the change in the N_2^+ 1N (0,1) rotational structure as a function of altitude. The information was then interpreted in terms of N_2 ground-state rotational temperature by use of the model discussed above.

Although the EBIL technique has found extensive laboratory application in the study of low-density gaseous flows (Muntz, 1968), its potential usefulness in upper-atmospheric research has yet to be fully realized.

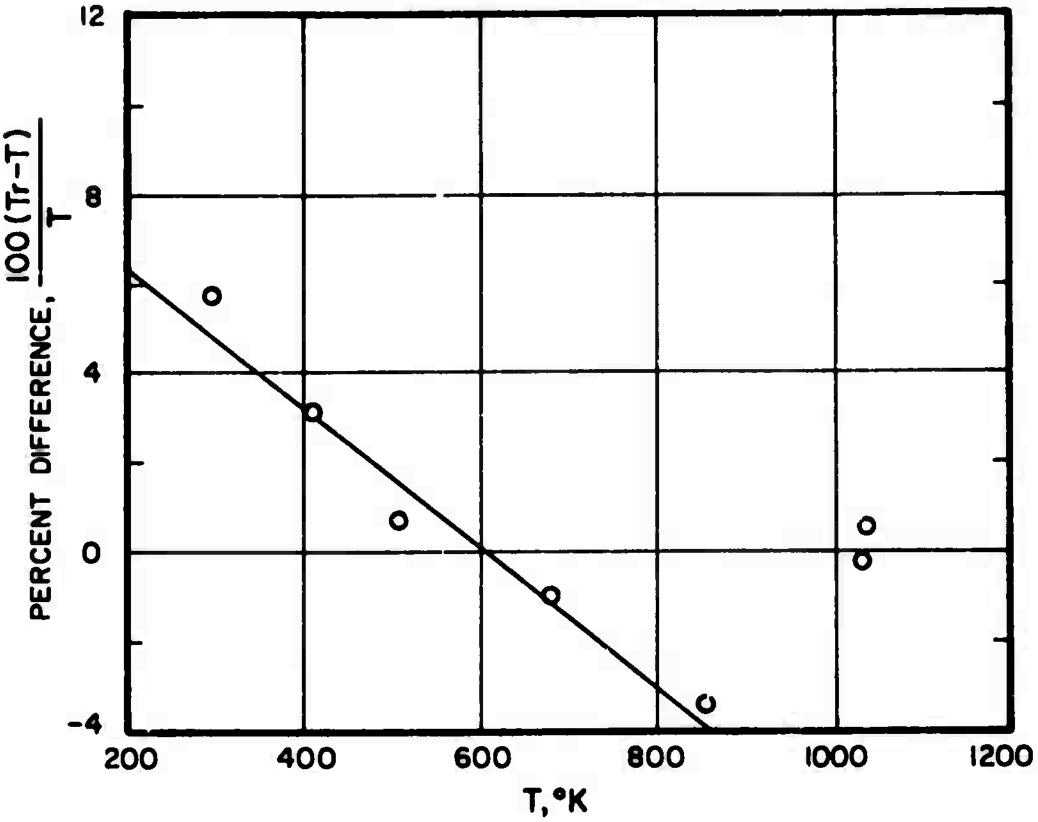

RESULTS OF T_r TESTS FOR TEMPERATURES OF 300° TO 1000° K. GAS NUMBER DENSITY OF 5×10^{15} cm^{-3}.

Figure 9. Comparison of $N_2(X^1\Sigma_g^+)$ rotational temperatures (T_r) with gas temperatures [after Hunter, 1967].

ELECTRON-BEAM-INDUCED LUMINESCENCE SYSTEM: DESIGN CONSIDERATIONS

A number of EBIL systems for laboratory studies of the properties of gaseous flows have been described in the literature. The review by Muntz (1968) identifies most, if not all, of the EBIL-related studies reported through mid-1968. Several such studies have subsequently been reported in the literature of rarefied-gas dynamics; however, it is beyond the scope of this report to cite all of the pertinent studies. The basic features common to the various EBIL systems are an electron-beam generator to stimulate the gaseous sample to emission, an optical detection system to monitor the intensities of spectrally-selected, beam-excited emissions, and in cases where the number density of the sample is of interest, a monitor to provide a measure of relative and/or absolute beam current. A number of methods exist both for generating the electron beam and for spectrally selecting the emission features of interest.

It appears that the first successful application of the EBIL technique to the study of selected properties of the upper atmosphere was carried out by DeLeeuw and Davies (1969), whose EBIL system has been reported (DeLeeuw and Davies, 1969). They used a dc-operated electron gun (2.5 keV) to stimulate the atmosphere to emission and a two-channel photometer to monitor the relative strengths of signals associated with the rotational development of the $N_2^+ 1N$ (0,1) band which then yielded $N_2(X^1\Sigma_g^+)$ rotational temperature. The investigation was carried out over the altitude range between about 65 and 150 km. Background luminescence, attributed to energetic electron bombardment of the collecting lens in their optical system, limited the useful measurement range of the instrument to pressures above about 10^{-5} Torr.

The work described herein was undertaken with minimal lead time (≈ 8 months) to develop a flight-worthy EBIL system. Consequently an attempt was made to use, to the maximum extent feasible, technological innovations which were already flight proven. For example, the electron gun adopted for use in the system was a unit developed by Ion Physics Corporation especially for a rocket-borne electron accelerator. The accelerator was launched in January 1969, prior to initiation of the present work, and an array of ten of the electron guns yielded outputs of up to 490 mA at 8.7 keV.

Similarly, a variant of flight-proven photometers developed at USU for auroral intensity measurements was adopted for use in monitoring the beam-excited emissions.

In this section of the report, consideration is given to several factors which are basic to the developement of a rocket-borne EBIL system. As indicated in the preceding paragraph, the short period of time available for developmental work resulted in the necessity of flying a system which did not offer "state-of-the-art" solutions to the various design criteria.

Selection of the Sample Region

In applying the EBIL technique to upper atmospheric measurements using sounding rockets, care must be exercised to ensure that the results are not seriously influenced by the vehicle. Ideally the sample region should be far enough from the vehicle to ensure that the results reflect the properties of the undisturbed atmosphere. The molecules in a given volume element near the vehicle may be classified according to their "origin." At least four classes of molecules are possible. These include: (1) ambient air molecules (undisturbed), (2) molecules which have interacted with the vehicle, (3) molecules associated with vehicle exhaust gases (or other gases escaping from the interior of the vehicle), and (4) molecules associated with outgassing from the surface of the vehicle.

It is of course desirable to minimize sources (2)—(4). Source (3) may be minimized by sealing the fuel and oxidizer tanks of the rocket motor soon after burnout. In addition, the influence of gases escaping from the interior of the vehicle can be minimized by using standard high-vacuum techniques in the construction of the payload and by providing a high conductance between the interior of vehicle and its surroundings. The high conductance will facilitate rapid clean up of the interior region.

In an attempt to minimize sources (2)—(4), DeLeeuw and Davies (1969) used a pre-evacuated, clam-shell nosecone which was deployed at a suitable altitude. They also separated the rocket motor from the experimental package after the clam shells had been jettisoned. The procedures resulted in dynamical stability problems with the payload section; however, the general concept is attractive from the standpoint of the ideal experiment.

The Aerobee 150 sounding rockets typically attain supersonic velocities at very low altitudes. Hence, a shock wave is produced by surfaces having a projection in the direction of motion. The cone within which the disturbances are confined, the so-called *Mach cone*, is characterized by the semivertex angle (Mach angle) which is related to the Mach number (M) by $\sin \alpha = (1/M)$. The Mach angle decreases until burnout occurs ($\approx$ T + 52 sec), whereupon it gradually increases up to altitudes $\approx$ 80-90 km. The shock structure becomes diffuse above roughly 90 km and the flow passes from the transitional regime in the region $\approx$ 90-110 km to free-molecule flow (FMF) above roughly 110 km.

Since it was originally anticipated that much of the useful data would be collected at altitudes above about 100 km, some attention was given to the theoretical description of the FMF field. Bird (1960) has treated the FMF fields of moving objects of varying geometry. However, his results are strictly valid only for points at distances from the object which are large compared with the typical dimensions of the object but somewhat less than the molecular mean free path. Bird further shows for a typical case that reasonable accuracy is obtained when the distance to the point in space is only slightly larger than a typical dimension of the body.

Bird's result for the number density of *reflected molecules* at a radial distance r from a cone of base radius r_0 and semi-vertex angle ζ is

$$N_r = \frac{N\chi}{4\pi} \left(\frac{r_0}{r}\right)^2 \sqrt{(T/T')}\, F_1(\phi_r,\zeta) \ , \qquad (19)$$

where

N ≡ the ambient number density,

$\chi \equiv \exp(-s^2 \sin^2 \theta) + \sqrt{\pi}\, s \sin \theta [1 + \mathrm{erf}(s \sin \theta)]$,

T' ≡ the temperature of the reflected molecules,

T ≡ the temperature of the ambient gas,

ϕ_r ≡ the angular position of the point as measured from the axis of the cone,

s ≡ ratio of the speed of the object to the most probable kinetic molecular speed,

$\theta \equiv$ the angle between the tangent line to the surface element and the direction of motion,

$$F_1(\phi_r,\zeta) = \cos\phi_r[\pi - \cos^{-1}(\cot\phi_r \tan\zeta)] +$$

$$\sin\phi_r \cot\zeta \sin[\pi - \sin^{-1}(\cot\phi_r \tan\zeta)], \text{ and}$$

$$\cos^{-1} a = \begin{cases} 0, & a > 1 \\ \pi, & a < -1 \end{cases} .$$

In deriving equation (19), it was assumed that diffuse reflection occurred and that the "angle of attack" was zero, in addition to the restrictions which have previously been mentioned.

It is seen that for fixed ϕ_r (and θ) the number density of reflected molecules decreases as $(r_0/r)^2$. Assuming $\zeta = 6°$, $\phi_r = 84°$ (along normal to surface of cone), $\theta = \zeta$, $s = 3$, and $T' = T$, one finds that (N_r/N) is less than 10 percent for $r > 3.6\ r_0$. The function $F_1(\phi_r,\zeta) \to 0$ as $\phi_r \to 174°$.

It is instructive to consider the case of a circular disk of radius r_0. The formalism of Bird (1960) yields the expression

$$N_r = \frac{N\chi}{4}\sqrt{(T/T')}\left(\frac{r_0}{r}\right)^2 \tag{20}$$

for the density of reflected molecules along the axis of the disk. In deriving the expression, it must be assumed that all of the surface elements of the disk are at the origin. When allowance is made for a *finite distribution* of surface elements, the result takes the form

$$N_r = \frac{N\chi}{2}\sqrt{(T/T')}\{1 - [1 + (\frac{r_0}{r})^2]^{-\frac{1}{2}}\} , \tag{21}$$

where r is measured from the center of the disk to a point P along the axis. If one assumes $\theta = \frac{\pi}{2}$, $s = 3$, and $T = T'$, he finds that the number density of reflected molecules along the axis is given by

$$N_r = (5.4\,N)\,\{1 - [1 + (\frac{r_o}{r})^2]^{-\frac{1}{2}}\} \qquad (22)$$

or when $r > r_o$

$$= (2.7\,N)\,(\frac{r_o}{r})^2\,[1 - \frac{3}{4}(\frac{r_o}{r})^2 + \cdot\cdot\cdot]. \qquad (23)$$

It is obvious from these considerations that the sample region should be as far away from the vehicle as is feasible from sensitivity considerations or other restrictions. It is also desirable to shield the critical surfaces aerodynamically so that a minimum number of molecules will strike them. The location of the EBIL experiment toward the nose of the rocket is desirable from the standpoint of minimum disturbance during the up-leg of a flight; however, during the down-leg the experiment will be predominantly in the "wake" unless an attitude-control system is employed to turn the vehicle around as it approaches apogee.

Electron Gun Requirements

The power, electron energy, and geometry of the beam formed by the electron gun are of concern in the design of a suitable probe system. In addition, the acceptable operating environment (total pressure and gas composition) for the gun must be known, especially if the gun is to be operated without recourse to differential pumping. Cathode poisoning (and erosion) and electrical high voltage breakdown must be considered.

The beam power must be sufficient to yield a statistically acceptable measure of the intensity of the spectral feature of interest under given conditions of electron energy, system geometry, detection-system responsivity, measurement time interval, and target density. The energy of the electrons will influence the intensity of the beam-excited emissions, the scattering of the beam electrons, and the magnetic rigidity of the beam. The emission cross sections for most of the spectral features of interest to this study exhibit broad maxima in the vicinity of 100eV. However, a somewhat higher energy is found to be desirable when scattering and magnetic rigidity of the beam are considered.

The electron energy should be high enough to ensure negligible scattering of the beam at the highest pressure of interest. In the present context, "negligible scattering" implies that an arbitrarily small fraction (say $< 10^{-2}$) of the beam electrons is scattered outside of the probing volume and the beam-collector entrance. The beam scattering at a given energy will depend on the target number density, composition (effective atomic number), scattering cross section, and path length. The attenuation of a well-collimated beam of monoenergetic electrons of initial intensity I_0 in traversing a uniform target of number density N is described by the equation

$$I(x) = I_0 \exp\left(-N q_s x\right) , \tag{24}$$

where I is the intensity of the unscattered component at depth x and q_s is the scattering cross section.

For electron energies above the minimum excitation threshold for the target molecules, the total scattering cross section may be represented by $q_s = q_e + q_i$ where q_e and q_i are the elastic and inelastic scattering cross sections, respectively. The angular distribution of the scattered electrons is dependent on the electron energy, and the scattering intensity rises sharply with increasing atomic number. The number of electrons which are scattered outside the aperture of the beam collector will thus depend on the beam energy and the effective Z of the target for fixed geometry and target density.

The ratio of the total inelastic—(q_i) to—elastic (q_e) scattering cross sections has been shown by Lenz (1954) to be given approximately by

$$(q_i/q_e) = (4/Z)\, \ell n\, (2\hbar\, v_e\, Z^{1/3}/I a_0) , \tag{25}$$

where Z is the atomic number of the target, I the ionization energy, v_e the electron speed, a_0 the radius of the first Bohr orbit, and $\hbar$ Planck's constant divided by 2π. Hence, elastic scattering becomes relatively more important the greater the atomic number of the scatterer and the lower the velocity of the electrons.

In order to ensure small beam attenuation at the highest pressures of interest, it is necessary that $N_m q_s L << 1$, where N_m is the maximum number density of the target and L is the path length between beam source and collector. The distance L must be sufficient to prevent serious flow-field perturbations of the target in the region where measurements are desired. Hence, the selection of L permits one to evaluate the required beam energy (E_e) provided $q_s(E_e)$ is known. For example, consider the case of 2.5-keV electrons incident on a 10^{-3} Torr (and 300°K) nitrogen target. The total scattering cross section is roughly 5×10^{-17} cm^2 which dictates that L be less than about 29 cm to ensure less than 5% scattering loss.

The intrinsic geometry of the beam formed by the electron gun together with the field of view of the optical detection system will affect the spatial resolution of the beam probe. The design of a suitable beam collector will also depend on the beam geometry. Owing to effects such as space-charge spreading and "gas focusing" the geometry of the beam will in principle be affected by the target density even in the single-collision domain. It is expected that space-charge spreading will become important at very low pressures where the positive ion density in the beam region is insufficient to effectively neutralize the negative space charge of the electron beam (Field, Spangenberg, and Helm, 1947). "Gas (or ion) focusing" may become important at higher pressures if the positive ion density in the beam region approaches or exceeds the effective electron density (Halsted and Dunn, 1966).

The properties of the electron gun which was adopted for use in the EBIL system will be described in the INSTRUMENTATION section of the report.

Detection System Sensitivity Requirements

The strength of the electron-beam-induced emission of interest and the optical coupling of the source to the detector are necessarily connected with the problem of instrument sensitivity requirements. The strength of the emission of interest may be estimated from Eq. (14) [or (15)] when it is known *a posteriori* that the equation is applicable. The quantities $\sigma_{v'v''} = (A_{v'v''}/A_{v'})\,\sigma_{v'}$, the so-called emission cross sections, are available in the literature for a relatively large number of molecular emissions. Hence, one may conveniently estimate the volume emission rate of photons in the (v', v'') transition by specifying a beam current density and a target number density. The throughput (product of collecting area, collecting solid angle, and transmission) of the optical system may then be used to estimate the irradiance at the detector. The bandpass characteristics of the spectrally selective component in the optical system must of course be used to determine the effective transmission factor for the rotational structure of the (v', v'') transition.

It is desirable to select a detector which offers a high quantum efficiency at the wavelength of interest and has a low intrinsic noise level. In the case of multiplier phototubes, the intrinsic (dark) noise may be markedly reduced by cooling the tube. However, in order to avoid the complications attendant with cooling, one may consider a tube which has the most favorable (largest) ratio of quantum efficiency (at the λ of interest) to dark noise in order to see if it meets the requirements of the experiment. The photomultipliers having bialkali (SbKCs) photocathodes offer quantum efficiencies ranging from 20 to 30% at the peak wavelength of 3800 Å coupled with very low dark currents at temperatures $\leq 20^{\circ}$C. Owing to the increase of photo-surface resistivity with decreasing temperature, the tubes are not generally cooled below about -5°C. The RCA-4516 photomultiplier tube was adopted for the present application. Its properties will be discussed under INSTRUMENTATION.

When the "light" signals to be measured result in photomultiplier currents which approach the level of the tube dark current, consideration should be given to the methods of photomultiplier noise suppression and to the relative advantages of operating the photomultiplier in the current (analog) mode as compared with the photon-counting (digital) mode. It has been shown (Alfano and Ockman, 1968) that under certain operating conditions the photon-counting mode of operation is superior to conventional analog techniques; however, in the present case, it was felt that the added cost, complexity, and developmental time did not justify the improved system performance which might accrue to the digital detection method.

In the interest of optimizing signal-to-noise in the analog mode and of rejecting potential background signals, the lock-in method of detection was selected. It was decided that a detection system bandwidth of about 35 *Hz* was desirable from the standpoint of recovering the important information-carrying frequencies of the signal. Hence, the signal was interrupted at a frequency (350—400 *Hz*) somewhat above the bandwidth figure (35 *Hz*), amplified at the chopping frequency, and then synchronously demodulated in order to recover the original signal information. A variant of the lock-in technique was used in the photometric instrumentation for the first EBIL system, whereas a standard version was used in the instrumentation for the second system.

When intrinsic photomultiplier noise dominates the noise contributions to the output of a lock-in amplifier, the signal-to-noise ratio (S/N) at the output is given by (Ridgway, 1967)

$$(S/N) = (\sqrt{2}/\pi)[f_s/\sqrt{(f_s + 2f_d)Bz}] \ , \tag{24}$$

where f_s is the signal photoelectron rate, f_d the "dark" photoelectron rate, B the bandwidth, and z an excess noise factor which is greater than 1 and may be as high as 4 for a poorer tube. Equation (24) applies under the assumption that a tuned amplifier selects the fundamental component of the square-wave signal.

The signal photoelectron rate required to yield a selected (S/N) value for a given tube (f_d & z) and bandwidth is seen to be

$$f_s = (\alpha/2)[1 + \sqrt{1 + (8f_d/\alpha)}] \ , \tag{25}$$

where $\alpha = (\pi^2/2)(S/N)^2Bz$. A selected RCA-4516 photomultiplier may have an anode dark current of $\simeq$ 0.03 nA at 20°C for a tube gain of $\simeq 10^5$. These figures correspond roughly to an f_d value of 2×10^3 sec^{-1}. If one assumes a bandwidth of 35 *Hz* and an excess noise factor of 2, approximately 4×10^4 signal photoelectrons per second are required to yield a (S/N) of 10. The required signal photon rate at the photocathode will of course depend on the quantum efficiency. For 4000-Å photons the quantum efficiency is about 20%; hence, an input photon rate of 2 x 10^5 sec^{-1} would be required. The corresponding incident power would be $\simeq 10^{-13}$ Watt. It is of interest to compare this figure with the value of approximately 1.8 μW/cm which applies to the power per unit of beam length radiated in the N_2^+1N (0,0) band when a 1-mA beam of 100-*eV* electrons passes through a 20°C, 1-*mT* target of N_2.

Isolation of Spectral Features

Eather and Reasoner(1969) have compared the performance of an interference-filter photometer with that obtainable from other spectrophotometric devices. They conclude that for studies where a bandpass of $\geq$ 2-3 Å is acceptable, the filter photometer has the advantages of higher throughput, smaller size, weight, simplicity, and cost when compared with the best grating spectrometers and Fabry-Perot interferometers. The fixed-filter photometer suffers from lack of wavelength-selection capability without changing filters. The tilting filter photometer surmounts this problem to a certain extent. However, the spectral interval which can be covered with a single filter is relatively small, even if one is willing to accept the complications introduced by the dependencies of instrument bandwidth and integrated transmission on tilt angle. For applications which do not require high-resolution spectral scanning or frequent changes in wavelength selection and bandpass characteristics, the filter photometer is an attractive choice.

The spectral resolution required by the EBIL technique depends on the desired information. For example, in the case of vibrational-temperature measurements, it is desirable to isolate individual vibrational bands of the molecular electronic band system of interest. Further, it is usually advantageous to compare the relative intensities of the members of a *sequence* (or *diagonal group*) [$v' - v'' \equiv$ constant]. As mentioned previously, the N_2^+1N band system was selected for the present application. The spacings between band origins for successive members of a given sequence vary slowly with the vibrational quantum number of the upper level. For the Δv = 0,-1, and -2 sequences, the spacings range from about 20 to 57 Å for members with $v'' \leq 4$.

The rotational structure of the N_2^+1N bands varies markedly with the rotational temperature of the $N_2(X^1\Sigma_g^+)$ molecules when the emissions are produced by energetic electron impact. The significant portion of the rotational structure is spread out over a spectral interval of roughly 30 Å at 300°K. In contrast, the appropriate spectral interval is roughly 70 Å for a rotational temperature of 1000°K. One finds that blending of the rotational structure of adjacent bands in a sequence becomes significant for $T_r \gtrsim 400$°K. Hence, spectral isolation of the bands is not possible at the higher rotational temperatures, and account must be taken of the blending in evaluating vibrational band intensities.

In attempting rotational-temperature measurements, it is desirable that the rotational fine structure of a given vibrational band be resolved and spectrally scanned. A spectral resolution of $\lesssim 0.5$ Å is required to satisfactorily separate the N_2^+1N R-branch rotational lines. The spacings of successive R-branch lines increase with increasing K' (or K''); hence, the required resolution varies across the branch. Such resolution is not adequate to resolve the finer details of the rotational structure (doublet structure of the lines), but this fact is taken into account in the analysis.

The measurement of rotational temperature can also be carried out without recourse to a detailed examination of the R-branch relative line intensities. Muntz and Abel (1964) describe the development of a two-channel, interference-filter photometer which is suitable for rotational-temperature measurements when it is known *a posteriori* that the "thermometric molecules" are distributed in a Boltzmann fashion over the accessible rotational levels. The technique utilizes the change in the ratio of two appropriately selected intensity samples from the (v',v'')-band rotational structure as an index of the rotational temperature. In practice, it is desirable that the system be calibrated over a range of temperatures; however it is also possible to predict the relative variation of the intensity ratio with rotational temperature and to normalize the result to the ratio observed at a single known temperature. The latter approach was followed in the present investigation.

In the case of number-density measurements, the spectral resolution desirable parallels that required for vibrational temperature measurements. The use of a broader passband, which encompasses more than one member of a sequence, is also permissable as long as the spectral region is free from interfering features.

Fabry-Perot type interference filters were selected for use in the present application. The filters easily satisfied the requirements for spectral resolution. Care was taken to ensure that the filters were used under conditions where the effective filter characteristics were not seriously degraded from those for the case of parallel illumination and zero incidence angle. Additional details regarding the application and characteristics of the filters are given in the section on INSTRUMENTATION.

Effect of the Magnetic Field of the Earth

The magnetic rigidity of the beam should be adequate to ensure negligible loss of beam from the collector even in the case of maximum beam deflection. It is also desirable that the beam remain in the field(s)-of-view of the photometer(s) or other spectrally selective optical system. If more than one photometer is used to view the beam emission and output ratios are of interest, the relative responses of the instruments to changes in beam position must be considered. In the case of a rocket-borne EBIL system, the motion of the rocket thorugh the magnetic field of the earth can result in a variable deflection of the electron beam. The possibility of variable deflection arises from the dependence of the deflecting force, $-e(\vec{v}_e \times \vec{B})$, on the angle between the beam direction and the direction of $\vec{B}$. A rapid, cyclic variation of the beam position should correlate with the spin motion of the rocket, and a slow, periodic variation should correlate with the precessional motion.

A beam of monoenergetic electrons initially moving with velocity $\vec{v}_e$ in a direction perpendicular to a uniform magnetic field $\vec{B}$ will follow a circular path of radius $R = (m\, v_e/Be)$, where m is the mass of the electron and e its charge. The deflection of the beam from its initial direction of motion is described by the equation

$$\delta\rho = R[1 - \sqrt{1 - (Z/R)^2}] \ , \tag{26}$$

where $Z \leq R$ is the distance from the initial point to the point where the deflection is being considered and $\delta\rho$ is measured along the perpendicular to the original direction of motion.

The magnetic rigidity, BR, of the electron beam is determined by the speed of the beam electrons or, equivalently, by the square root of the beam voltage for fixed B. In the present application, it was anticipated that the path length between electron gun and beam collector would be ~0.5 m. It is desirable to have R somewhat greater than this figure. The R for a 2.5-keV electron beam is approximately 3.4 m in a magnetic field of 0.5 gauss, and the maximum deflection is expected to be about 4 cm when Z = 0.50 m. If the observation region is located at ($Z/2$), the maximum deflection at this position becomes approximately 1 cm. Preliminary calculations indicated that deflections of this magnitude at the observation region and at the collector could be tolerated for the EBIL system which was envisioned.

Rejection of Background Radiation

Nighttime background sources which could in principle affect the measurements of interest include aurora, airglow, moonlight, starlight, and zodical light. Aerobee AO 3.006-1 was flown into a rather intense auroral display. In order to prevent the photometric instruments from viewing the auroral emissions, a low-reflectance optical backstop was used to essentially fill the fields of view of the beam-oriented photometers (Fig. 12). Auroral emissions were no doubt produced in the region between the photometers and the optical backstop; however, the integrated effect should have been essentially negligible owing to the rather small ratio ($J_{\text{auroral}}/J_{\text{beam}}$), where the J's refer to electron current densities. The contributing volumes are of course different, but not nearly enough to offset the difference in current densities. Aerobee AO 3.910-1 was flown under conditions where background should have been minimal, and, as a result, the optical backstop was eliminated.

In order to further reduce background problems, lock-in detection systems, or a variant thereof, were used. The rejection of asynchronous optical signals by the first-generation instruments, which utilized a dc-reset amplifier, was found to be somewhat less than anticipated; however, the use of standard lock-in amplifiers in the second-generation units resulted in much improved rejection characteristics. The signal information was chopped electrically at a rate of about 400 *Hz*, amplified by a bandpass amplifier ($\Delta f \simeq 30$ cps) at that frequency, and then synchronously rectified and converted to an equivalent bandwidth at zero frequency.

It appears that the most troublesome background signal arose from the interaction of beam-associated electrons with as yet unidentified components of the payload. A similar problem occurred during laboratory calibration of the two payloads. Fairly extensive tests were conducted in an effort to identify, and possibly eliminate, the background source; however, no satisfactory solution was forthcoming. The beam-induced background problem will be discussed in more detail in a later section of the report.

Vehicle Charge Build-Up

The free-space capacitance of the rocket is so small (~ 100 pF) that charge loss during operation of the electron gun is potentially of concern. In order to reduce the problem, a beam collector may be used; however, several factors operate to reduce the collection efficiency to less than 100%. The loss of electrons from the rocket system tends to drive the potential of the vehicle positive with respect to the surrounding ionospheric plasma. The vehicle will then act much like the Langmuir probe and will begin to draw a return current through the plasma. If the plasma is not capable of providing an adequate return current for a given potential difference, one might expect the potential difference to increase until an adequate return current is reached.

The problem of vehicle voltage-versus-current characteristics has been considered by Hess *et al.* (1969) who provide several pertinent references. The Langmuir probes included in the two Aerobee payloads supplied information on the vehicle-to-plasma potential. The results will be discussed in a later section of this report.

INSTRUMENTATION

General Description of Payloads

The payloads for the two Aerobee rockets were similar in design. The primary instrumentation consisted of a pulsed "electron accelerator" for stimulating the atmosphere to emission and an array of photometers, phase-locked to spectrally-selected, beam-excited emissions, for obtaining ambient atmospheric temperature and density information. The EBIL system also contained a boom-mounted Faraday collector which provided a return path for the charge associated with the electron beam. Although not highly efficient, the beam collector served to reduce vehicle-charging effects to an acceptable level.

The EBIL system for Aerobee A03.006-1 also contained an optical backstop which prevented the beam-oriented photometers from viewing unwanted auroral emissions. The optical backstop was omitted from the EBIL system for Aerobee A03.006-1 since it did not appear to be a necessity under anticipated flight conditions. However, an in-flight calibration light was added to the second system in an effort to reduce the uncertainty of the temperature and number density measurements.

In addition to the EBIL system, each of the payloads contained instrumentation to provide supporting measurements and other measurements of interest to the solar-terrestrial relationship. A summary of the various instruments contained in each of the payloads is presented in Tables I and II. The instruments are discussed in moderate detail later in this section of the report.

Aerobee A03.006-1 was designed for measurements during active auroral conditions when enhanced $N_2(X)$ vibrational temperatures may occur. Views of the payload configuration are shown in Figs. 10 and 11. The nosecone contained doors and a nose tip which were ejected after the vehicle had passed through the dense portion of the atmosphere. The first door to be ejected exposed the soft-electron spectrometer and the energetic particle counter both of which had look angles centered 30° above the normal to the spin axis of the rocket. Next the boom doors and nose tip were simultaneously ejected. Ejection of the nose tip exposed the nominally

Table I. Payload Instrumentation: Aerobee A03.006-1

Measurement	Instrument	Spectral Feature or Response
T_v of $N_2(X)$	EBIL system	N_2^+ 1N (0,1); (0,2); (1,2); and (2,4)
$[N_2]$	EBIL system	N_2^+ 1N (0,1)
T_e and N_e	Langmuir probe	
Primary auroral electron flux	Geiger counters	Range: (1) $E_e \geq 6.5$ keV (2) $E_e \geq 17$ keV (3) $E_e \geq 42$ keV (4) $E_e \geq 90$ keV
Primary & secondary auroral electrons	Soft-electron spectrometer	50 eV - 12 keV
Auroral emissions	dc-logarithmic photometers	N_2^+ 1N (0,0) [OI] $^1S \rightarrow {}^1D$

Table II. Payload Instrumentation: Aerobee A03.910-1

Measurement	Instrument	Spectral Feature or Response
T_v of $N_2(X)$	EBIL system	N_2^+ 1N (0,1); (1,2); (2,4); and (3,5)
T_r of $N_2(X)$	EBIL system	N_2^+ 1N (0,1); two samples
$[N_2]$	EBIL system	N_2^+ 1N (0,1) and (1,2)
$[O_2]$	EBIL system	O_2^+ 1N $\Delta v = +1$ sequence
T_e and N_e	Langmuir probe	
Earth shine	IR earth-scan radiometer	
[O]	Thin-silver-film "resistivity" sensor	

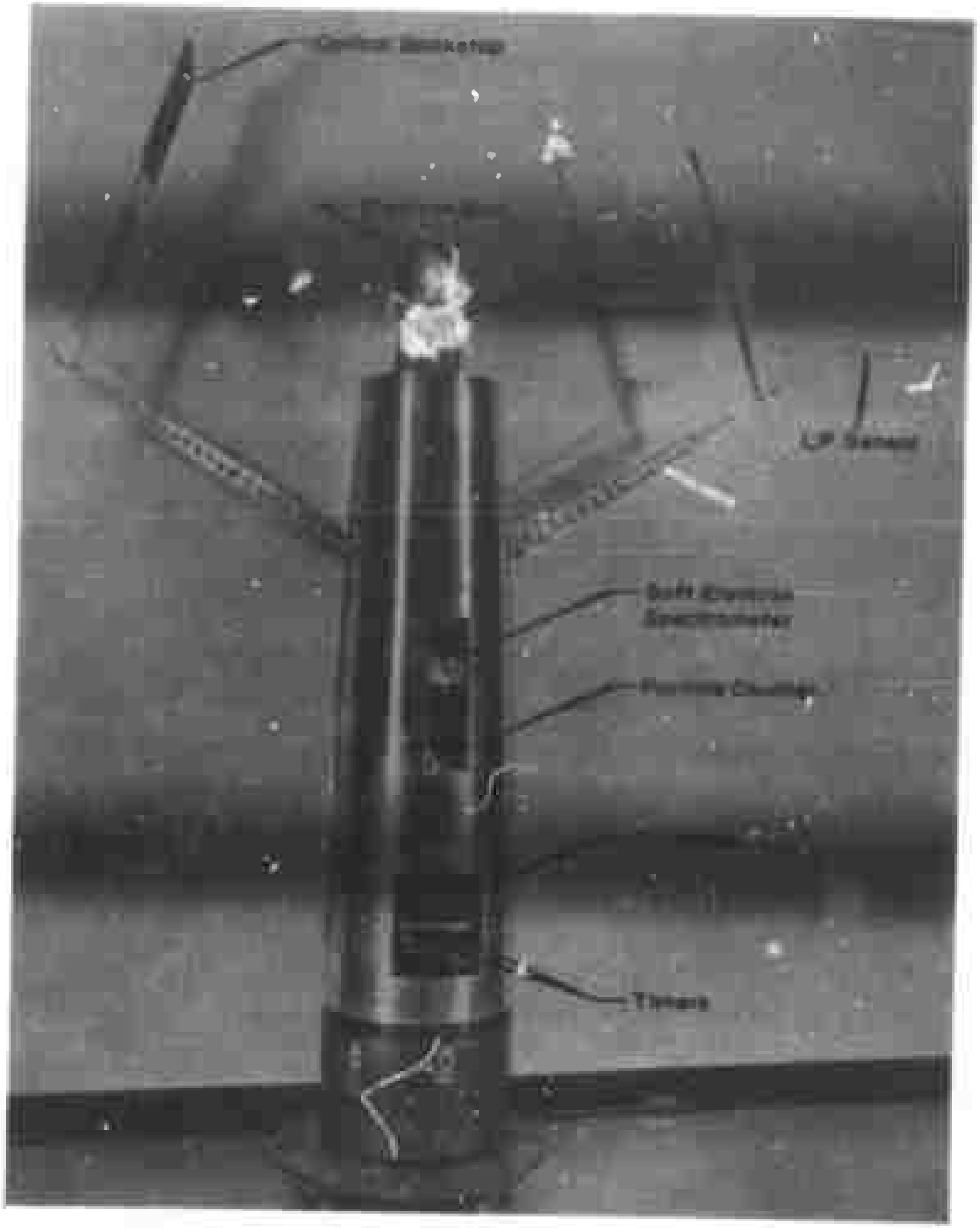

Figure 10. Aerobee A03.006-1 payload with nose cone.

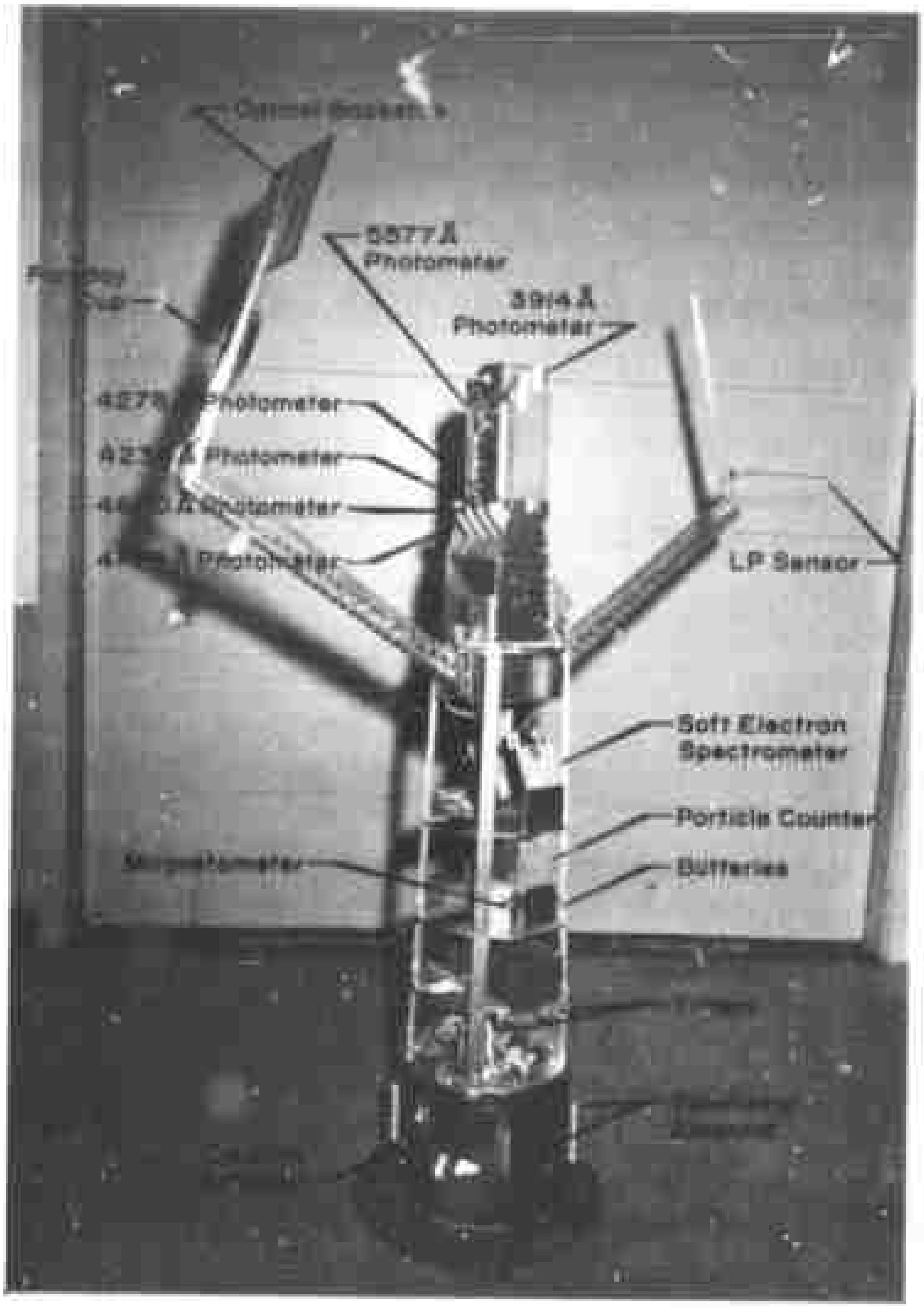

Figure 11. Aerobee A03.006-1 payload without nose cone.

vertically-viewing auroral photometers (3914 and 5577 Å), as well as the electron-gun system and the beam-oriented photometers. The booms were then elevated after a delay of a few seconds.

The boom adjacent to the front ends of the electron gun and beam-oriented photometers carried the Faraday collector and optical backstop. A Langmuir-probe sensing element was mounted on the second boom. The Langmuir probe was included to provide measurements of T_e, N_e, and the vehicle-to-plasma potential. The geometrical configuration of the components of the EBIL system is depicted in Fig. 12. High voltage was applied to the SES and the EPC at an altitude of approximately 90 km where the ambient air density was sufficiently low to permit safe operation of the curved-channel electron multipliers (Bendix Channeltrons) associated with the instruments. The final timed function on the up-leg of the flight was the opening of the electron gun at an altitude of approximately 140 km.

The payload section of Aerobee A03.910-1 (hereafter Aerobee II), shown in Figs. 13-15, was similar to that of Aerobee A03.006-1 (hereafter Aerobee I). However, the EBIL system was expanded to provide information concerning $[O_2]$ and $N_2(X^1\Sigma_g^+, T_r)$, in addition to the $[N_2]$ and $N_2(X, T_v)$ measurements. The electron-gun system was also redesigned to provide an average beam current of up to 50 mA. Additional changes included the elimination of the optical backstop, the inclusion of an in-flight calibration source, and the placement of a beam-current monitor at the output of the electron gun. The auroral support instrumentation was eliminated; however, a Langmuir probe, atomic oxygen sensor, and an IR earth-scan radiometer were included. The geometry of the EBIL system is depicted in Fig. 16. The instrument shown on top of the electron-gun package was eliminated in the final design.

Both of the Aerobee payloads were recovered by severing the payload from the motor section after the payload had descended below the altitudes of interest. Following severance from the motor, a parachute was deployed to return the payload to the earth without major damage.

Each of the payloads was equipped with a radar beacon transponder to facilitate tracking the vehicle. In addition, Aerobee I carried a recovery beacon which transmitted after impact to provide a homing signal to assist in locating the payload. Each payload operated on a single telemetry link. Aerobee I used the standard VHF telemetry band; whereas Aerobee II carried an S-band telemetry system.

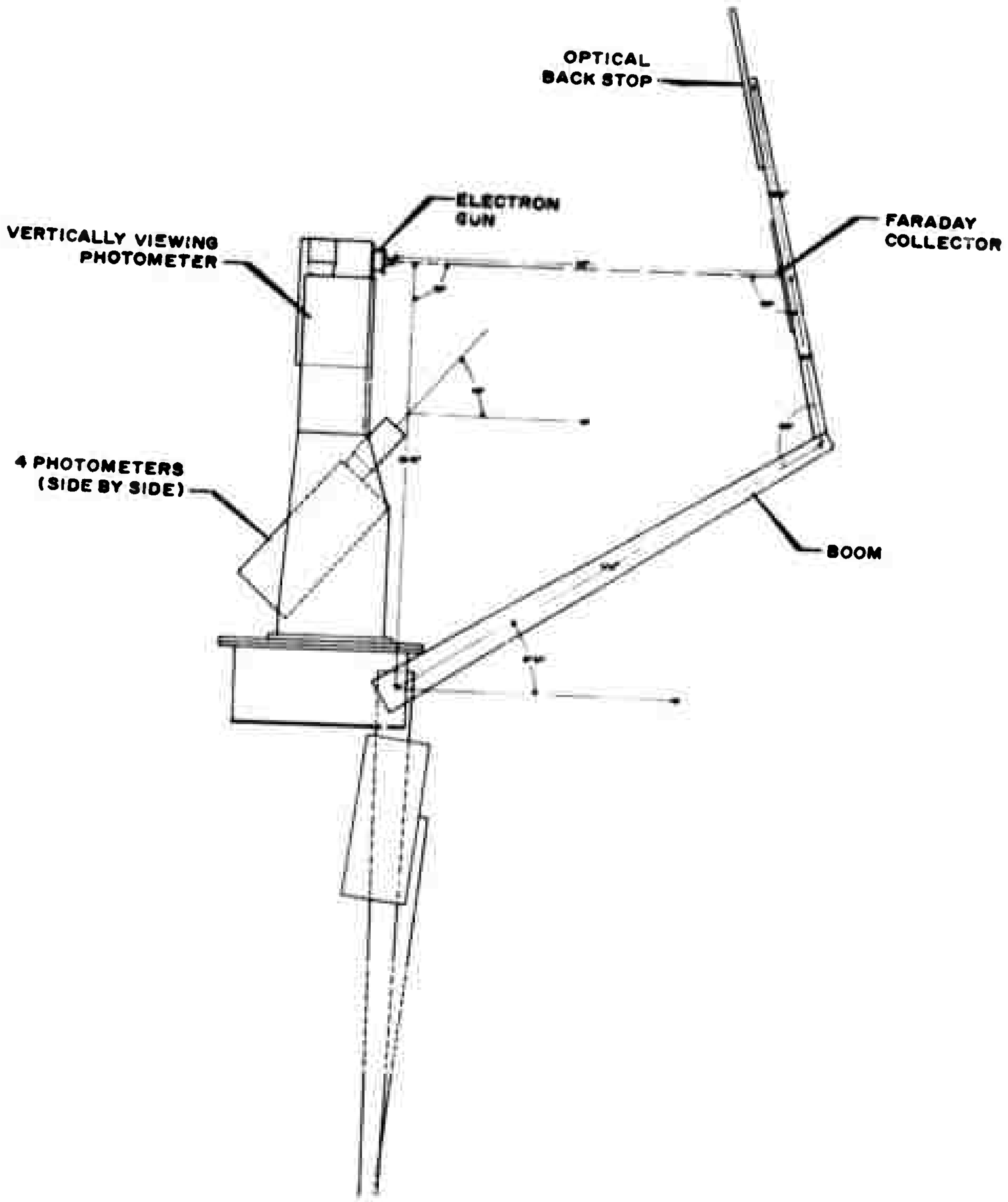

Figure 12. Geometry of EBIL system for Aerobee AO 3.006-1.

Figure 13. Aerobee A03.910-1 payload with nose cone, doors, and nosetip.

Figure 14. Aerobee A03.910-1 payload with doors and nosetip removed.

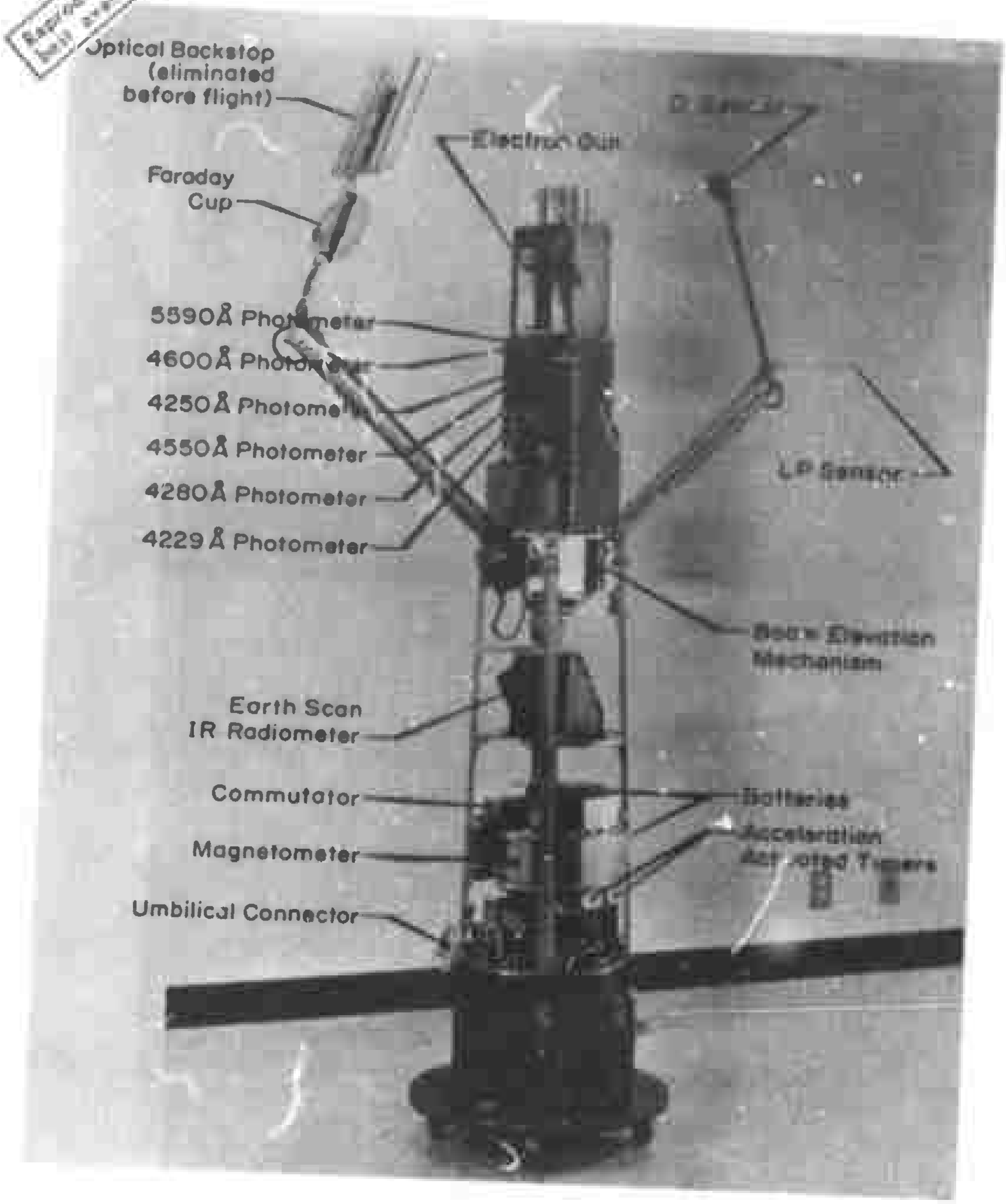

Figure 15. Aerobee A03.910-1 payload with nose cone-assembly removed.

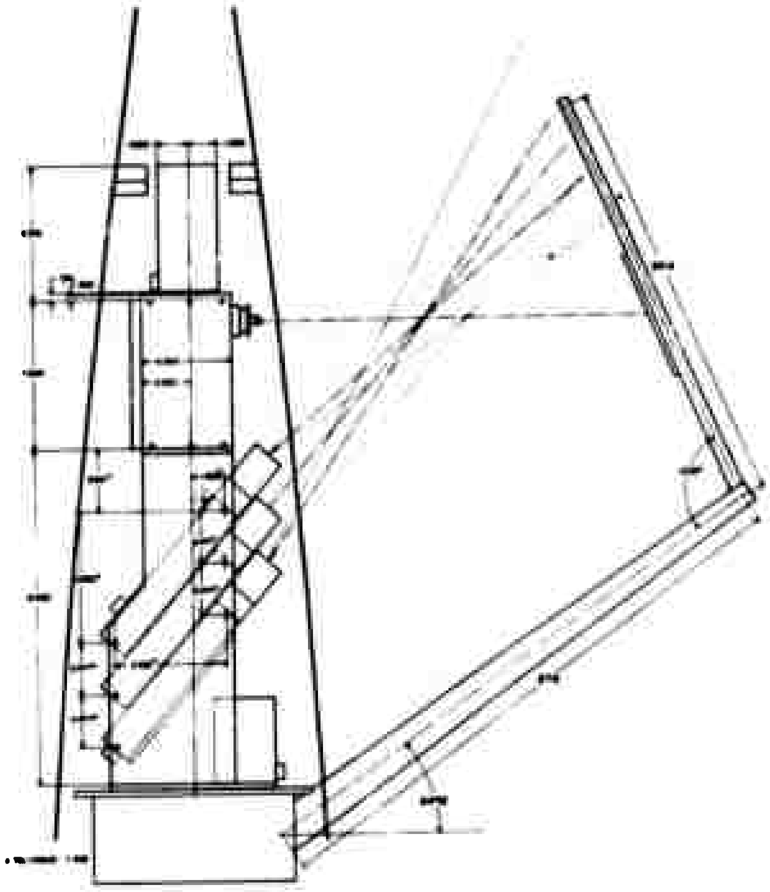

Figure 16. Geometry of EBIL system for Aerobee AO 3.910-1.

The mechanical functions of nosetip ejection, door ejection, and boom elevation were controlled by mechanical, acceleration-activated timers which were tripped during vehicle liftoff. At preselected times, switches in the timers were closed resulting in the discharge of pyrotechnic devices which accomplished the desired functions. The mechanical timers also controlled the power to the break-seal unit of the electron gun, thus permitting selection of the altitude at which the gun was opened. Power to the electron gun on Aerobee I was similarly controlled. The parachute recovery system and fuel shutoff to the Aerobee motor were controlled independently by other timing devises.

The information listed in Tables III and IV show the precise timer settings for Aerobees I and II, respectively. A backup timer was incorporated in each payload to ensure reliable operation in the event of a failure in the primary system.

Table III. Timer settings — Aerobee A03.006-1

Primary timer setting (seconds after lift off)	Secondary Timer setting (seconds after lift off)	Function
61	62	SES and PC door ejection
68	69	Boom doors and nose-tip ejection
72	73	Boom elevation
85	86	SES and PC high voltage turn on
123	125	Electron gun break-seal activation

Table IV. Timer settings — Aerobee A03.910-1

Primary timer setting (seconds after lift off)	Secondary timer setting (seconds after lift off)	Function
61.2	62.4	Nose-tip ejection
65.5	67.0	Door ejection
72.9	72.5	Boom elevation
75.7	76.4	[O] sensor opening
106.5	108.4	Electron gun break-seal activation
108.1	109.1	Electron gun turn on

In the material which follows, each of the instruments in the two payloads will be described. The approach which will be followed entails a functional description built around simplified diagrams. (Circuit diagrams are included in the appendices.) The support instrumentation is described first followed by a description of the EBIL (or primary) instrumentation.

Langmuir Probe

The Langmuir-probe technique for measuring electron temperature and density was provided as a supporting measurement to the electron-beam probe. Inasmuch as this technique is well established for use in sounding rocket measurements [Baker, *et al.*, 1970; Willmore, 1970; Smith, 1969; Seljaas, 1968; and Seljaas and Burt, 1967], the discussion here will be limited to the Langmuir probes which were flown on Aerobees I and II and will omit a detailed general discussion of Langmuir-probe theory.

The measurements of electron temperature and density are accomplished by applying a programmed dc voltage to a sensor which is immersed in the ionospheric plasma. The resulting current-voltage relationships are monitored through two telemetry channels to provide the necessary information.

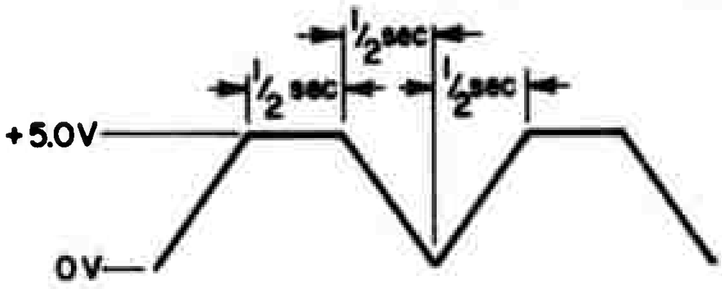

Figure 17. Aerobee A03.006-1 Langmuir probe sweep voltage.

Figure 17 shows the waveform of the programmed dc voltage applied to the sensor of Aerobee I.

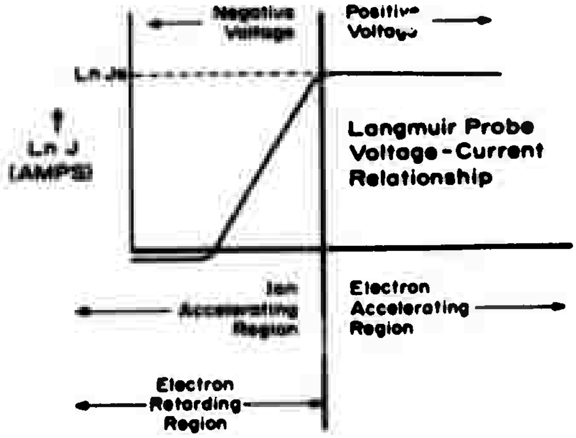

Figure 18. Sketch of Langmuir probe sensor current.

The sensor current sketched in Figure 18 illustrates how the current waveform may be divided into three regions for analysis. The regions are: (1) the electron retarding and positive ion accelerating region, (2) the point of inflection, and (3) the electron accelerating and positive ion retarding region. The analysis of the above curve can be broken down as follows:

(*i*) Electron density is very nearly proportional to the electron current in the electron accelerating region (for a fixed accelerating potential). Although electron density may be analytically calculated from electron current and the sensor geometry, experience has indicated that the Langmuir probe is better for measurement of *relative electron density* with ionosondes or other techniques providing an absolute calibration point.

(*ii*) Electron temperature is directly related to the shape of the current waveform in the electron retarding region.

(*iii*) Vehicle-to-plasma potential may be determined by defining the sensor voltage at the point of inflection.

In the electron retardation region, the probe current I is related to the sensor-to-plasma voltage V by the expression

$$I = I_0 \exp (eV/kT_e) \ , \tag{27}$$

where I_0 is the electron current when the sensor is at the plasma potential (point of inflection), e the electronic charge, k Boltzmann's constant, and T_e electron temperature.

The electron temperature is found by taking the logarithm of this expression giving

$$T_e = (eV/k)[\ell n(I/I_0)]^{-1} \ . \tag{28}$$

Thus, the electron temperature may be found from the slope of the $\ell n(I/I_0)$ versus V curve. In practice the amplifier measuring the sensor current, I, has a logarithmic characteristic which serves the dual purpose of simplifying the temperature analysis and also increasing the range of temperatures which may be measured.

The potential of the vehicle with respect to the plasma may be found from the electron current waveform by noting the function generator potential at the time corresponding to the point of inflection.

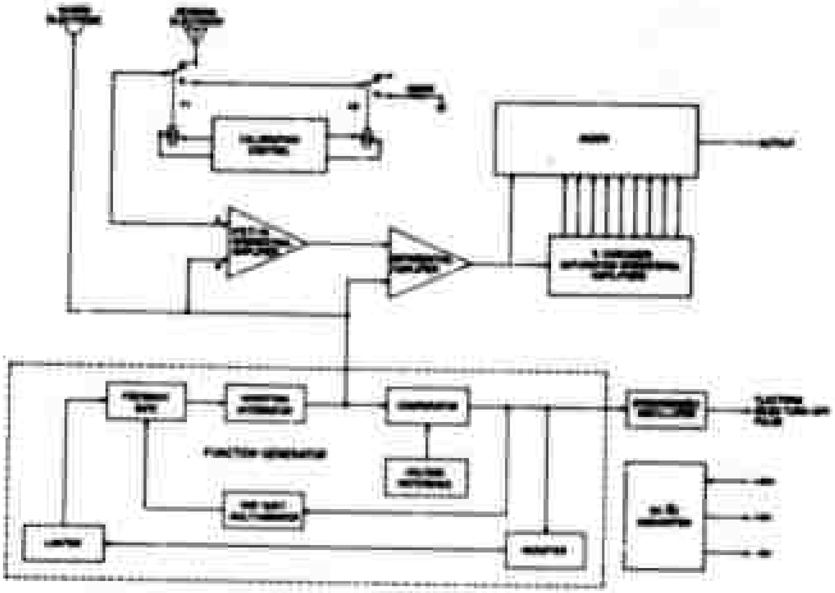

Figure 19. Block diagram of Langmuir probe LP69B-1.

The block diagram of the Langmuir probe flown on Aerobee I is shown in Fig. 19. The function generator produces a repetitive trapezoidal waveform which starts at -1 volts and sweeps linearly to +5 volts in 0.5 sec. This waveform is applied through the input of an operational amplifier to the sensor immersed in the plasma. The sensor, shown in Figure 20, consists of a gold-plated brass rod 0.094 inches in diameter and 5.5 inches long. The wiring to the sensor is guarded (shielded) by driving the stainless steel tubing in which the sensor is mounted and also the coaxial cable shield which connects to the stainless steel tube with the same function generator voltage as is applied to the amplifier. The guarding helps shield the amplifier input from stray noise pickup and also reduces the sensor-to-rocket capacitance.

Charge flow from the sensor to an FET input operational amplifier is converted to a voltage at the output which is proportional to the sensor current plus the function generator voltage. This output is fed into the non-inverting input of a differential amplifier. By feeding the inverting input of the differential amplifier with the function generator voltage, the differential amplifier output voltage becomes proportional to only the sensor current.

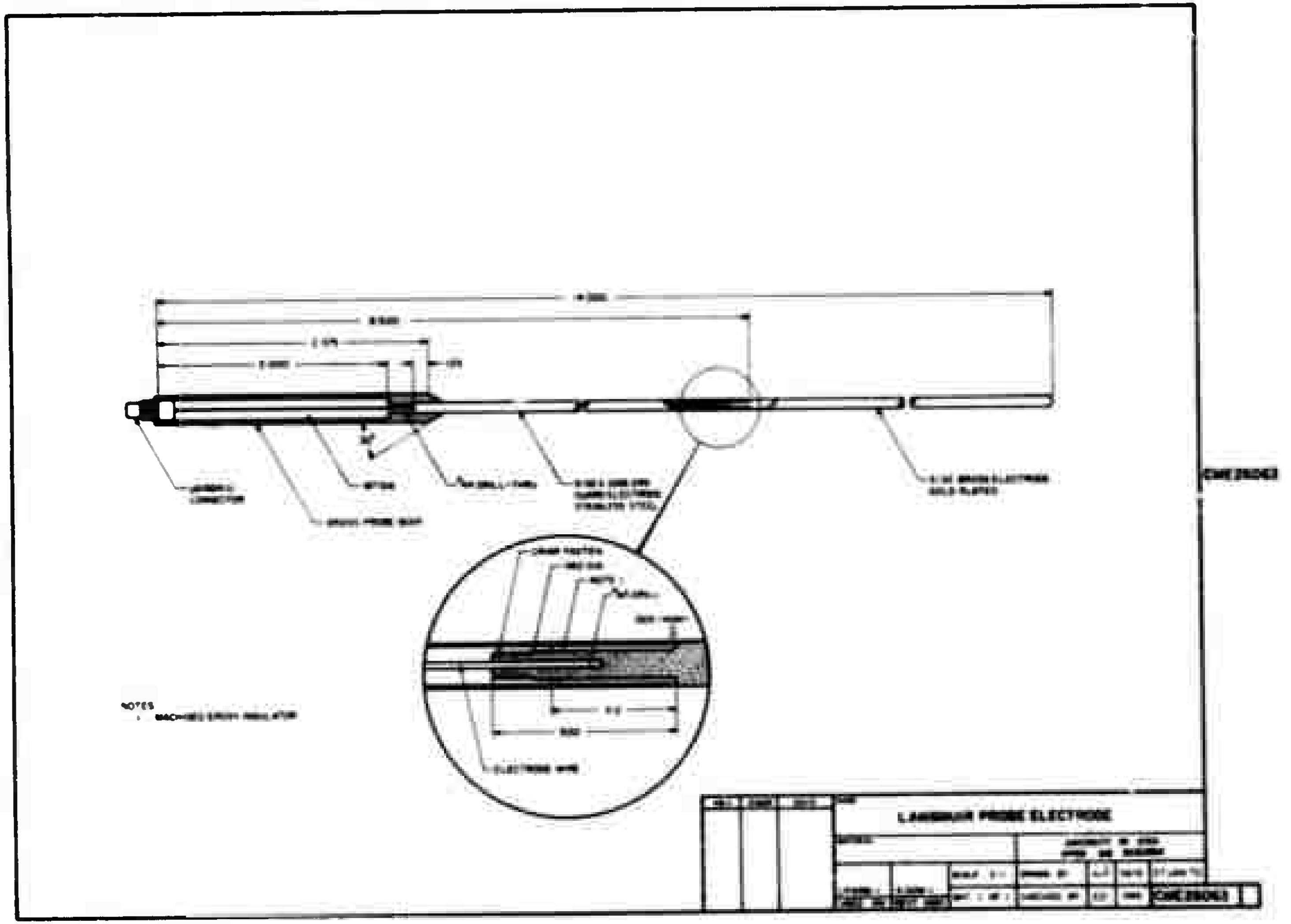

Figure 20. Langmuir probe electrode LP 69A-1.

The differential amplifier output is logarithmically compressed by summing terms of a series expansion approximating the logarithmic function. This is accomplished electronically by feeding the differential amplifier output into the first of nine saturating amplifiers connected in series. Each amplifier has a voltage gain of 3.00, and the output is clipped by zener diodes at 5.1 volts. The outputs of each of the amplifiers are summed by an operational amplifier to provide the logarithmic response. The measured input-current-to-output-voltage relationship for the above electronics is shown in Figure 21.

Since the loss of electrons from the electron beam probe could cause major perturbations in vehicle-to-plasma potential, the Langmuir probe was modified to provide a pulse once every 14.5 seconds which would turn the electron gun off and allow the Langmuir probe to make a measurement with vehicle potentials closer to normal.

The Langmuir probe flown on Aerobee II was very similar to the probe described above in all but two areas. The logarithmic amplifier for the Aerobee II Langmuir probe used the exponential characteristics of a forward biased diode to function as the feedback element around an operational amplifier instead of series saturating amplifiers. The diode-feedback technique provides a smoother logarithmic compression by eliminating the small discontinuities in slope of the amplifier response curve generated as the amplifiers reach saturation. One drawback to the diode-feedback technique is that the forward diode characteristics are not only a function of current (or voltage) but also temperature. To eliminate temperature dependence, it is necessary to maintain the feedback diode at a constant temperature in an electronically-controlled oven. The characteristic input current-output voltage curves for the Langmuir probe used on Aerobee II are shown in Figure 22. Complete schematic drawings of both Langmuir probes are included in the appendices.

The voltage sweep for the Aerobee II Langmuir probe was increased from -1 → +5 to -1 → +10 V. This was done in an effort to overcome possible significantly positive vehicle potentials when the electron gun is operated.

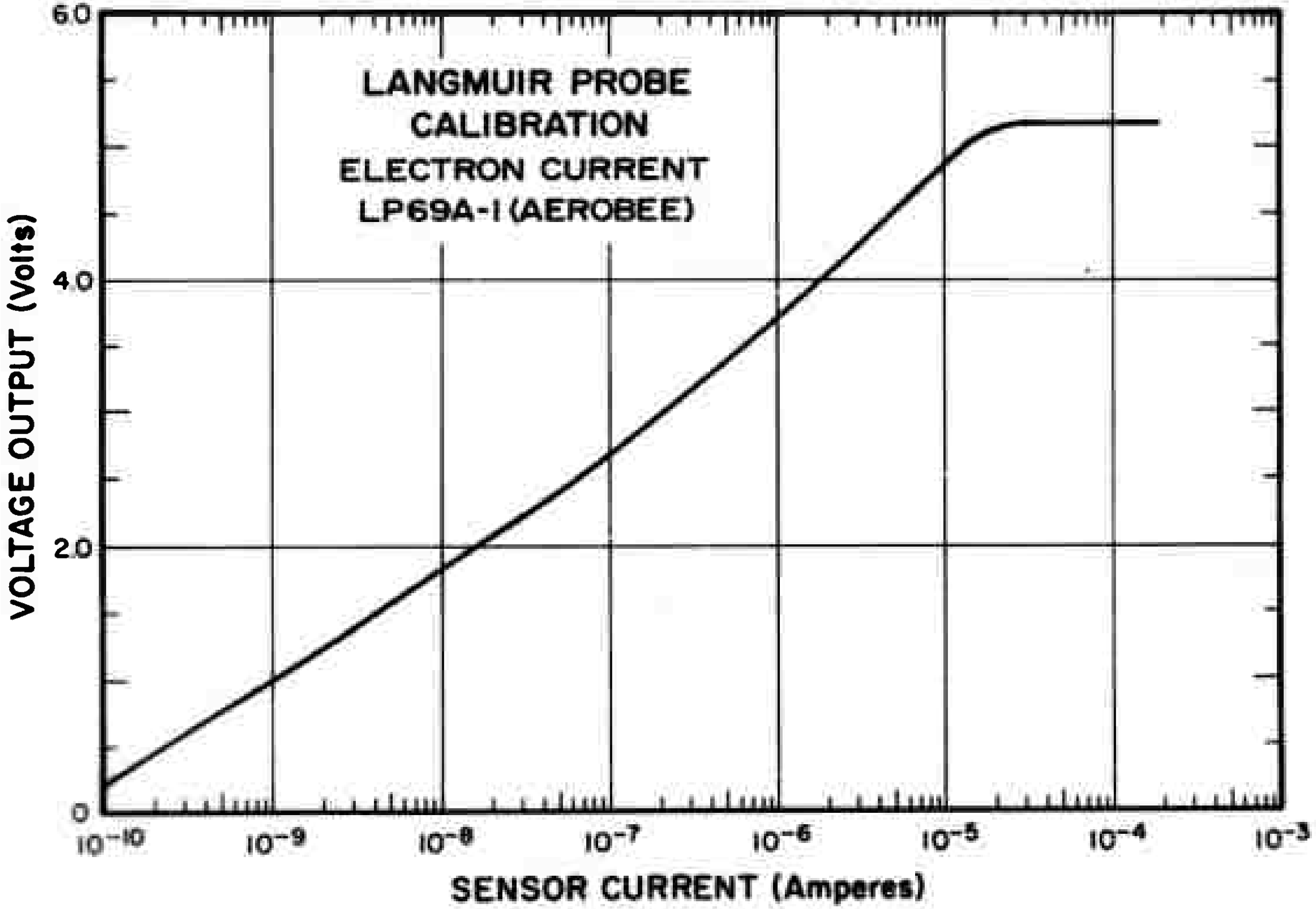

Figure 21. Langmuir probe LP 69A-1 calibration curve.

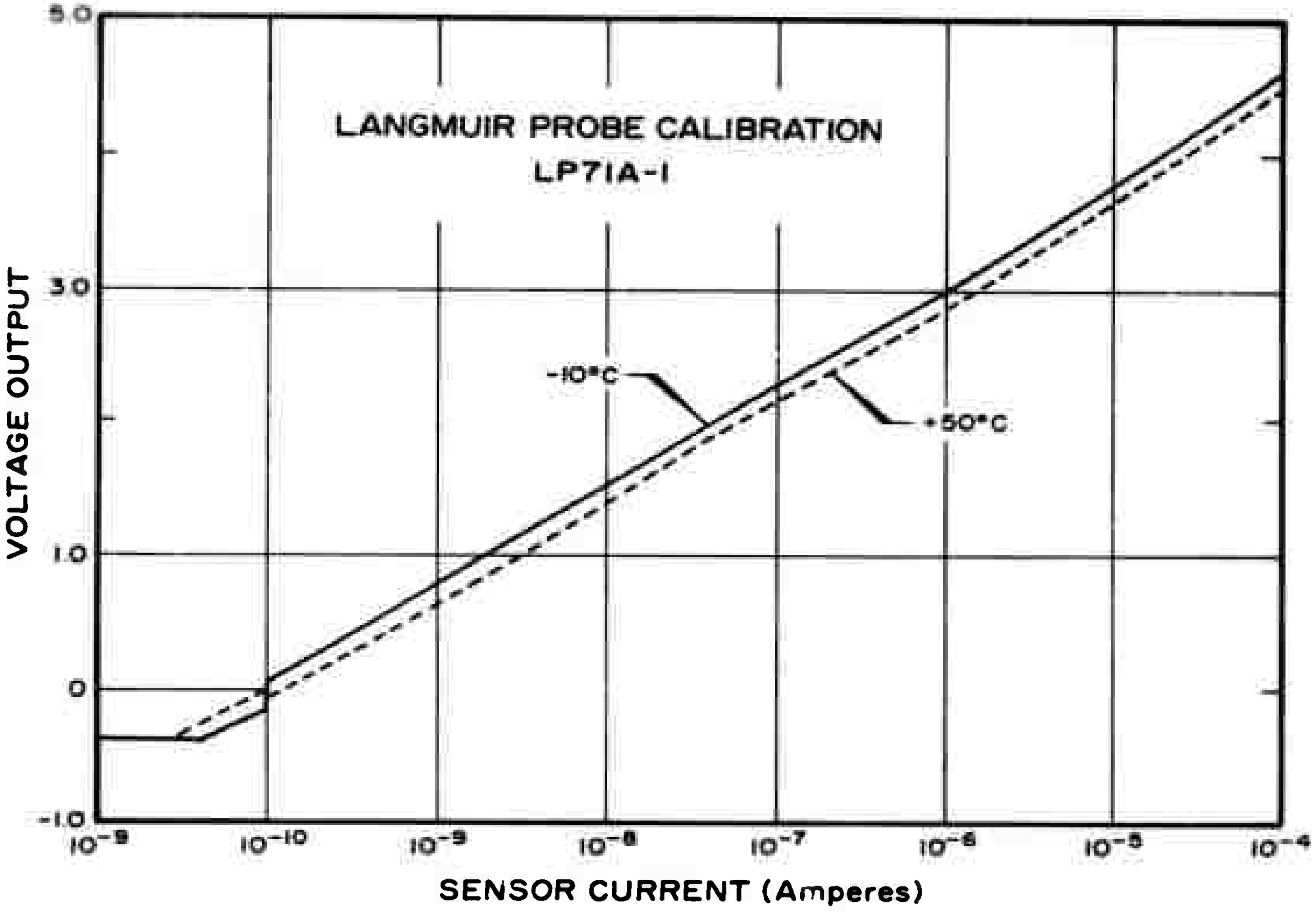

Figure 22. Langmuir probe LP 71A-1 calibration curve.

5577 and 3914 Å Photometers

Two vertically viewing photometers were included in the Aerobee I payload to provide information on the important 5577 and 3914-Å auroral emissions. The photometers consist of an optical system to define the field of view and spectral bandpass, a ruggedized photomultiplier detector, high voltage power supply, and a logarithmic amplifier all self-contained in a hermetically-sealed case. The specifications for the two photometers are summarized in Table V.

Table V. Specifications: 3914 and 5577 Å photometers.

Model (Serial)	WT-4 (Serial No. 5)	WT-4 (Serial No. 15)
Filter Center Wavelength	3910 Å	5577 Å
Filter Bandwidth	40 Å	35 Å
Filter Peak Transmission	34%	82%
Field of View	10° (.024 sr)	10° (.024 sr)
Maximum Signal	6.2×10^5 Rayleighs	4.2×10^6 Rayleighs
Minimum Signal	7.4 Rayleighs	15 Rayleighs

Curves providing the instrument output voltage as a function of irradiance and temperature-monitor output as a function of temperature are included in the appendices.

Particle Counter

Since Aerobee I was launched during an auroral event, a particle counter was included to provide information on the flux and energy spectrum of energetic primary electrons producing the aurora. The particle counter shown in the block diagram in Fig. 23 is a four-channel instrument designed to measure electrons in four energy ranges: (1) energy $\geq$ 6.5 keV;

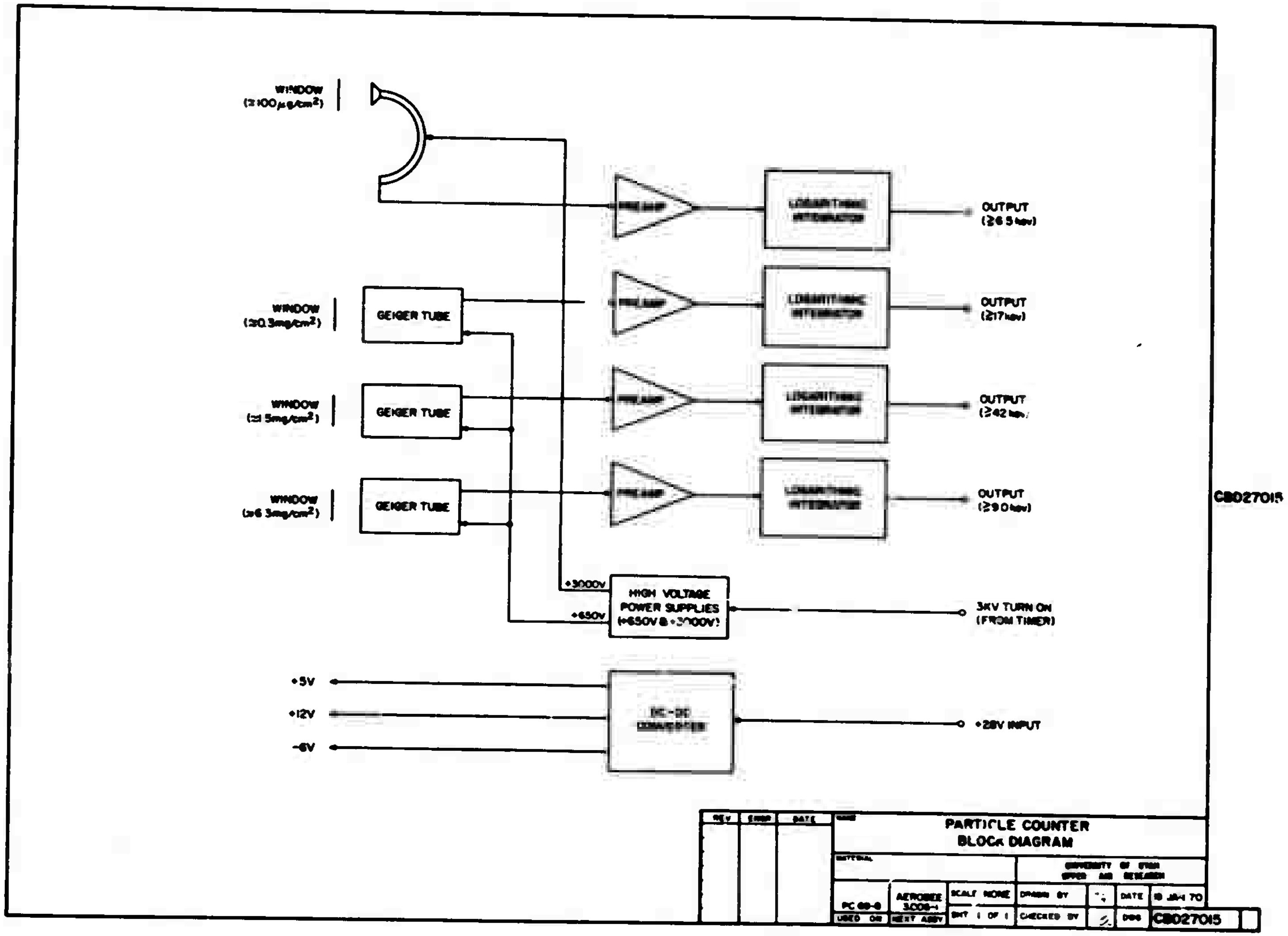

Figure 23. Block diagram of energetic particle counter.

(2) energy $\geq$ 17 keV; (3) energy $\geq$ 42 keV; and (4) energy $\geq$ 90 keV. Discrimination of particle energy is achieved by the electron transmission cutoffs of the particle detector entrance windows. The three higher energy channels use end-window geiger tubes as detectors while the 6.5-keV channel employs a curved-channel electron multiplier as the detector. The outputs from each of the detectors are conditioned and fed into a logarithmic integrator which provides an output voltage which is approximately proportional to the logarithm of the count rate. The logarithmic integrators have a response time constant of approximately 5 x 10^{-2} sec which is a compromise between providing a smooth output and being able to follow rapidly changing flux rates due to vehicle motion and auroral activity.

Since the geiger tubes and channeltron operate at high voltages ($\simeq$650 V and 3,000 V, respectively) considerable care was exercised to prevent arcs and corona discharges at any ambient pressure. Further precautions were taken to ensure that if an arc or corona did occur there would be no damage to either the particle counter or any of the instruments aboard the vehicle. This was accomplished by housing the three geiger tubes in a pressure-tight compartment with the high voltage power supply. Only the geiger-tube windows were exposed to vacuum during flight. Inasmuch as the channeltron must be at pressures < 10^{-4} Torr in order to operate, it was placed outside the pressure-tight compartment and was provided with ample open spaces for rapid pumpout during ascent. The 3 kV supplied to the channeltron was turned on by a timer-actuated high voltage reed relay at approximately 90-km altitude.

A complete schematic drawing of the particle counter and calibration curves for the logarithmic integrators are included in the appendices. Geometric factors are shown in Table VI.

Table VI. Geometric factor for energetic particle counter.

Channel Energy	Geometric Factor
E _ 6.5 keV	9.36 x 10^{-6} cm^2 steradian
E _ 17 keV	4.92 x 10^{-3} cm^2 steradian
E _ 42 keV	7.095 x 10^{-2} cm^2 steradian
E _ 90 keV	7.095 x 10^{-2} cm^2 steradian

Soft Electron Spectrometer

The soft electron spectrometer is designed to measure electron fluxes from 50 eV to 12 keV in six broad energy ranges. The instrument operates by collimating the incident electrons and allowing them to pass through a known magnetic field. Three sensors are appropriately placed to count electrons whose paths are bent to predetermined radii by the magnetic field.

As shown in the soft electron spectrometer block diagram (Fig. 24), three curved-channel electron multipliers are used to count the electrons following the different radii of curvature in the magnetic field. Two ranges of operation are made possible for each curved-channel multiplier by switching the magnetic field intensity between two fixed levels. The field switching thus provides a total of six energy channels although measurement may be made with only three channels at a time.

The range of operation of each sensor is determined by a free-running multivibrator which controls the current output of a regulator feeding the electromagnetic field coils. The current regulator alternately sets the magnetic field at 25 gauss for 120 msec and 103 gauss for 120 msec. The radii of curvature for acceptance by the three channeltrons are approximately 1.0 cm, 1.5 cm, and 2.0 cm for channels one, two, and three, respectively. The above combination of magnetic field, radii of curvature, collimation effectiveness, and size of the sensitive area on the channeltrons result in the energy responses tabulated in Table VII and shown in Fig. 25.

When an electron is detected by one of the curved-channel multipliers, a signal is generated which is amplified and then counted by six flip flops connected as a ripple counter. The flip-flop outputs are summed to produce a 64-step staircase voltage between the limits of +5 V and 0 V. Each step in the staircase voltage represents a single counted electron. At the completion of the staircase (64 counts) the process is repeated.

In order to differentiate between high and low energy counts from each channel as determined by the strength of the magnetic field, signature pulses are generated by the instrument. High energy counts from each channel follow a +5 volt, 5-msec-wide pulse and low energy counts

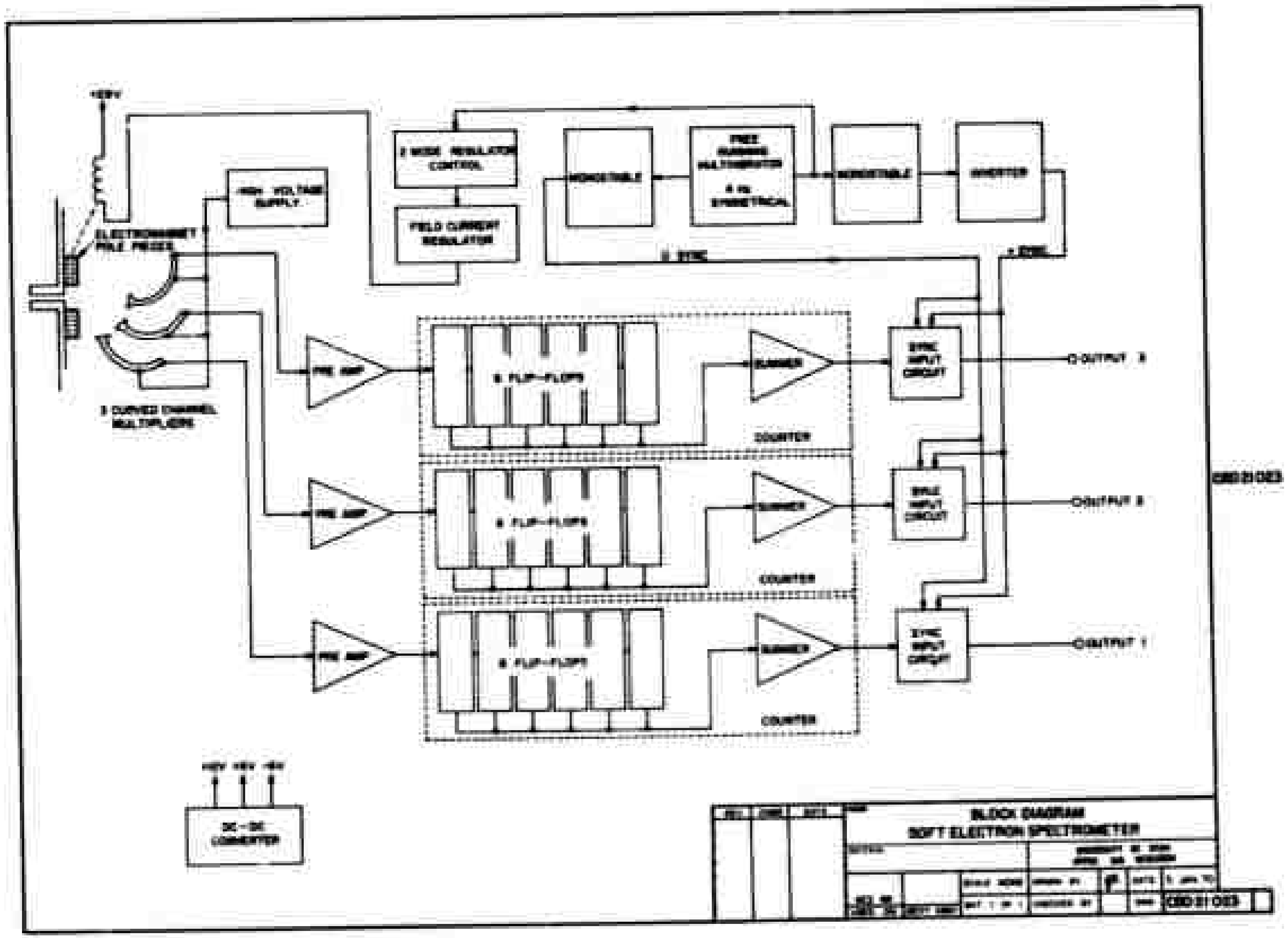

Figure 24. Block diagram of soft-electron spectrometer.

Table VII. Soft electron spectrometer: response versus magnetic field strength.

Channel Number	Field Strength (Gauss)	Electron Energy for Peak Response	Half Peak Response Energy Limits
1	25	65 eV	50-90 eV
	103	1.1 keV	0.85-1.6 keV
2	25	150 eV	120-250 eV
	103	2.7 keV	2.0-4.5 keV
3	25	250 eV	220-700 eV
	103		4.0-13.0 keV

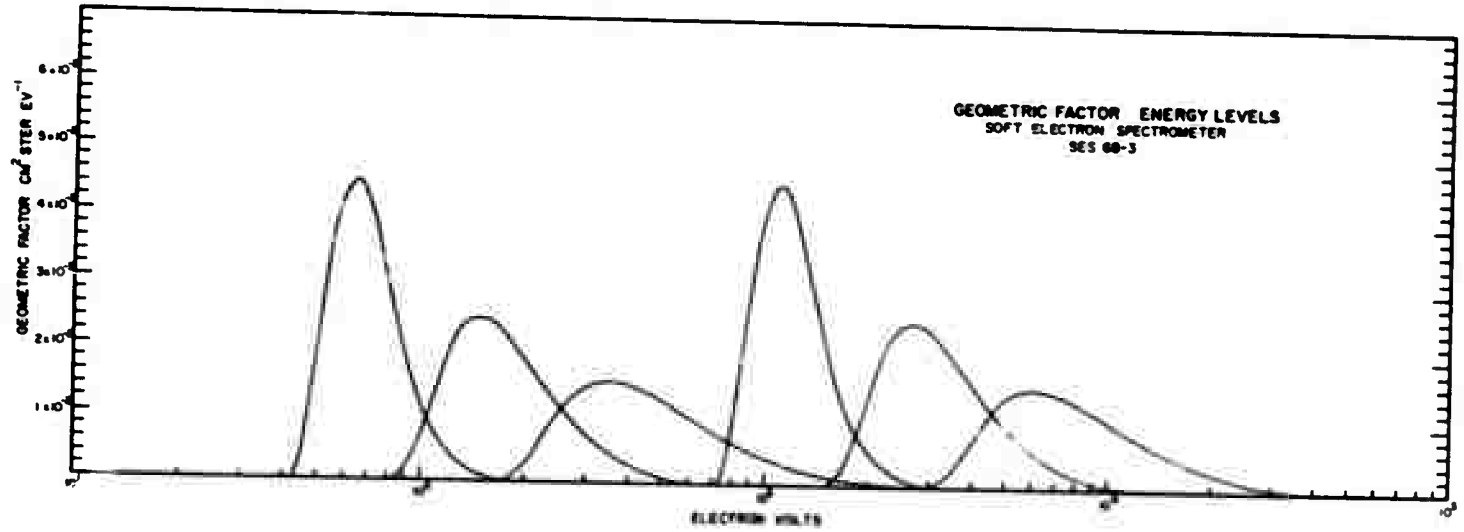

Figure 25. Energy response curves for soft-electron spectrometer channels.

follow a zero volt, 5-msec-wide pulse. These pulses are imposed on the outputs of each of the three data channels. Figure 26 shows typical output waveforms from the soft electron spectrometer including the energy-range signature pulses.

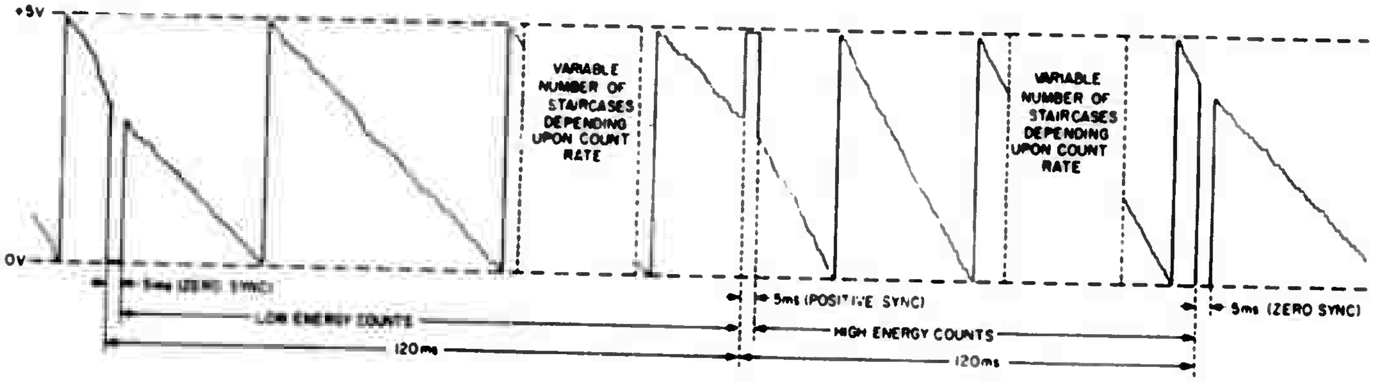

Figure 26. Typical output waveforms from the soft-electron spectrometer.

Geometric factors for the various energy ranges are shown in Figure 25. Efficiency curves for the channeltrons and a complete schematic drawing of the instrument are included in the appendixes.

Atomic Oxygen Detector

The highly reactive nature of atomic oxygen is used as the basis for its measurement on Aerobee II. The measurement is made by exposing a thin film of metallic silver to the atmosphere and then measuring the change in resistance of the film as the silver is oxidized by the atomic oxygen. The sensors consist of small glass rods on which a thin (≈150 Å) film of metallic silver is deposited by conventional techniques [Henderson, 1970]. Four coated rods were used to make simultaneous measurements. The sensors were maintained under vacuum until the vehicle reached an altitude of approximately 75 km. A dimple motor was then detonated to open the container and expose the sensors. The sensor package was mounted on the end of one of the booms to position it as far from the rest of payload as possible. This was done to minimize the possible perturbing effects of the vehicle on the atomic oxygen density near the vehicle. Since the oxidation of the metallic silver is also dependent upon the flow rate of the atomic oxygen, it proved desirable to move the sensors as far as possible from the rocket body thus allowing a better estimate of the flow rate.

The oxidation of the four sensors was monitored by four circuits each approximating a logarithmic ohmmeter. The outputs from the four circuits were commutated by an electronic commutator having the format shown in Table VIII. The commutator output was fed to a continuous telemetry channel for transmission. The logarithmic-ohmmeter circuitry is shown in Fig. 27, and the calibration data showing output voltage as a function of resistance for each of the four channels are included in the appendices.

Table VIII. Commutator format for atomic oxygen detector.

Segment	Function
1	+5 V
2	+5 V
3	+5 V
4	0 V
5	Detector 1
6	Detector 2
7	Detector 3
8	Detector 4
9	Detector 1
10	Detector 2
11	Detector 3
12	Detector 4
13	Detector 1
14	Detector 2
15	Detector 3
16	Detector 4

Electron-Beam-Induced Luminescence Systems

Simplified block diagrams of the basic EBIL systems which were flown on Aerobees I and II are presented in Figs. 28 and 29, respectively. The connections of the individual blocks (where appropriate) to the primary power source have been omitted for the sake of clarity. The

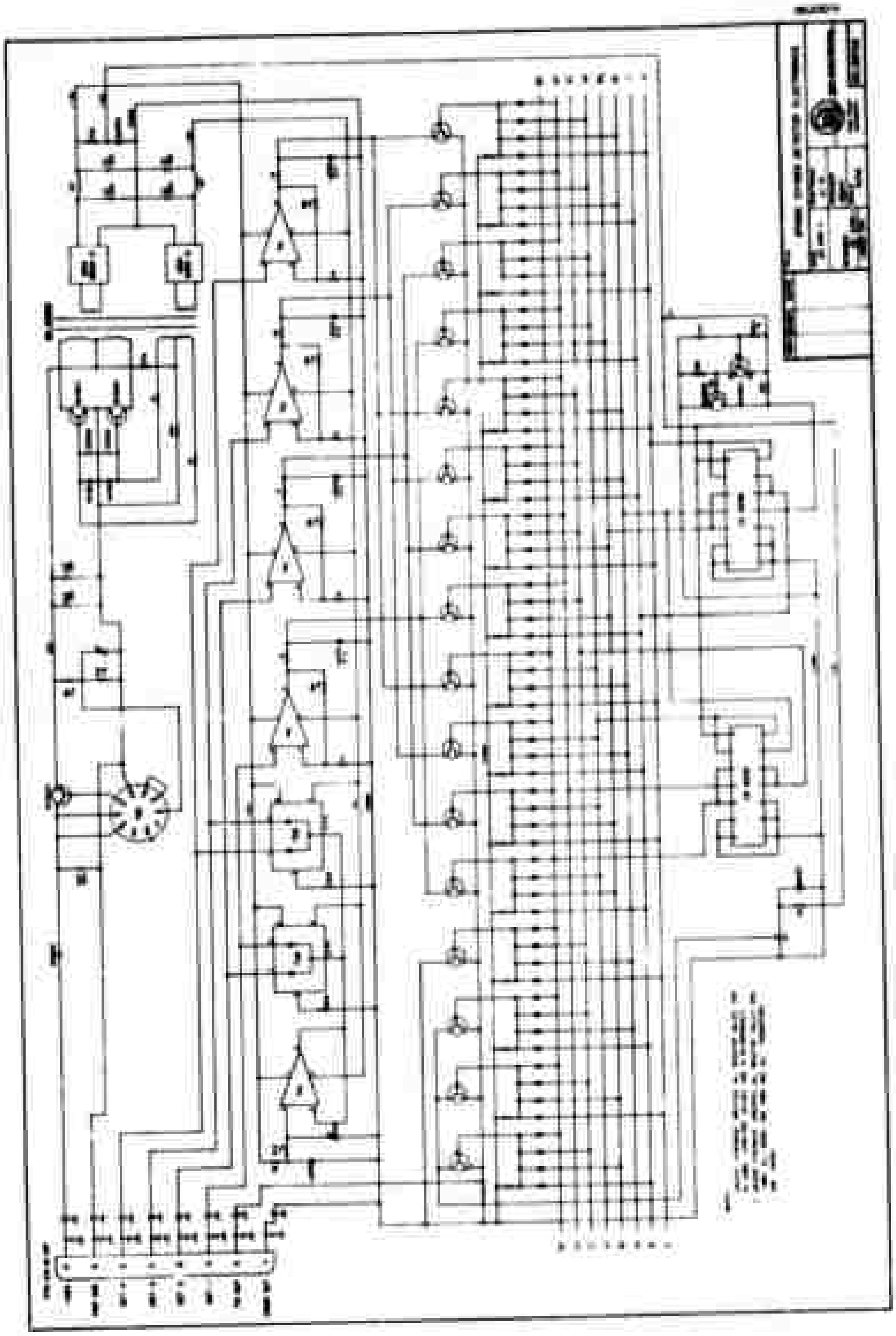

Figure 27. Atomic oxygen detector, logarithmic ohmeter schematic diagram.

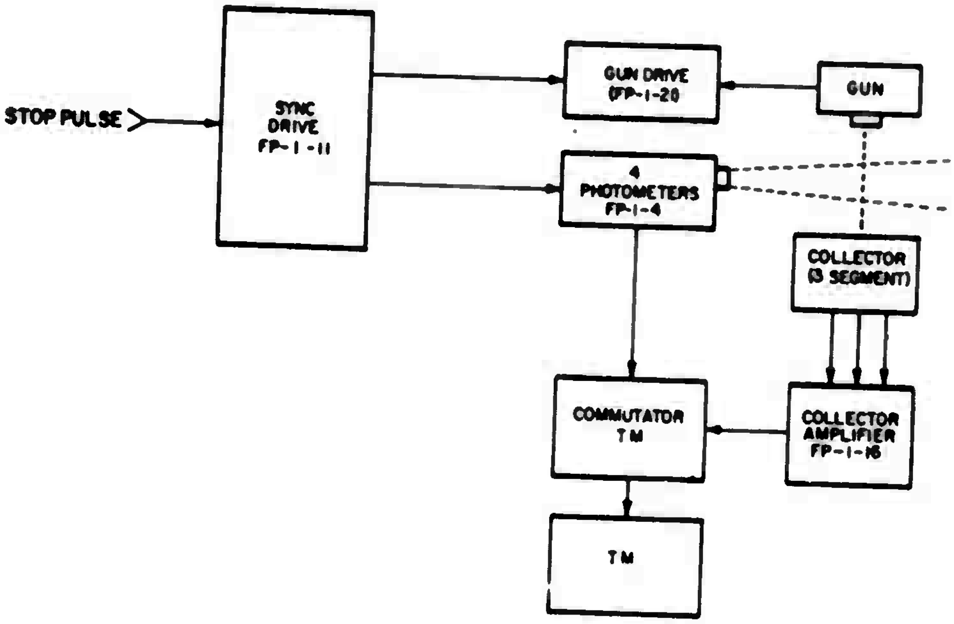

Figure 28. Block diagram of EBIL system for Aerobee AO 3.006-1.

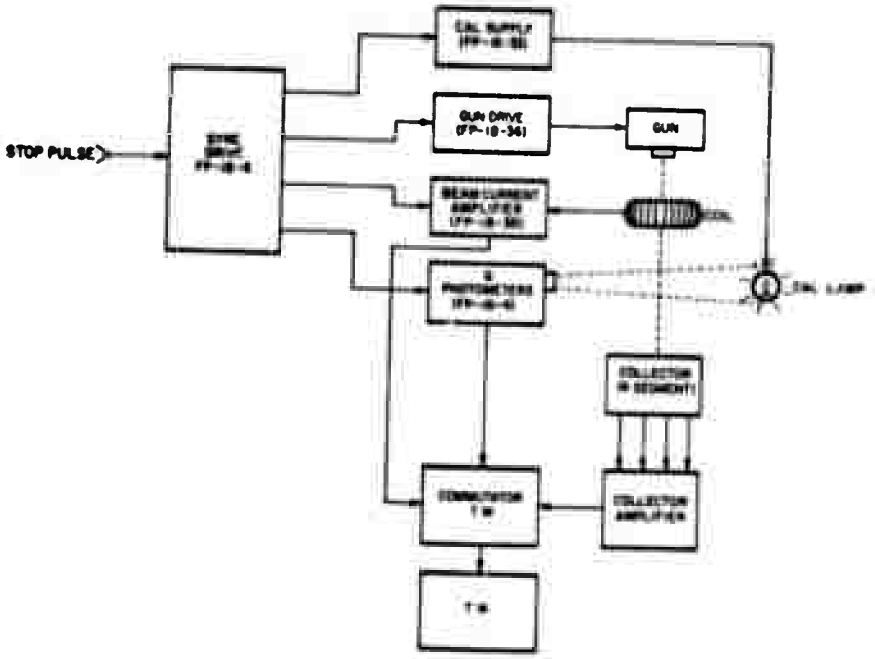

Figure 29. Block diagram of EBIL system for Aerobee AO 3.910-1.

indication of a connection of the electron gun break-seal tabs to the power supply and control circuitry is also omitted. Features common to the two systems will be discussed first; this discussion will be followed by a consideration of basic system differences.

A Machlett Laboratories' Type EE-65 electron tube was used in each of the systems. As mentioned previously, the EE-65 tube was developed especially for rocket instrumentation (Hess *et al.*, 1971). The tubes feature planar-type metal-ceramic construction, an indirectly-heated cathode consisting of an oxide-impregnated porous nickel matrix on a base nickel disc,a high-mu control grid, a simple two-element electrostatic lens for beam formation and focusing, and a special end-cap assembly which may be removed by a thermal-shock procedure (see discussion below). The electron gun was designed to provide beam currents of up to 100 mA at 10 keV. According to the manufacturer (Machlett Laboratories, 1969), the gun is capable, theoretically of putting 90% of the beam within a 2-cm-diameter circle located 30 cm from the anode of the gun. Subsequent tests have confirmed, and in some instances possibly exceeded, this expectation.

The Type EE-65 tubes are delivered as a sealed unit with the cathode properly conditioned for use. The front end of the gun consists of a tubular ceramic section which is bonded on one end to the open anode structure and on the other to the metallic end cap. A ribbon-like metallic band is bonded circumferentially to the ceramic section in the region between the anode and the end cap. Tabs or leads are brazed to the band and provide a convenient means for applying power. Upon sudden application of (15 ±1)*V* from a low internal resistance source, the band is heated sufficiently fast to shock the ceramic and produce a clean fracture encircling the ceramic section. Mechanical separation of the parts is facilitated by spring loading the end cap; however, the break is normally clean enough and violent enough to result in separation unless the orientation of the tube is such as to prevent it. A picture of the EE-65 showing the end cap separated from the gun section is shown in Fig 30.

Each of the systems was controlled by a SYNC DRIVE unit which consisted of a master clock, shown in Fig 31, and appropriate gating circuitry

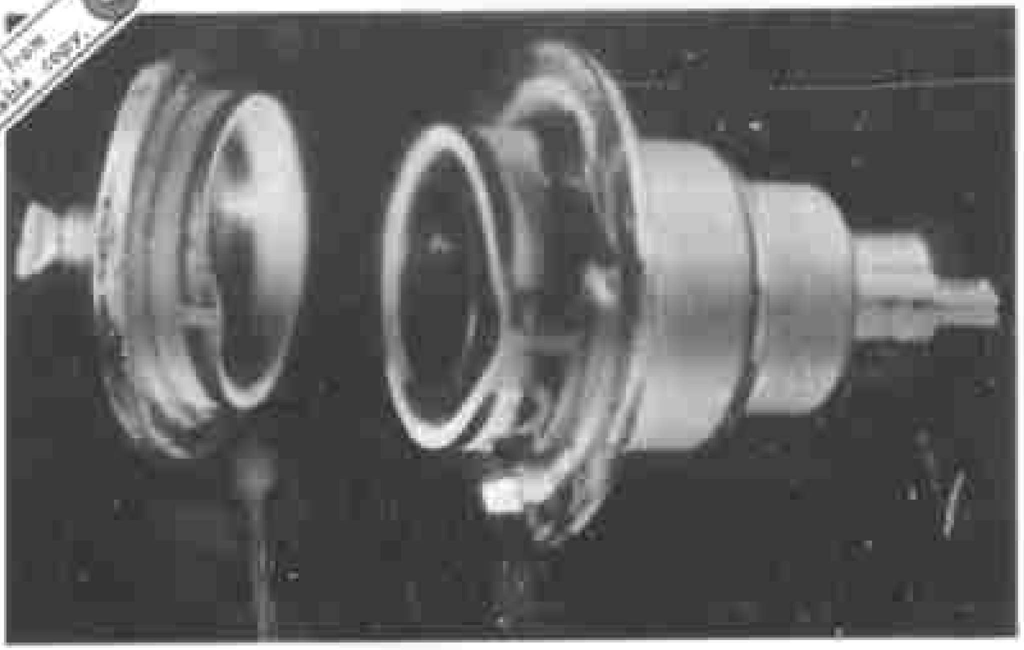

Figure 30. Machlett Laboratories Type EE-65 electron gun.

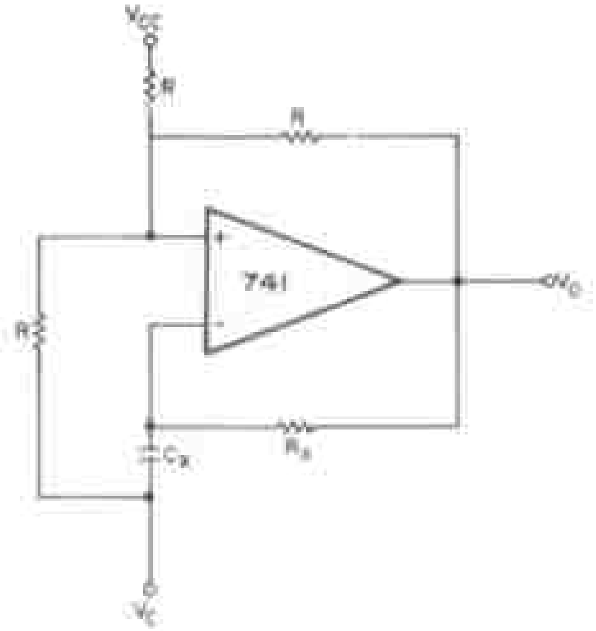

Figure 31. Master clock for EBIL systems (free-running, square-wave oscillator).

to synchronize the electron gun unit and the photometers. In the second-generation system (Fig. 29), the SYNC DRIVE unit also gated the in-flight calibration source and the synchronous rectifier in the beam current amplifier. The master clock (Fig. 31) was a free-running square-wave oscillator built around a type 741 IC operational amplifier. The operating frequency was selected by adjusting the time constant R_xC_x. The operating frequency was set at approximately 350 Hz in the first system and at approximately 400 Hz in the second. The signal-carrying frequency was selected to be roughly ten times (10X) the design bandwidth (≈35 Hz) of the optical detection system, thus permitting effective filtering of the synchronously-rectified square-wave signal.

Phase and symmetry adjustments were required for proper operation of the systems. The SYNC signals fed to the photometers, electron gun, beam-current amplifier, and in-flight calibration source were adjusted for proper phase and symmetry by means of the circuit shown in Fig. 32. The SYNC input (A) from the master clock is fed to monostable multivibrator (1) which produces an output pulse of variable width occuring at the end of

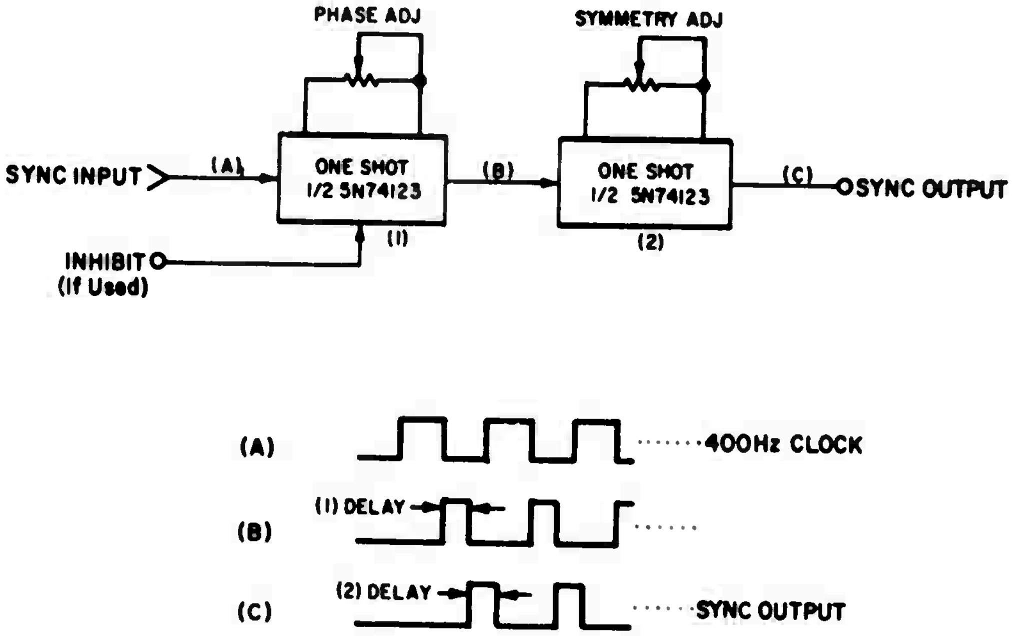

Figure 32. Phase and symmetry controls for operation of the phase-sensitive detectors.

the clock pulse. The output (B) of the monostable or *one-shot* multivibrator is then fed to a second "one shot" (2) which produces the SYNC output (C), again of variable width. The combination of "one shots" thus permits control of both the phase and symmetry relationships between the clock pulses and the SYNC output pulses. The STOP pulse input to the first "one-shot" inhibits its action and thus prevents the generation of the SYNC output. The importance of this feature will become apparent later.

The collector amplifiers (Fig. 33) were essentially identical in the two systems. The input current from the beam-current collector is fed to an inverter and then to a DC amplifier which acts as a current-to-voltage converter. The square-wave voltage signal from the amplifier is then filtered by an active, low-pass filter (Fig. 34) with a bandwidth of about 35 Hz. The filter has less than 1% overshoot and a roll off of about 60 db/decade as indicated in the response curve of Fig. 35. The same type of filter was also used to smooth the outputs of the synchronous (and dc reset) amplifiers in the photometer units and in the beam current amplifier. The amplifiers were designed to provide high- and low-gain outputs which differed in level by a factor of ten.

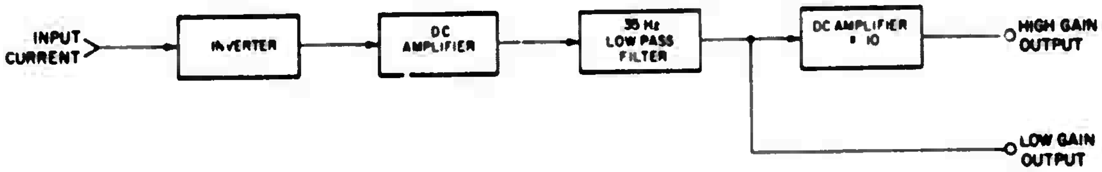

Figure 33. Block diagram of Faraday collector beam-current monitors.

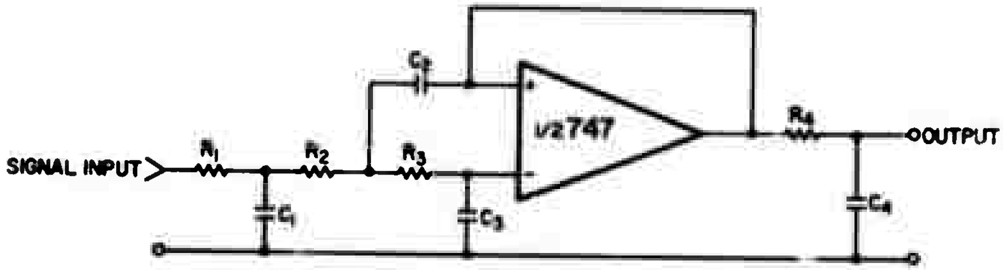

Figure 34. Active, low-pass filter used in EBIL system.

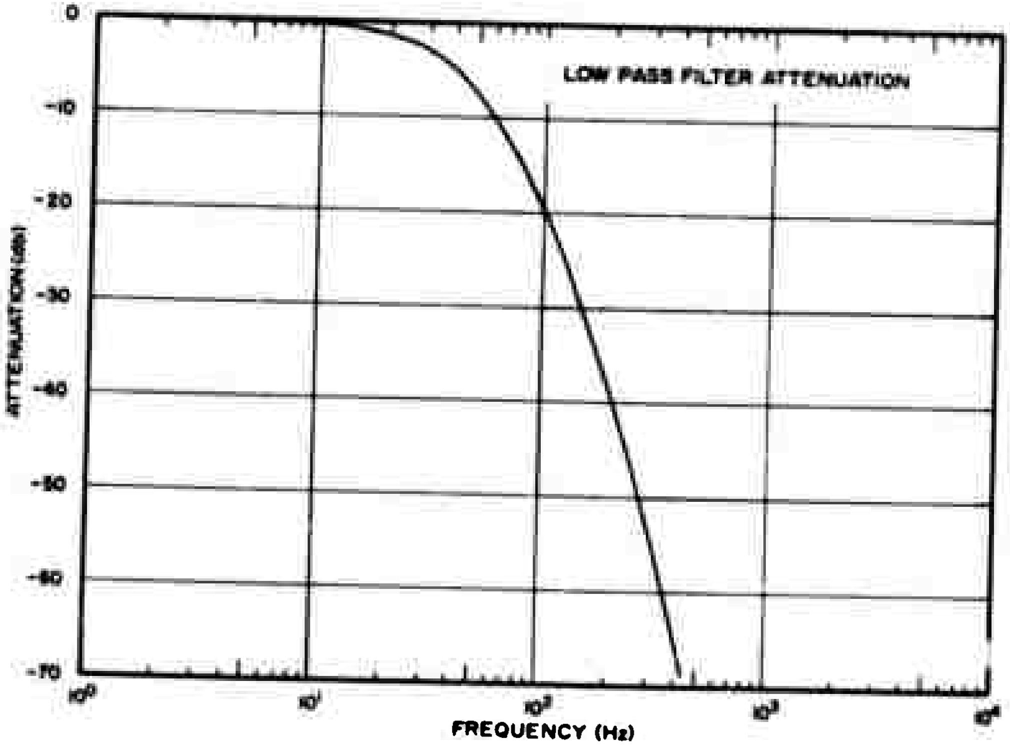

Figure 35. Frequency-response characteristics of the low-pass filter.

Several photometric channels were deemed desirable to secure the spectral information of interest. The possibility of using a single collector together with beam splitters in order to effect a multi-channel instrument was considered. However, the idea was discarded in favor of the use of an array of photometers which were variants of a flight-proven design. Two factors influenced the choice: (*i*) the limited developmental time available for designing and fabricating the first instrument and (*ii*) the proven reliability of the photometers after which the flight instruments were patterned.

The photometers were completely self-contained, hermetically-sealed instruments designed especially for operation in an aerospace environment. The basic photometric system was built around selected RCA-4516 photomultiplier optical detectors and, in addition to the tube, consisted of a well-regulated, high-voltage power supply, a signal-conditioning amplifier with associated low-voltage power supply, and a removable optical head which contained a field stop, lens, interference filter, and a thin wedge (prism) of glass or fused silica. The RCA-4516 is a 3/4 - inch diameter, 10-stage, head-on photomultiplier which employs a bialkali photocathode. The tubes feature high quantum efficiency in the blue and near ultraviolet spectral regions (QE $\simeq$24% @ 4000 Å) and low dark current.

A photograph of one of the sealed photometers is shown in Fig. 36. The overall dimensions of the instrument are approximately 1.56 in. x 3.68 in. x 12.4 in. A simplified drawing of the optical system used to couple the source to the detector is presented in Fig. 37. A thin wedge (A) turns the center line of the instrumental field of view (FOV) through an angle Θ_{ni} appropriate for viewing the beam region of interest. The wedges are selected for each of the instruments to yield a common point of intersection of the FOV center lines with the electron beam axis.

A portion of the light accepted by the wedge is passed to a Fabry-Perot type interference filter (B) for spectral selection. A half-power bandwidth of about 10 Å was typical of the filters which were used. (Transmission curves for the various filters used in the two EBIL systems appear in the appendices.) A plano-convex lens (C) condenses the radiation from the filter on a square aperture (D) which acts as a field stop. The radiation which passes through the field stop is then intercepted by the

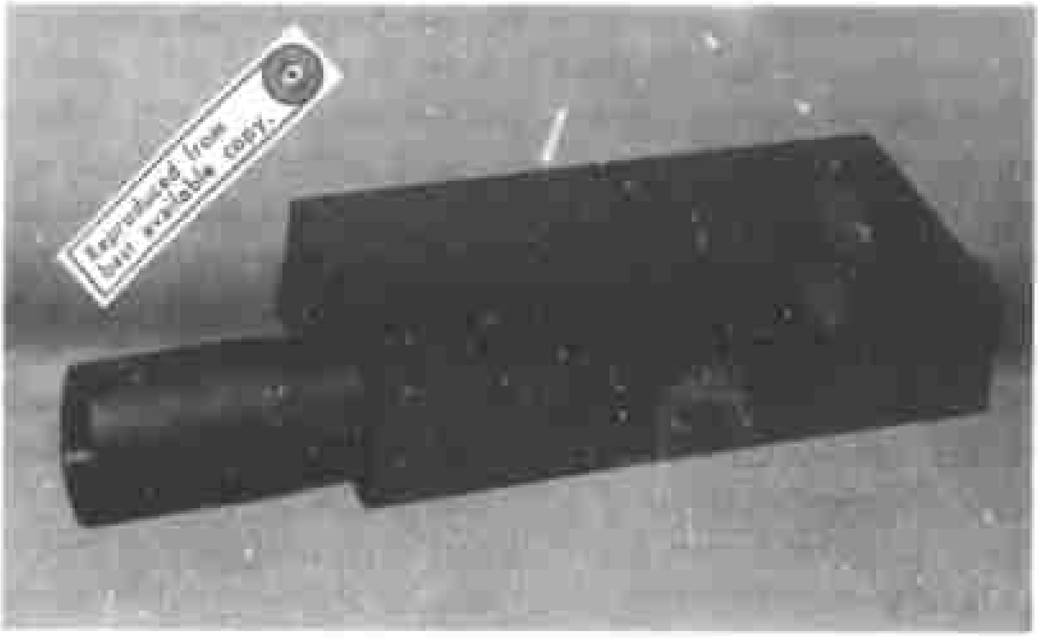

Figure 36. Photograph of photometer.

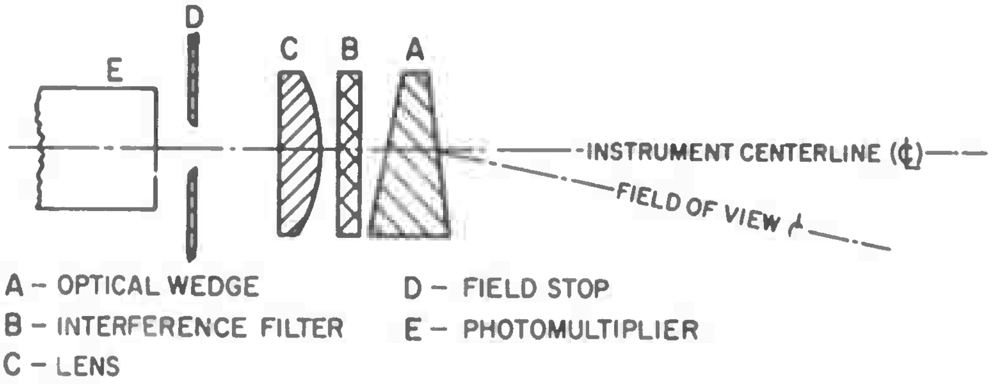

Figure 37. Simplified drawing of the photometer optical system.

detector (E). The half-power fields of view of the instruments were determined to be roughly 2-inches "square" in a plane normal to the FOV center line and located 14.5 inches (appropriate for EBIL system geometry) from the lens. A typical result for the FOV determination is given in the appendices.

In the first-generation EBIL system, the photomultiplier signal was fed to a dc-reset amplifier, a variant of the conventional phase-sensitive amplifier. A block diagram of the dc-reset amplifier is shown in Fig. 38.

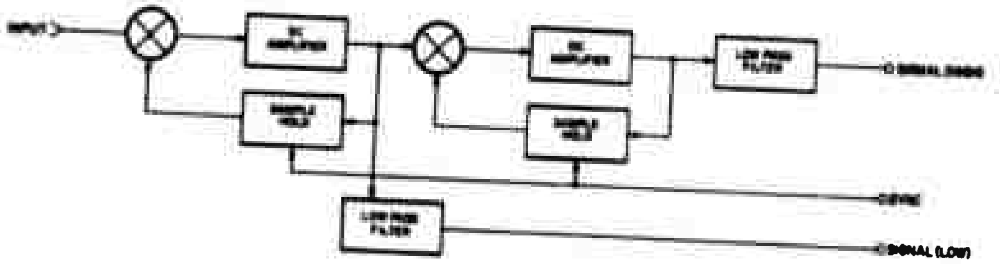

Figure 38. Block diagram of the DC-reset amplifier.

In effect, the dc-reset amplifier is a wide-band, direct-coupled amplifier whose output is forced to zero in the absence of a phase-locked input signal. The amplifier was designed to eliminate from the output signal contributions from the photomultiplier dark current and from the component of the anode current assocated with slowly-varying, asynchronous optical sources.

During the half-cycle of operation corresponding to "electron-gun on", the SYNC input switches the sample-hold integrator (SHI) to "hold". The integrator then stores a charge which corresponds to the voltage required to force the output to zero. In contrast, during the half-cycle of operation corresponding to "electron-gun off", the SYNC signal switches the SHI to "sample-integrate". In this state, the integrator produces a correction voltage at the summing junction such that the output is approximately zero. Hence, in principle the output signal should not reflect contributions from tube dark current and from other sources which, on the average, contribute equally during each half on an operating cycle.

The output of the amplifier is then smoothed by the previously-mentioned low-pass filter (Figs. 34 and 35). Two signal channels, each limited at 5 Volts, were provided to increase the dynamic range of the system. The level of the signal from the high-gain channel exceed that of the low-gain channel by approximately a factor of fifty. If one assumes a lower limit of 0.1 V (~telemetry noise) for useful information on the high-gain channel, then the total dynamic range is seen to be 2,500.

The second-generation system employed a conventional lock-in amplifier for processing the signal information from the photomultiplier tube. The change was made after tests revealed the superiority of the lock-in amplifier, as compared with the dc-reset amplifier, in rejecting asynchronous background signals. A block diagram of the lock-in amplifier is shown in Fig. 39.

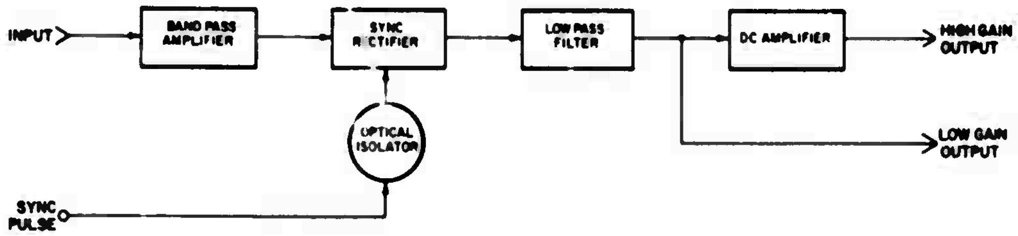

Fiugre 39. Block diagram of the lock-in amplifier.

The 400-Hz input signal from the photomultiplier was amplified by a band-pass amplifier of appropriate center frequency and a Q of about 15. The amplified signal was synchronously rectified and then filtered by the previously-mentioned low-pass filter. In the high-gain channel,the low-pass filter was followed by a X50 dc-amplifier. The low gain output was tied directly to the output of the low-pass filter.

The electron-gun control circuitry for the two systems was similar. In the first system, the high voltage (2.5 kV) for the electron gun was provided by a commercial dc-to-dc converter rated at 20 watts. Power for the electron gun heater was also supplied by a commercial unit rated at 7.5 Watts. The bias voltages for the control grid and preaccelerator were furnished by a mercury battery and an auxilliary power supply, respectively. A beam-current regulator was added during the final stages of preparing the first payload. The regulator sensed the cathode current (or a proportional voltage), compared it with a reference source, and, if required, corrected the control-grid voltage.

The second-generation electron-gun control unit employed the same type of heater supply as that used in the first unit. However, most of the remaining control circuitry was modified to permit operation of the gun at average beam-power levels of up to 125 Watts. The grid-drive circuitry used in the unit is shown in simplified form in Fig. 40. A reference voltage is switched on and off by the 400 Hz SYNC signal from the SYNC logic. An error signal is generated at the summing junction when the output voltage of the anode-current monitor (output voltage proportional to anode current) differs from the reference voltage. The error signal is then amplified by the grid-drive amplifier and applied to the control grid. The action of the loop thus tends to force the error signal toward zero. The grid drive is referenced to the cathode (-2.5 kV) and is decoupled from the SYNC signal source by means of an optical isolator. This feature is necessary since the SYNC circuitry is referenced to the telemetry common.

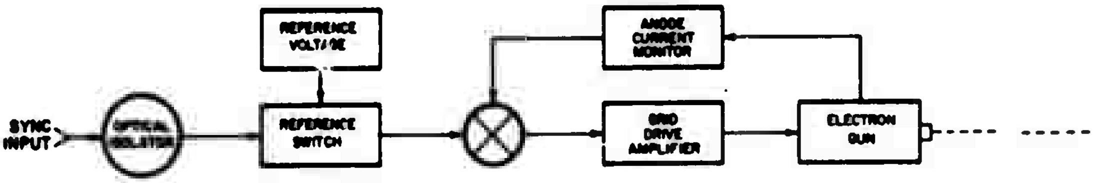

Figure 40. Block diagram of the grid-drive circuit for electron-gun (Aerobee AO 3.910-1).

The preaccelerator voltage was obtained from a tap on the "bleeder" of the high-voltage supply. The necessity of using a tap on the "bleeder", as opposed to a separate supply, arose from the desirability of making a "last-minute" change in the preaccelerator voltage.

In addition to the basic components of the first-generation EBIL system, the second-generation system contained an in-flight calibration light and an inductive-type current monitor which was mounted close to the anode of the electron gun. The calibration light consisted of an Amperex Type 6977 subminiature, voltage-indicator tube together with appropriate control circuitry. The control circuit (Fig. 41) consists of an input voltage regulator, a dc-to-dc converter (outputs of +70 V, +1.25 V, and -3.0 V), and a transistor switch which is operated by the CAL SYNC signal from the SYNC DRIVE unit. The CAL SYNC signal is normally 0 V. However, when the electron gun is periodically turned off for a 1.5-sec interval, the CAL SYNC signal (0 → 5 V, 400 Hz square wave) then switches the grid voltage between -3 V and 0 V. The CAL SYNC signal is only present during the first half of each 1.5-sec "gun-off" period. The last half of the "gun-off" period is used to obtain a zero reference for the photometer outputs.

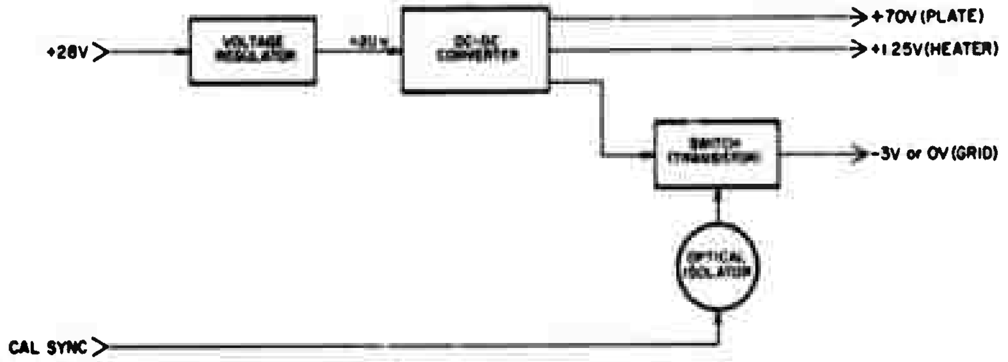

Figure 41. Block diagram of control circuit for calibration light.

The voltage induced in the current monitor coil (Fig. 29) by the chopped electron beam was fed to a phase-sensitive amplifier (Fig. 39). The low-gain channel was designed to provide a responsivity of 0.1 V/mA, whereas the figure for the high-gain channel was 1.0 V/mA. The responsivity figures are expressed in terms of dc output voltage per unit (mA) of average beam current (excluding any dc beam component). A dc component to the beam, which might arise from insufficient control-grid bias, should not in principle contribute to the outputs of the beam-current amplifier or the photometers. In contrast, the Faraday-collector-type beam monitor employed a dc amplifier which should (and did) respond to a dc beam.

During the operation of the complete payload system, a periodic pulse (with a period of about 14 sec in the second-generation system) was supplied by the Langmuir-probe circuitry to the EBIL system. The pulse was fed to a one-shot multivibrator in the SYNC DRIVE unit. The *one-shot* provided a 1.5-sec-wide output pulse which inhibited (clamped off) the SYNC signal to the electron gun grid driver. The signal from the Langmuir probe also triggered a second *one-shot* which controlled the on-period (0.75 sec) of the calibration source. The 1.5-sec "off period" of the electron gun thus permitted: (*i*) a check of the response of the photometers to the calibration light, (*ii*) a zero (base-line) check of the photometer outputs during the last half of the "gun-off" period, and (*iii*) hopefully an unperturbed measurement of the ambient electron temperature and density by the Langmuir probe.

The Faraday collector in the first system consisted of a 6-inch-diameter, copper-clad disk with glass-epoxy base. The copper covering was etched to provide three electrically isolated collection zones, a central two-inch-diameter disk and two concentric annular zones each one-inch wide. The collecting areas of the inner, middle and outer zones were ($\pi/4$), ($3\pi/4$), and ($5\pi/4$) sq. in., respectively. A high-transparency, knitted-morel mesh was mounted in front of the collecting surfaces. The mesh was biased approximately 50 V negative with respect to the collecting surfaces. The screen effectively acted as a suppressor grid to reduce the probability of escape of secondary electrons generated at the collecting surfaces. A segmented collector was introduced in the hope that potentially useful information on changes in beam position during the actual experiment might be obtained.

In view of the anticipated beam-power level in the second-generation system (up to 125 Watts), the Faraday collector was of metal-ceramic construction. A segmented collector was again used. However, four thin, electrically-isolated quadrants of stainless steel were mounted on a thin ceramic disk to form a circle of approximately 6-inches diameter. It was anticipated that this configuration of collecting zones would remove some of the ambiguity inherent in the first design. If the diameter of the beam at the collector were as anticipated and if its current density were uniform, it would be possible in principle to approximate both the radial displacement of the beam from the center of the collector and its azimuthal position from the observed distribution of current over the four quadrants. In practice, several factors (such as the secondary-electron problem) contribute to the ambiguity of the interpretation. Hence, care must be exercised if quantitative results on beam position are desired.

A set of circuit diagrams covering the two EBIL systems is included in the appendices. Features of the systems not mentioned above included temperature and high-voltage monitors for each of the photometers and for the electron-gun units. Calibration data for these monitors has also been included in the appendices.

PREFLIGHT CALIBRATION OF ELECTRON-BEAM-INDUCED LUMINESCENCE SYSTEMS

The responsivity of the photometers may be defined in the usual manner as

$$R = \left[V_0/A\int_0^{\infty} H(\lambda)\ T(\lambda)d\lambda\right] , \tag{29}$$

where V_0 is the output signal voltage, A the effective collecting area of the instrument, and $\int_0^{\infty} H(\lambda)\ T(\lambda)d\lambda$ the effective irradiance accepted by the detection system. (When a phase-sensitive detection system is employed, normally the rms values of the fundamental components of the signal voltage and the incident radiation are used in defining the responsivity.)

Although absolute calibration of the photometers was not an essential part of the EBIL-system calibration procedure, as will shortly be discussed, it was nevertheless carried out in an attempt to evaluate the performance characteristics of the photometers. An Electro-Optics Associates Model L-101 Spectral Irradiance Standard (quartz-iodine lamp) and P-101 power supply were used in the calibration. The output of the lamp was chopped mechanically at a rate of either 350 Hz (first system) or 400 Hz (second system) as determined by a Hewlett-Packard Model 5321 A electronic counter. The frequency of the chopper was stabilized by regulating the input to the chopper motor. The chopping frequency was monitored continuously during calibration and was adjusted to the proper frequency when required. The output of the first-generation photometers, which employed dc-reset amplifiers, was not sensitive to reasonable variations in the chopping frequency; however, the output of the second-generation instruments was sensitive to the chopping frequency since they employed lock-in amplifiers.

The light source was placed approximately ten feet from the photometer, which was positioned so that the source was in the center of the field of view. Since the optical wedges turn the fields of view, it was necessary to adjust each instrument until the desired condition was realized. Calibrated neutral-density filters were used to vary the irradiance at the photometer. Account was taken of the nonadditive nature of the densities which occurs when two or more filters are stacked roughly parallel to each other. The effect of stacking was checked by tipping the filters so that the reflections passed out of the system. The irradiance levels were then varied over the dynamic range of the instrument.

In carrying out the calibration, it was of course necessary to derive a SYNC signal from the chopper. This was done photoelectrically by means of a small incandescent light and a photodiode mounted on opposite sides of the chopper blade. The SYNC signal derived from the photodiode was then fed to a unit which provided for phase-and-symmetry adjustment. (See discussion relating to Fig. 32.) The output of this unit provided the SYNC input for the photometers. In operation, the phase and symmetry were adjusted to realize maximum response to the standard lamp.

Although the photometers were designed to view an object approximately 14-inches distant, computations revealed that with the standard lamp 10-ft away the cone of light from the collector should still pass through the field stop without obscuration. Responsivity data were then determined by noting the response of the instrument to various levels of irradiance. The slope of the resulting curve (straight line) was taken to be the responsivity. A summary of the results is presented in the appendices.

The fields of view of the instruments were also checked. A ground-glass plate was covered with an opaque mask containing a pinhole aperture. The chopped radiation from the standard lamp was then used to illuminate the pinhole thus effecting a modulated point source. The field-of-view data were then obtained by means of a rotating table which permitted controlled rotation of the photometer about an axis through the collecting lens. The results were checked by means of an independent system built around one of the Amperex 6977 light sources. Typical FOV results are presented in the appendices.

The EBIL section of each of the payloads was demountable. (See Figs. 11, 12, 15, and 16.) This feature served a two-fold purpose: (*i*) it permited calibration of the EBIL system in a somewhat smaller vacuum chamber than would have been required to accomodate the entire payload and (*ii*) it permitted calibration to be carried out while preserving the EBIL-system geometry appropriate to the flight.

The calibration tests were conducted using an 0.8-meter-diameter vacuum chamber at AFCRL. The chamber was evacuated by an NRC HS32-32,000 oil diffusion pump backed by a Kinney KMBD-1600/KDH-150 booster and fore-pump combination. The oil diffusion pump was capped by a liquid-nitrogen-cooled baffle which served as the pumping throat for the vacuum chamber. During the calibration of the first EBIL system the background pressure in the chamber dropped as low as $\approx 7 \times 10^{-7}$ Torr after several hours of pumping; however, the background (base) pressure during the calibration of the second system did not drop below about $2\text{-}3 \times 10^{-6}$ Torr.

In effecting a calibration, the responses of the photometers to beam-excited emissions were recorded over a range of target pressures. Most of the measurements were made using targets of pure N_2 and air in the case of the first system. The targets used in calibrating the second payload included pure N_2, air, pure CO_2, and CO_2-N_2 mixtures. The tests were conducted with room-temperature ($\approx 294°K$) targets since the facilities were not designed to permit control of the gas temperature.

In the initial calibration efforts, the outputs of the photometers and two of the three Faraday collector amplifiers were simultaneously recorded on a visicorder as the target pressure was varied stepwise over the range from 10^{-6} to nearly 10^{-3} Torr. Subsequently, more accurate measurements of signal levels were obtained through the use of calibrated digital voltmeters. Target chamber pressures were initially monitored by means of an NRC Bayard-Alpert type ionization gauge. Most of the subsequent pressure measurements were carried out with both the ionization gauge and an MKS Instruments capacitance manometer which had been calibrated against a McLeod gauge.

The results of one of the first calibration runs (first payload) are shown in Fig. 42. The average collector current was about 2.5 mA. The data points above 8×10^{-6} Torr have been corrected for a slight change in beam current. It is of interest to note that the photometer outputs appear to be linear with N_2 pressure for fixed beam current and that extrapolation of each of the linear response curves to zero pressure yields a non-zero intercept. The slope of the instrument response curve for the rather weak N_2^+ $1N$ (2,4) band is hardly discernable in the figure. Measurements extending upward to 4×10^{-4} Torr yielded the value of the slope of the response curve associated with this band.

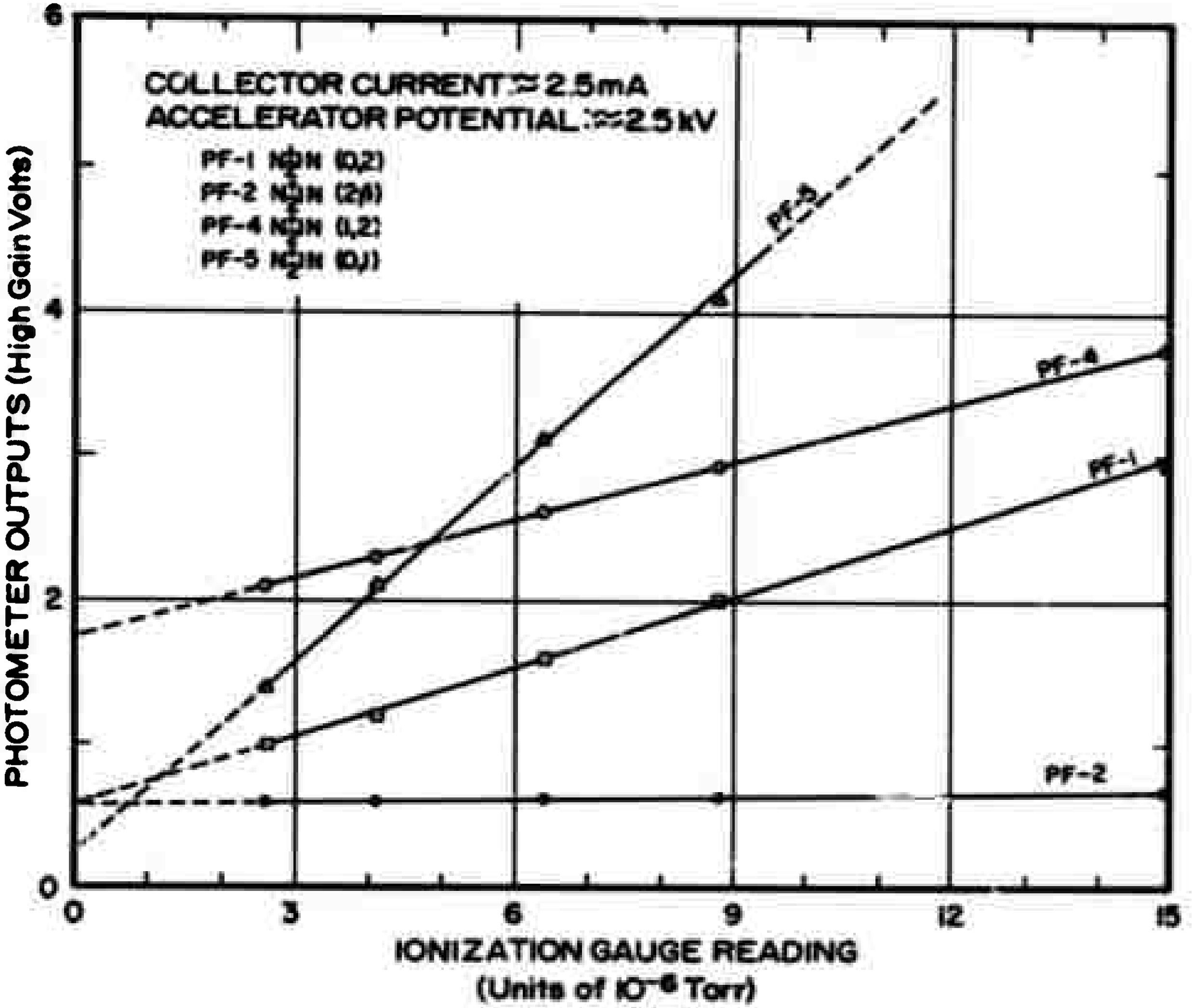

Figure 42. Response of photometers to electron-beam-induced emissions -- Aerobee AO 3.006-1.

The technique which was envisioned for determining atmospheric N_2 vibrational temperatures entailed a comparison of selected signal ratios obtained from the flight record with the corresponding ratios obtained during laboratory calibration of the EBIL system. The inability to vary the N_2 vibrational temperature during calibration necessitated normalization of the flight ratios (corrected) by the values observed with a vibrationally-cool ($\approx$294°K) target. The resulting ratios, e.g. $[V_{(1,2)}/V_{(0,1)}]_{\mathrm{FLIGHT}}/[V_{(1,2)}/V_{(0,1)}]_{\mathrm{LAB}}$ when properly corrected for background, for effects associated with changes in the rotational structure of the bands, and for possible contamination by other spectral features could then be compared with the predicted variation with vibrational temperature (Fig. 6). Assuming the validity of the "transfer curve" (See discussion on pg. 18), one could then read from the curve the vibrational temperature corresponding to the observed departure from unity.

Initial calibration ratios of about 0.36, 0.29, and 0.0083 were obtained for (0,2)/(0,1), (1,2)/(0,1), and (2,4)/(0,1), respectively. Subsequent tests led to improved values of 0.23 and 0.0075 for the latter ratios.

Some attention was also given to the change in signal ratios with beam deflection. Deflection plates were mounted close to the anode of the electron gun, and photometer and beam collector readings were recorded for several sets of deflection-plate voltages. Readings were taken at base pressure and with a pure N_2 target of about 5 x 10^{-5} Torr, the highest pressure which would permit arc-free operation of the deflection plates. Analysis of the results led to the following observations: (*i*) the photometer outputs were relatively insensitive to beam deflection at base pressure, and (*ii*) although the photometer outputs were more sensitive to beam deflection at an N_2 pressure of 5 x 10^{-5} Torr (changing by as much as 25%), the *output ratios* in general exhibited less than 10% change as the beam was deflected over a relatively wide range. The constancy of the (1,2)/(0,2) ratio was particularly noteworthy since it varied by a maximum of less than 4% for the deflection voltages which were used.

The zero-pressure intercepts in Fig. 42 suggest a pressure-independent contribution to the total photometer signal. Luminescence produced within the vacuum chamber was visible even at the lowest pressures where emissions from the beam region could not be seen. The precise source of the background signals was not immediately identified, and, indeed, a positive identification has not yet been made, although several related tests have been carried out. The flight data also exhibited a background signal. However, the information which is presently available does not suggest that the backgrounds necessarily arise from the same source.

The calibration procedure for the second EBIL system paralleled that of the first. In view of the interest in including an instrument for [CO_2] measurements, the calibration procedure entailed the use of several gases and gas mixtures. It also proved desirable to use a quadrupole mass spectrometer for analysis of the target composition. Figure 43 presents some of the calibration data for the second EBIL system.

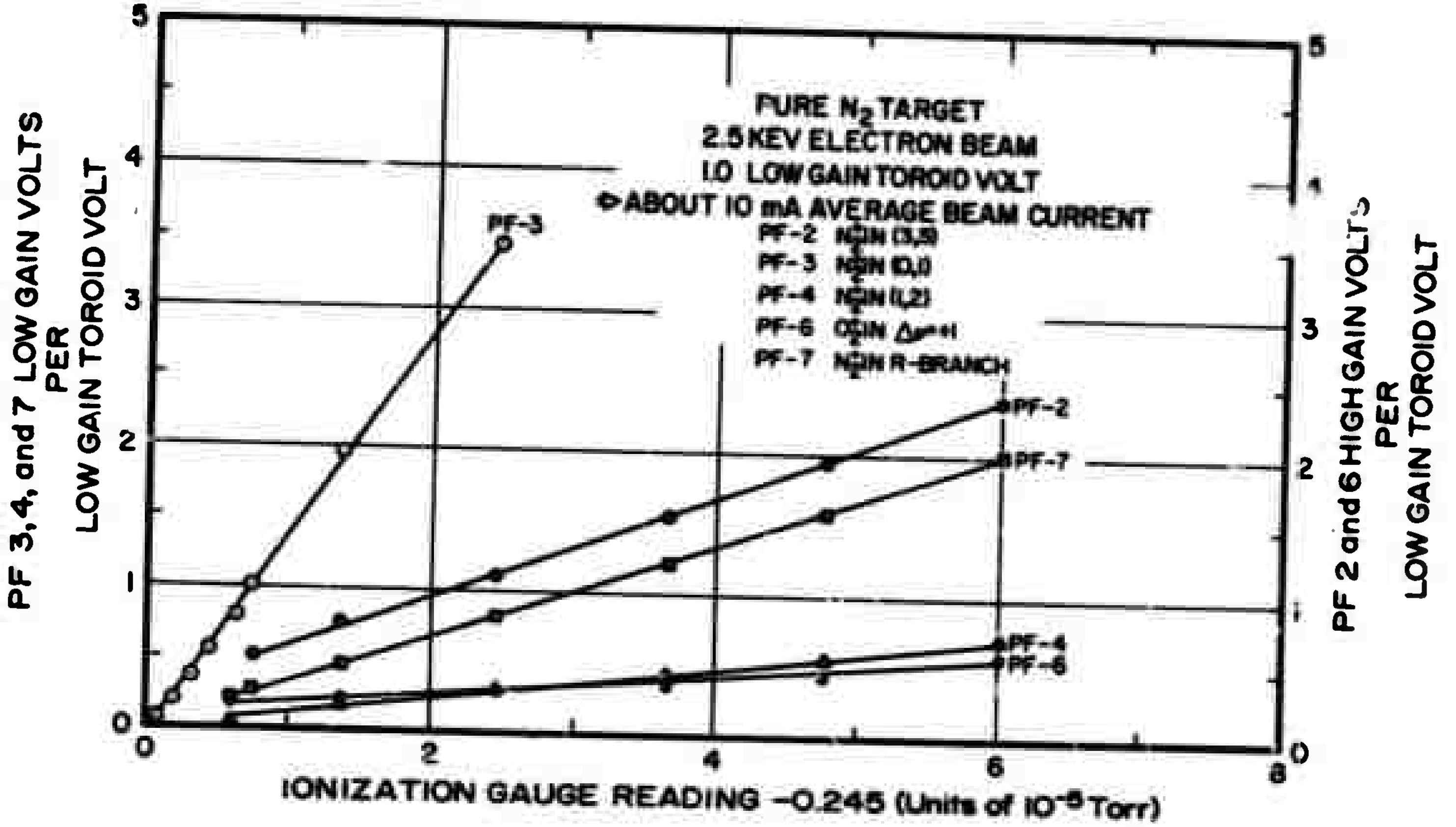

Figure 43. Response of photometers to electron-beam-induced emissions -- Aerobee AO 3.910-1.

GROUND SUPPORT FOR AND PERFORMANCE OF AEROBEES I AND II.

The first EBIL system and supporting instrumentation were launched aboard Aerobee I from the Churchill Research Range, Fort Churchill, Manitoba, Canada, at approximately 06:18:25 GMT on 13 March 1970. The rocket reached an apogee of 206.3 km at roughly T + 243 sec. Magnetometer records indicate that the payload was stable. The spin period of the rocket was about 0.4 sec after completion of boom erection and other mechanical functions, as evidenced by spin modulation of the data. A precessional period of about 50 sec was also inferred from the flight information. The housekeeping commutator record indicated that all mechanical and electrical functions were accomplished as scheduled. A curve of altitude versus time is presented in Fig. 44.

In addition to radar tracking, the Churchill Range provided optical ground support instrumentation consisting of an all-sky camera, photometers, and a scanning spectrometer to aid in determining auroral conditions during the flight. The all-sky-camera photographs shown in Figs. 45 through 47 were obtained from a 70 mm f/1.0 camera which provided a 150° field of view. Two-second exposures were taken every 5 seconds. The photographs reproduced in the figures have been selected to include a couple of frames near the time of lift off and every third or fourth frame through the significant portions of the remainder of the flight. The photographs were taken from Twin Lakes and have an indicated azimuth of 156.6° and an elevation of 55.0° which correspond to the predicted vehicle position at 100-km altitude on the down leg. All of the other ground-based optical instruments were aimed toward the above point during the flight.

The all sky camera photographs indicate that the rocket passed through some relatively intense auroral activity during ascent up to the time the electron gun was opened. During the remainder of the flight somewhat less intense auroral conditions prevailed.

During the flight of Aerobee I four ground-based photometers were used to measure the auroral intensity at a point having an elevation of 48.3° and an azimuth of 154.3° from the Churchill Auroral Observatory. This point corresponds to the predicted vehicle position at an altitude

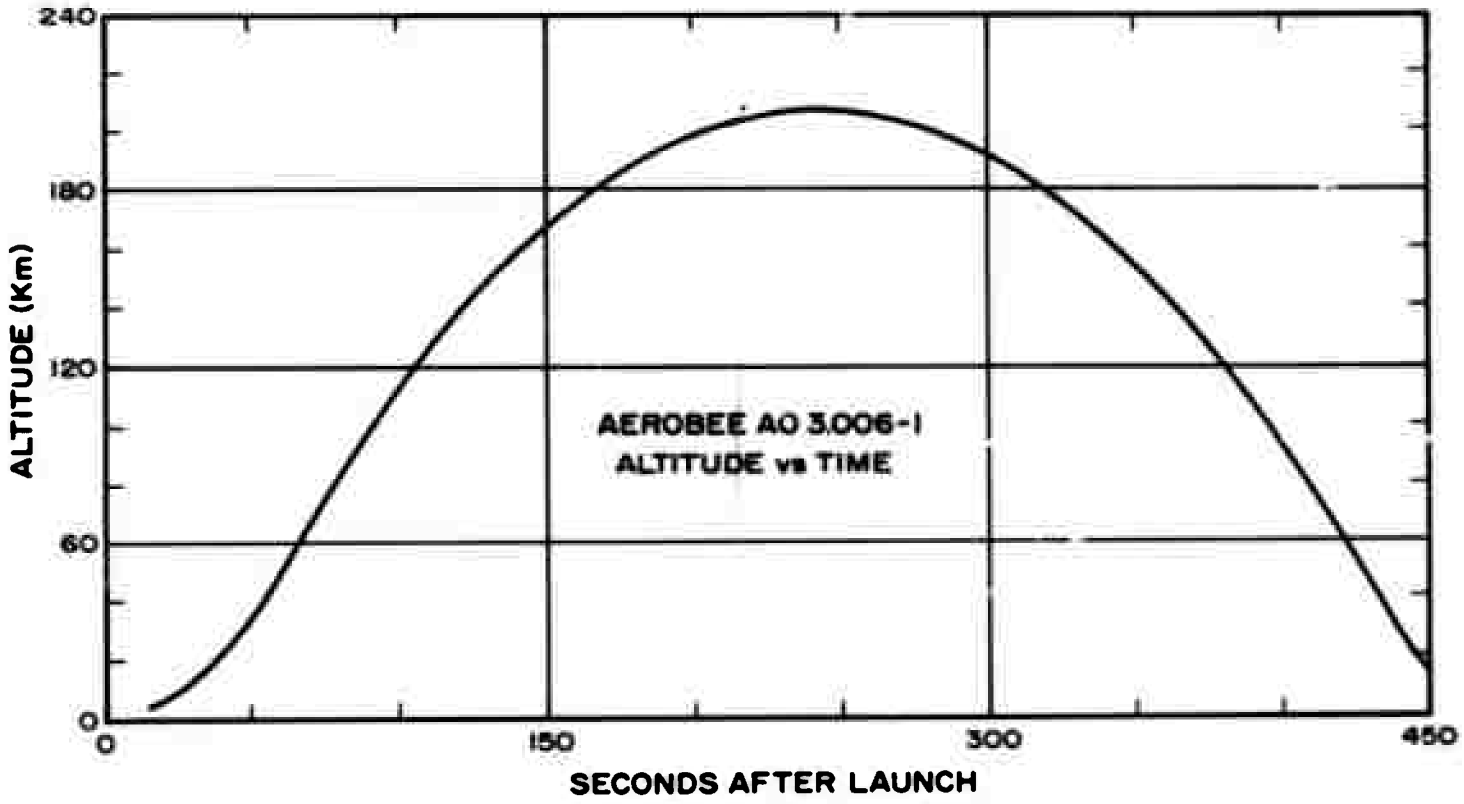

Figure 44. Altitude versus time after launch for Aerobee AO3.006-1.

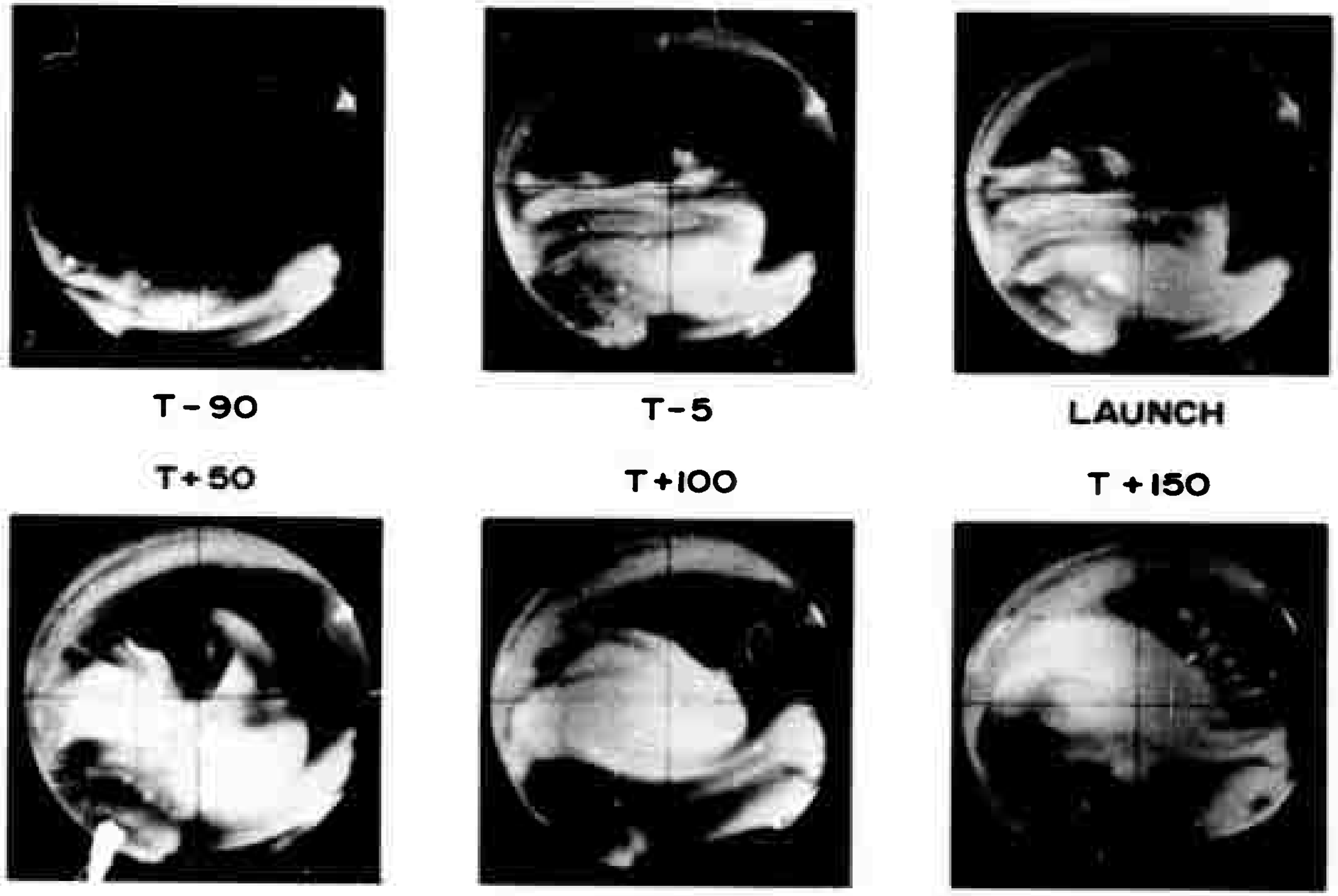

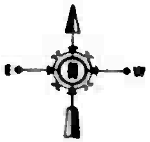

Figure 45. Churchill Research Range Auroral Observatory All Sky camera photographs taken in conjunction with the flight of Aerobee A03.006-1. Exposures were for 2 seconds every 5 seconds. The predicted payload location at 100 km (descent) is marked in each frame. This area was viewed by the ground support photometers throughout the flight to provide a time history of the auroral activity.

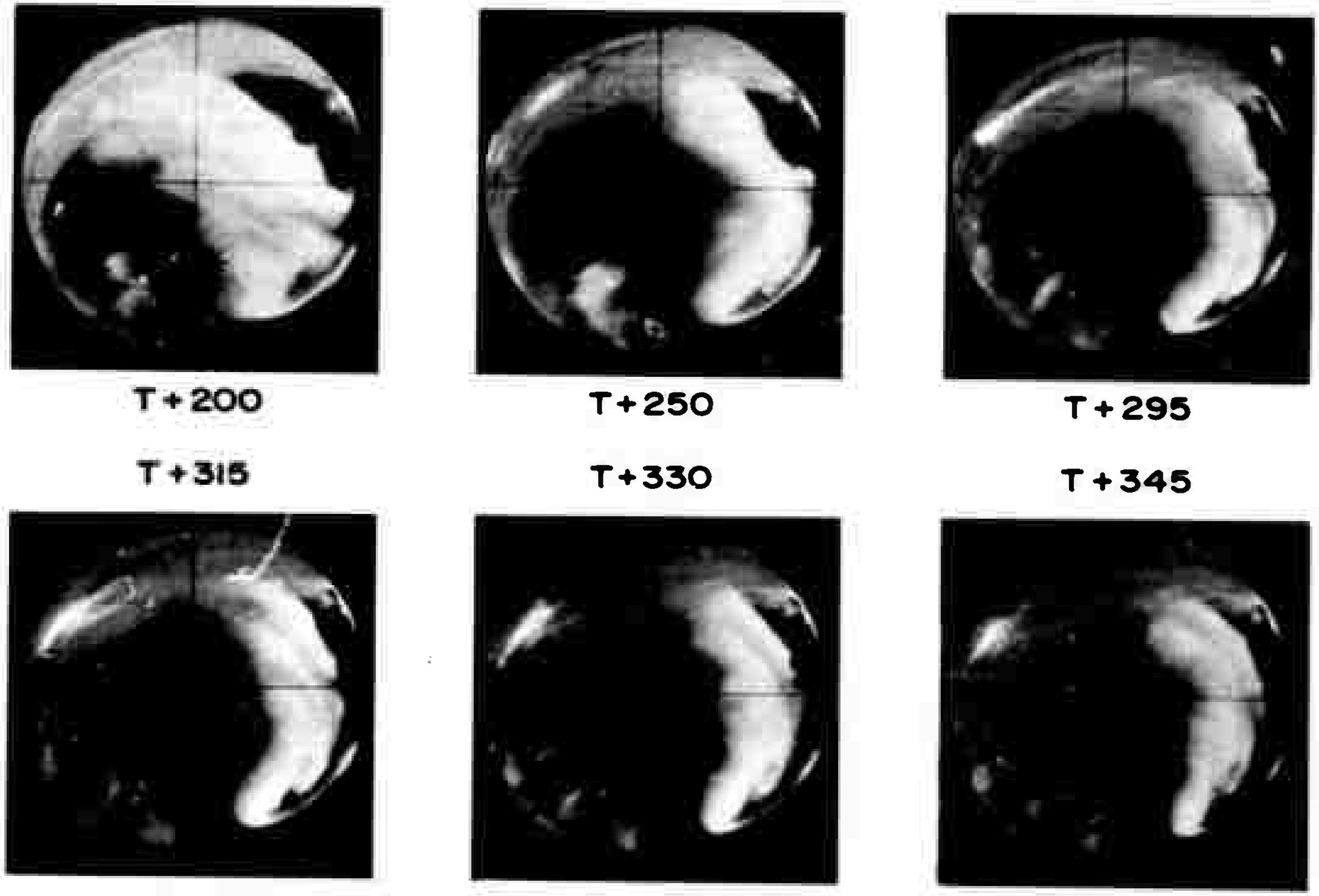

Figure 46. Churchill Research Range Auroral Observatory All Sky camera photographs taken in conjunction with the flight of Aerobee A03.006-1. Exposures were for 2 seconds every 5 seconds. The predicted payload location at 100 km (descent) is marked in each frame. This area was viewed by the ground support photometers throughout the flight to provide a time history of the auroral activity.

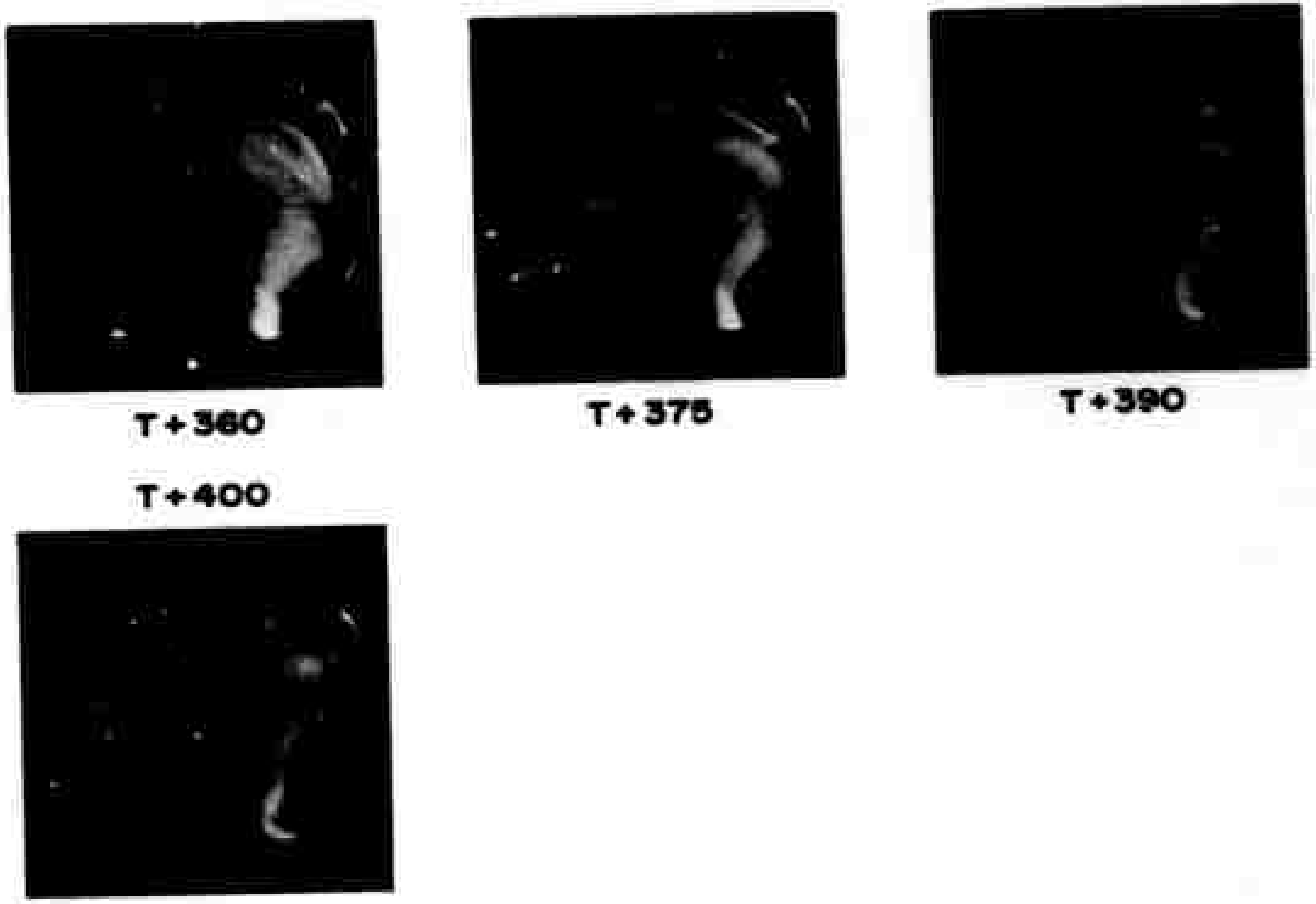

Figure 47. Churchill Research Range Auroral Observatory All Sky camera photographs taken in conjunction with the flight of Aerobee A03.006-1. Exposures were for 2 seconds every 5 seconds. The predicted payload location at 100 km (descent) is marked in each frame. This area was viewed by the ground support photometers throughout the flight to provide a time history of the auroral activity.

of 115-km on the down leg of the flight. The four photometers measured the intensity of emissions at wavelengths λ 4236 Å, 5577 Å, 3914 Å, and 6300 Å. Each photometer had a field of view of 2°. A spectrometer scanning from 3950 Å to 6600 Å having a spectral slit width of 15.8 Å provided a measurement of auroral intensities of the 5577, 6300, and 6364 Å lines. Riometer and ionosonde support measurements were also provided by the range.

Aerobee II was launched from White Sands Missile Range at 20:31:07 MDT on 15 October 1971. Onboard monitors indicated a normal, stable flight with all electrical and mechanical functions operating as designed. An apogee of 214.0 km was reached at approximately T + 246 sec. Radar tracking yielded the altitude-versus-time curve shown in Fig. 48. The spin period of the rocket during the data-taking portion of the flight was approximately 0.63 sec.

Both payloads were recovered by parachute. Damage to the instrumentation was not severe in either case; however, in both instances, the booms were destroyed.

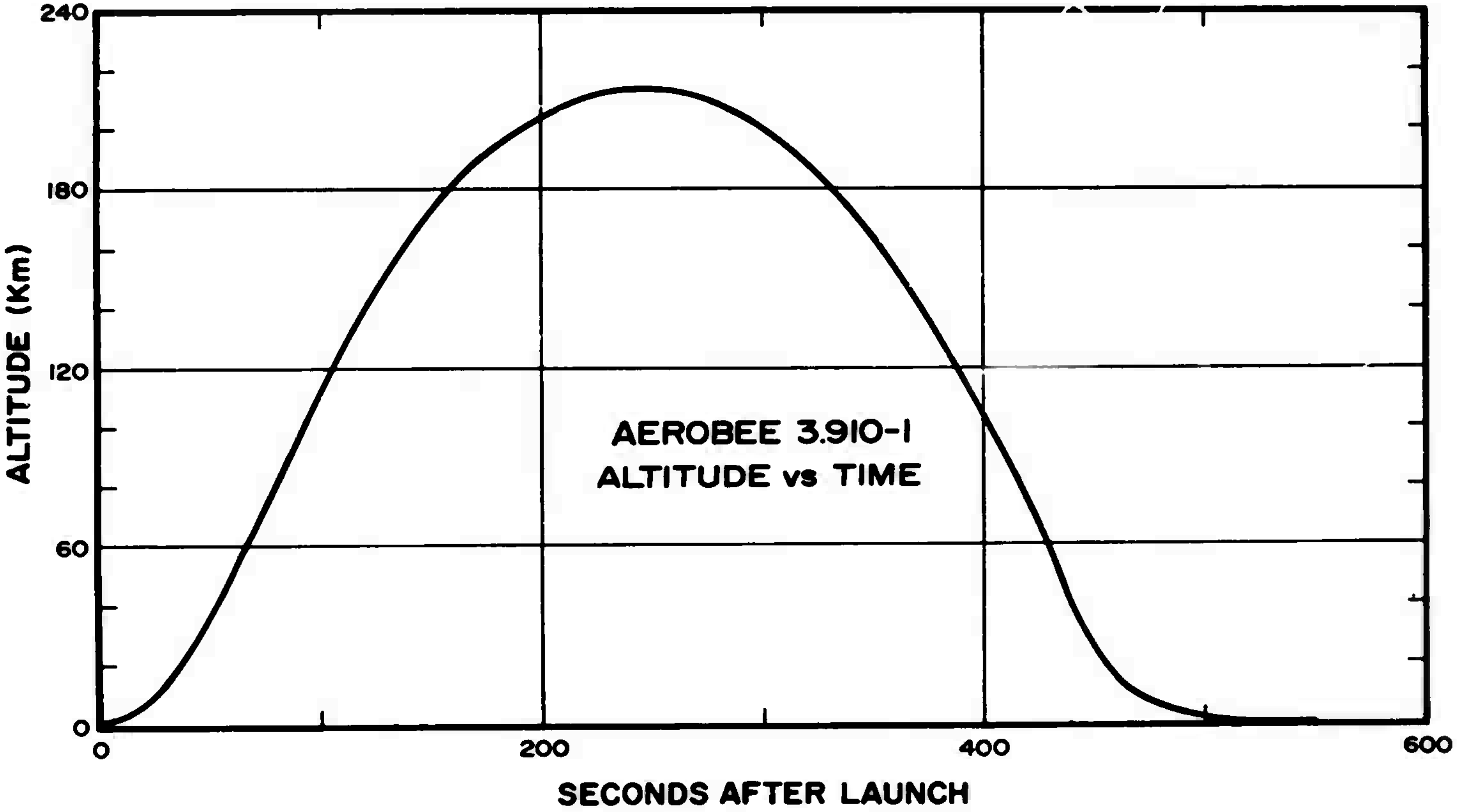

Figure 48. Altitude versus time after launch for Aerobee A03.910-1.

OBSERVATIONS AND RELATED DISCUSSION

Aerobee I was launched into a relatively intense auroral display. Some of the onboard instrumentation, as well as some of the ground-based instruments, were used to provide information on the nature of the event. Data obtained from the support instrumentation will be presented first. This discussion will be followed by a summary of the results obtained with the EBIL system.

The time history of the auroral intensity in the λ 3914 Å, 4236 Å, 5577 Å, and 6300 Å features as measured from the ground is shown in Fig. 49. Each of the photometers had a 2° conical field of view and was directed toward a point having an elevation of 48.3° and an azimuth of 154.3° from the Churchill Auroral Observatory, as mentioned earlier. This position corresponded to the 100-km level on the down-leg of the anticipated trajectory. For the view angles previously specified, the intensity in λ 5577 Å did not exceed about 16.5 kR during the flight period. The intensity ratio I(5577)/I(3914) is of fundamental importance. The data of Fig. 49 indicate a variable ratio during the flight with values lying between the limits of 0.6 and 1.6. Rees (1959) was led to the conclusion that [I(5577)/I(3914)] ≈2.0 with little variation; however, several observations which contradict this conclusion have been reported [Romick and Belon (1967); Murcray (1969); Brekke and Omholt (1968)]. Vallance Jones (1971) suggests continued use of 2.0 as an *average value* for the ratio. The intensity ratio I(4236)/I(3914) remained roughly constant during the flight at a value of about 3 x 10^{-2}. Vallance Jones (1971) suggests a value of 3.8 x 10^{-2} for this ratio in a normal IBC 3 aurora.

The results obtained from the rocket-borne, vertically-viewing auroral photometers (λ 3914 Å and 5577 Å) are presented in Fig. 50. The trajectory data were used to reduce the flight records to emission profiles. The data indicate that the vehicle entered a relatively intense auroral form as it was breaking up. Both spatial and temporal variations are inferred from the photometer data indicating that the auroral form was changing in position and/or intensity as the vehicle passed through the active region.

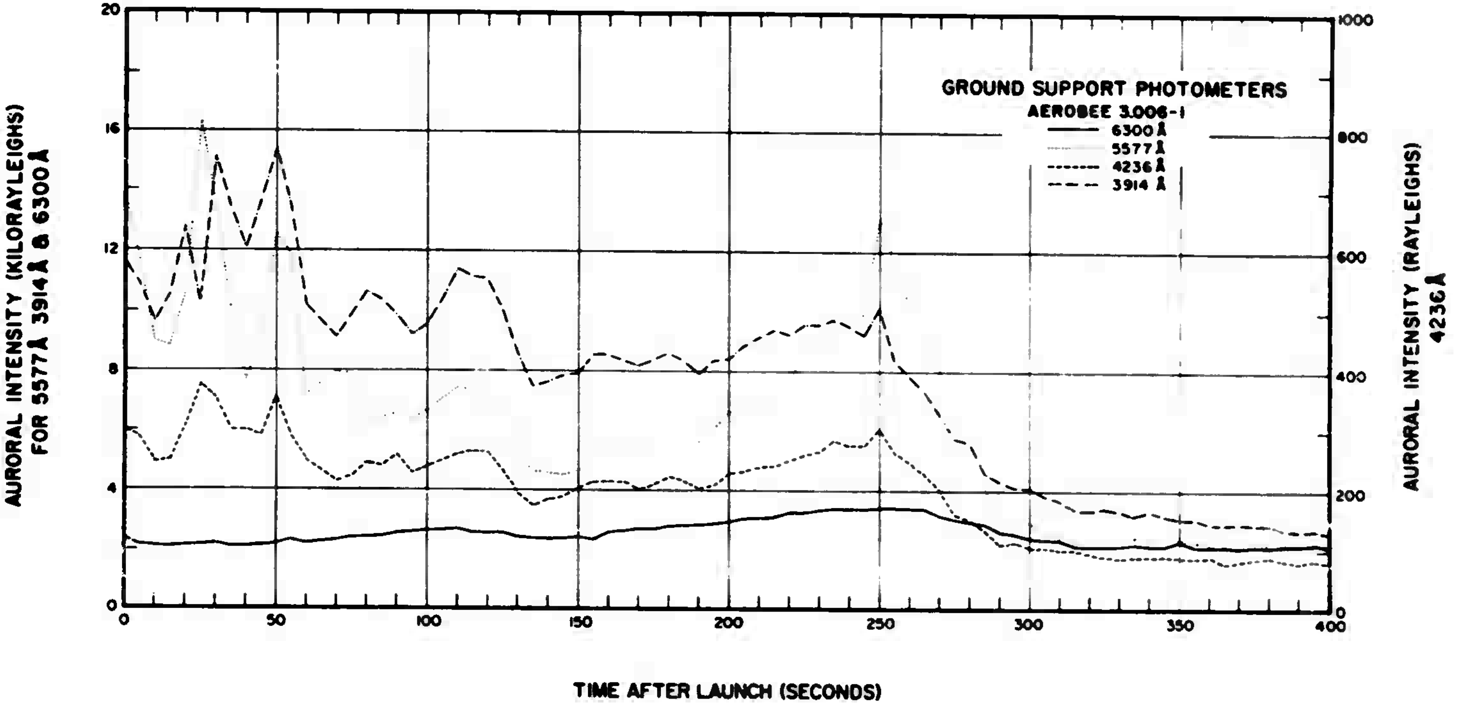

Figure 49. Time history of the auroral intensity in the λ 3914, 4236, 5577, and 6300 Å features as measured from the ground.

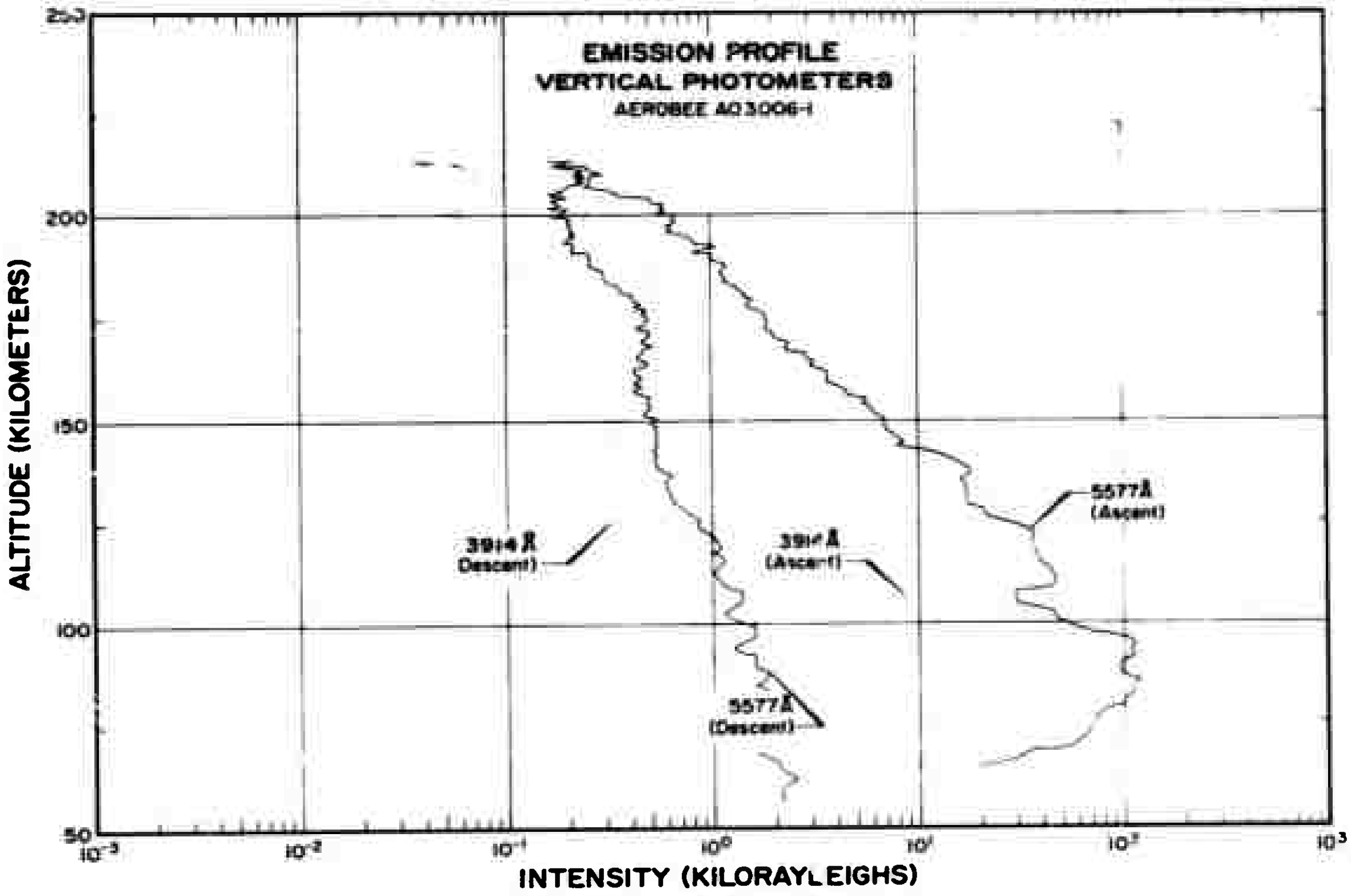

Figure 50. Emission profiles for λ 3914 Å and 5577 Å.

The Langmuir probes aboard Aerobees I and II were included for the primary purpose of measuring electron temperature and secondarily for measuring relative electron density and vehicle potential.

During the payload checkout for Aerobee I, it was noted that the Langmuir probe was receiving interference from the VHF telemetry transmitter. The interference effect was seen as a DC low-current offset produced by rectification of the rf pick up by the Langmuir probe circuitry. To minimize the interference, the payload was rotated approximately 90° with respect to the telemetry transmitter section. The Langmuir-probe sensor was thereby positioned in a relative null in the near field transmitter radiation pattern. Although the effects of the rf interference were evident in the flight data, they were not serious enough to prevent data analysis.

The results of the temperature analysis of the Aerobee I Langmuir-probe data are shown in Fig. 51. Each of the plotted points represents the temperature from either the leading or trailing edge of the sweep waveform as a function of altitude. The small crosses are from the leading edge of a sweep and the diamonds are from the trailing edges. The data indicate that the electron temperature was significantly elevated with respect to that of the normal nighttime quiet ionosphere. The temperature at 200 km was approximately 2000°K.

The vehicle-potential data for Aerobee I, shown in Fig. 52, indicate that the vehicle was negative at low altitudes but became less negative with increasing altitude, apparently owing to loss of electrons from the EBIL system. Finally, at an altitude near apogee, the vehicle potential became positive, thus preventing additional measurements by the Langmuir probe.

Figure 53 shows the Langmuir probe sensor current profile obtained from the flight record of Aerobee I. The current profile can essentially be linearly related to electron density either from the sensor geometry and theoretical calculations, or it may be effectively normalized by means of an independent measurement of electron density such as may be obtained from an ionosonde or rf probe. Experience has shown that the calibration from another independent measurement yields the most reasonable and consistent absolute electron density information.

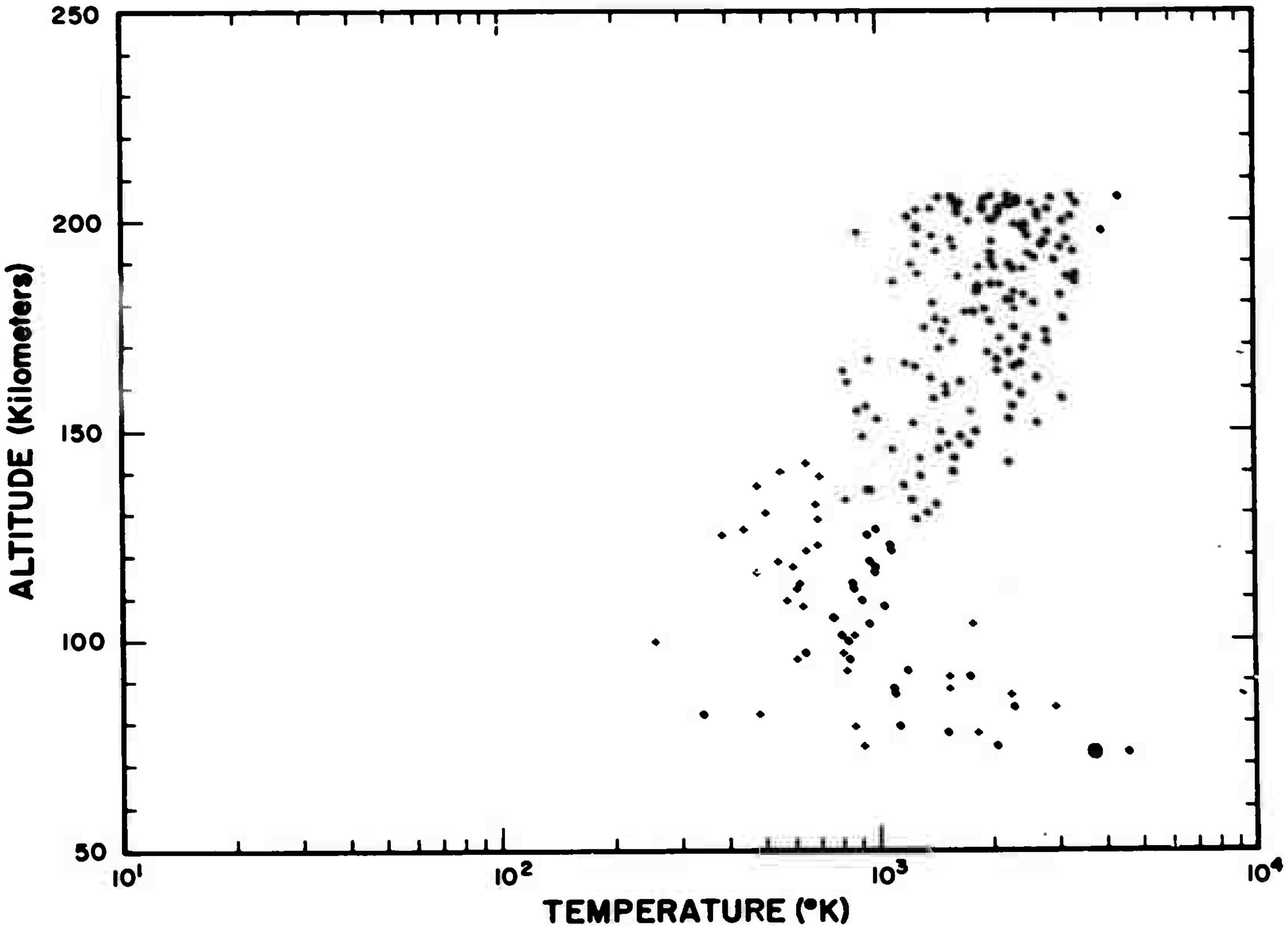

Figure 51. Electron temperature results from the flight of Aerobee AO 3.006-1.

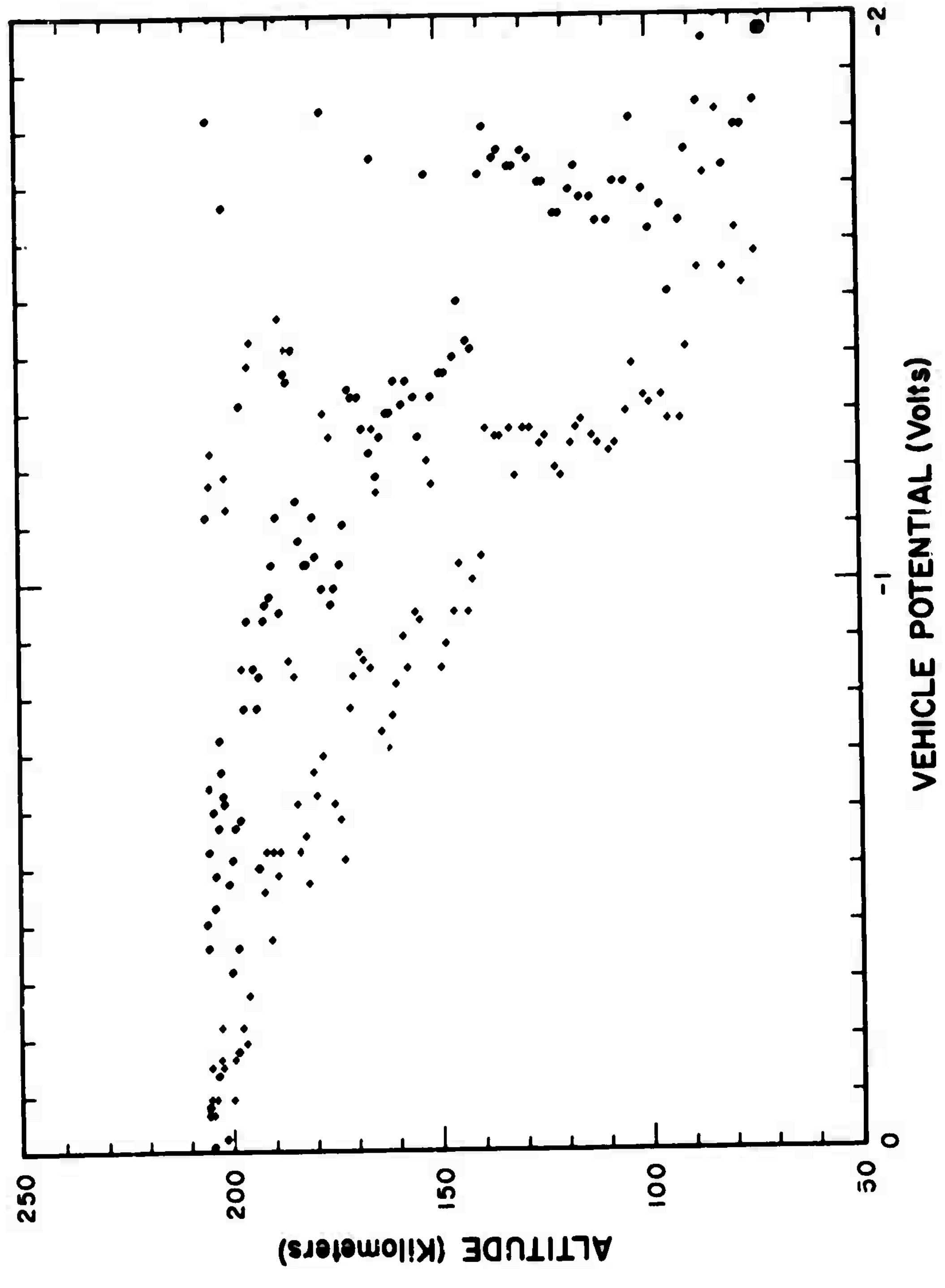

Figure. 52. Vehicle-to-plasma potential from the flight of Aerobee AO 3.006-1.

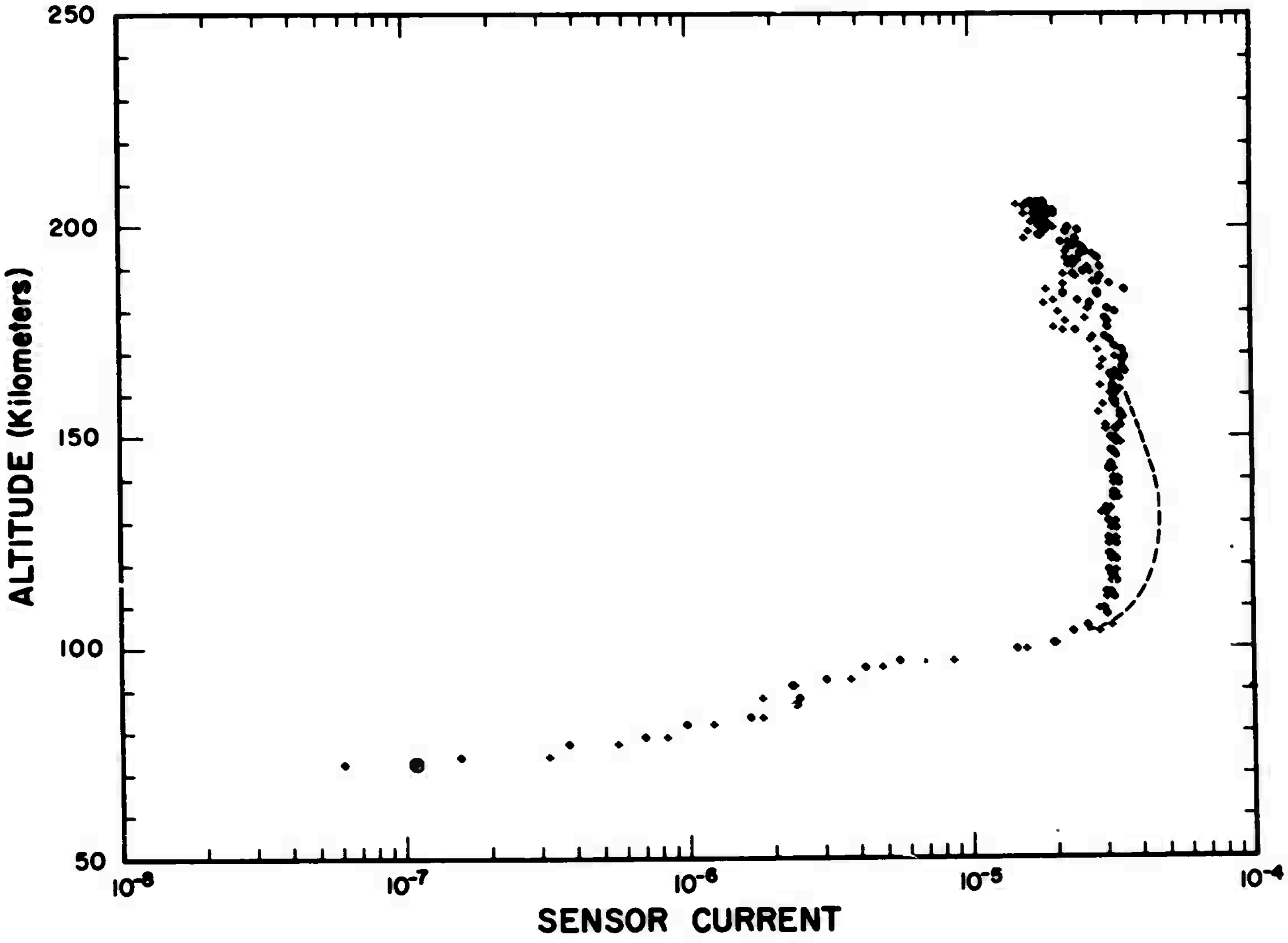

Figure 53. Langmuir probe sensor current profile -- Aerobee AO 3.006-1.

In as much as the auroral activity and energy input to the ionosphere on the up-leg portion of the flight were exceptionally high, the electron density was sufficient to saturate the Langmuir-probe amplifier. The saturation is evidenced by the nearly vertical section of the curve (Fig. 53) corresponding to a current of about 3 x 10^{-5} amp. The dashed curve represents the "best guess" at the electron density profile during active auroral conditions.

The Langmuir-probe data from Aerobee II has presented some unusual problems. A segment of the oscillograph record from this flight is shown in Fig. 54. The upper trace represents a monitor of the sweep voltage applied to the sensor during the 1.5-sec "off interval" of the electron gun. The particular sweep shown was taken from a portion of the flight just shortly after apogee. The lower trace shown in the figure is the logarithm of the sensor current. Ideally, during the period of time that that sweep voltage is negative with respect to the plasma potential, the probe output should be changing linearly with time thus producing a straight line the slope of which can be directly related to electron temperature. However, the only straight-line segments in the sweep which is illustrated correspond to unreasonably low electron temperatures (far lower than the lowest anticipated gas-kinetic temperature). Another disturbing characteristic of the Aerobee II Langmuir-probe data is that the vehicle potential

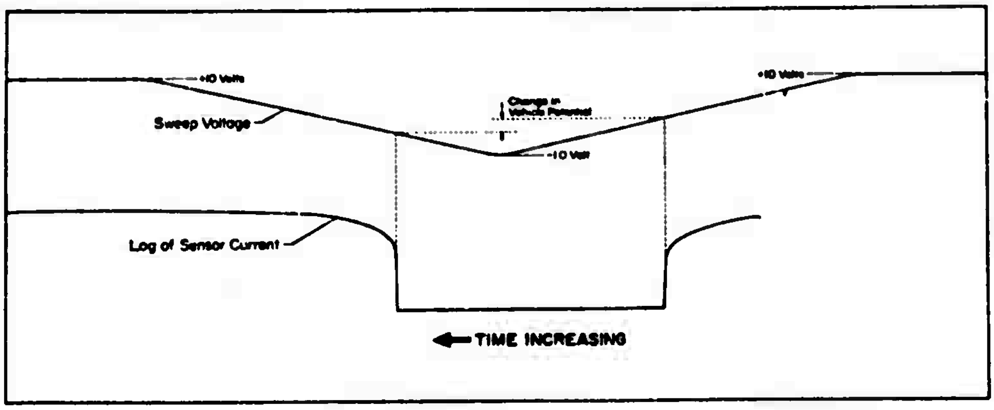

Figure 54. Segment of Langmuir-probe record from the flight of Aerobee AO 3.910-1. (Upper trace -- sweep voltage; lower trace -- logarithm of sensor current).

was several volts negative. This observation is very surprising in view of the presence of the high-current electron gun in the system. Furthermore, by comparing the vehicle potential from leading and trailing edges of a sweep, the vehicle potential rapidly (in the order of several volts/sec) becomes more positive with increasing time from when the electron gun was turned off. It appears that the effect of the electron gun on vehicle potential is not simple and that the large and transient nature of the vehicle potential following cessation of operation of the electron gun prevents normal operation of the Langmuir probe.

In view of these complications, one might wonder why the Langmuir-probe data from Aerobee I did not exhibit similar effects. This question has prompted a re-examination of the Aerobee I data. Interestingly, there were portions of the flight record showing two distinct linear regions in the sensor-current record, one corresponding to a very low temperature. In addition, the vehicle-potential data of Fig. 52 reveal that the vehicle potential was changing between the times of leading and trailing edges of a sweep. The temperature results obtained from the leading and trailing edges also differ with the trailing edges consistently yielding larger temperatures. It should be noted that two possibly significant differences existed between the Langmuir probe operating conditions on the flights: (*i*) a somewhat higher electron-beam current was used during the second flight and (*ii*) the ambient electron temperature and density were much higher during the first flight.

The particle counter aboard Aerobee I was used to provide a measurement of the spectral distribution of the incident energetic electron flux producing the aurora. All data channels from the three geiger tubes and one curved-channel electron multiplier operated essentially normally. The data from these four channels are shown in Fig. 55—58 and correspond to lower cutoff energies of 6.5, 17, 42, and 90 keV, respectively. In each case the actual count rate has been converted to carry the dimensions of electrons $cm^{-2}sec^{-1}ster^{-1}$. In comparing the above count rates with the auroral activity shown in the all-sky-camera photographs and particularly with the outputs of the 3914 Å and 5577 Å vertically-viewing photometers, it appears that a major burst of electrons precipitated into the atmosphere while the vehicle was at an altitude of about 97 km at approximately

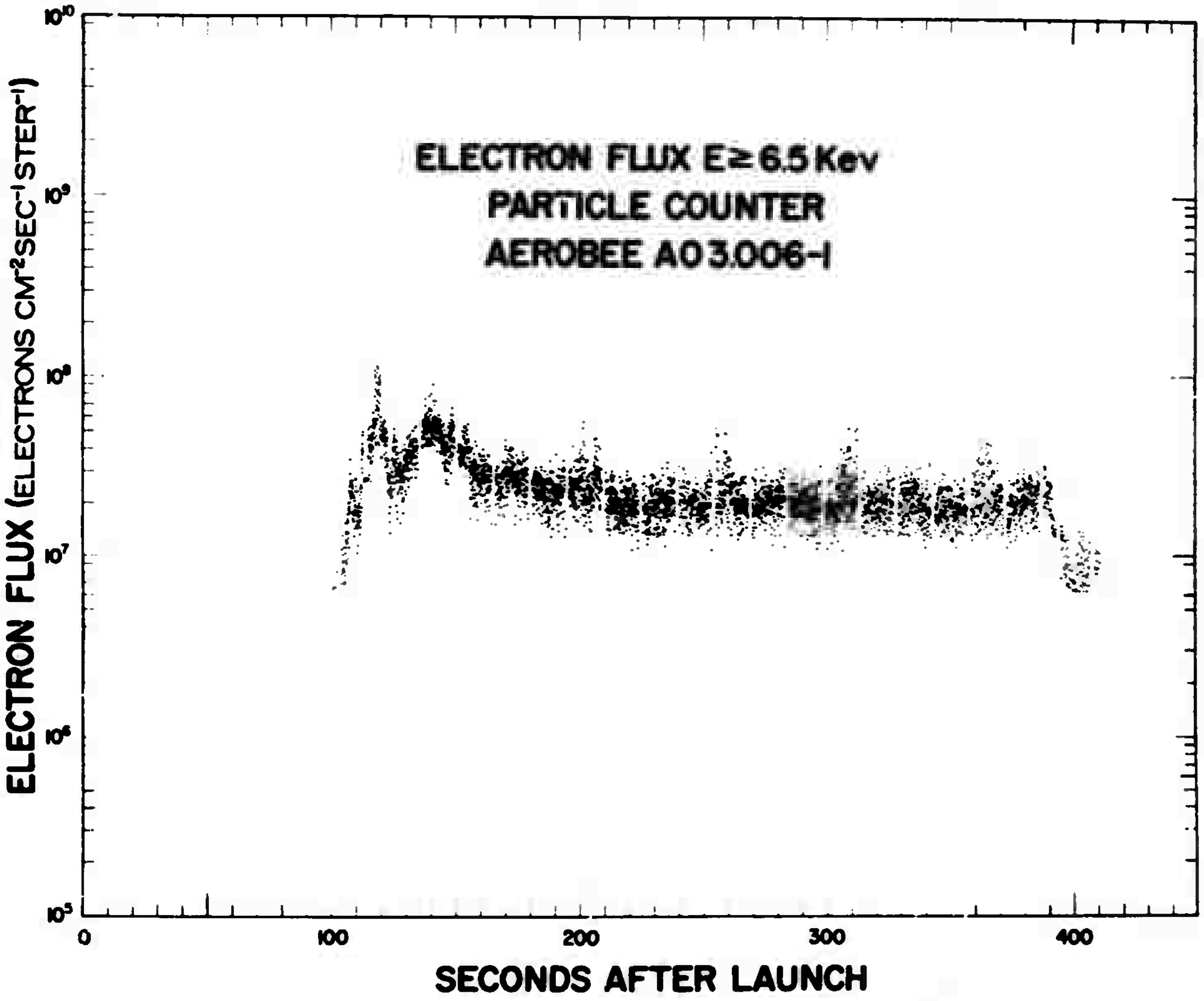

Figure 55. Energetic particle counter data from Aerobee AO 3.006-1 -- Channel No. 1 ($E_m \geq 6.5$ keV).

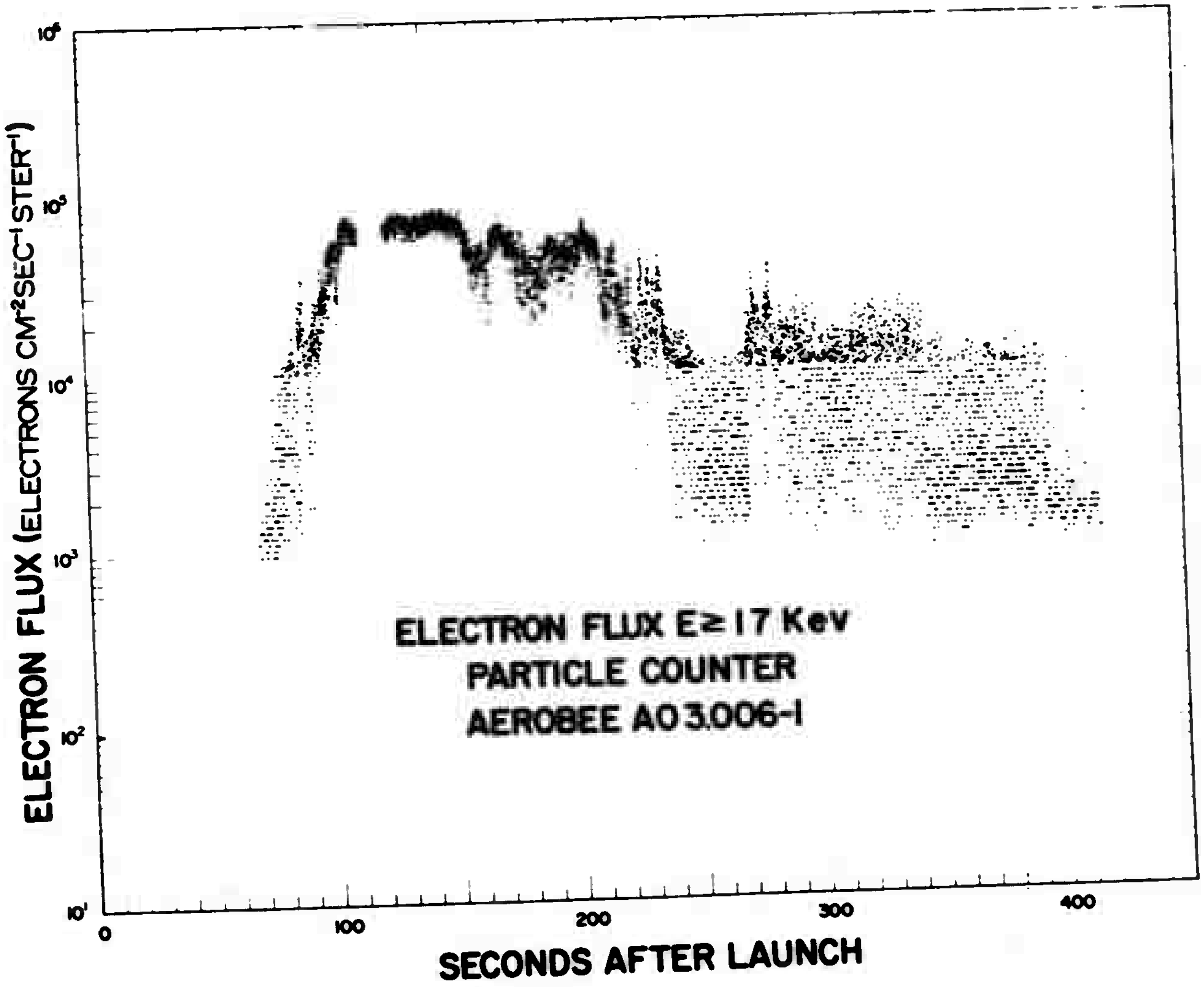

Figure 56. Energetic particle counter data from Aerobee AO 3.006-1 -- Channel No. 2 ($E \geq 17$ keV).

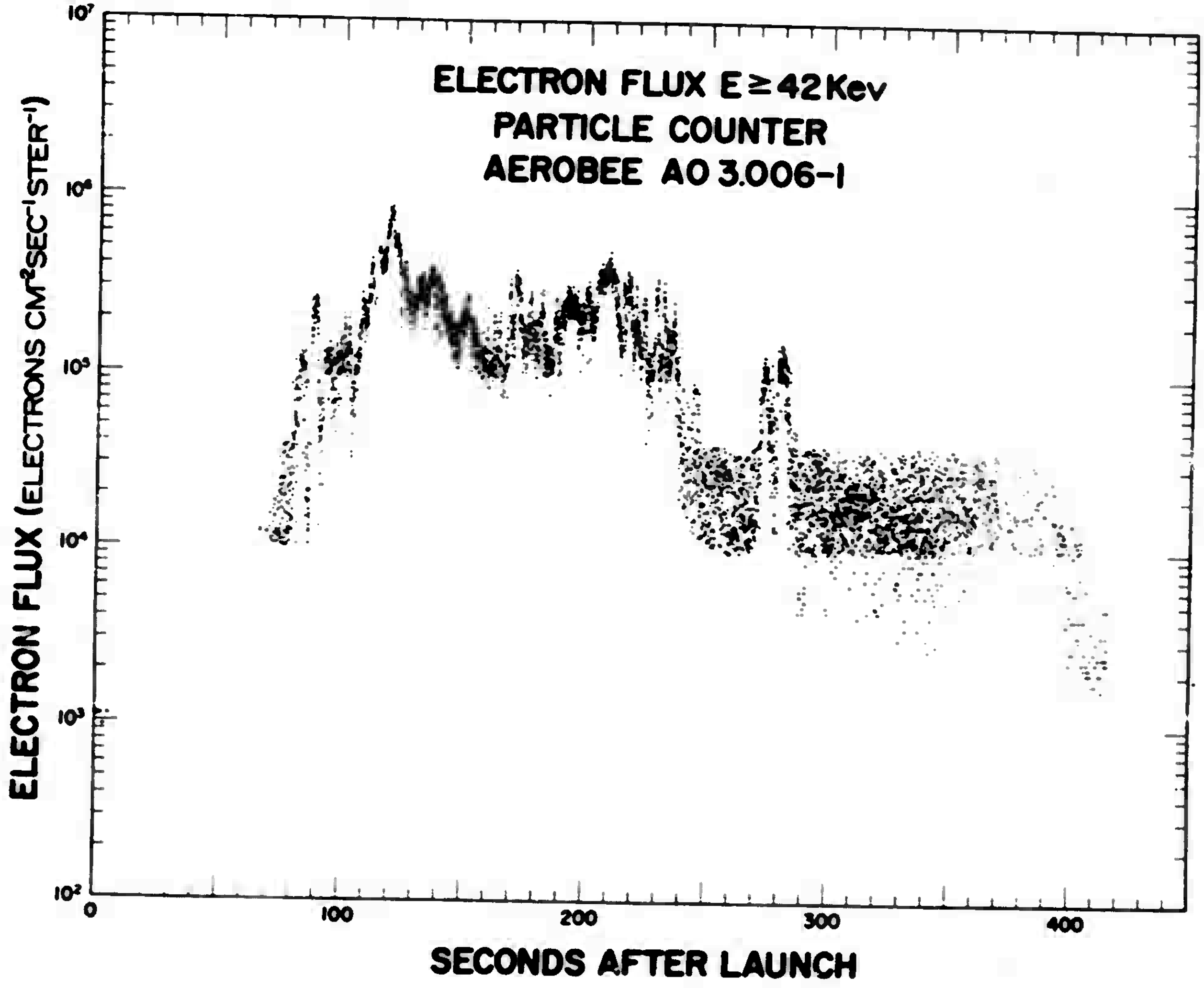

Figure 57. Energetic particle counter data from Aerobee AO 3.006-1 -- Channel No. 3 (E $\geq$ 42 keV).

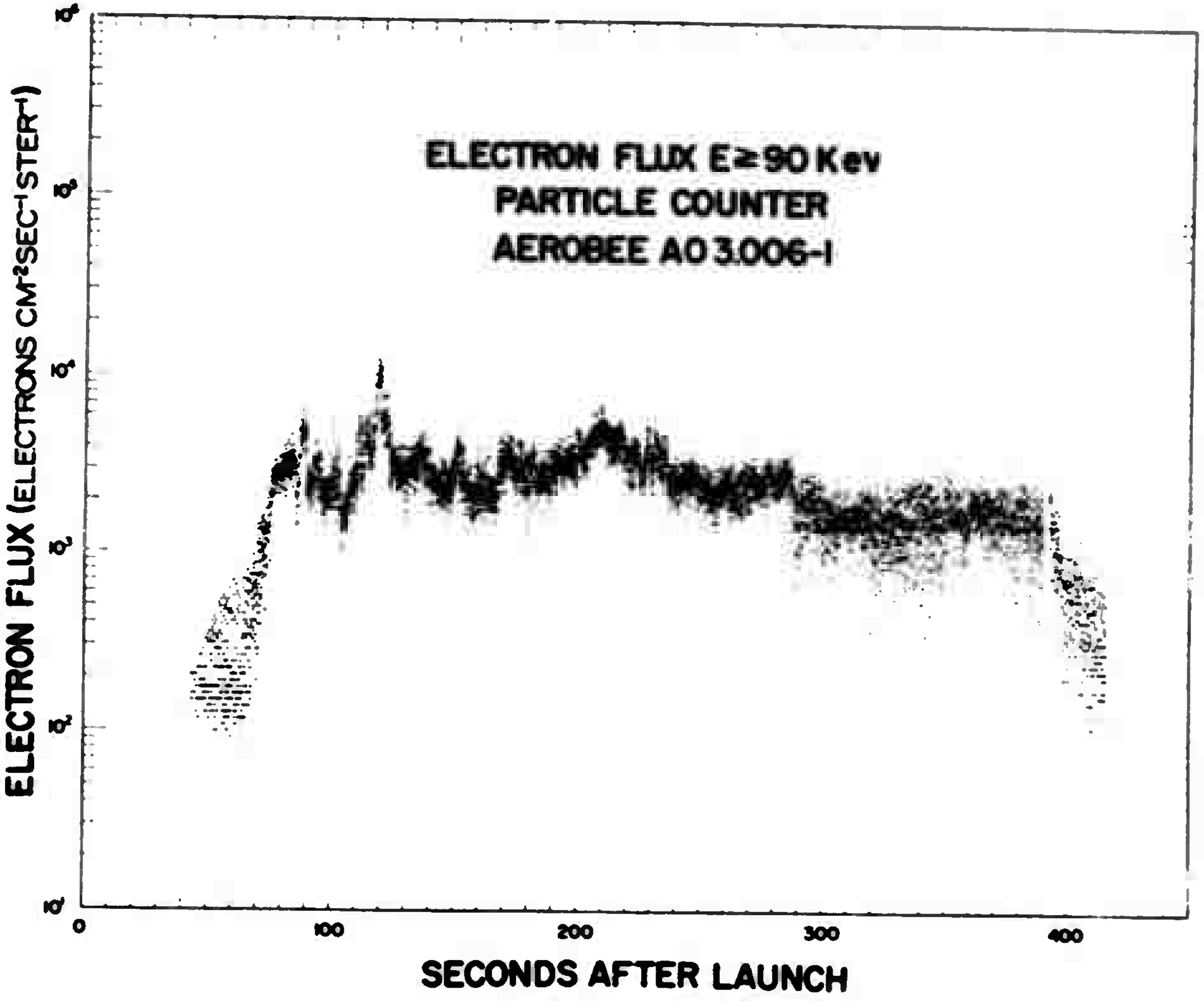

Figure 58. Energetic particle counter data from Aerobee AO 3.006-1 -- Channel No. 4 ($E \geq 90$ keV).

T + 88 sec. The increase in auroral intensity correlates with an increase in particle counter count rate shown in all geiger channels (the H.V. to the channeltron had not yet been turned on). Using the amount of absorption in the atmosphere for particles to penetrate to the appropriate vehicle altitude, it is estimated that the energy input to the aurora was in the order of a few tens of ergs $cm^{-2}sec^{-1}$.

As the payload ascended, both spatial and temporal variations are seen in the count rates. At approximately T + 119 sec, when the vehicle was at about 134 km, the particle counters recorded another burst of electrons, the effects of which were also seen in the vertically-viewing photometers. It should be noted that the geiger tube having a 17-keV-threshold window failed to count this burst of electrons. The count rate dropped very low and is not shown in Fig. 56. Very little structure appears in the output of the 17-keV geiger tube for a period of approximately 40 sec following the "drop out"; whereas, the outputs of the other channels show very high count rates and significant structure during this period. The lack of structure in the output and "drop out" at high flux levels is attributed to deterioration of the resolving-time in the geiger tube. Although all of the geiger tubes were checked at high flux levels before installation in the instrument, a post-flight check revealed that the resolving time for the 17-keV geiger tube had seriously deteriorated and was significantly poorer than at the time of the flight.

In view of the difficulty with the 17-keV channel, the remaining channels were used to estimate the spectral shape of the electron energy distribution. Although the energy resolution of such a system is very poor, it appears that the measurements are consistent with an exponential electron energy distribution having an e-folding value of approximately 3 keVe with a high energy tail habing an e-folding value of ≈ 25 keV.

The telemetry records from the flight of Aerobee I revealed that the EBIL system performed nearly as intended. The Type EE-65 tube opened at 140 km on ascent yielding a 6.2-mA electron beam as determined from the total response of the Faraday collector ($I_{beam} = \sum_{i=1}^{3} I_i$). The beam-current measurements are summarized in Fig. 59.

Shortly before the vehicle reached apogee, the output of the monitor circuit for collector segment I_3 (Fig. 59) suddenly increased to the zener-diode-limited value and remained there through loss of telemetry signal at

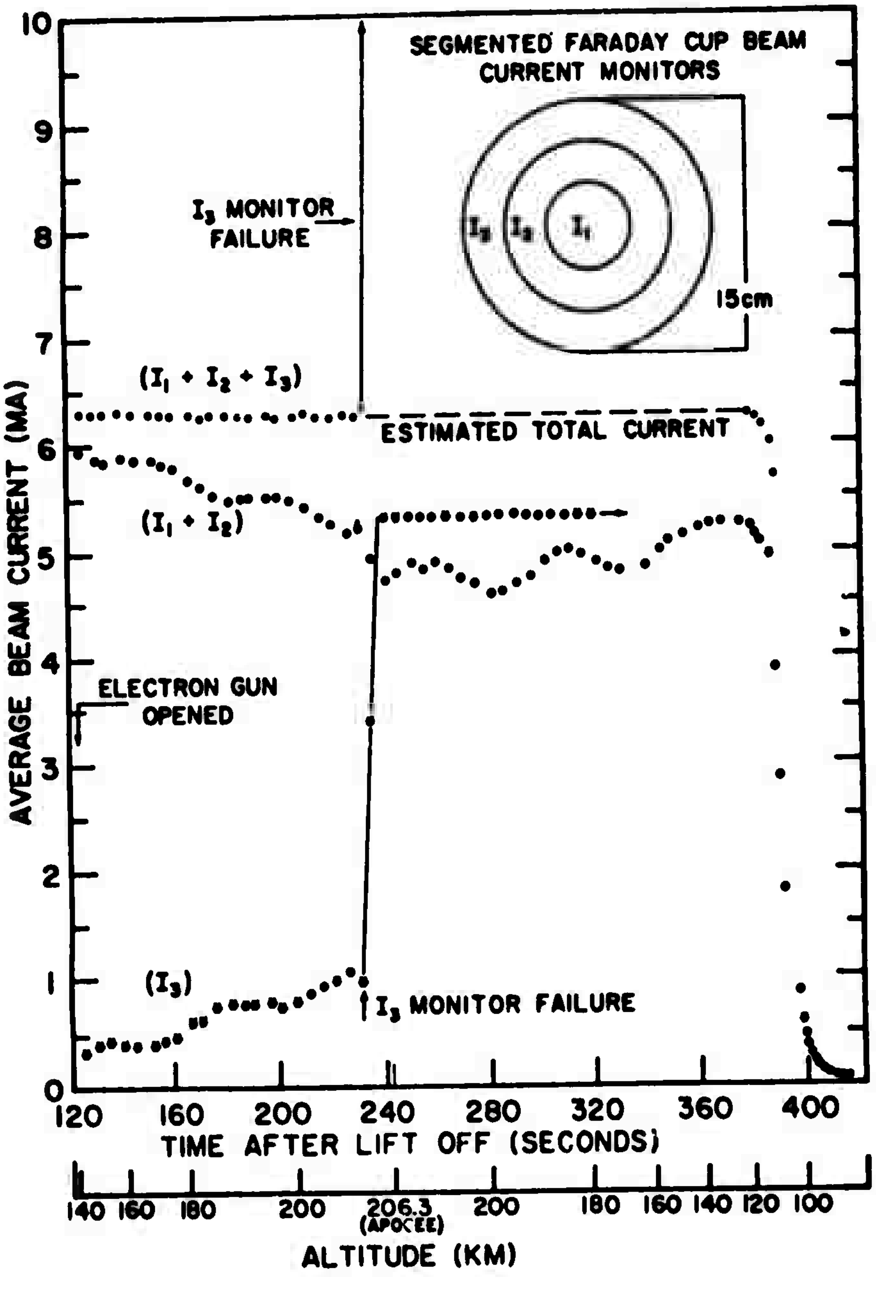

Figure 59. Summary of beam current supplied by Type EE-65 during the flight of Aerobee AO 3.006-1.

about 75 km. During the period when all three monitors were operating, the sum $I_{beam} = \sum_{i=1}^{3} I_i$ remained essentially constant at 6.2 mA, even though variations in the individual monitor outputs did occur. The data obtained prior to the failure of monitor I_3 suggest that the total beam current probably remained constant at 6.2 mA until relatively severe poisioning of the oxide-coated cathode occurred near 107 km. Below this altitude, the beam-current regulator was no longer capable of compensating for the degradation in cathode emission.

A portion of the data record from the downleg of the flight is shown in Fig. 60. Two effects are apparent from the record: (*i*) both the photometer and current monitor outputs exhibit a 2.5-Hz spin modulation, and (*ii*) the N_2^+ 1N (0,1), (0,2) and (1,2) outputs tend toward constant values above roughly 140 km. It is also seen that the N_2^+ 1N (2,4) output does not appear to change significantly over the altitude range of the figure.

The well-defined phase relationship between changes in beam-current distribution and changes in the photometer outputs tends to confirm the preflight observations (pg. 89) that the photometer outputs are affected by changes in beam position. However, also in accord with preflight observations, the *signal ratios* are relatively insensitive to the point during the spin cycle at which the ratio is computed. The modulation depth of each of the photometer signals is similar, and ratios computed at the maxima and minima exhibit a rather small spread.

The modulation depth was observed to vary with the precessional motion (coning) of the vehicle spin axis, as evidenced by a 50-sec periodicity in the modulation envelope. (This interpretation is also supported by the data from the payload magnetometer.) As the rocket spin axis approached alignment with the $\vec{B}$ field of the earth (e.g., at about T + 362 sec. in Fig. 60), the spin modulation was minimized owing to the nearly constant angle between $\vec{v}_e$ and $\vec{B}$ (pg. 35) during the spin cycle. This condition results in maximum beam deflection with minimum beam excursion during the spin cycle.

The photometer outputs have been averaged over one-second intervals (approximately 2.5 spin cycles) in order to improve the signal-to-noise ratios and to reduce the effects of spin modulation. Results obtained from the data record for the N_2^+ 1N (0,1) instrument are shown in Fig. 61.

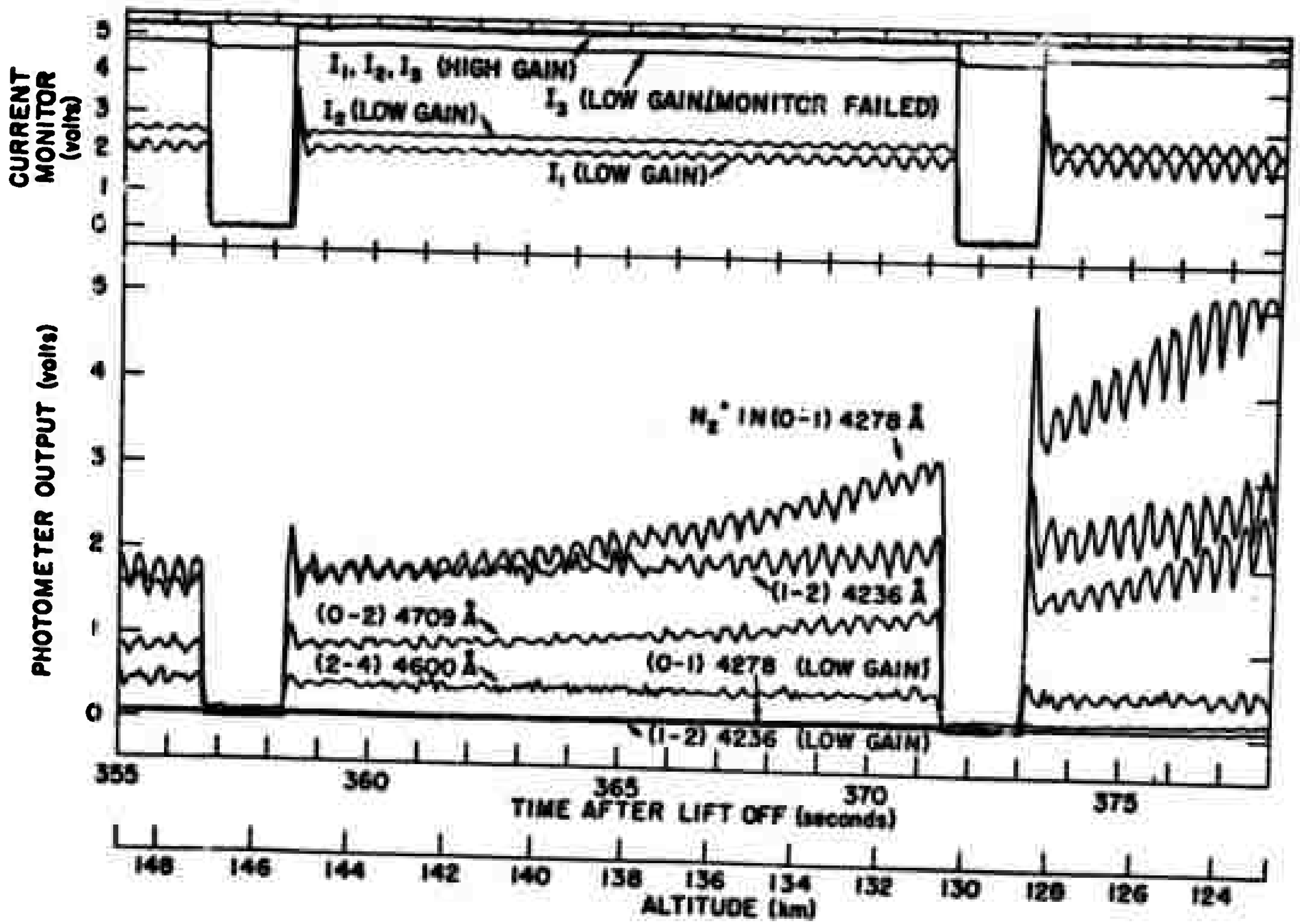

Figure 60. Current monitor and photometer output signals during a portion of the downleg of the flight of Aerobee AO 3.006-1.

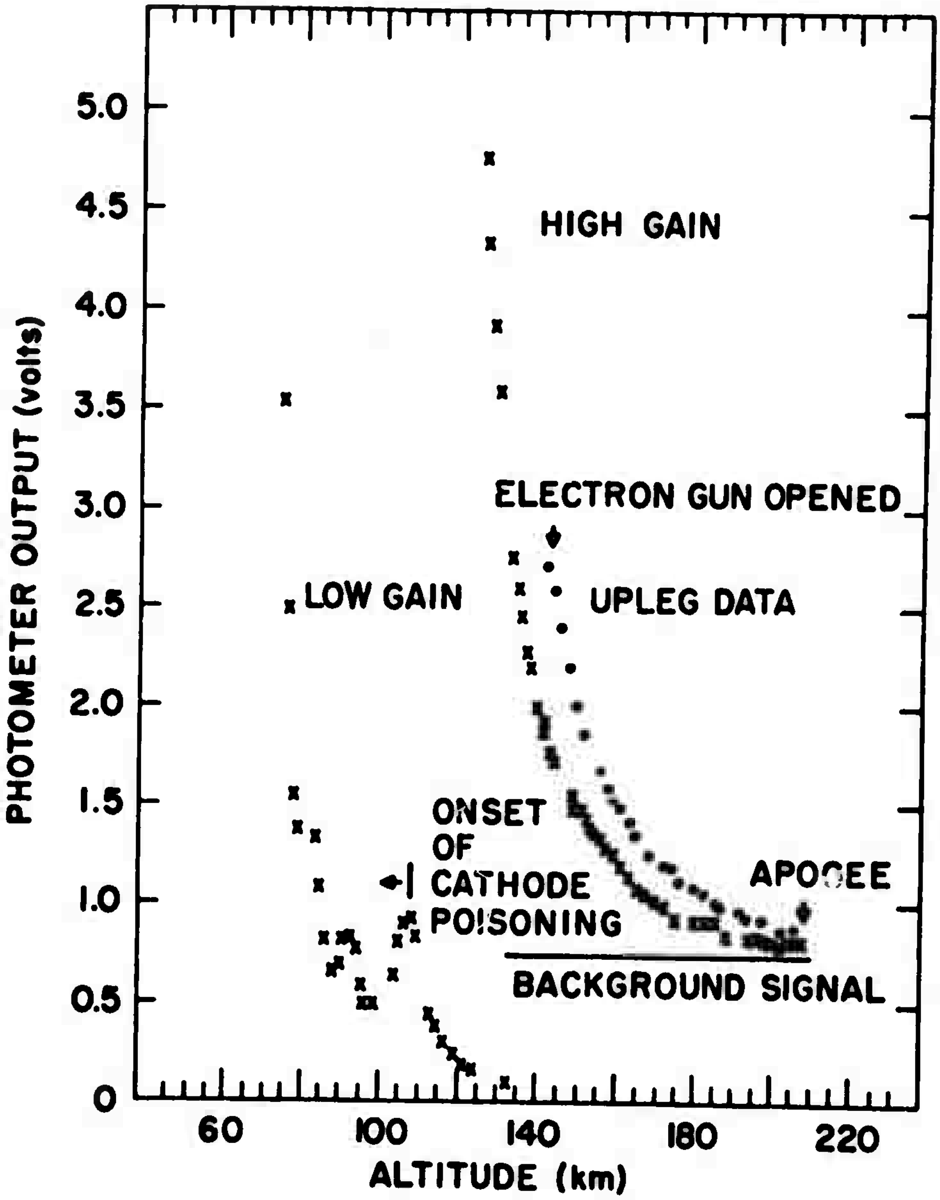

Figure 61. Record of the output signal of the N_2^+ 1N (0,1) instrument during the flight of Aerobee AO 3.006-1. (Each data point in the figure represents the average signal during a one-second interval of the flight record).

The previously mentioned background signal, which was apparent in the case of the N_2^+ 1N (2,4) output at the altitudes of Fig. 60, is more apparent near apogee in the case of the N_2^+ 1N (0,1) measurement. It is also seen from Fig. 61 that on upleg--downleg disparity in the absolute output at a given altitude occurs.

The source of the background signals (Fig. 60) is not well defined at present; however, it may be the result of electron-impact-induced luminescence of some surface [e.g., the outer surface of the optical wedge (A in Fig. 37)] within the fields of view of the photometers. A similar situation was encountered in the preflight calibration of the EBIL system where background signals (Fig. 42) were present on all of the instruments.

Post-flight tests of an electron beam collector similar to the one used during the first flight suggested that a significant number of secondary (and backscattered) electrons are generated at the collecting surfaces and at the suppressor screen. The "secondary electrons" produced a visible glow at the walls of the vacuum chamber used for instrument calibration. The pattern and intensity of the wall fluorescence could be easily and dramatically altered by moving a small permanent magnet over the exterior surface of the vacuum chamber, in accord with the secondary-electron hypothesis. A comparison of the output current of the electron gun, as measured by an inductive-type monitor mounted near the anode of the electron gun, with the Faraday collector reading revealed a difference commensurate with the measured optical transparency of the suppressor screen.

Additional consideration has been given to both the background signal and the upleg-downleg disparities; however, the stated purpose of this report precludes a detailed exposition on the results of the two flights, as these will be reported elsewhere. Preliminary results from the first flight have previously been reported (O'Neil, Hart, and Pendleton, 1971; O'Neil, Pendleton, Hart, and Stair; 1971). Submission of a final report of the findings to an aeronomy-related journal is planned for the near future. A preliminary report of some of the results from the second flight have been submitted for possible presentation at the May, 1972 COSPAR meeting scheduled for Madrid, Spain (O'Neil and Pendleton, 1972).

The basic EBIL-related results from the first flight are summarized in Figs. 62-64. The quantity Δ_0^1 of Fig. 62 [and similarly for Δ_0^2 of Fig. 63] is the corrected ratio $[V(1,2)/V(0,1)]_{\mathrm{FLIGHT}}/[V(1,2)/V(0,1)]_{\mathrm{LAB}}$, where $V(1,2)$ and $V(0,1)$ represent the corrected output signals of the N_2^+ 1N (1,2) and (0,1) instruments, respectively. The output signals, averaged over one-second intervals, were corrected for the aforementioned background signal, for changes in effective optical-system transmission of the band radiation due to altitude-correlated changes in the rotational temperature, and for blending at higher rotational temperatures of the rotational structure of adjacent bands in a sequence.

The appropriate corrections for the background signal were estimated at or near apogee. Allowance was made for the N_2^+ 1N component of the total signal through estimates based on the preflight calibration results and model atmosphere (CIRA 1965 or 1966 U.S. Standard) N_2 concentrations appropriate to the apogee (or near apogee) altitude. The N_2^+ 1N (0,1) contribution to the near-apogee signal for the N_2^+ 1N (0,1) instrument was estimated to be ~0.1 V with somewhat smaller contributions (Fig. 42) for the other measurements. It was assumed that the background signals were constant during the constant-beam-current portion of the downleg. The near constancy of the output signals in the region near apogee where the background signal dominates and where the vehicle spends, relatively speaking, considerable time supports the assumption that the background signal does not change significantly during the constant-beam-current portion of the downleg. Also, the output of the N_2^+ 1N (2,4) instrument is seen (Fig. 60) to be nearly independent of altitude for downleg altitudes between apogee and ≈130 km, in support of this hypothesis.

The correction factors for the changes in effective band transmission factors and for (1,2)—(0,1) blending, both depending on the rotational temperature of the gas, were computed from measured filter transmission curves and computed relative rotational line intensities for the rotational lines of the pertinent bands. The description of the N_2^+ 1N rotational structure followed the treatment of Muntz (1962). The computations provided the effective filter transmission factor for the design transition and in the case of the (1,2) and (2,4) transitions, also provided the effective transmission factor for the generally more intense adjacent band

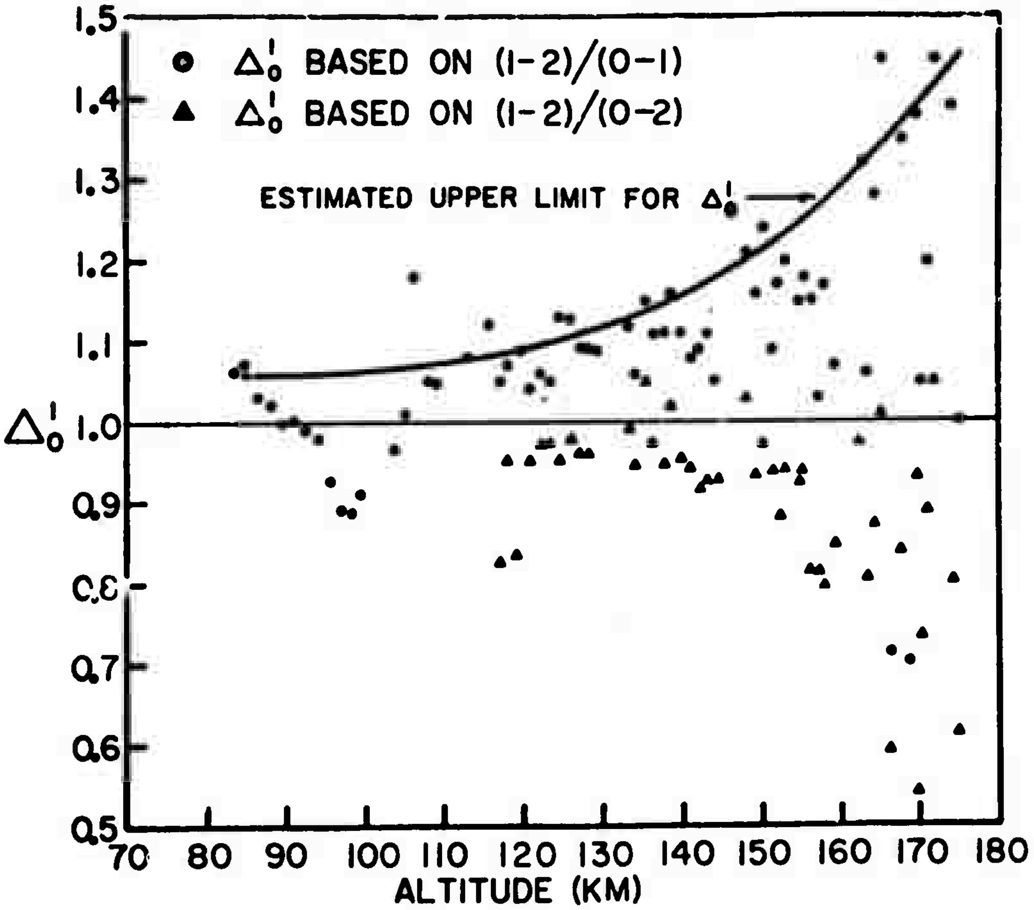

Figure 62. Normalized ratio (Δ_0^1) of the N_2^+ B-state v' = 1 to v' = 0 vibrational populations versus altitude. (Results apply to the flight of Aerobee AO 3.006-1).

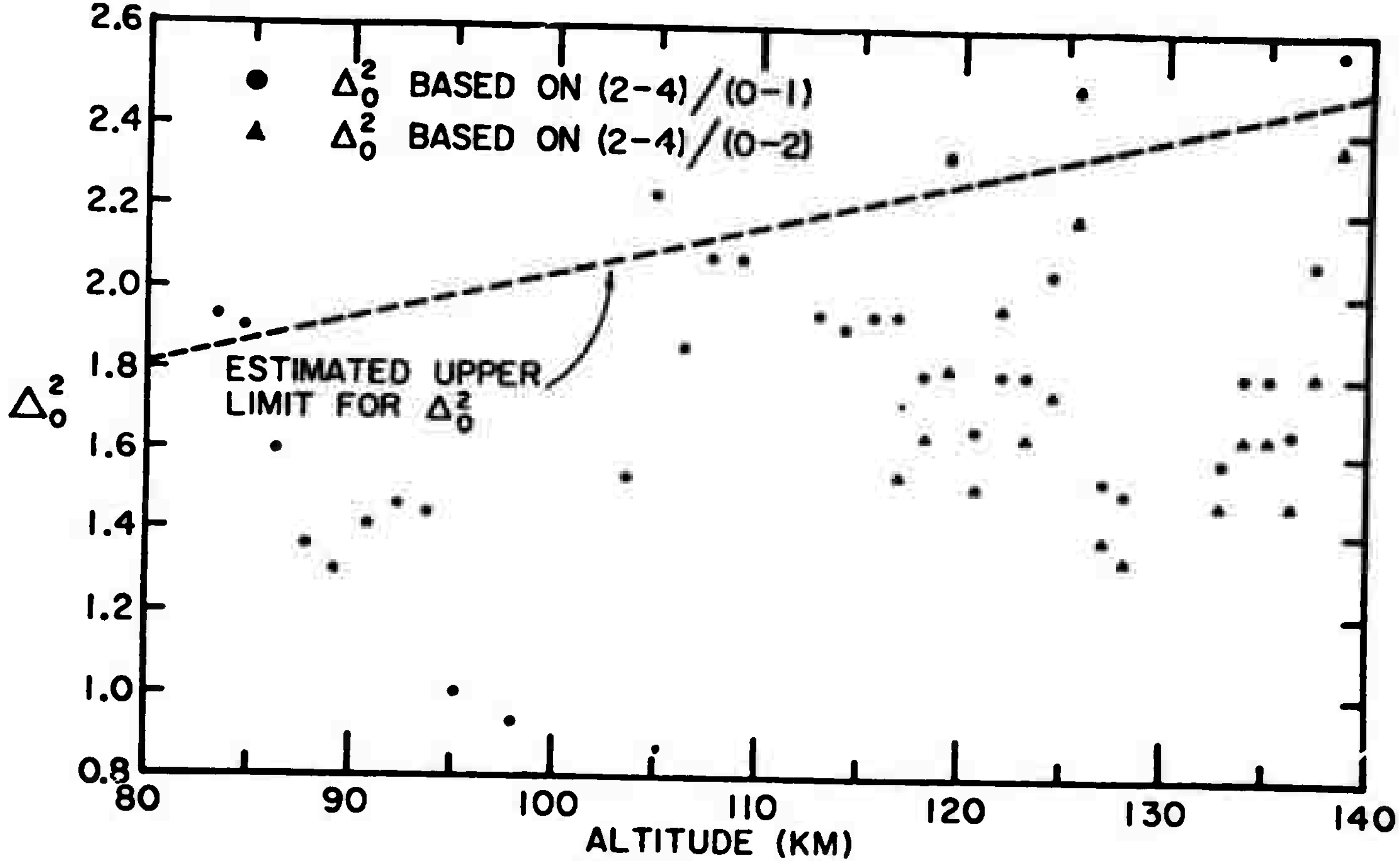

Figure 63. Normalized ratio (Δ_0^2) of the N_2^+ B-state $v' = 2$ to $v' = 0$ vibrational populations versus altitude. (Results apply to the flight of Aerobee AO 3.006-1).

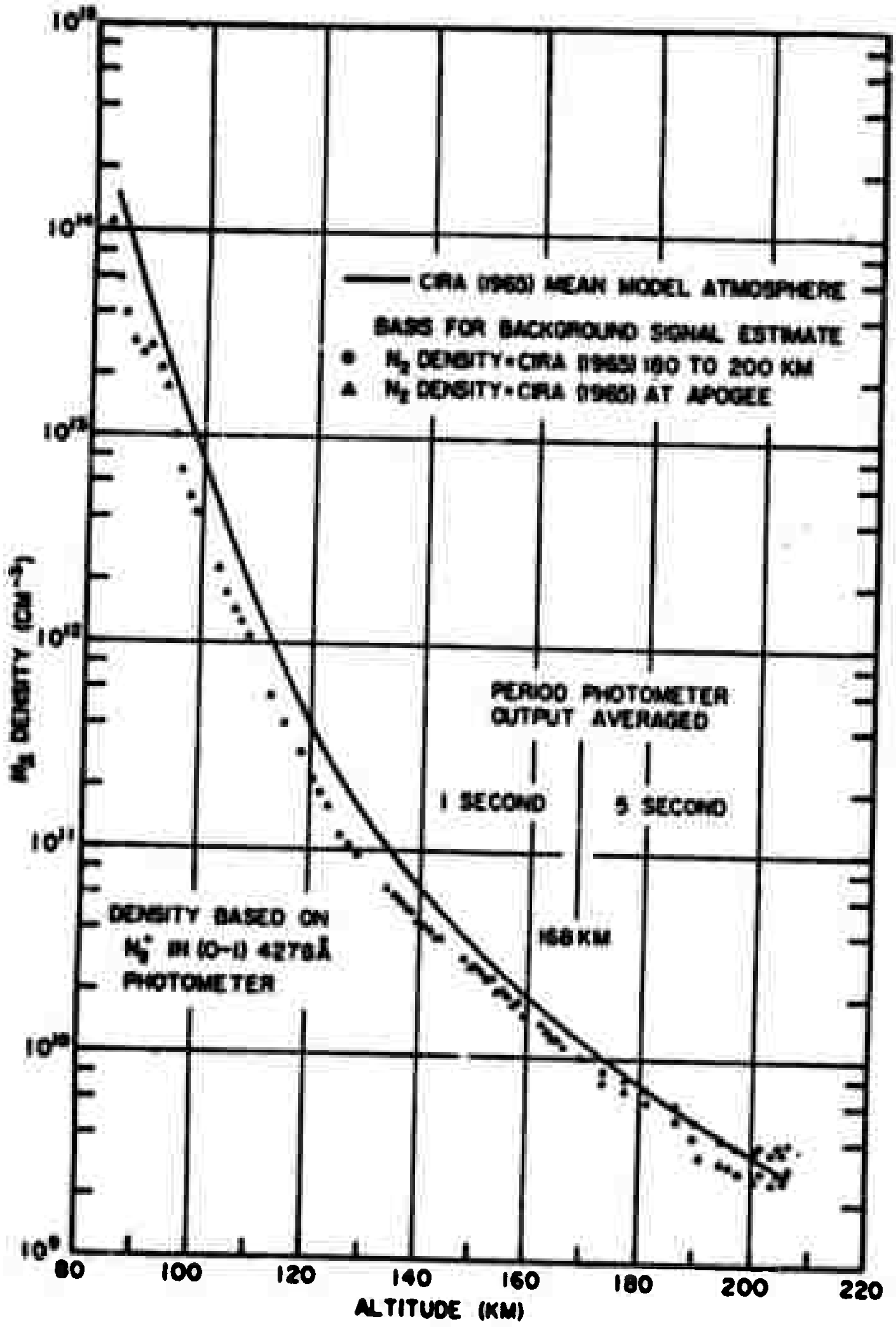

Figure 64. N_2 number density height profile from the flight of Aerobee AO 3.006-1.

on the long-wavelength side [(0,1) in the case of the (1,2) band and (1,3) in the case of the (2,4) band].

The preflight calibration results were adjusted by the appropriate correction factors (294°K target) and were used as the vibrationally cool normalizing ratios in calculating the quantites Δ_0^1 and Δ_0^2. The initial correction of the flight data was made by assuming LTE conditions with a temperature at each altitude determined by the appropriate model atmosphere. An iterative process could then be employed using as the starting point for the given iteration the vibrational temperature [and consequently band intensity ratio] results of the preceding iteration. However, it was found that the initial computations yielded results which varied almost insignificantly from the vibrationally-cool case. Hence, the iterative procedure did not appreciably affect the final result.

It is seen from Fig. 62 that the corrected signal ratios from the flight data do not depart significantly from the preflight calibration ratio. Below 150 km, the double ratio Δ_0^1 is, for the most part, within ±10% of unity, and when the ratios based on both (0,1) and (0,2) are considered the spread in values in nearly symmetric about unity. The ratios pertaining to higher altitudes are somewhat less certain owing to the increasing importance of the background signal and of the effective filter transmission corrections and to the decreasing signal-to-noise ratio of the averaged flight data.

The results depicted in Fig. 63 indicate a departure of Δ_0^2, based on both (2,4)/(0,1) and (2,4)/(0,2), from unity. However, the (2,4) flight measurement is felt to be contaminated by OII (and NII) emissions which occur within the bandpass of the N_2^+ 1N (2,4) photometer. The preflight calibration was carried out using pure N_2. Hence, the NII contamination was present, but the OII contamination was not included. Rough estimates of the anticipated correction yield values of Δ_0^2 which are much closer to unity.

Upper limits for $N_2(X^1\Sigma_g^+)$ vibrational temperature were estimated from the upper bounds for Δ_0^1 and Δ_0^2 indicated in Figs. 62 and 63, respectively. The upper bounds were somewhat arbitraily set such that they exceeded 90% of the data. The *upper limit* determined from Δ_0^1 varies from about 750°K at altitudes $\lesssim$ 100 km to about 1200°K at about 175 km. The upper-limit results from Δ_0^2 extend only between 80 km and about 140 km owing to the altitude-limited information available on the (2,4) channel. The upper limit results based on Δ_0^2 exceed those based on Δ_0^1 by a roughly constant value of 200°K over the altitude range common to the two sets of data. However, the Δ_0^2 results are felt to be less reliable owing to the aforemention contamination of the (2,4) measurement and to an additional uncertainty associated with the nature of the excitation mechanisms for the N_2^+ B-state $v' = 2$ level (Pendleton and O'Neil, 1972).

The results for the number density of molecular nitrogen are presented in Fig. 64. The number densities are based on data from the N_2^+ 1N (0,1) photometer. The photometer output was averaged over 5-sec intervals above 168 km in order to improve the S/N ratio, whereas below this altitude the previously mentioned 1-sec interval was used. Estimates of the background signal at apogee and over the altitude range between 180 and 200 km yielded lower-altitude N_2 density values which were essentially the same below 175 km. The departure from the CIRA 1965 model atmosphere is seen to be significant.

Only partial results from the second flight are presently available. The N_2 vibrational-temperature information appears to be consistent with the results from the first flight, indicating vibrational temperatures which may not be perceptibly different than the gas-kinetic temperature. The results from the two flights suggest that with the present technique and experimental system an upper limit for E-region N_2 vibrational temperatures is probably all that can be realized except under "abnormal conditions". Molecular nitrogen and oxygen number densities from the second flight appear to be significantly lower than those of the CIRA 1965 mean model atmosphere over the altitude ranges of the two measurements.

REFERENCES

Alfano, R.R. and N. Ockman, *J. Opt. Soc. Am.* 58, 90 (1968).

Baker, K.D., D.A. Burt, L.C. Howlett, G.D. Allred, Final Report AFCRL 70-0251, Contract No. F19(628)-67-C-0275, University of Utah, Salt Lake City, Utah, 1970.

Bauer, E., R. Kummler, and M.H. Bortner, *Applied Opt.* 10, 1861 (1971).

Belon, A.E., G.J. Romick, and M.H. Rees, *Planet. Space Sci.* 14, 597 (1966).

Bird, G.A., in *Rarefied Gas Dynamics*, edited by L. Talbolt, (Academic Press, New York, 1960) p. 245.

Black, G., D.C. Lorents, and D.J. Eckstrom, Stanford Research Institute Semiannual Technical Report No. 1, U.S. Army Research Office--Durham, Contract No. DAHC 04-70-C-0036 (December7, 1970).

Bond, J.W., Jr., K.M. Watson, and J.A. Weich, Jr., *Atomic Theory of Gas Dynamics*, (Addison-Wesley Publishing Company, Inc., Reading, Massachusetts, 1965), p. 330.

Brekke, A. and A. Omholt, *Planet. Space Sci.* 16, 1259 (1968).

Broadfoot, A.L. and D.M. Hunten, *Can. J. Phys.* 42, 1212 (1964).

Burt, D.A. and K.G. Seljaas, Scientific Report No. 6, AFCRL 66-738, Contract No. AF 19(628)4995, University of Utah, Salt Lake City, Utah, 1966.

Cartwright, D.C., private communication, (1971).

Dalgarno, A., M.B. McElroy, M.H. Rees, and J.C.G. Walker, *Planet. Space Sci.* 16, 1371 (1968).

DeLeeuw, J.H. and W.E.R. Davies, *Small Rocket Instrumentation Techniques*, (North-Holland Publishing Company, Amsterdam, Holland, 1969), p. 144.

Eather, R.H. and D.L. Reasoner, *Applied Optics* 8, 227 (1969).

Fastie, W.G., H.M. Crosswhite and T.P. Markham, *Ann. Geophys.* 17, 109 (1961).

Field, L.M., K. Spangenberg, and R. Helm, *Elec. Commun.* 24, 108 (1947).

Halsted, A.S. and D.A. Dunn, *J. Appl. Phys.* 37, 1810 (1966).

Henderson, W.R. and H.I. Schiff, *Planet. Space Sci.* 18, 1527 (1970).

Herzberg, G., *Molecular Spectra and Molecular Structure I. Spectra of Diatomic Molecules*, second edition (D. Van Nostrand Co., Inc., Toronto, Canada, 1950), p. 552.

Hess, W.M., M.C. Trichel, T.N. Davis, W.C. Beggs, G.E. Kraft, E. Stassinopoulos, and E.J.R. Maier, *J. Geophys. Res.* 76, 6067 (1971).

Hoppe, J.C., NASA TN D-4892 (1968).

Hunter, W.W., Jr., NASA TN D-4500 (1967).

Isler, R.C. and W.G. Fastie, *J. Geophys. Res.* 70, 2613 (1965).

Kummler, R.H. and M.H. Bortner, abstract f.31, COSPAR (Seattle, Washington, 1971).

Lenz, *Z. Naturforsch*, 9a, 185 (1954).

Machlett Laboratories, private communication (1969).

Morgan, J.E., L.F. Phillips, and H.I. Schiff, *Disc. Faraday Soc.* 33, 118 (1962).

Muntz, E.P. and S.J. Abel, Third Hypervelocity Techniques Symposium (Denver, Colorado, Mar [illegible], 1964).

Muntz, E.P., *Phys. Fluids* 5, 80 (1962. NATO AGARDograph 132 (1968).

Murcray, W.B., *Planet. Space Sci.* 17, 1429 (1969).

Nicholls, R.W., *J Quant. Spectrosc. Radiat. Transfer* 2, 433 (1962).

Noxon, J.F., *J. Chem. Phys.* 52, 1852 (1970).

O'Neil, R.R., A.M. Hart, and W.R. Pendleton, Jr., in *The Radiating Atmosphere*, edited by B.M. McCormac, (D. Reidel Publishing Co., Dordrecht-Holland, 1971), p. 195.

O'Neil, R.R., W.R. Pendleton, Jr., A.M. Hart, and A.T. Stair, Jr., COSPAR (Seattle, Washington, 1971).

Opal, C.B., H.W. Moos, and W.G. Fastie, *J Geophys. Res.* 75, 788 (1970).

Peek, H.M., *J. Geophys. Res.* 75, 6209 (1970).

Pendleton, W.R., Jr., and R.R. O'Neil, *J. Chem. Phys.* (to appear in 1 Jun 72 issue).

Peterson, J.R., private communication of recent reuslts of G. Black *et al.* at SRI (March, 1972).

Phillips, L.F. and H.I. Schiff, *J. Chem. Phys.* 36, 3282 (1962).

Rees, M.H., *J. Atmos. Terr. Phys.* 14, 325 (1959).

Ridgway, S.L., Princeton Applied Research Corp., *Signal Notes* V.I, No. 1 (November, 1967).

Romick, G.J. and A.E. Belon, *Planet. Space Sci.* 15, 1695 (1967).

Schmeltekopf, A.L., E.E. Ferguson, and F.C. Fehsenfeld, *J. Chem. Phys.* 48, 2966 (1968).

Schulz, G.J., *Phys. Rev.* 135, A988 (1964).

Schunk, R.W. and P.B. Hays, *Planet. Space Sci.* 19, 1457 (1971).

Seljaas, K.G., Scientific Report No. 1, AFCRL 68-0306, Contract No. AF19(628)-67-C-0275, University of Utah, Salt Lake City, Utah (1968).

Sharp. W.E., *J. Geophys. Res.* 76, 987 (1971).

Shemansky, D.E. and A. Vallance Jones, *Planet. Space Sci.* 16, 1115 (1968).

Smith, L.G. in *Small Rocket Instrumentation Techniques* edited by K.I. Maeda (North-Holland Publishing Co., Amsterdam, Holland, 1969), p. 1-15.

Spencer, N.W., L.H. Brace, G.R. Carignan, D.R. Taueseh and H. Niemann, *J. Geophys. Res.* 70, 2665 (1965).

Stanton, Paul N. and R.M. St. John, *J. Opt. Soc. Am.* 59, 252 (1969).

Vallance Jones, A., *Space Sci. Rev.* 11, 776 (1971).

Walker, J.C.G., *Planet. Space Sci.* 16, 321 (1968).

Walker, J.C.G., R.S. Stolarski, and A.F. Nagy, *Ann. Geophys.* 25, 831 (1969).

Willmore, A.P., *Space Sci. Rev.* 11, 607 (1970).

Young, R.A., G. Black, and T.G. Slanger, *J. Chem. Phys.* 49, 4758 (1968).

Zipf, E.C., W.L. Borst, and T.M. Donahue, *J. Geophys. Res.* 75, 6371 (1970).

APPENDIX A

AEROBEE AO 3.006-1

INSTRUMENT SCHEMATICS AND CALIBRATIONS

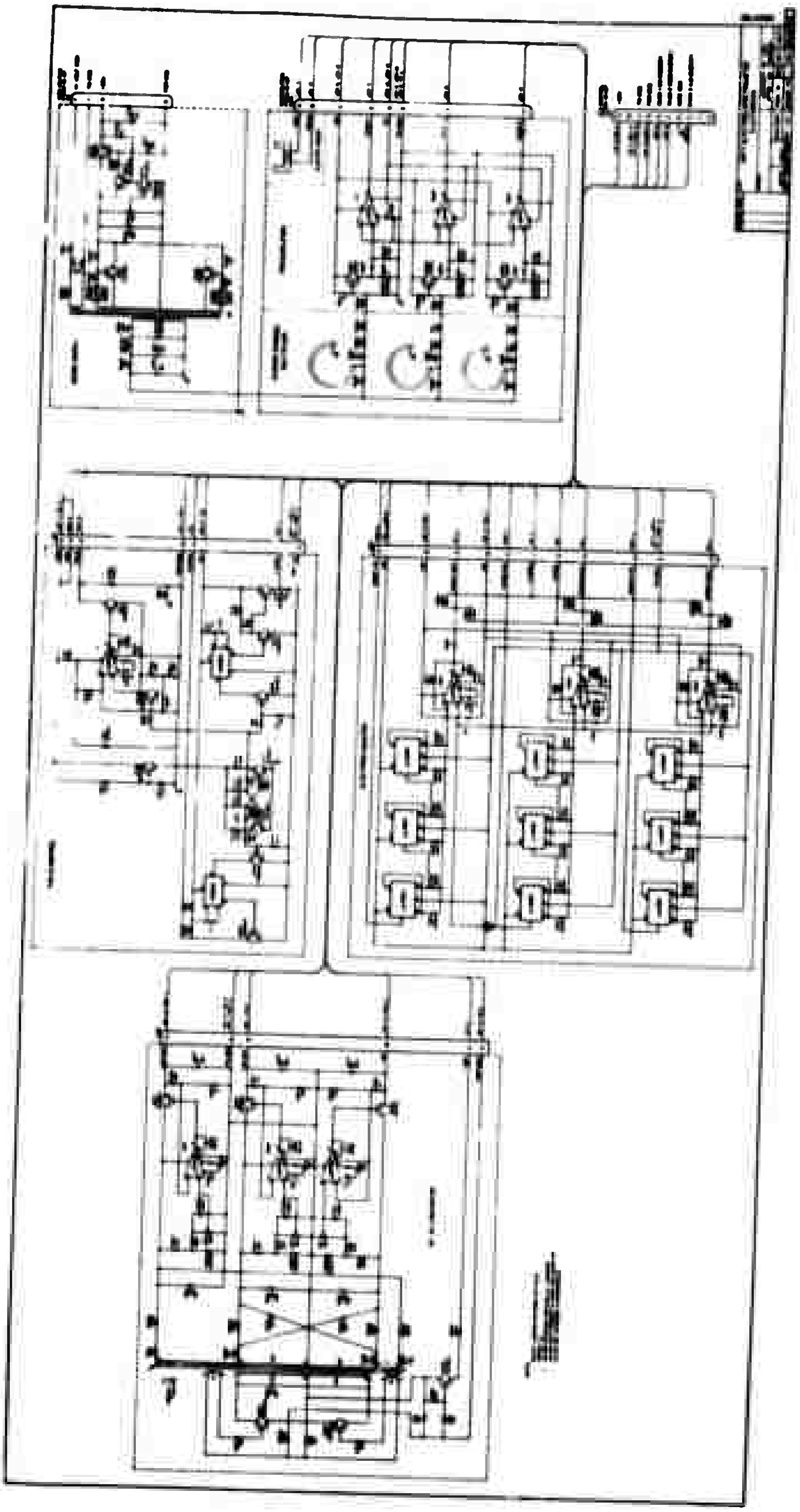

Figure A-1. Schematic diagram of soft electron spectrometer circuitry.

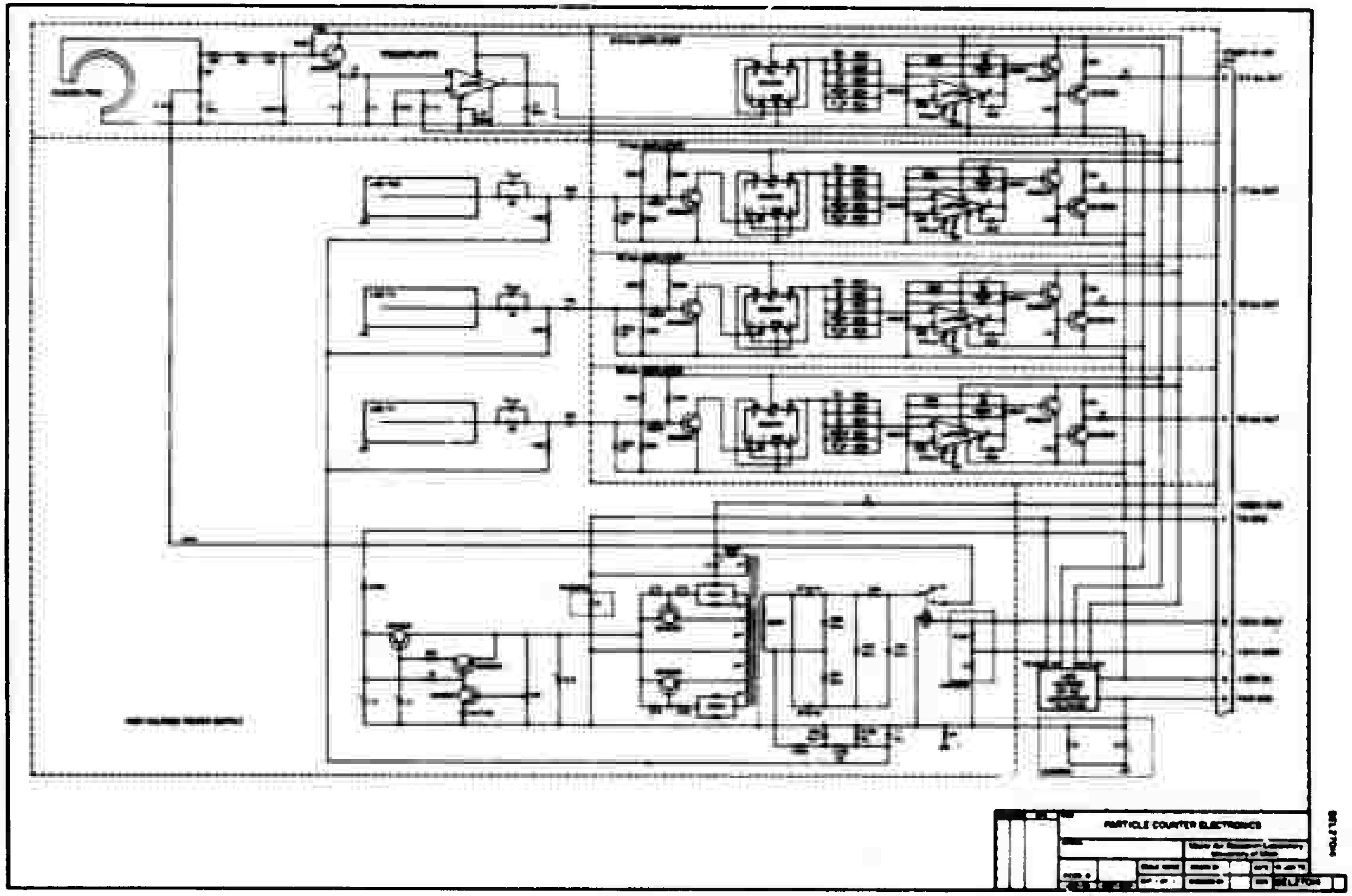

Figure A-2. Schematic diagram of energetic particle counter circuitry.

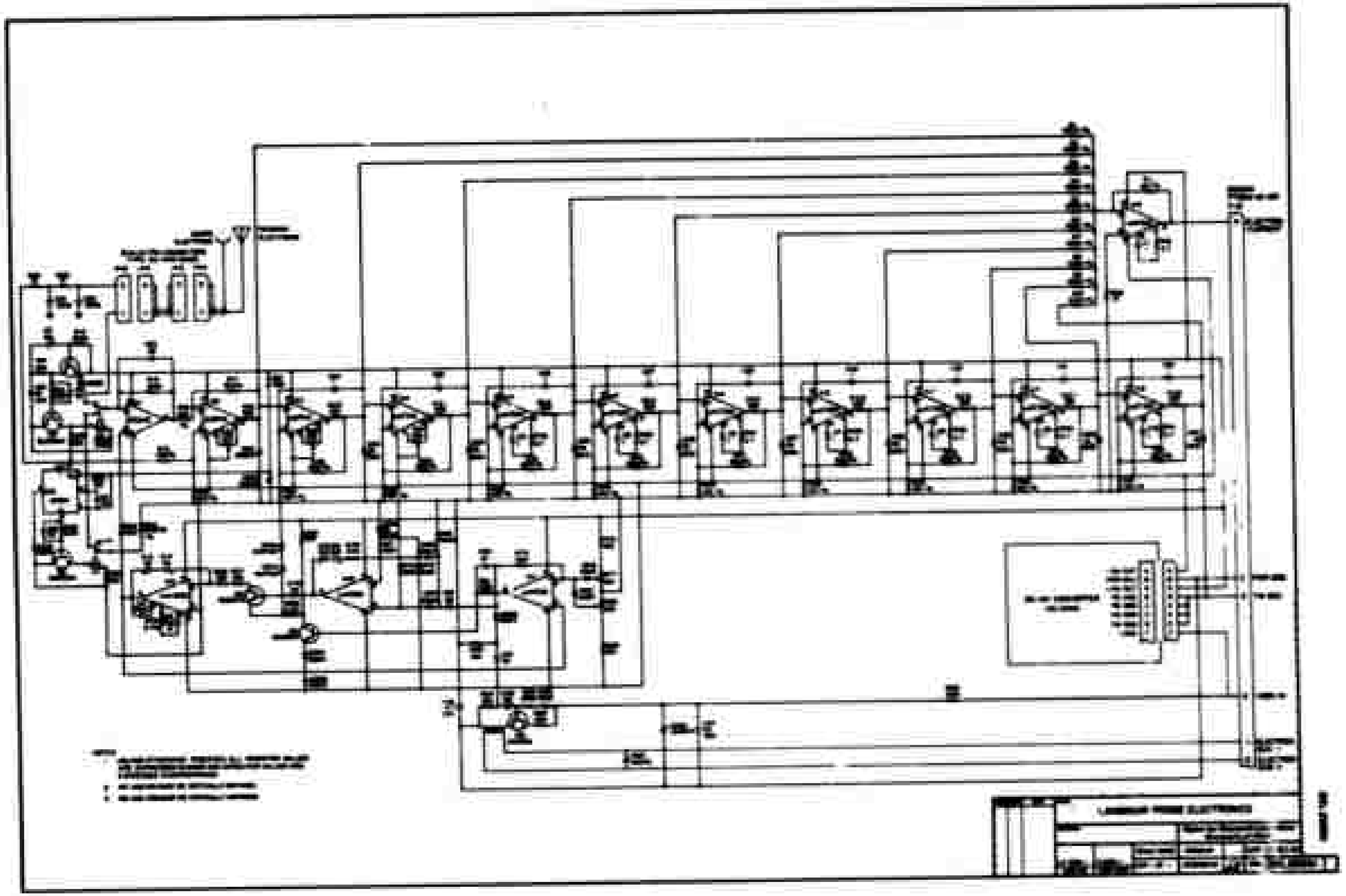

Figure A-3. Schematic diagram of Langmuir-probe circuit.

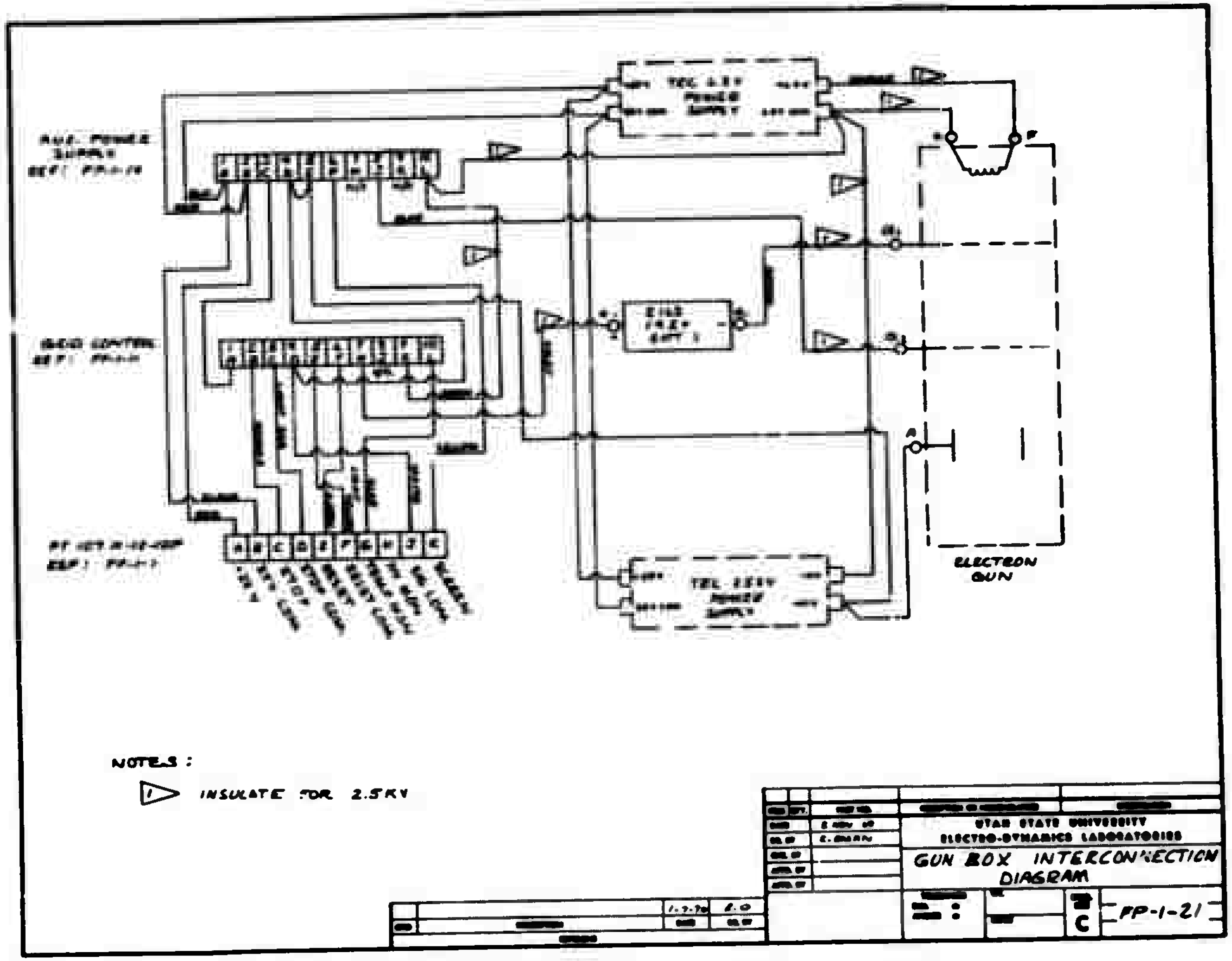

Figure A-4. EBIL gun box interconnection diagram with beam-current regulator circuitry.

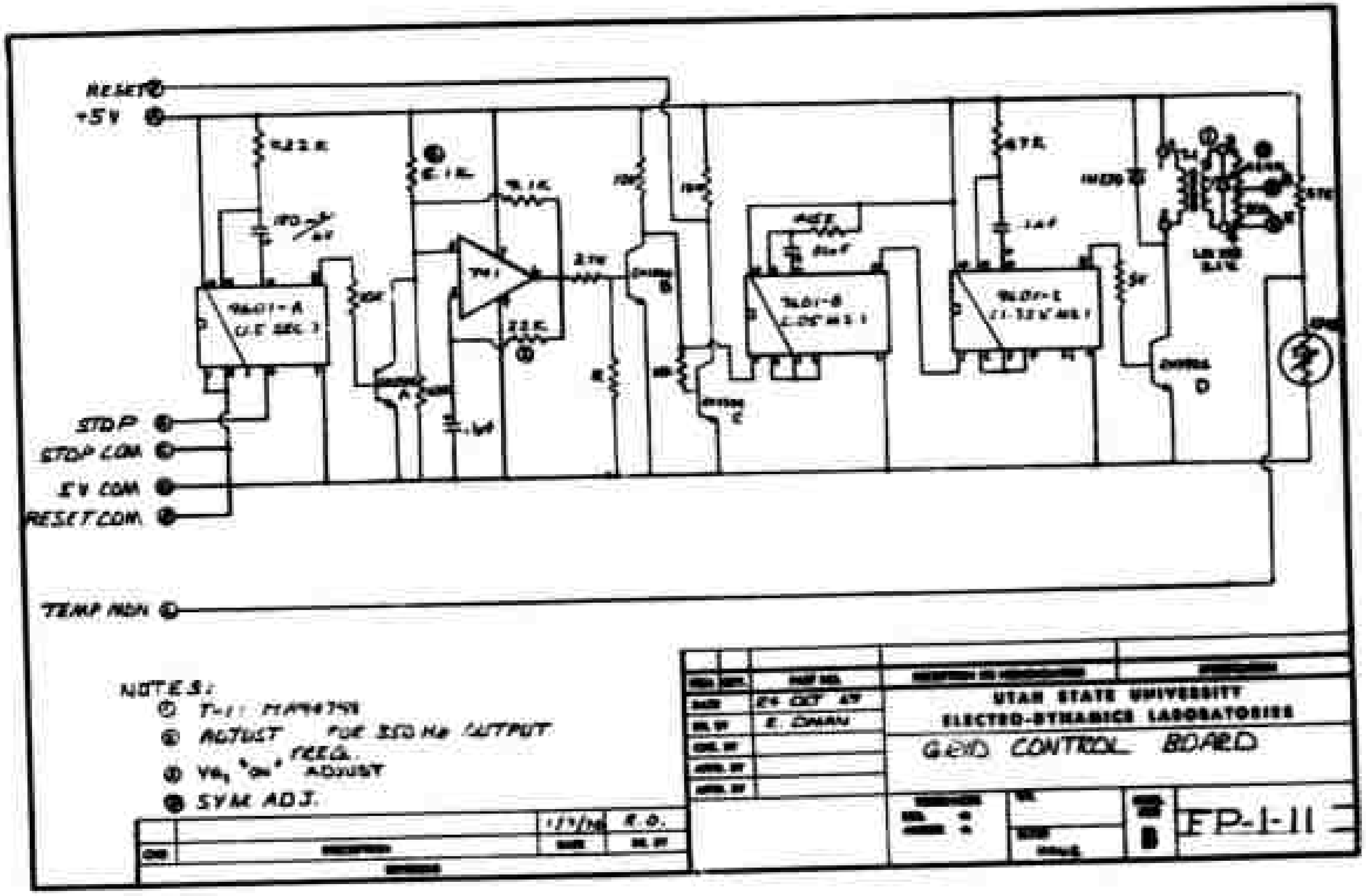

Figure A-5. Grid-control circuitry for electron gun.

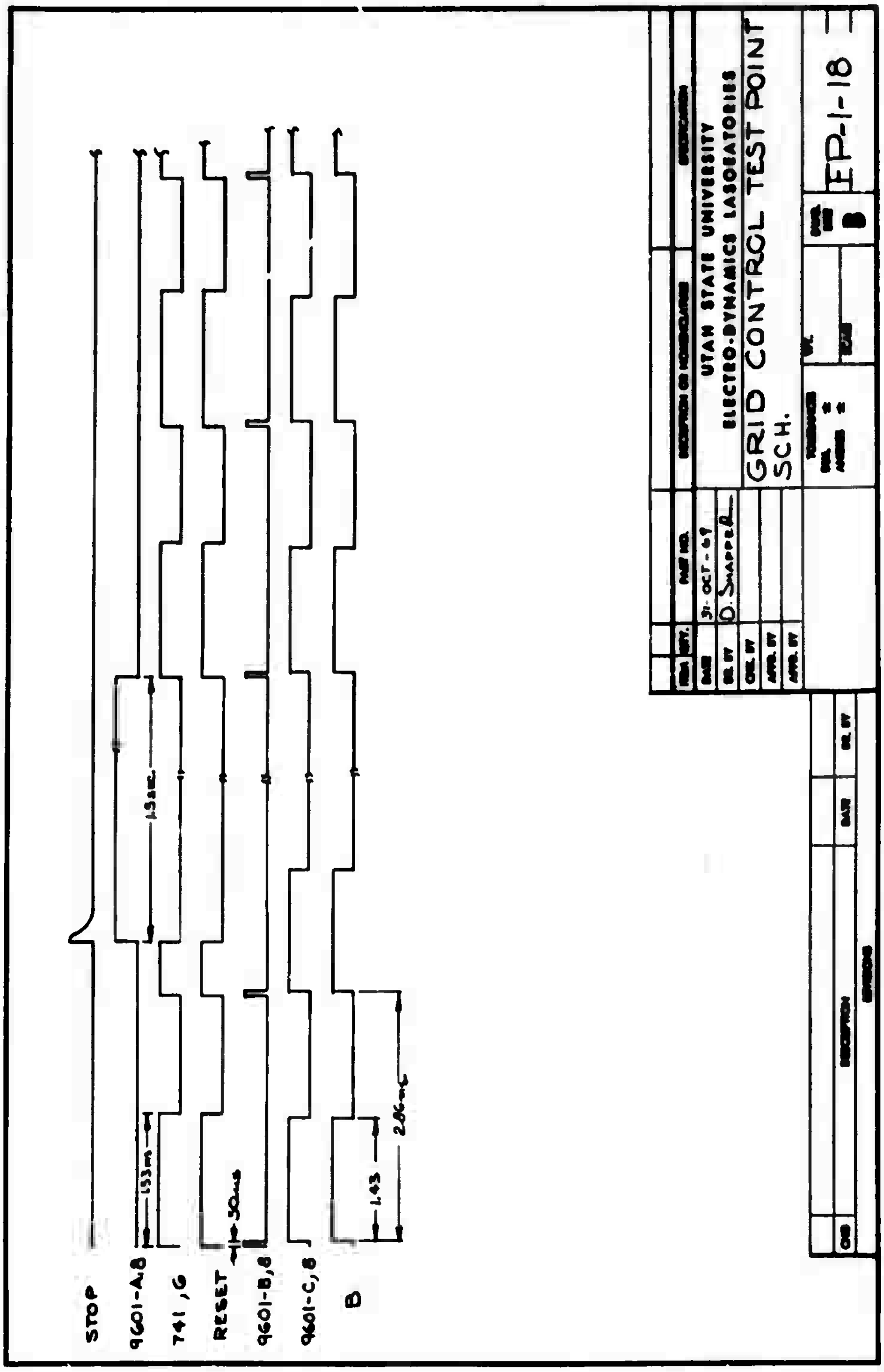

Figure A-6. Test point waveforms on grid-control board.

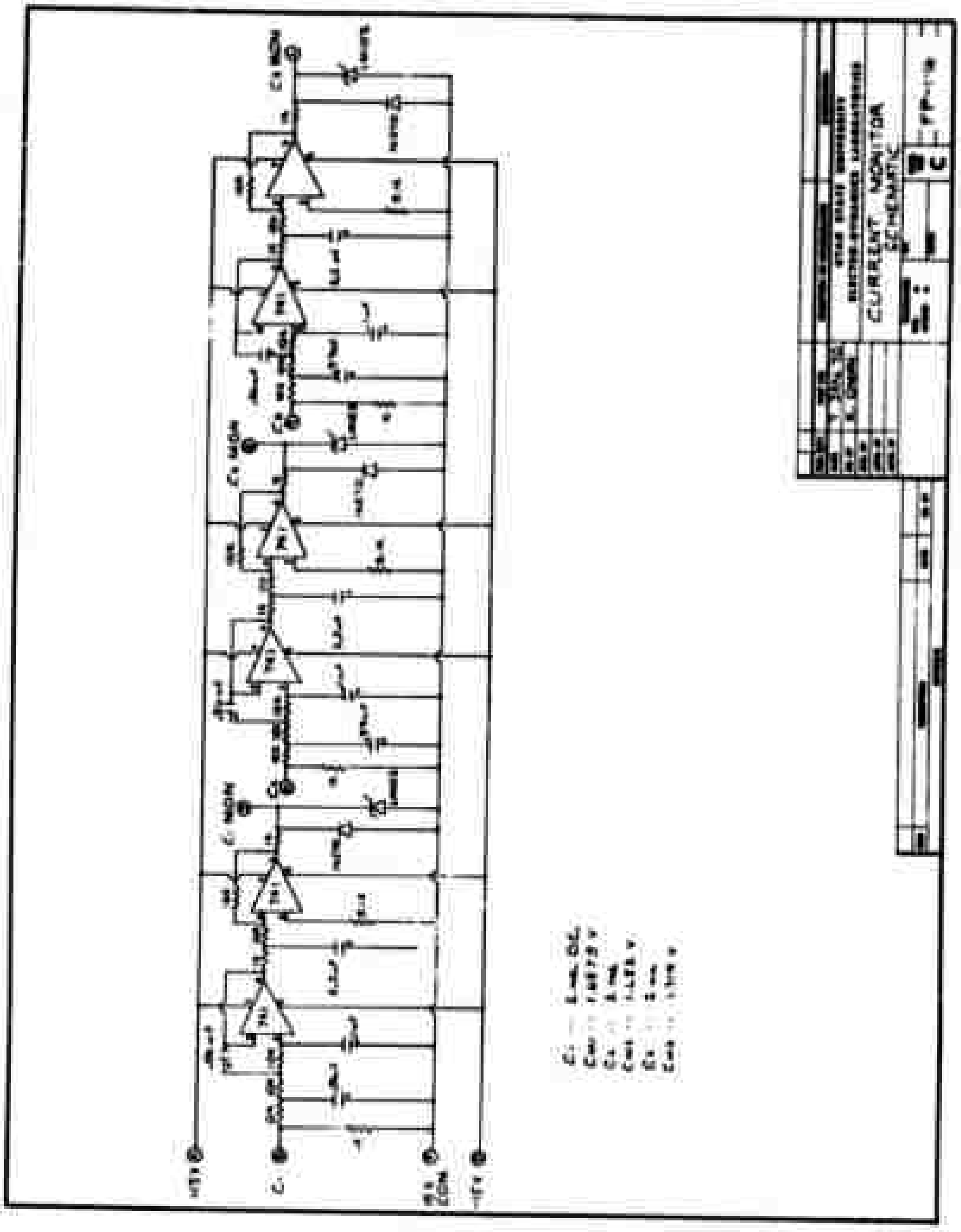

Figure A-7. Schematic diagram of current monitor amplifier.

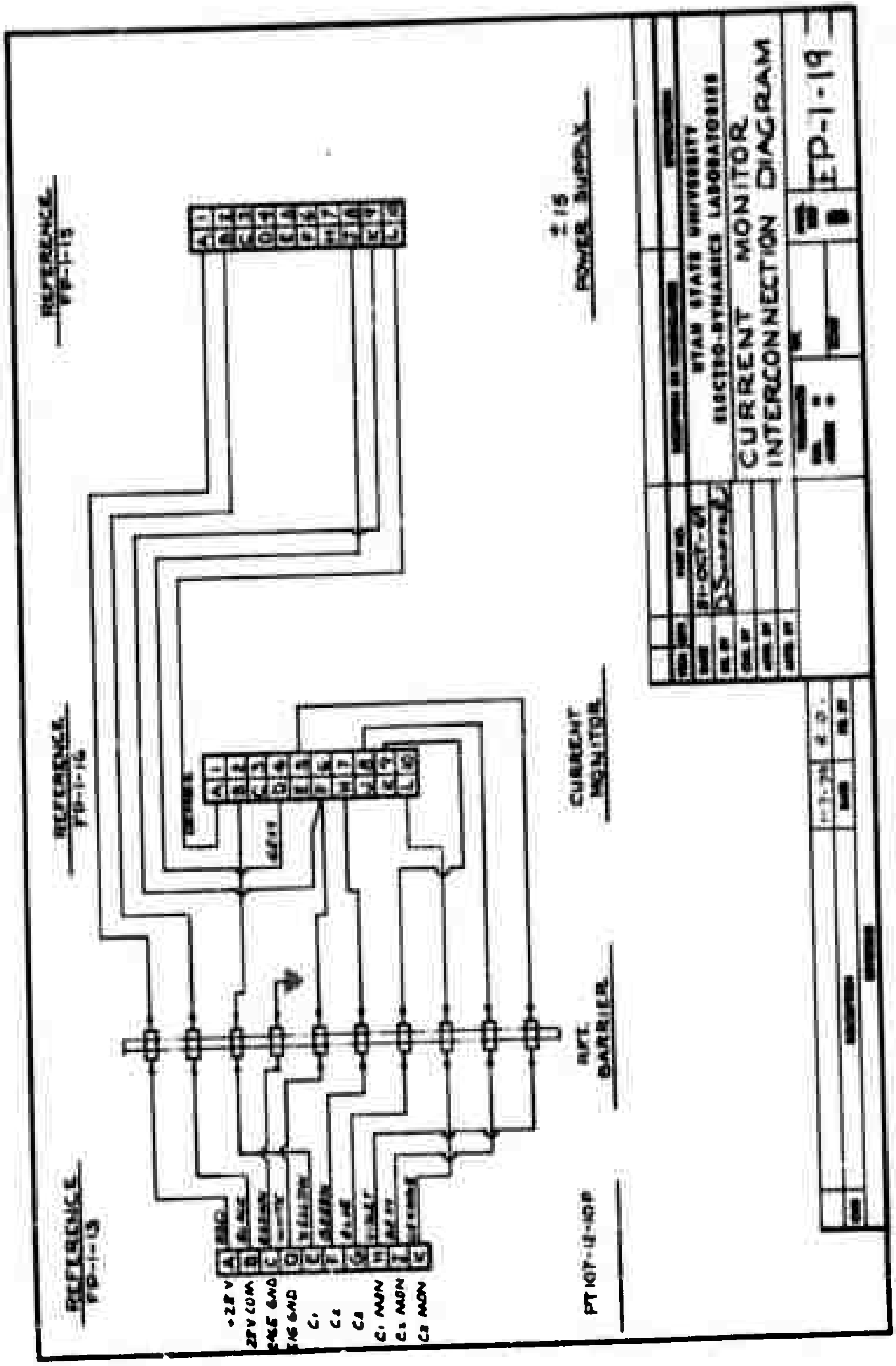

Figure A-8. Current monitor interconnection diagram.

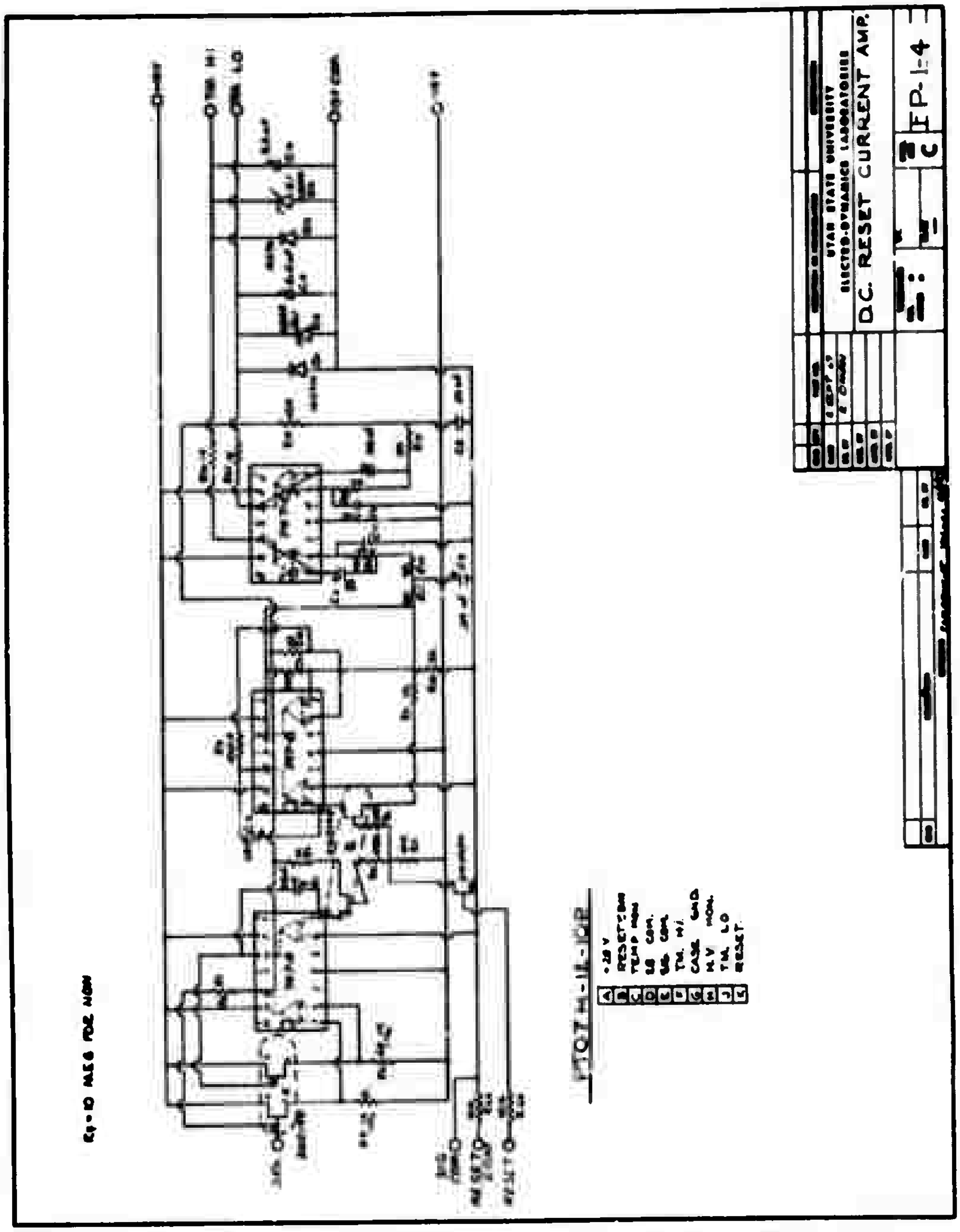

Figure A-9. Schematic diagram of DC reset amplifier.

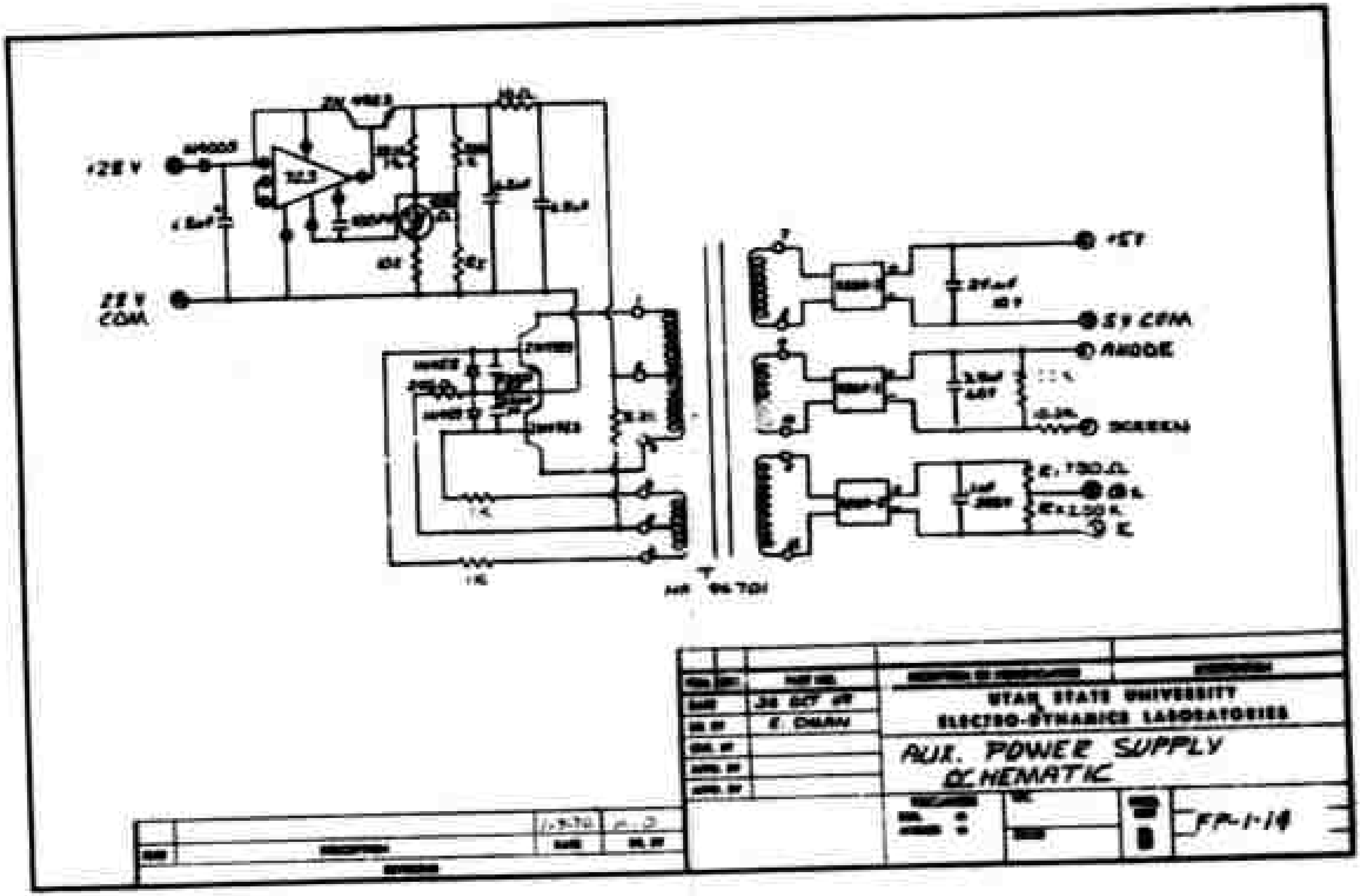

Figure A-10. Schematic diagram of auxiliary power supply.

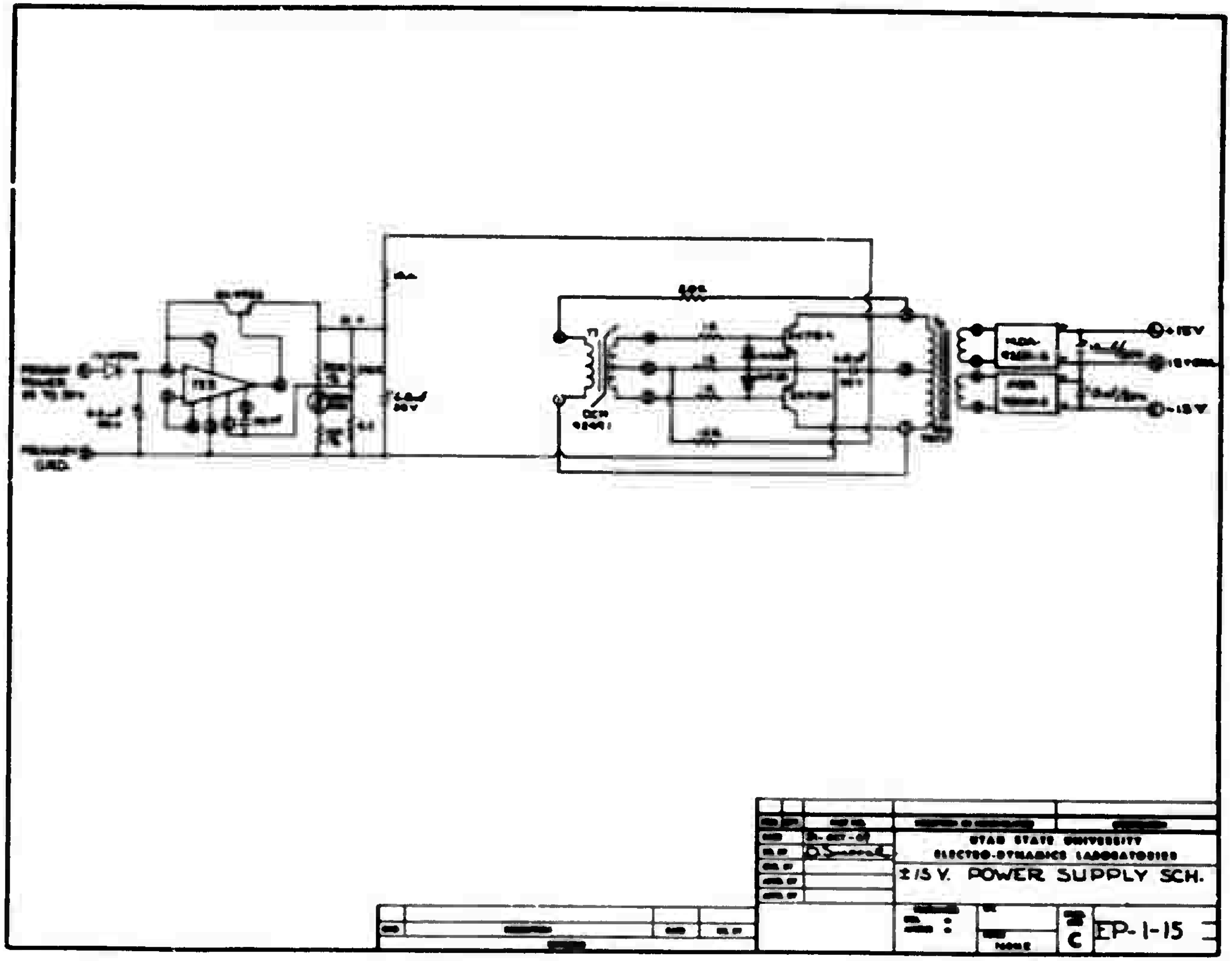

Figure A-11. Schematic diagram of ±15 volt power supply.

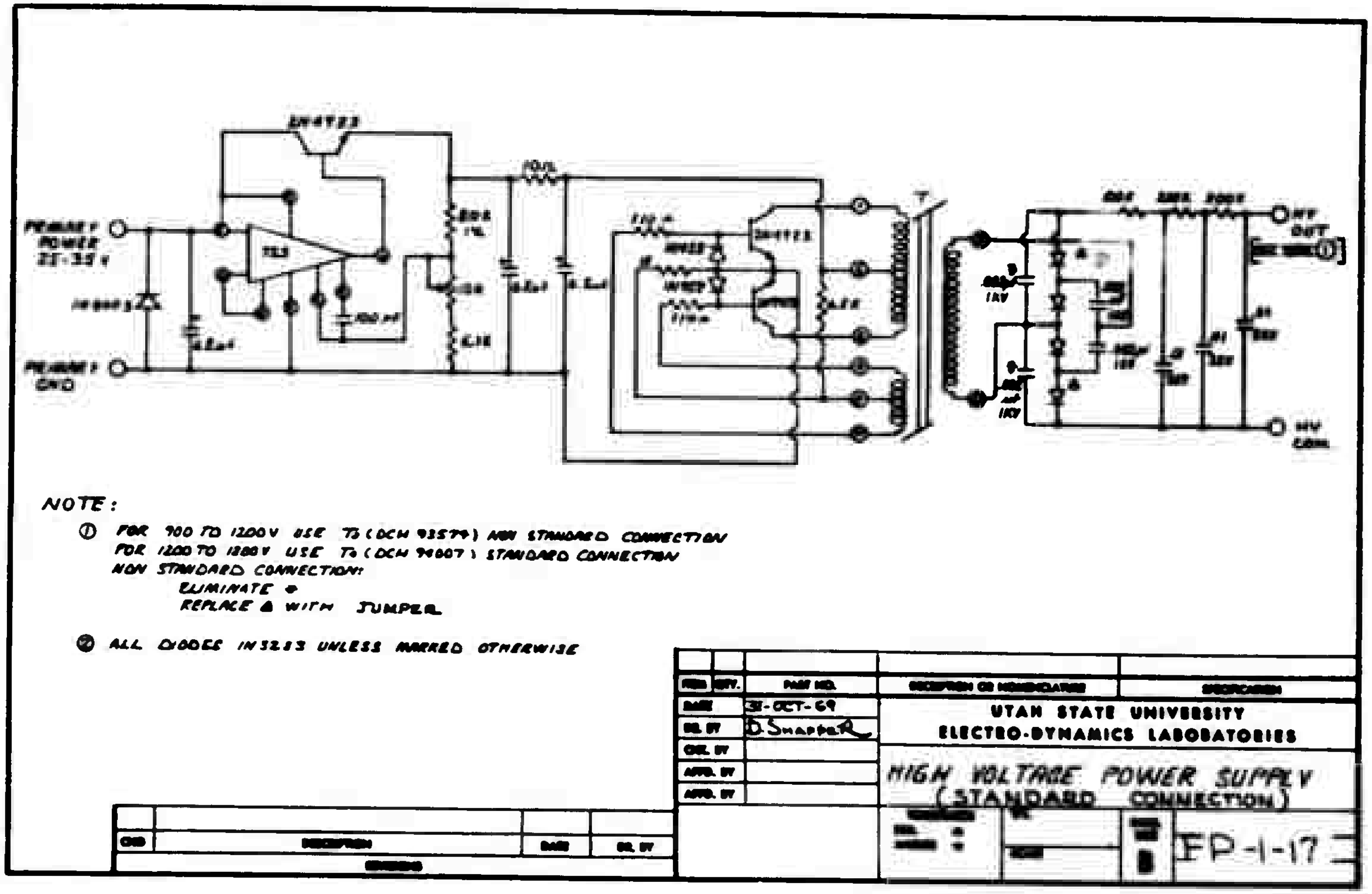

NOTE:

① FOR 900 TO 1200V USE T3 (DCH 93579) NON STANDARD CONNECTION
FOR 1200 TO 1800V USE T3 (DCH 94007) STANDARD CONNECTION
NON STANDARD CONNECTION:
ELIMINATE ●
REPLACE ▲ WITH JUMPER

② ALL DIODES IN3253 UNLESS MARKED OTHERWISE

Figure A-12. Schematic diagram of photomultiplier high-voltage power supply.

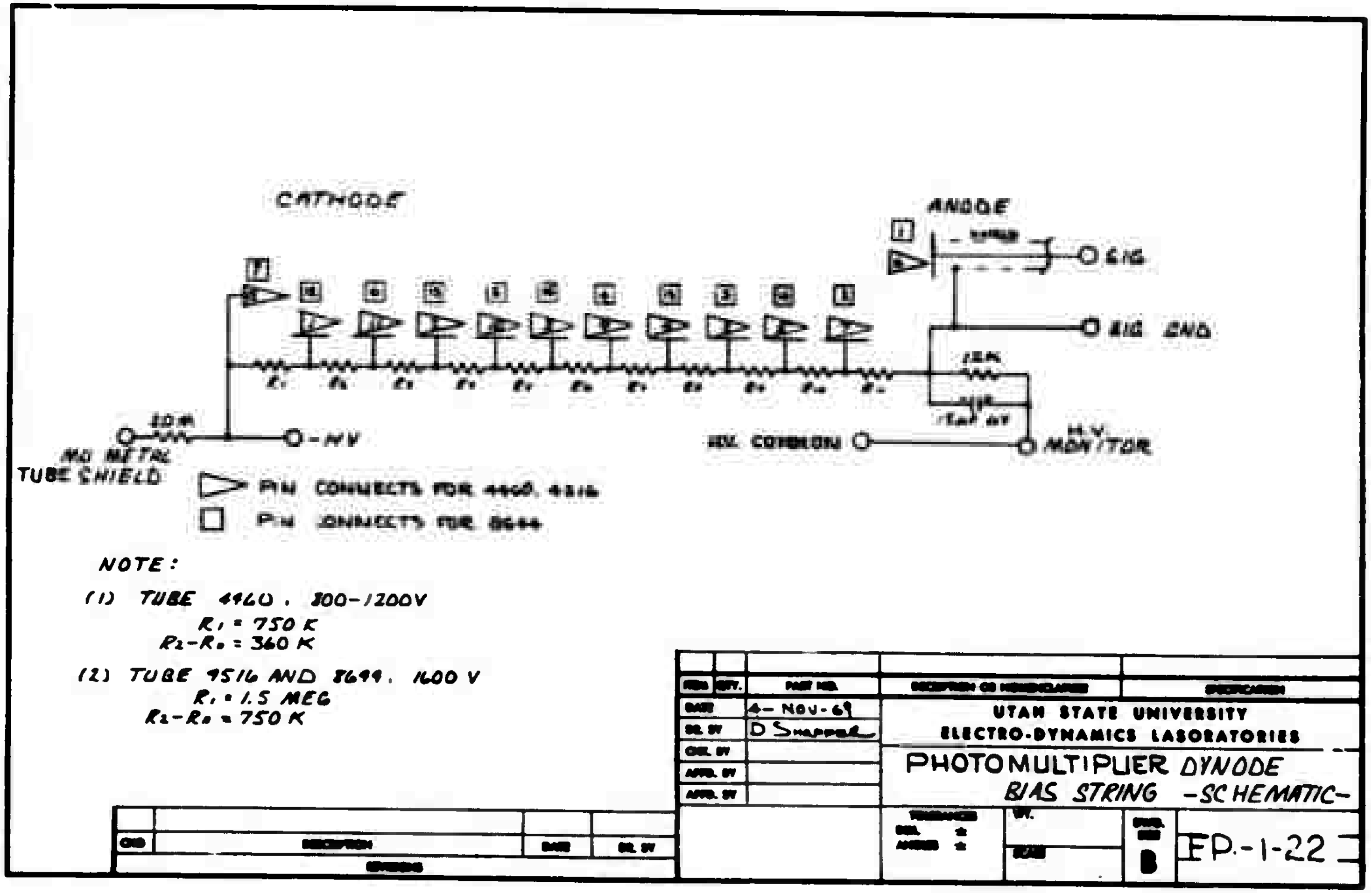

Figure A-13. Schematic diagram of voltage divider for distribution of MPT dynode voltages.

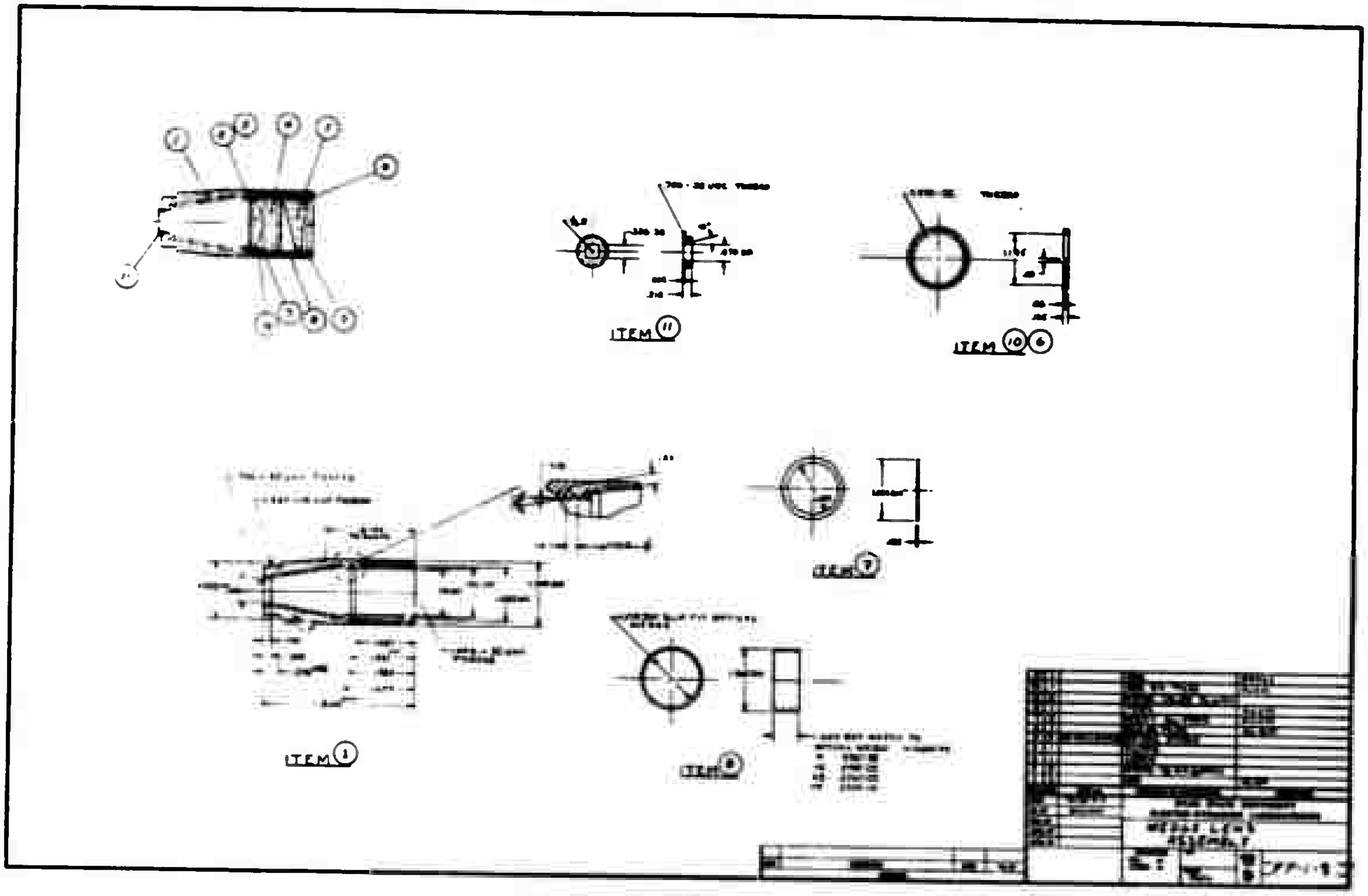

Figure A-14. Optical assembly for photometers.

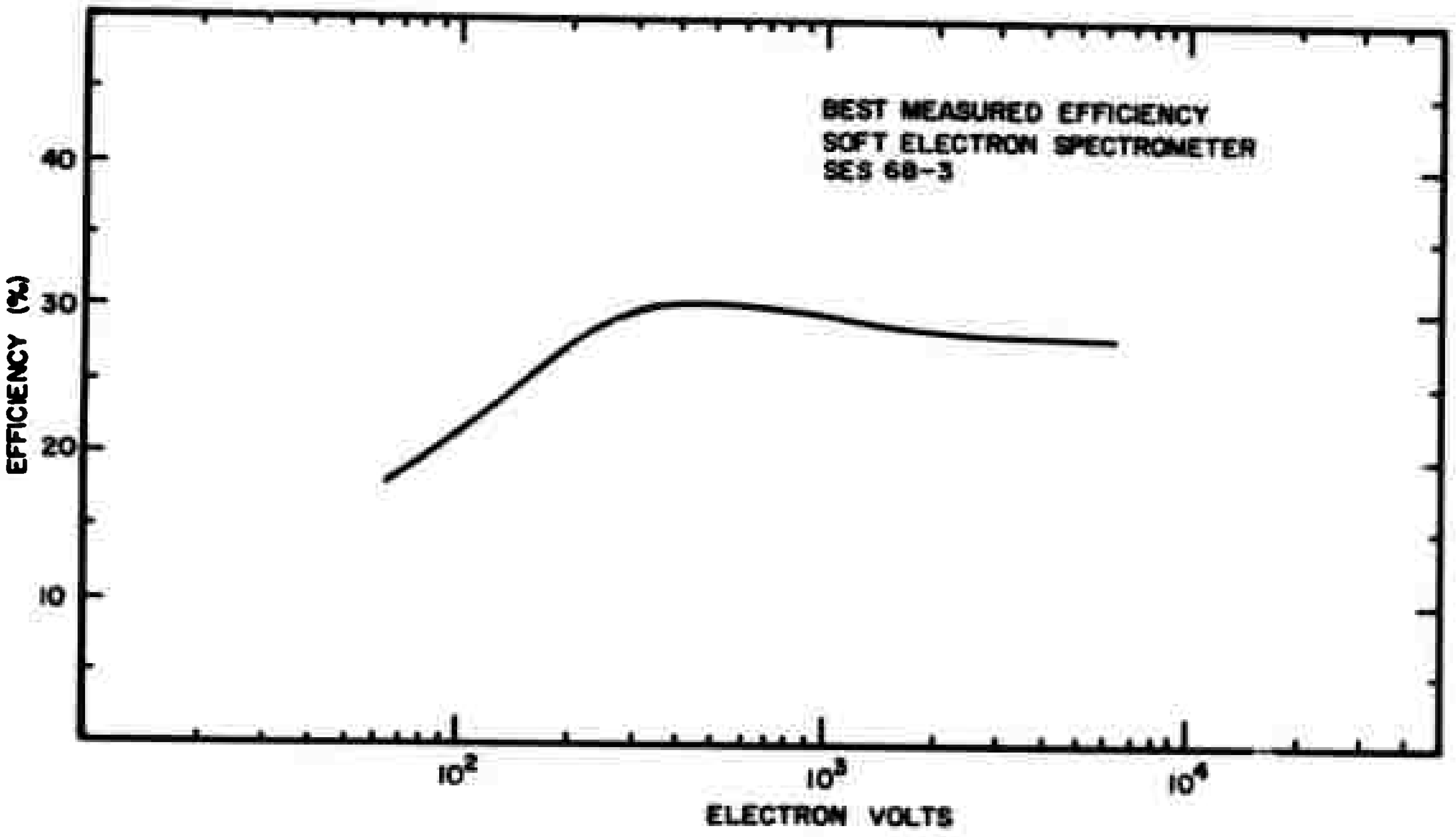

Figure A-15. Efficiency curve for soft electron spectrometer.

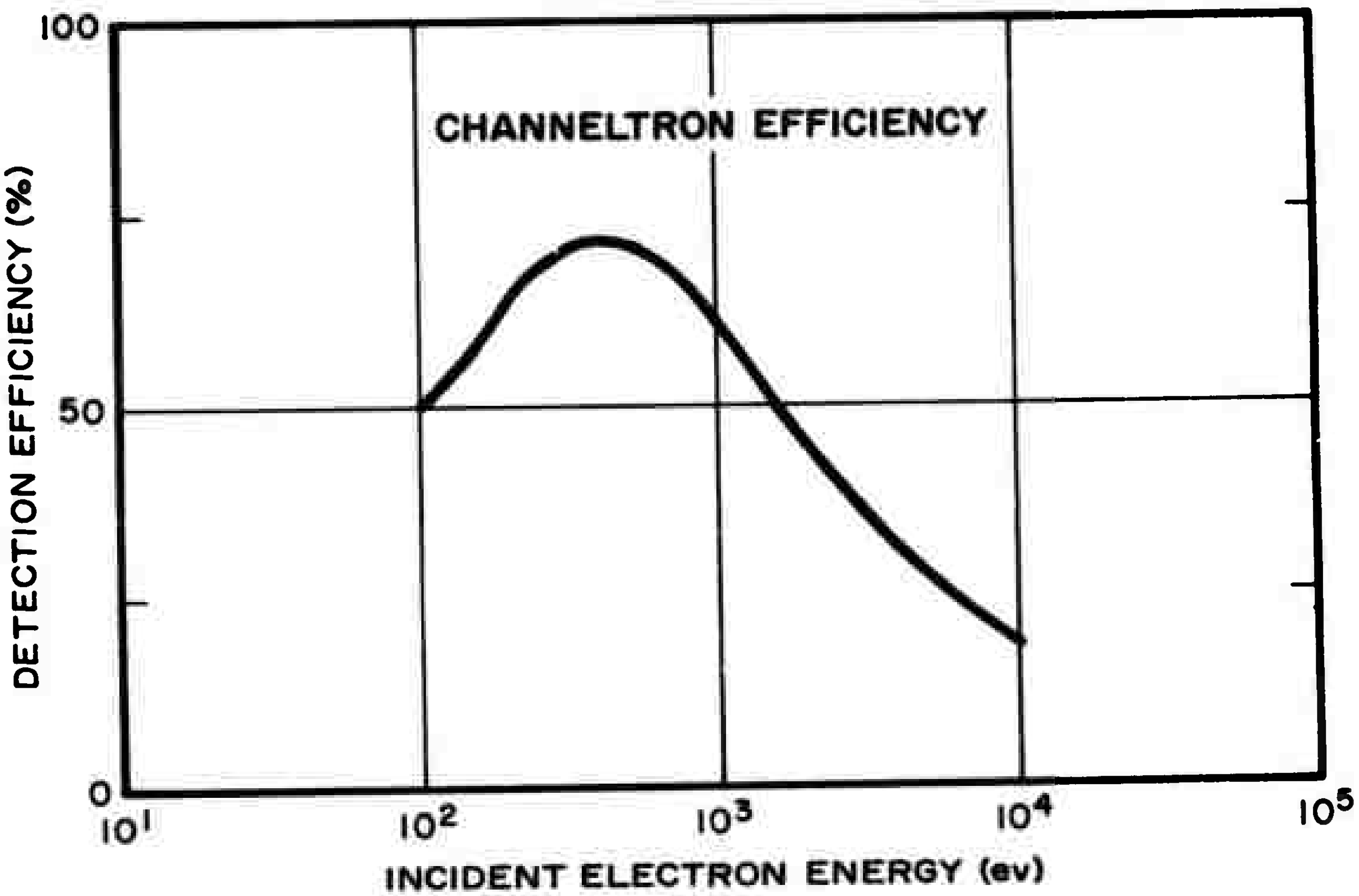

Figure A-16. Efficiency curve for channeltron.

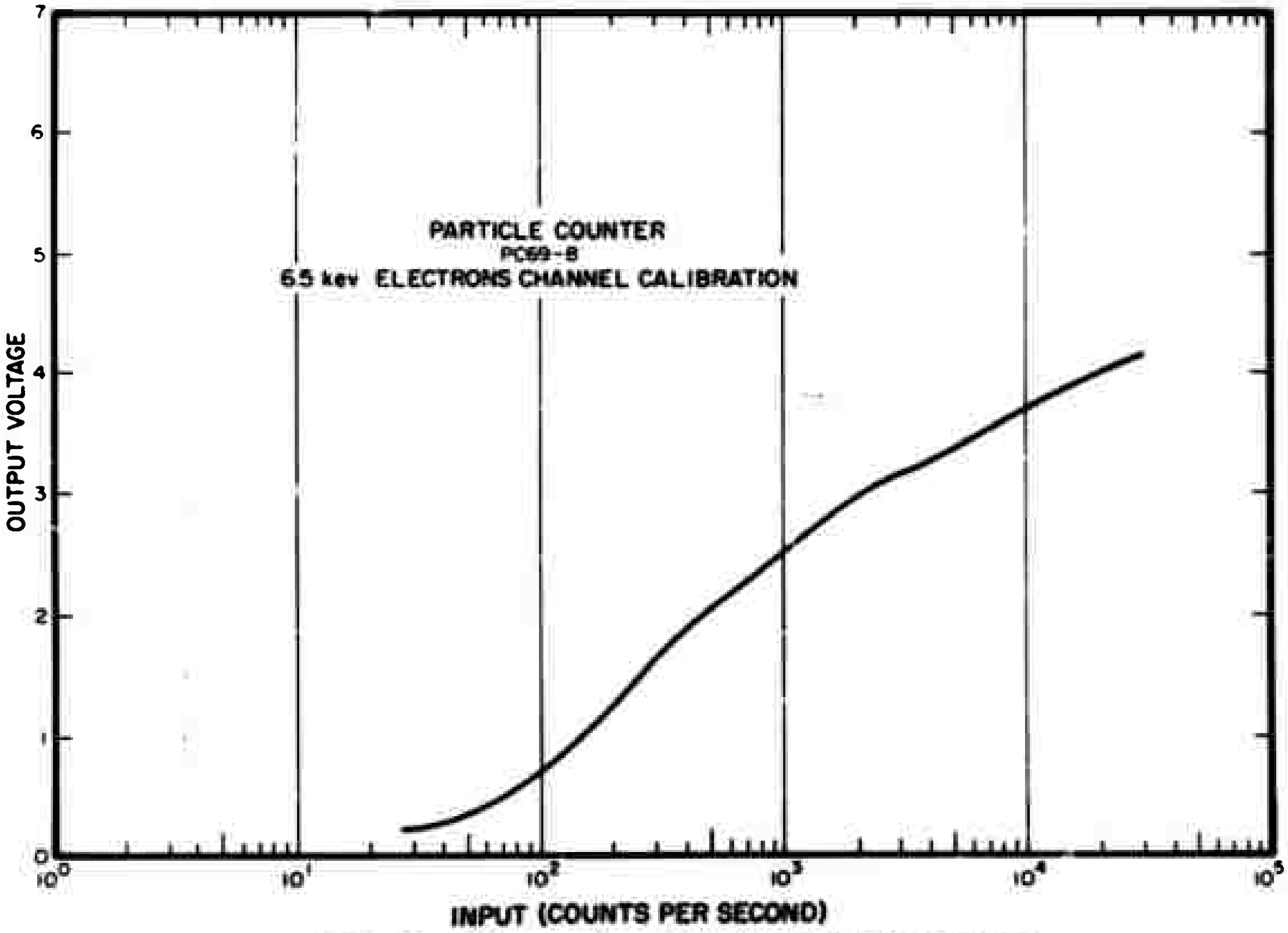

Figure A-17. Particle counter calibration: 6.5-keV channel.

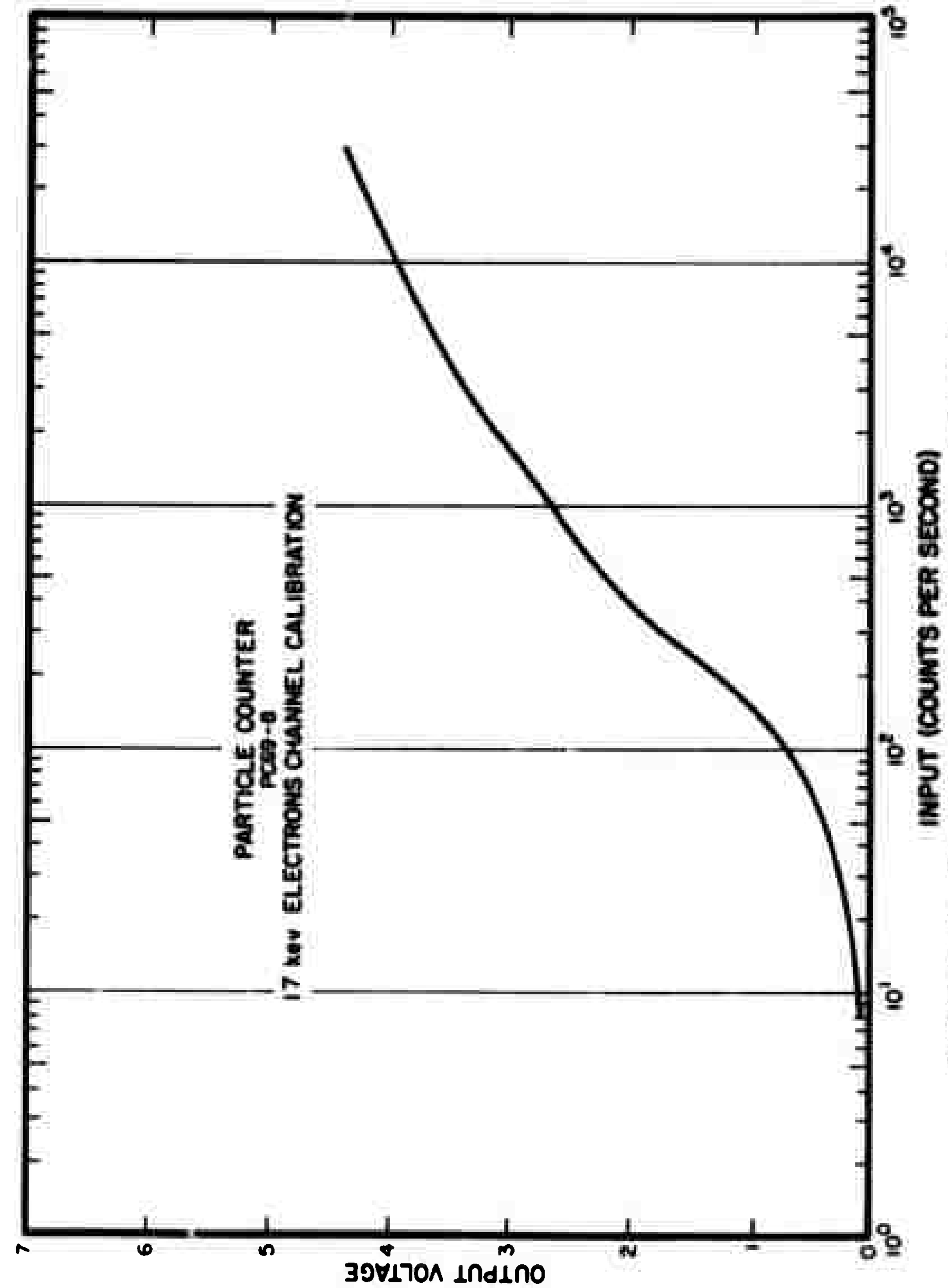

Figure A-18. Particle counter calibration: 17-keV channel.

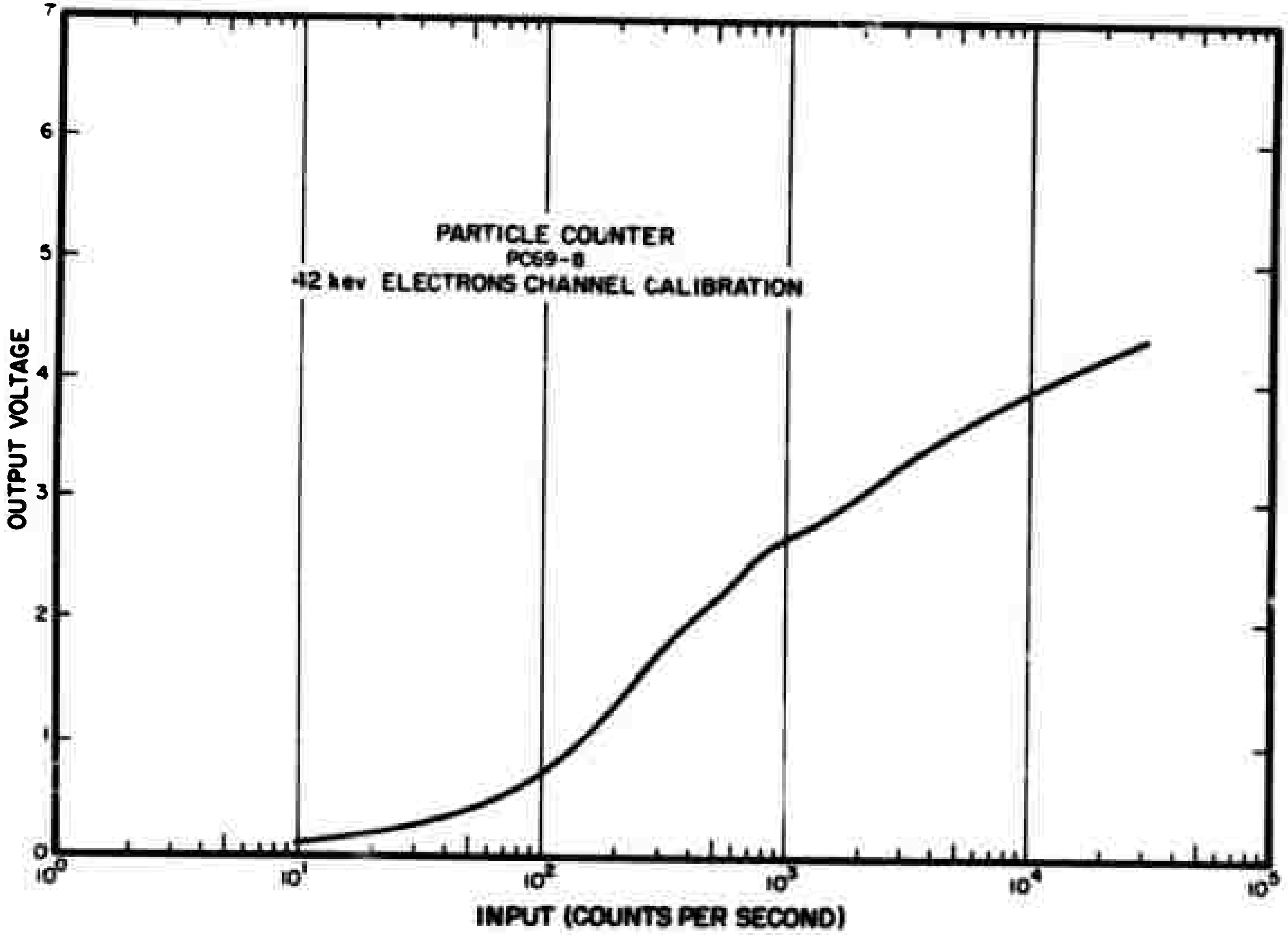

Figure A-19. Particle counter calibration: 42-keV channel.

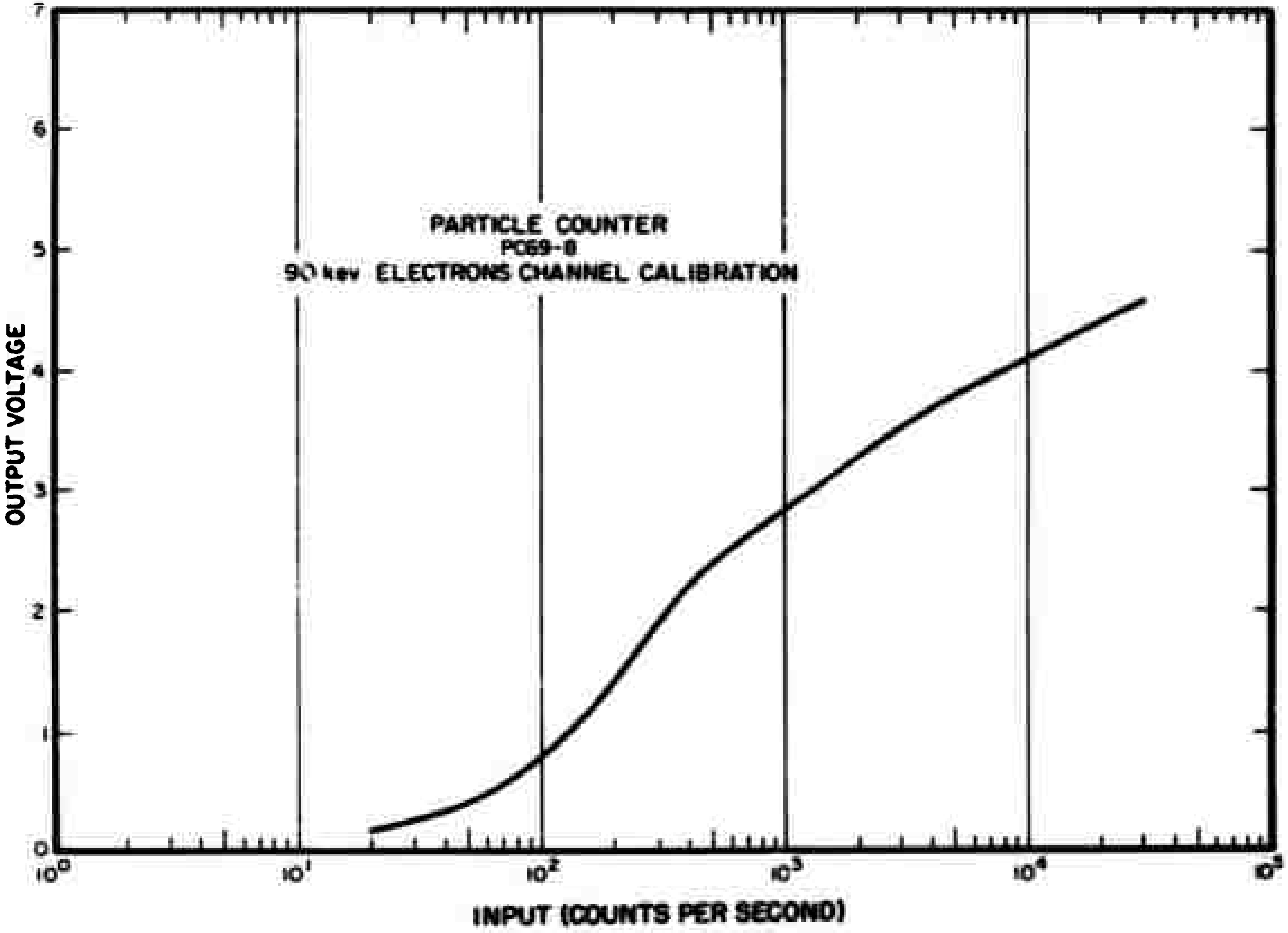

Figure A-20. Particle counter calibration: 90-keV channel.

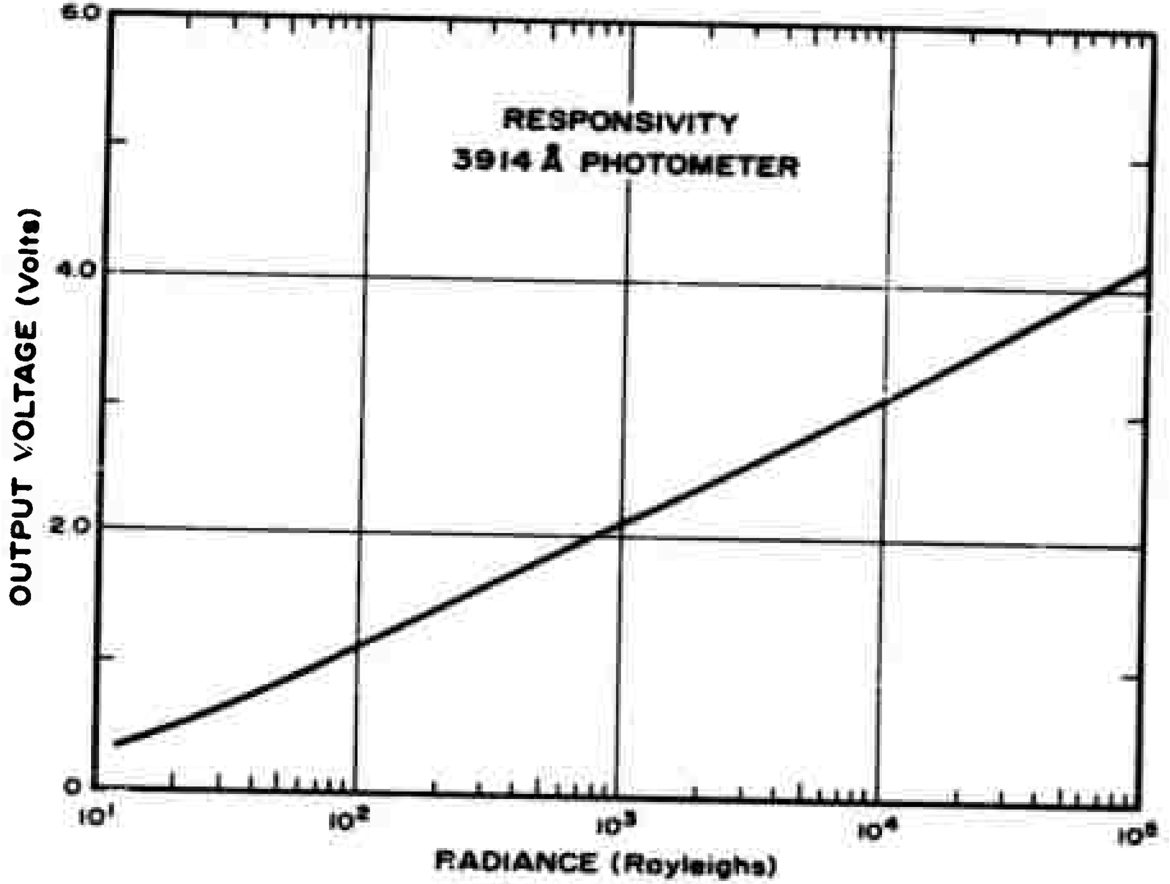

Figure A-21. Responsivity curve: λ 5577 Å auroral photometer.

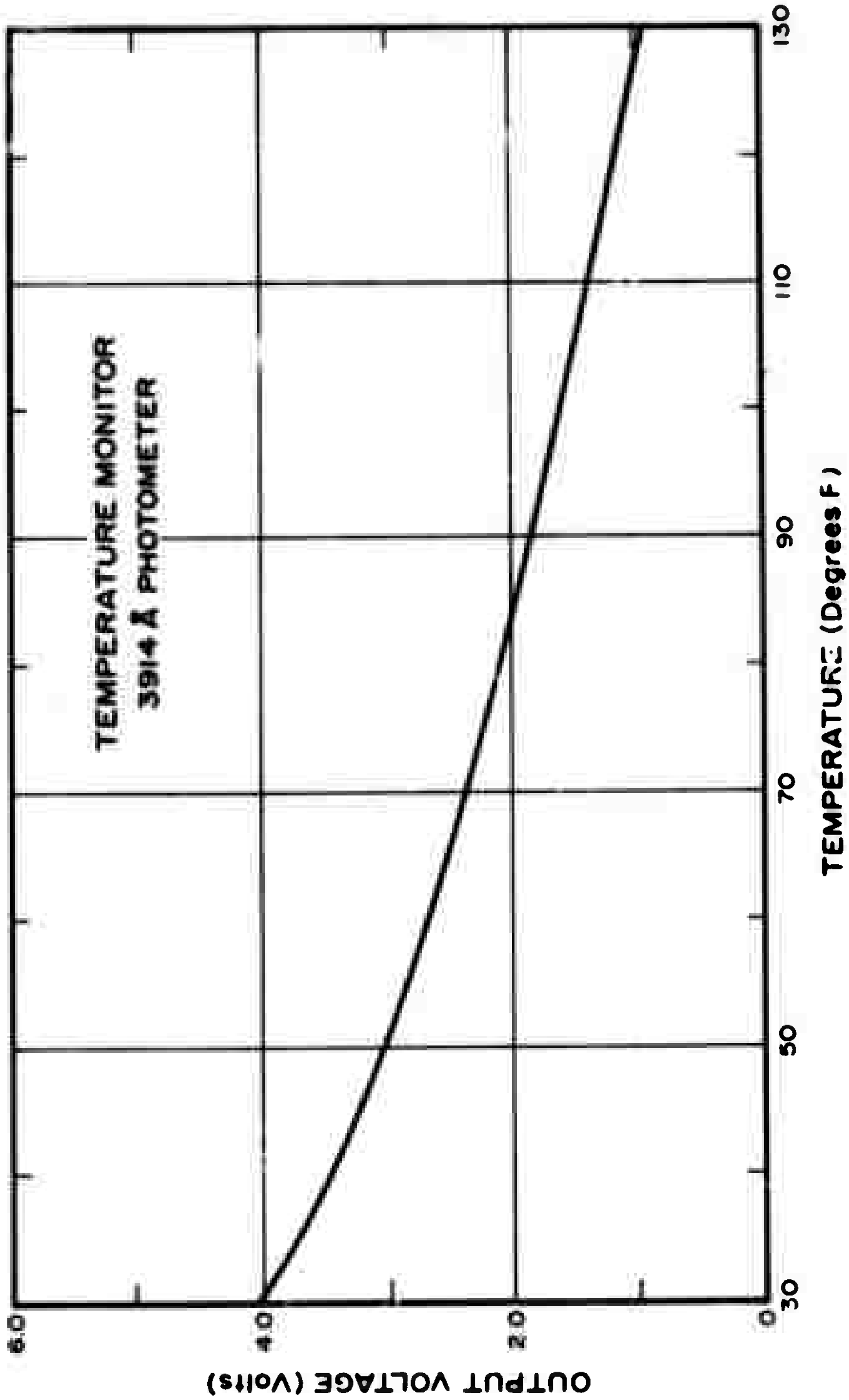

Figure A-22. Temperature monitor calibration curve: λ 3914 Å auroral photometer.

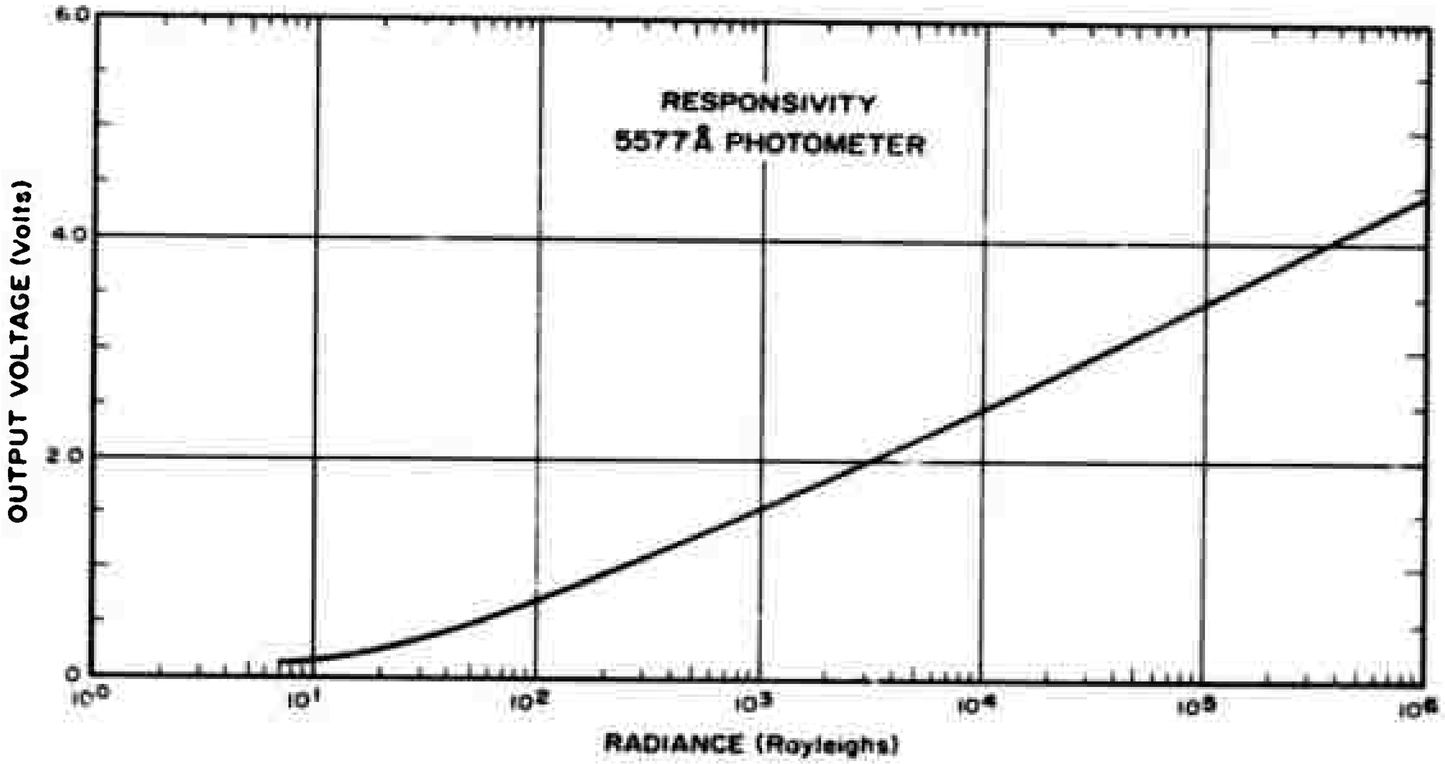

Figure A-23. Responsivity curve: λ 5577 Å auroral photometer.

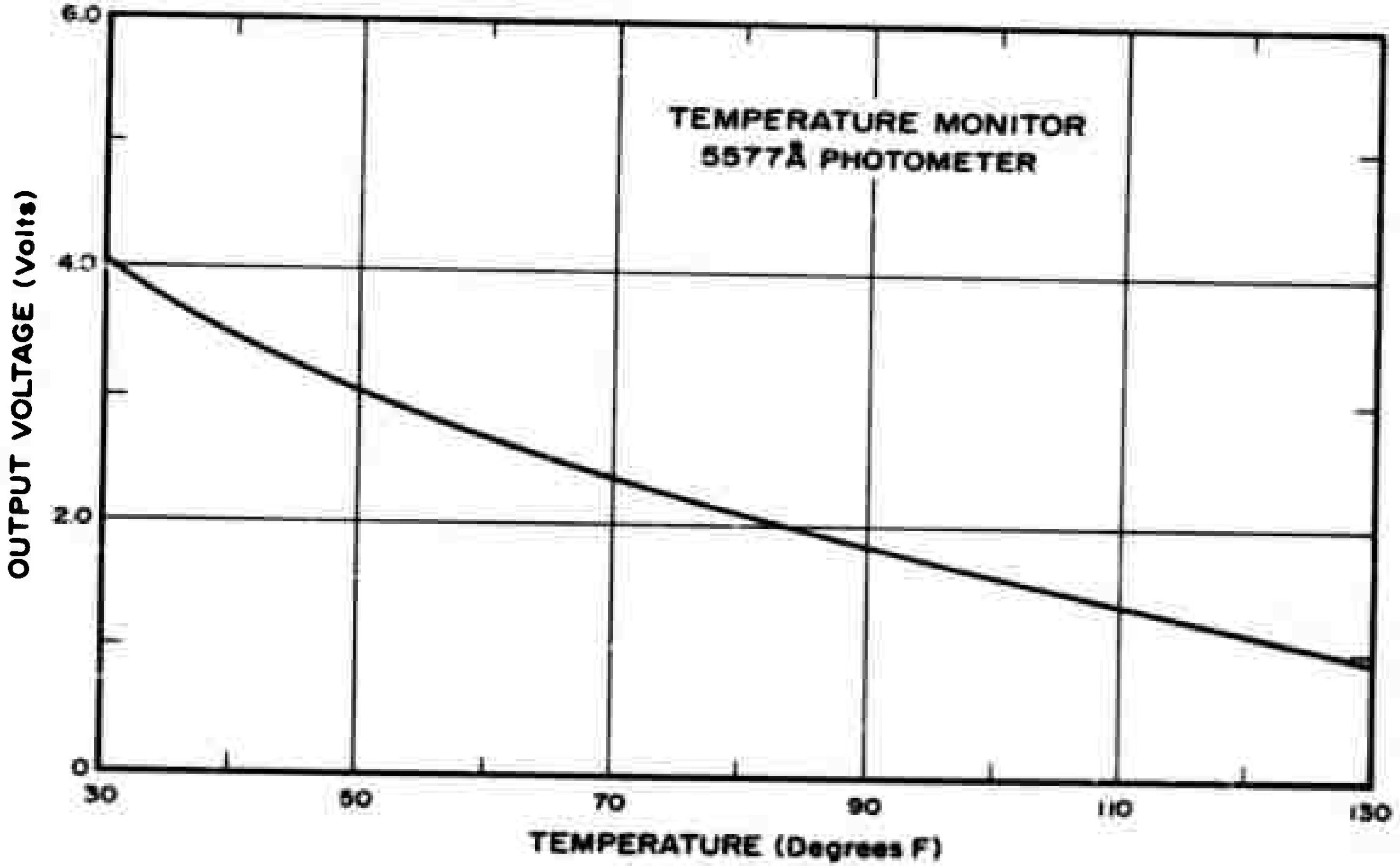

Figure A-24. Temperature monitor calibration curve: λ 5577 Å.

APPENDIX B

AEROBEE AO 3.910-1

SCHEMATIC DIAGRAMS AND CALIBRATIONS

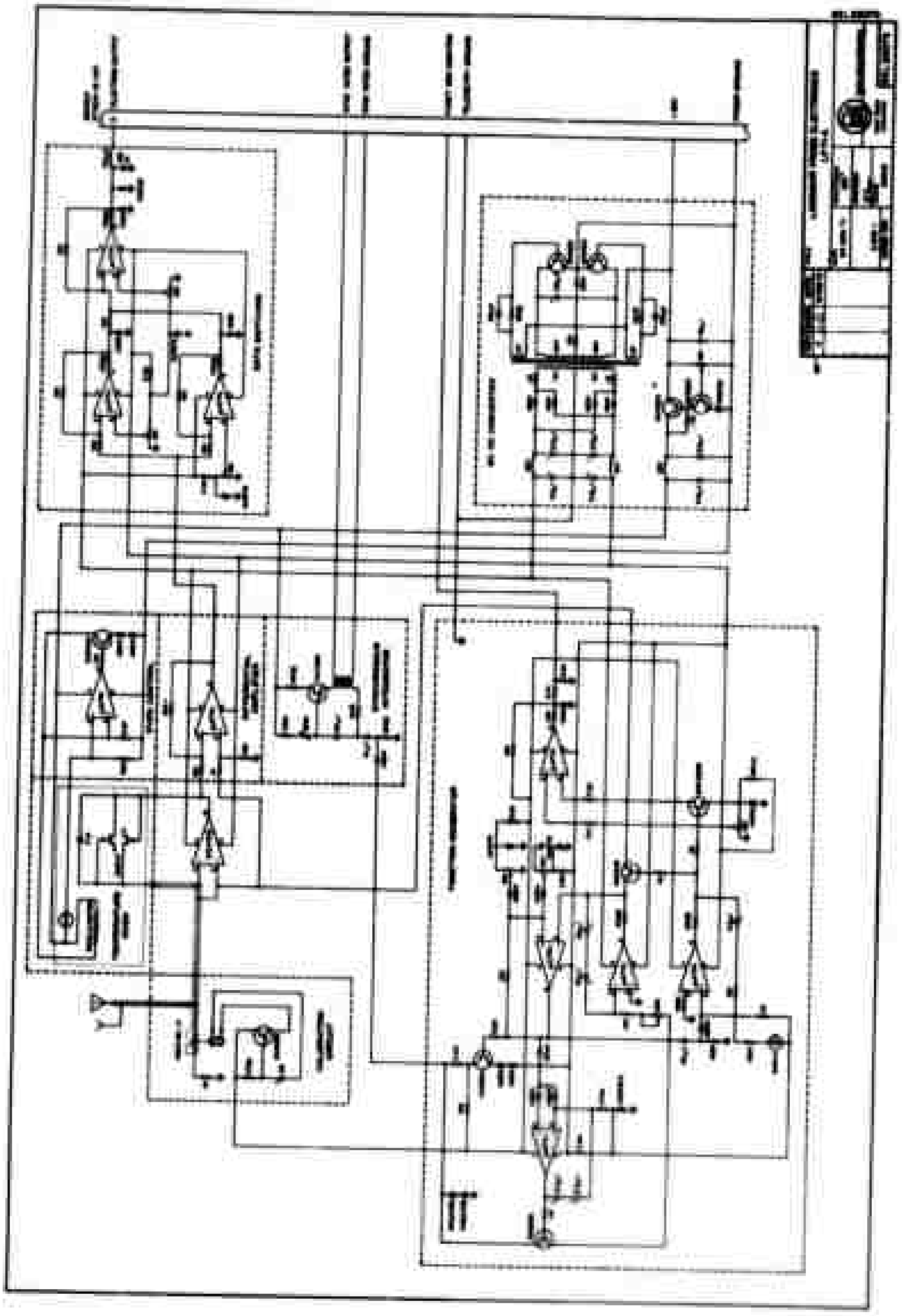

Figure B-1. Langmuir-probe circuit diagram.

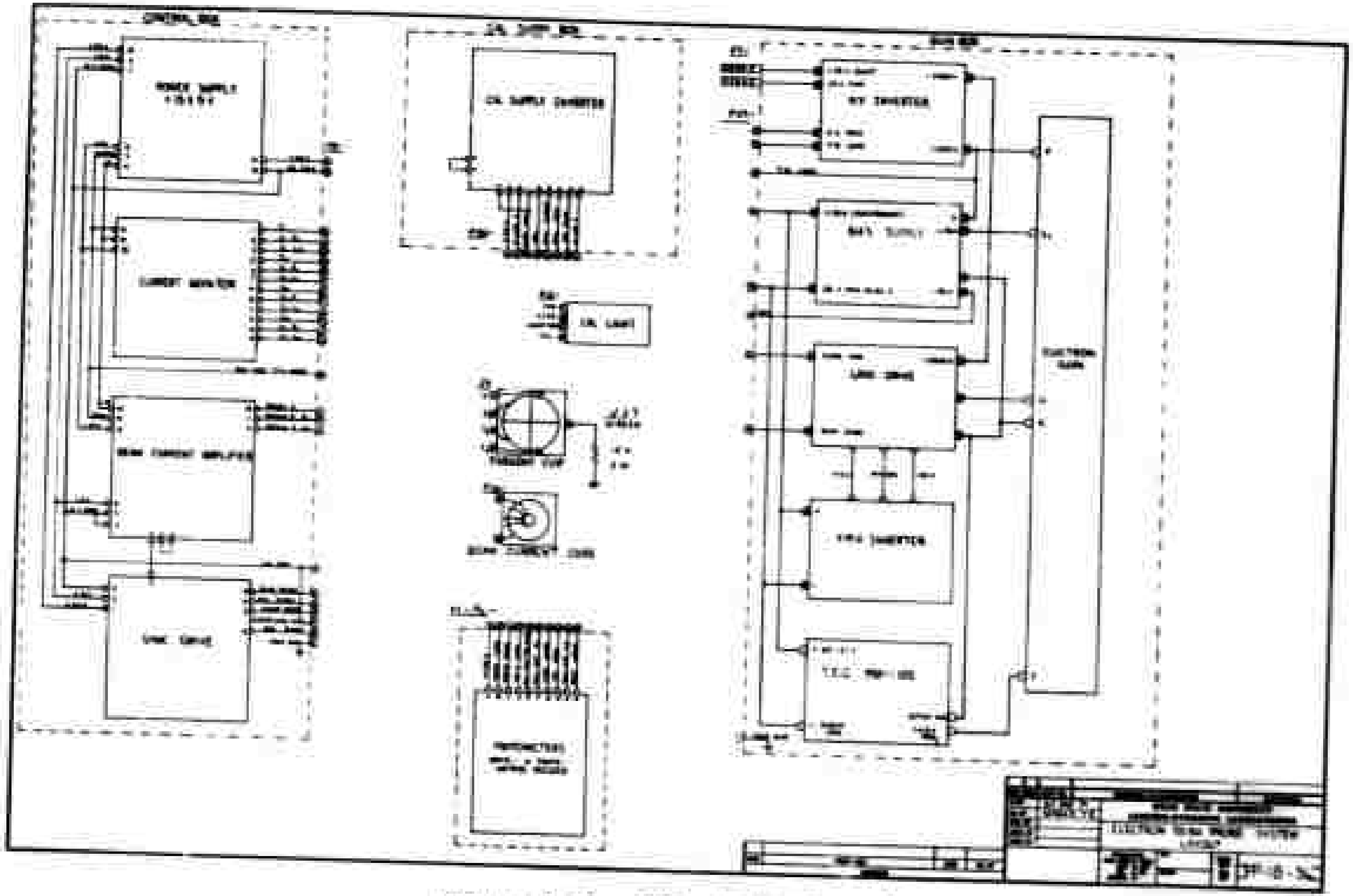

Figure B-2. EBIL system layout.

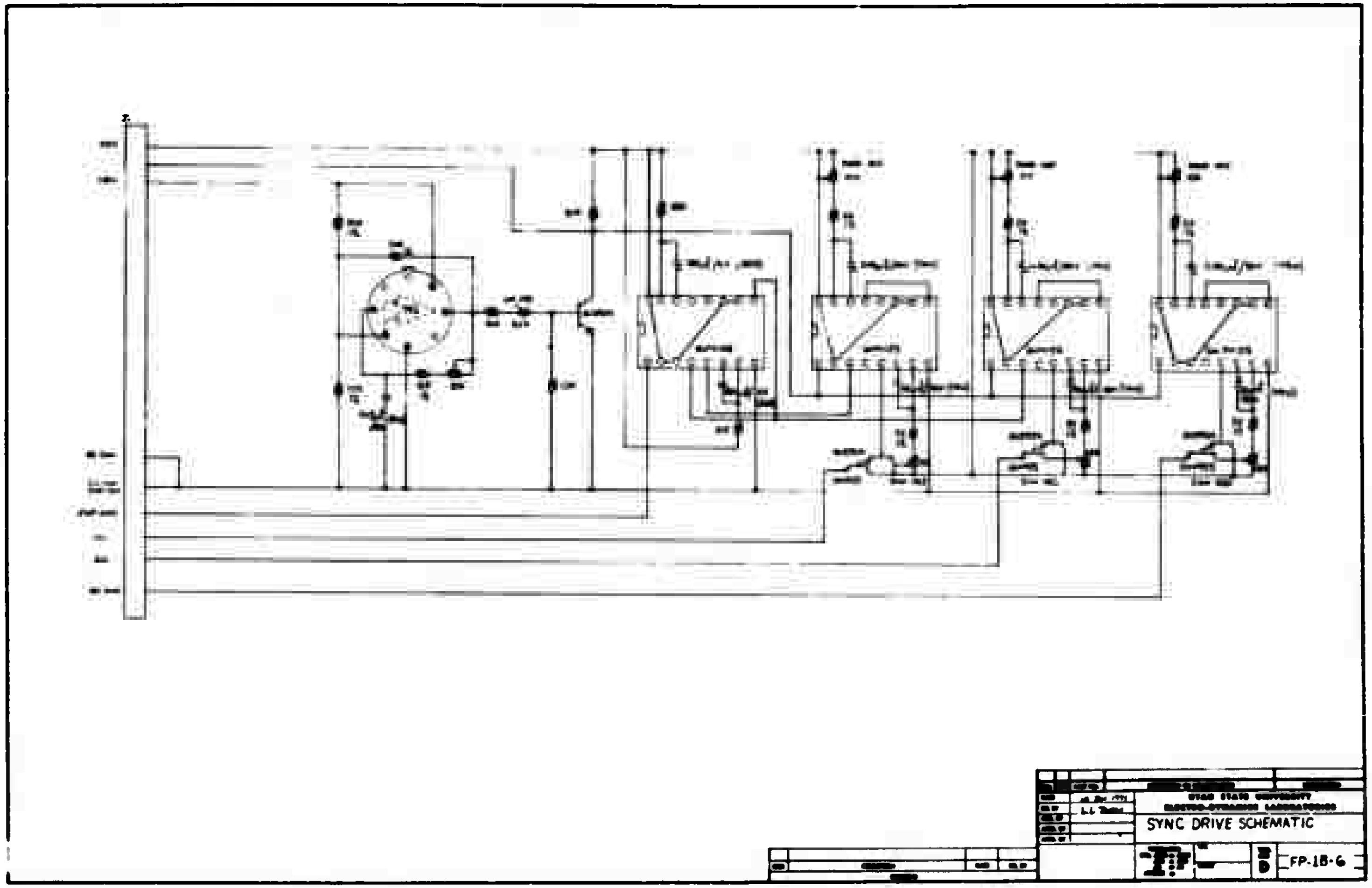

Figure B-3. Schematic diagram of SYNC DRIVE circuitry.

B-4

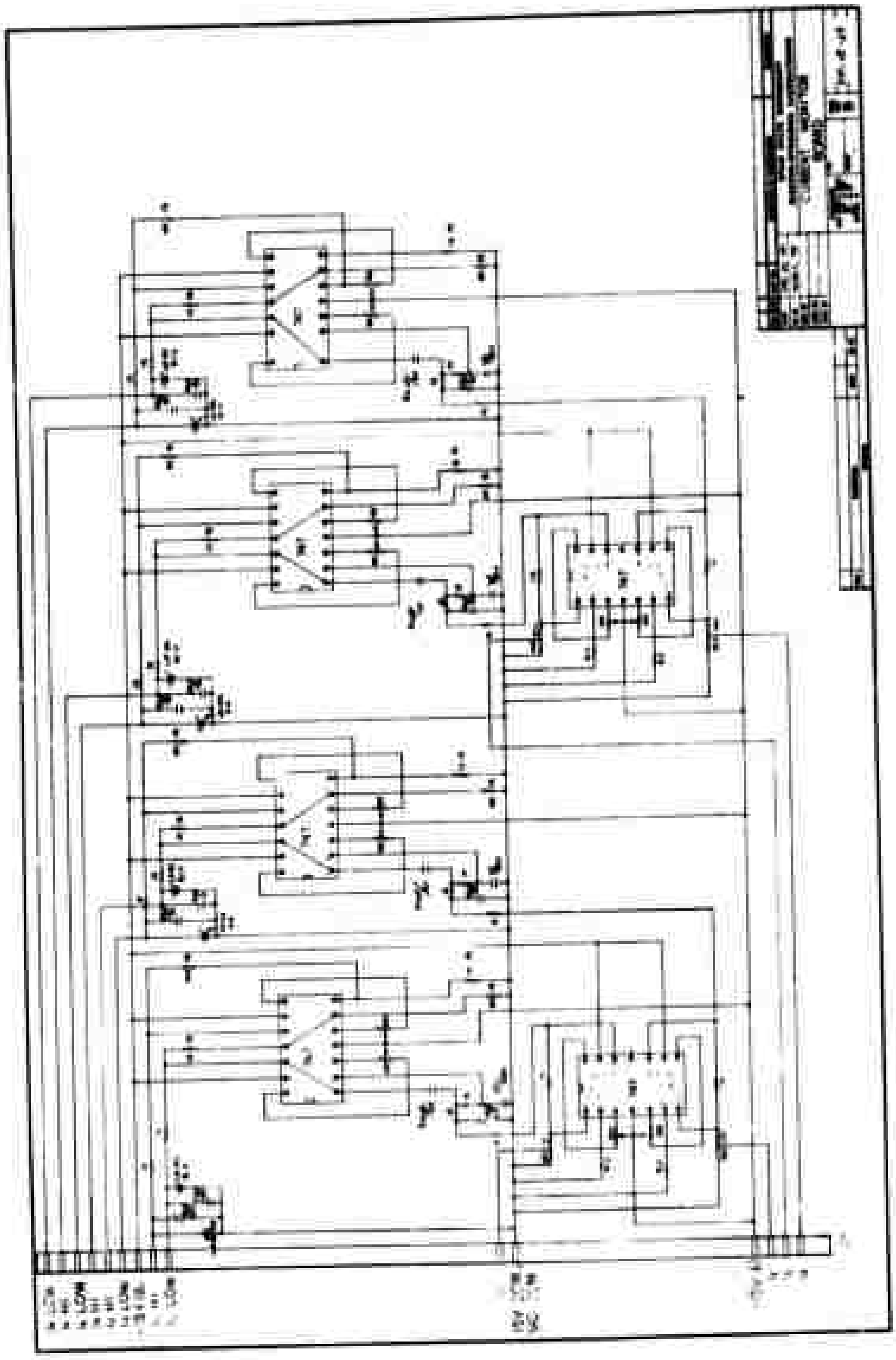

Figure B-4. Schematic diagram of current monitor (Faraday collector) circuitry.

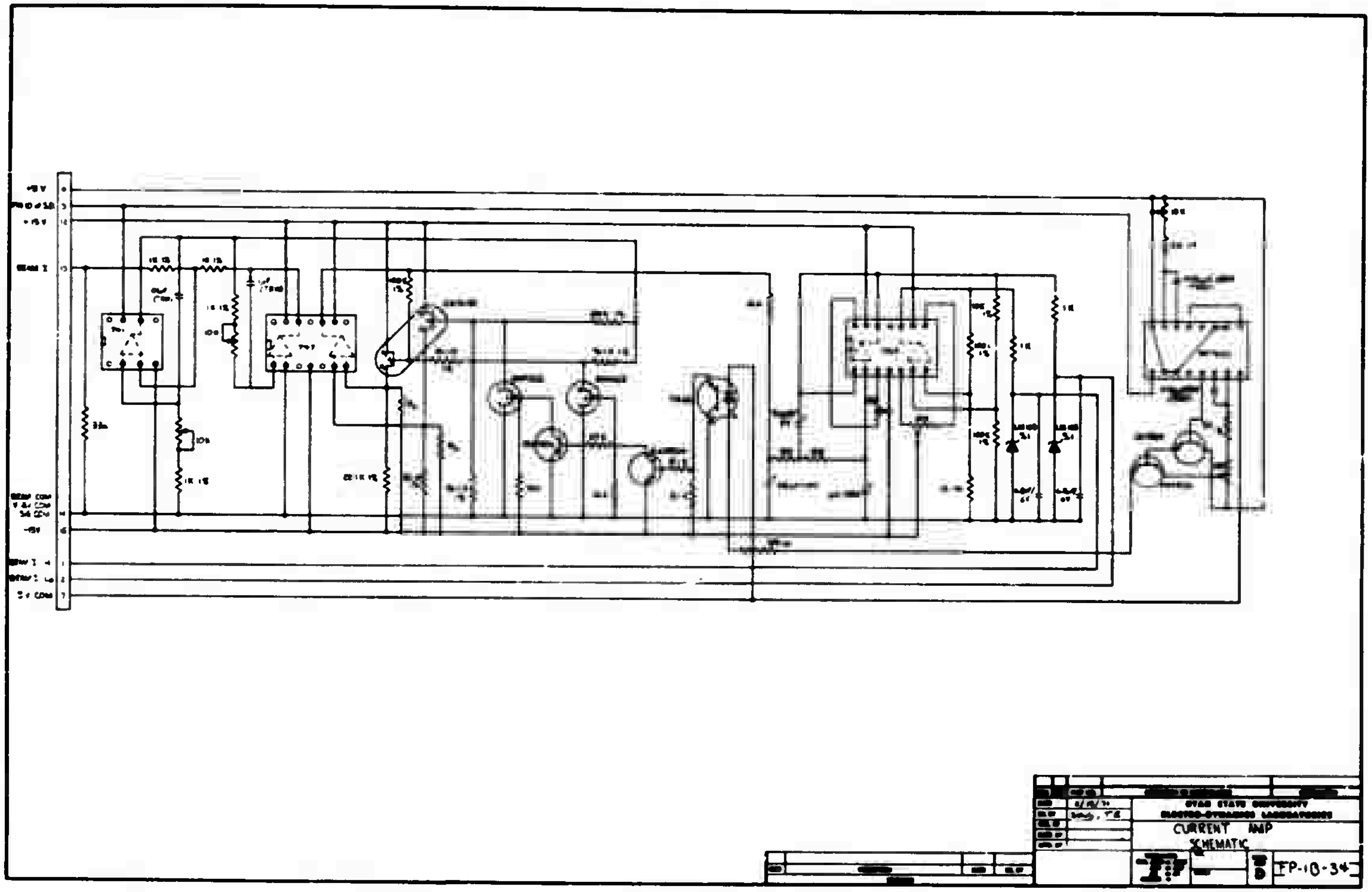

Figure B-5. Schematic diagram of current amplifier (toroid) circuitry.

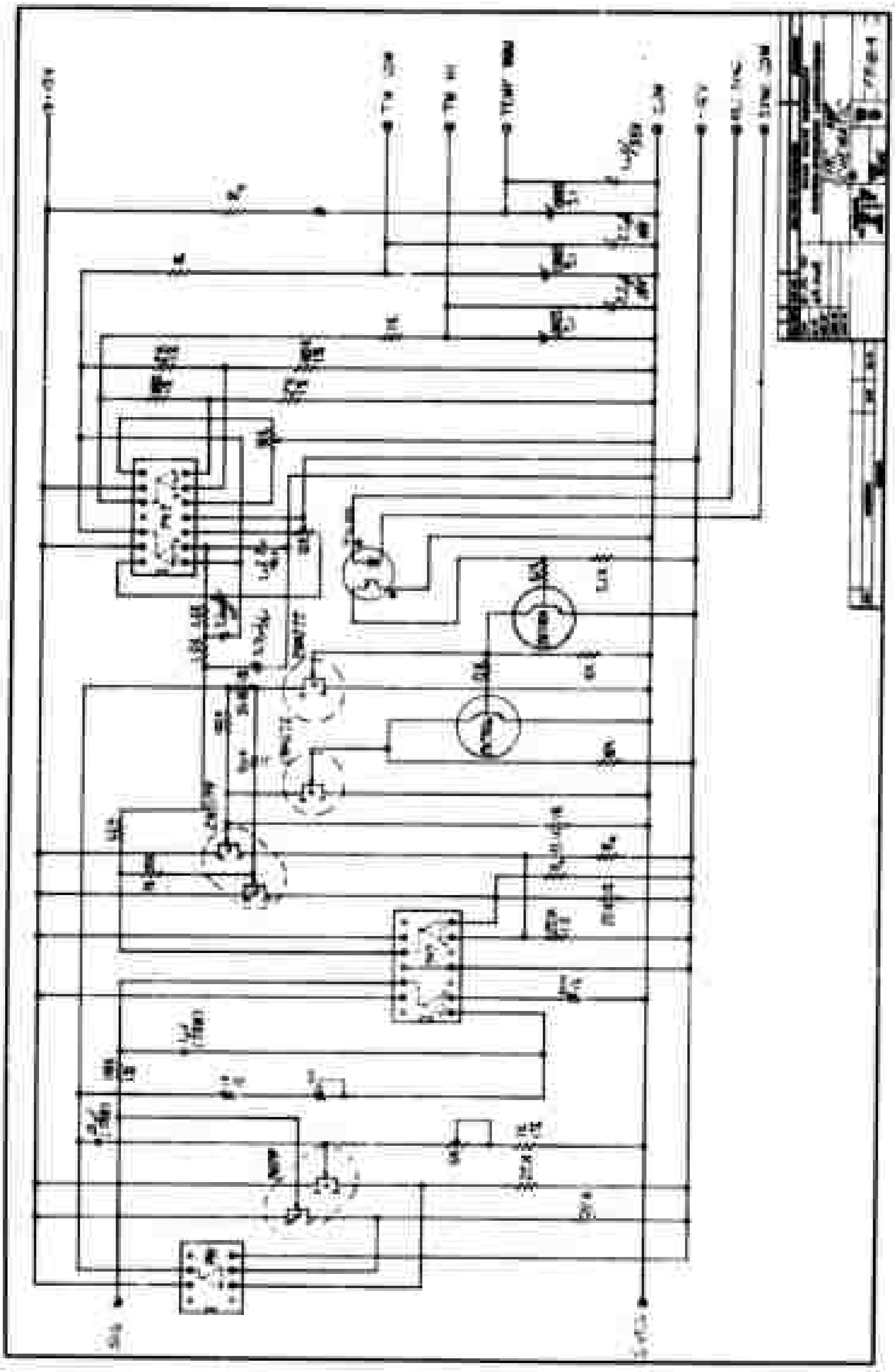

Figure B-6. Schematic diagram of synchronous amplifier.

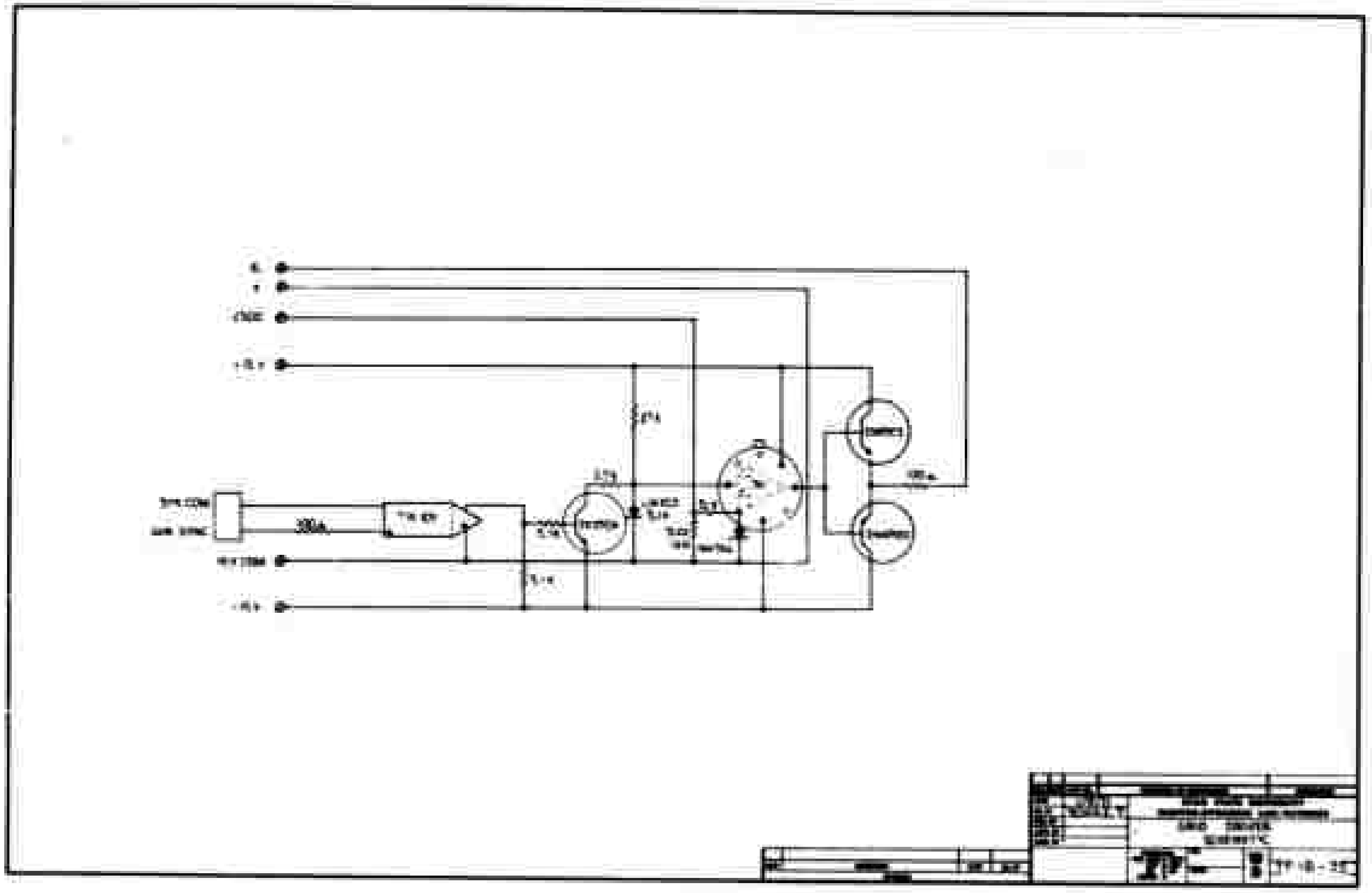

Figure B-7. Schematic diagram of electron gun grid-drive circuitry.

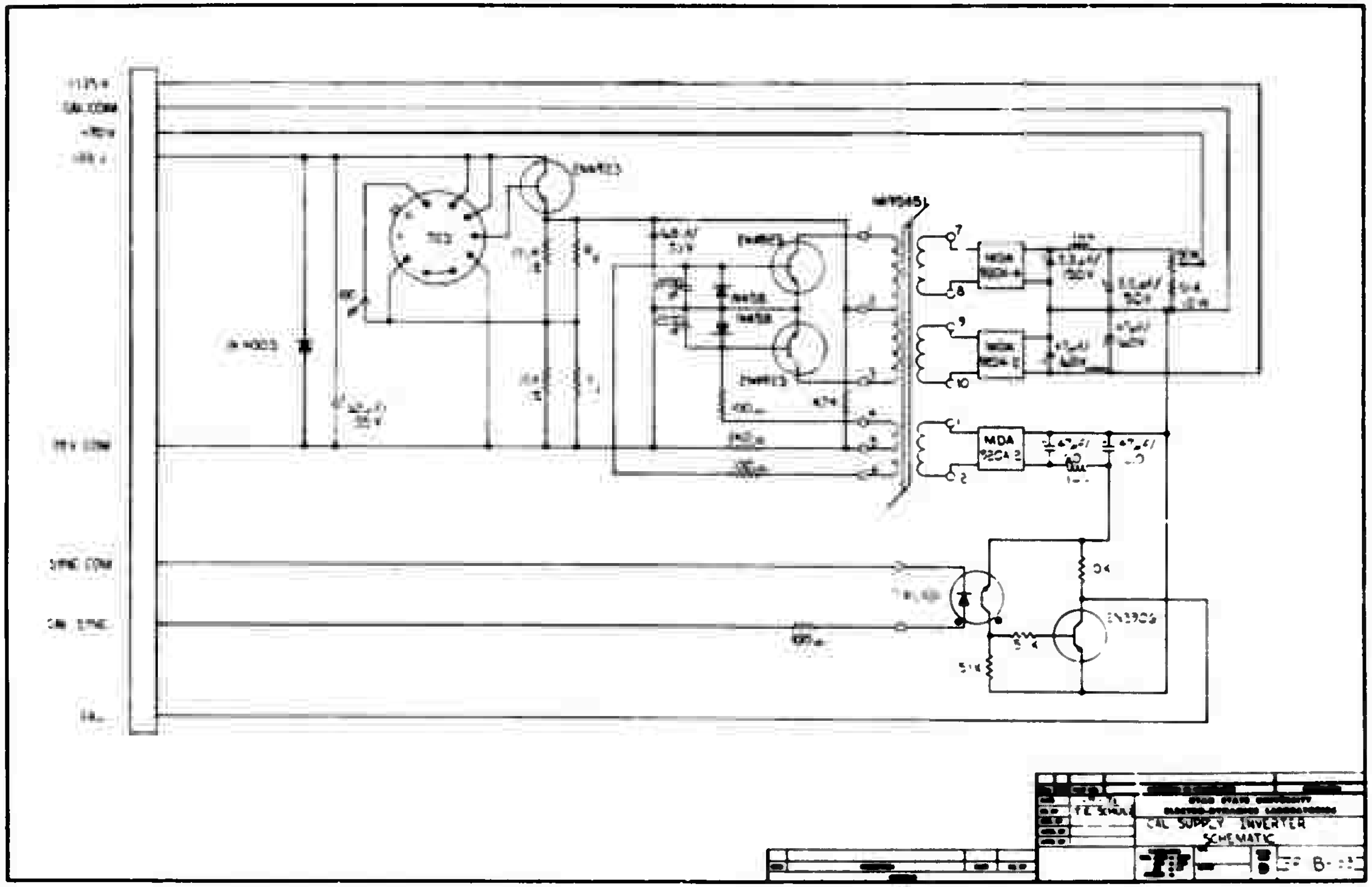

Figure B-8. Schematic diagram of control circuit for in-flight calibration light.

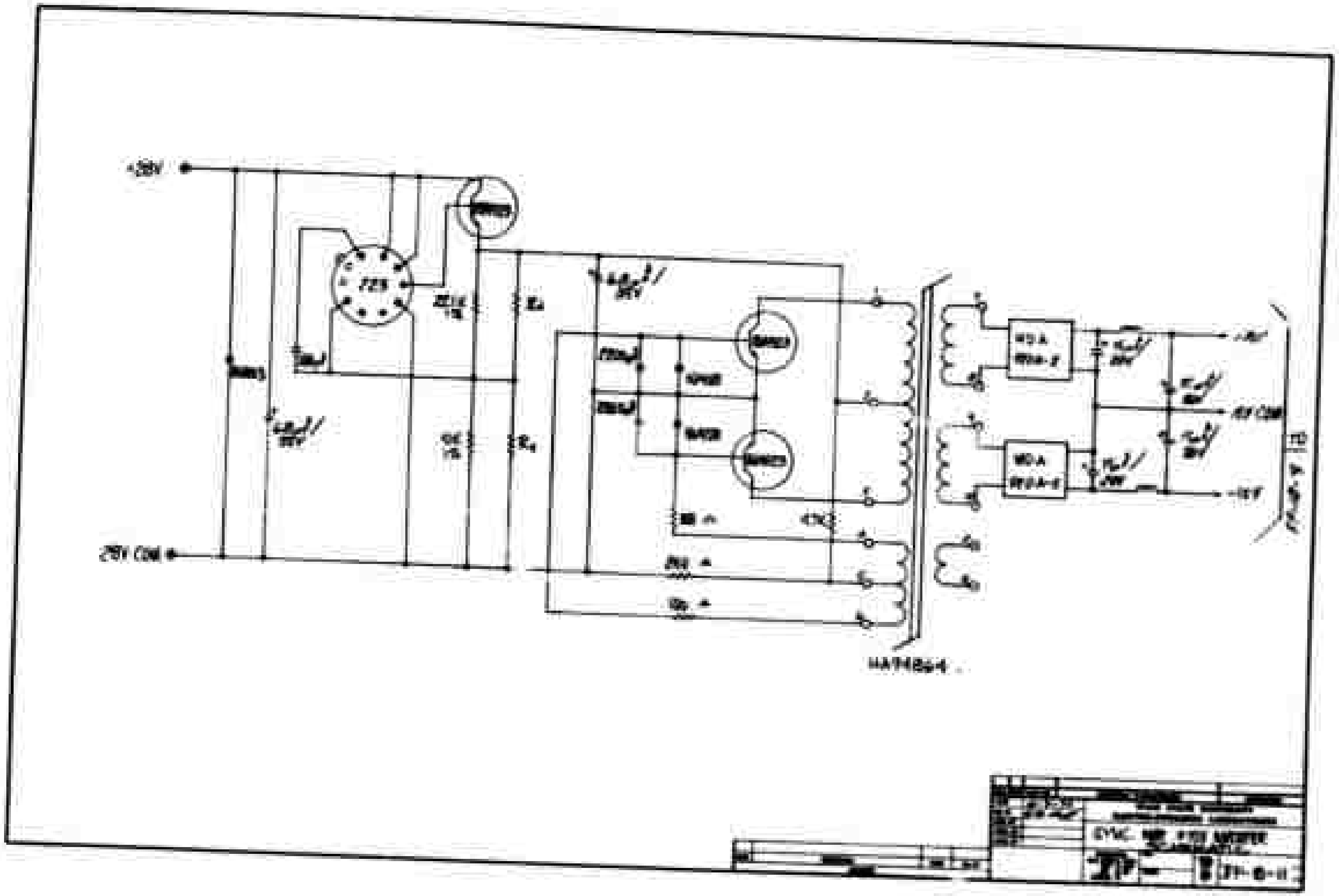

Figure B-9. ±15 V supply for synchronous amplifier.

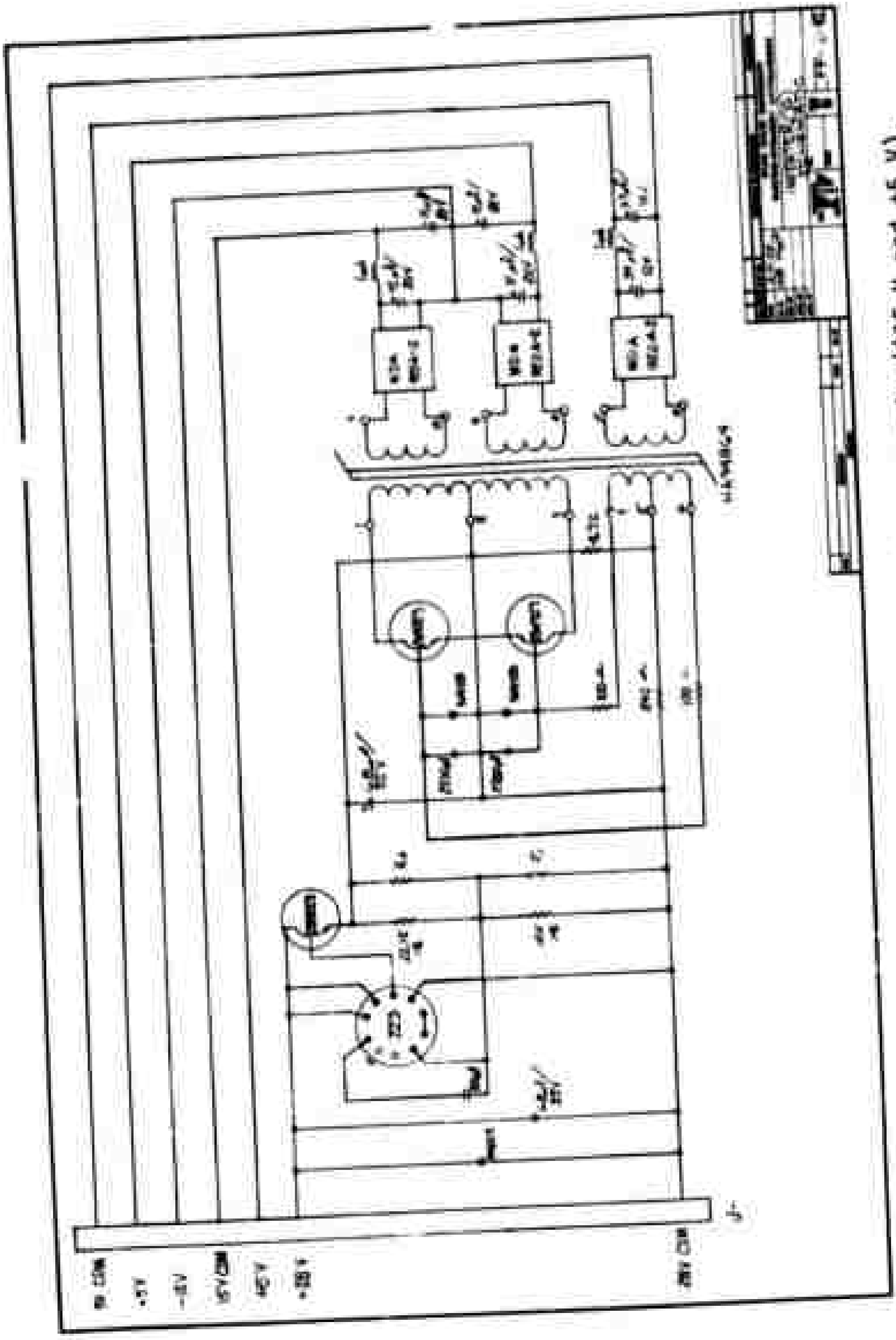

Figure B-10. Schematic diagram of low-voltage supply (±15 V and +5 V).

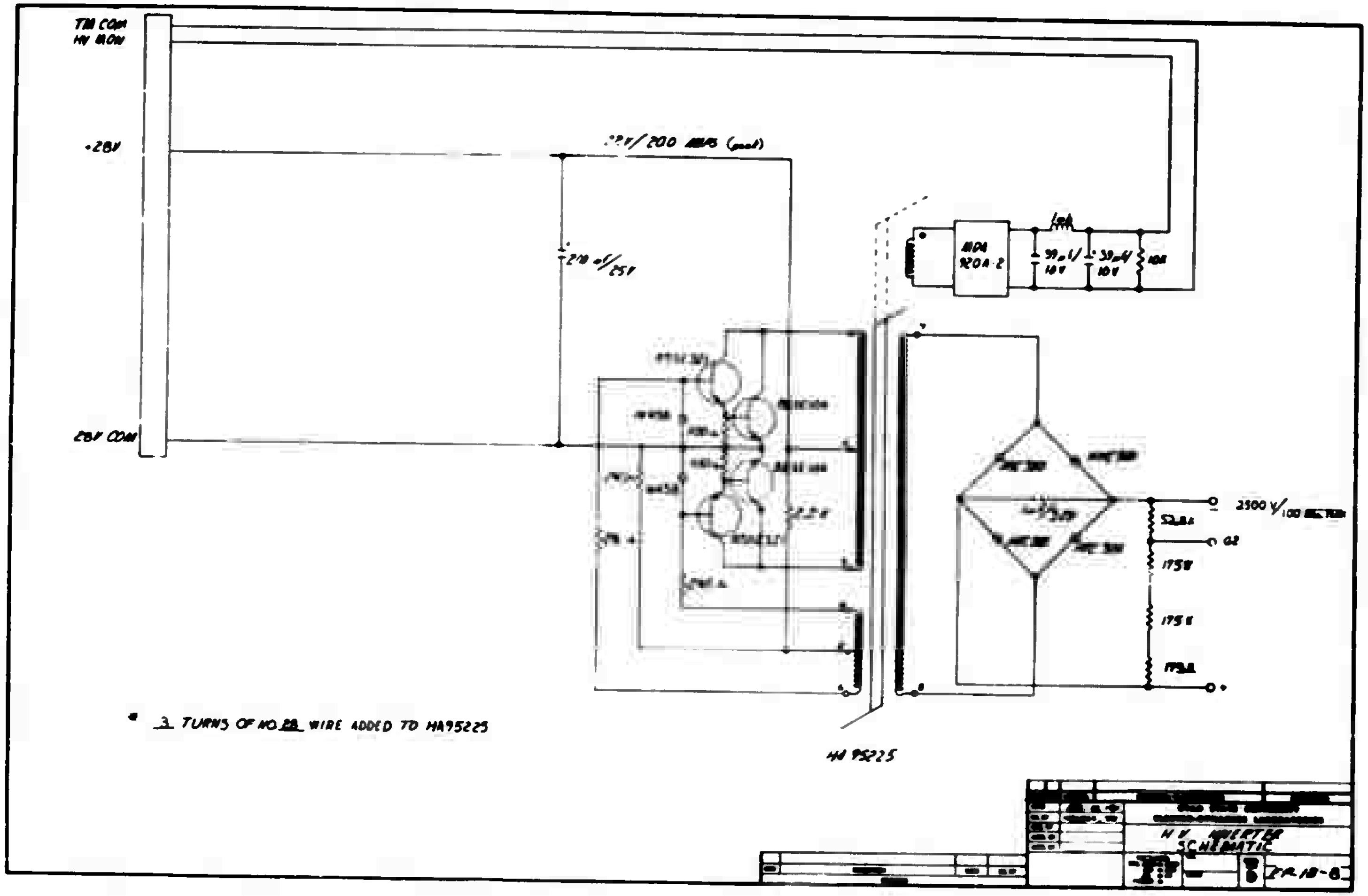

Figure B-11. Schematic diagram of electron gun high voltage and preaccelerator supply.

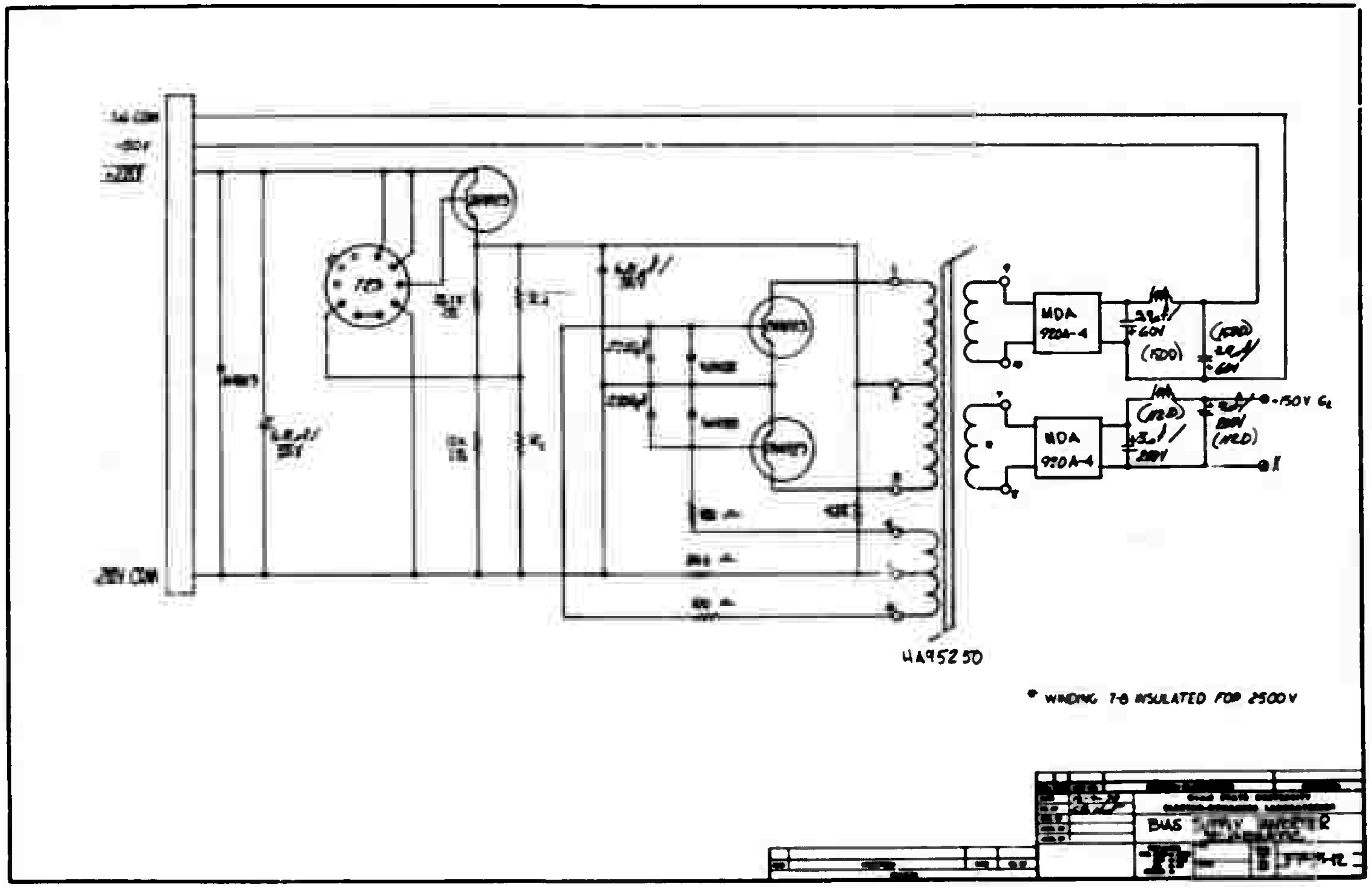

Figure B-12. Schematic diagram of bias supply for Faraday collector screen.

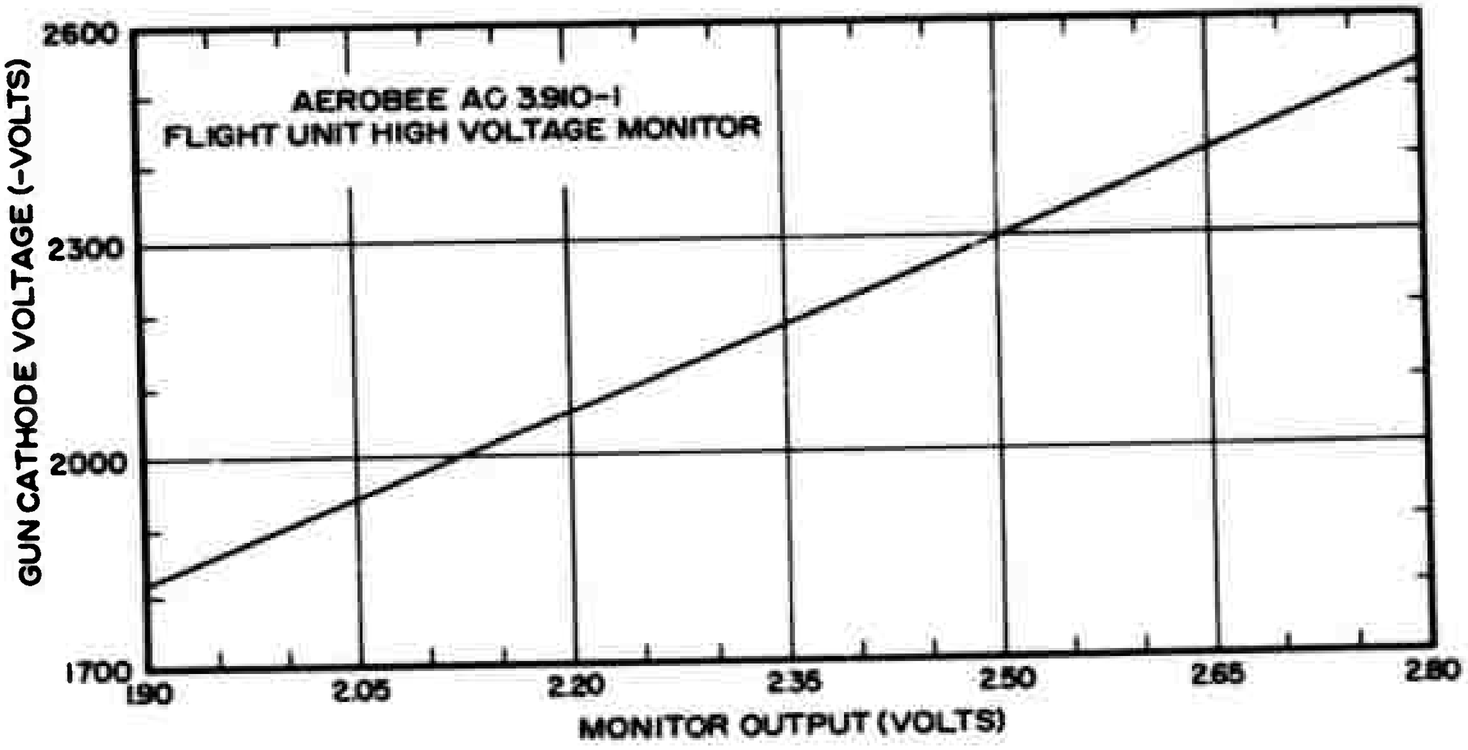

Figure B-13. Calibration curve for electron gun high voltage monitor.

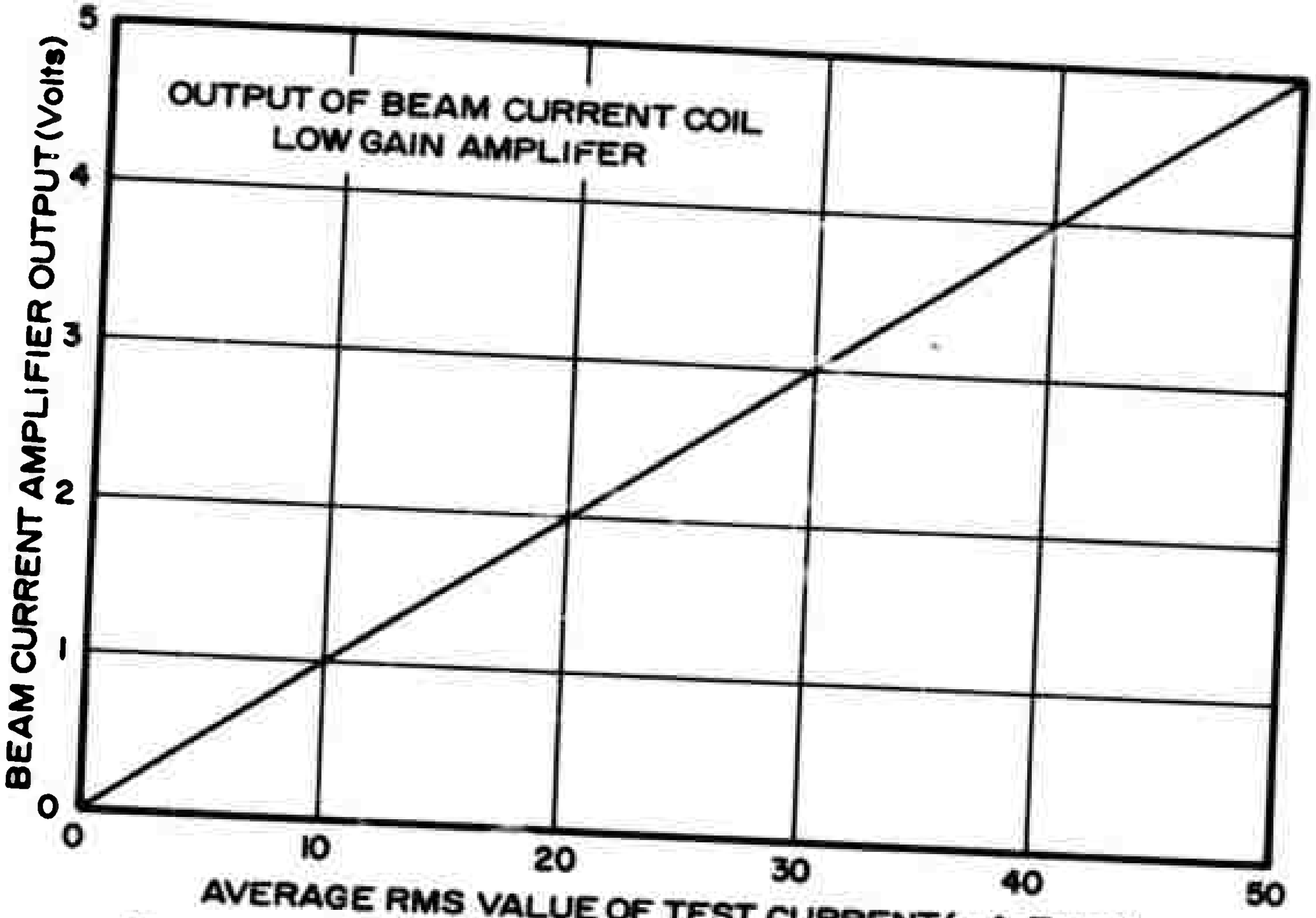

Figure B-14. Calibration curve for beam current monitor (toroid).

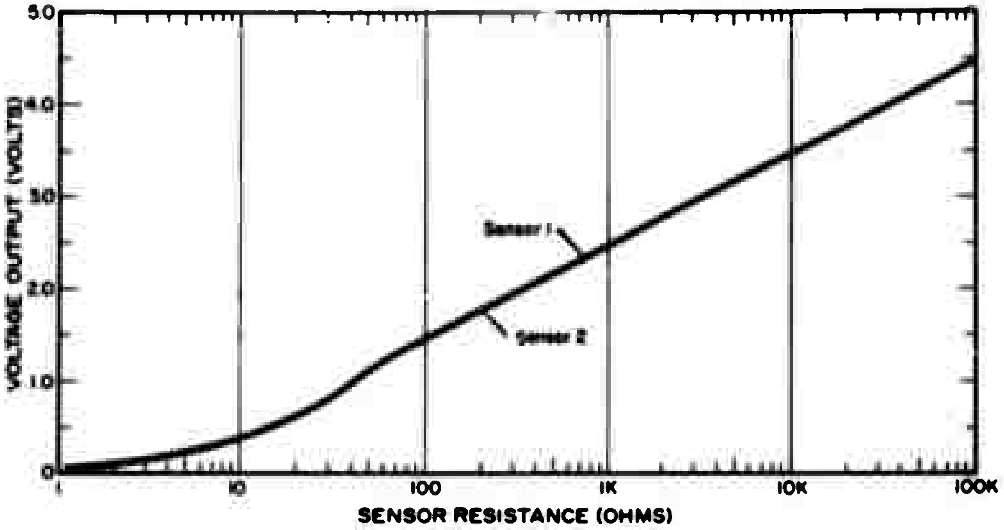

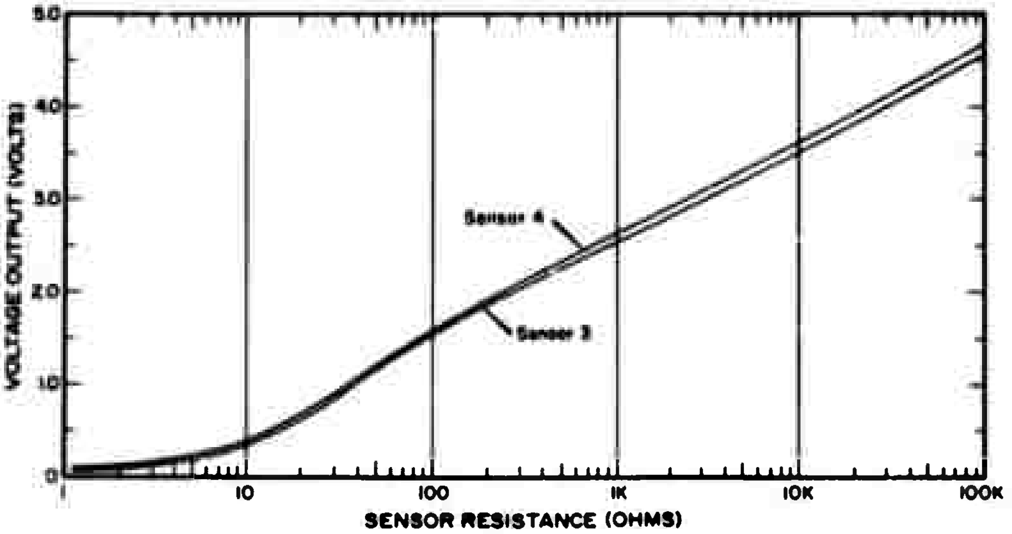

Figure B-15. Output voltage versus sensor resistance for the atomic oxygen detectors.

APPENDIX C

FILTER TRANSMISSION CURVES AND RELATED ITEMS FOR EBIL SYSTEM

Note: Unless otherwise indicated filter transmission curves refer to illumination by nearly parallel light at normal incidence.

Figure Page

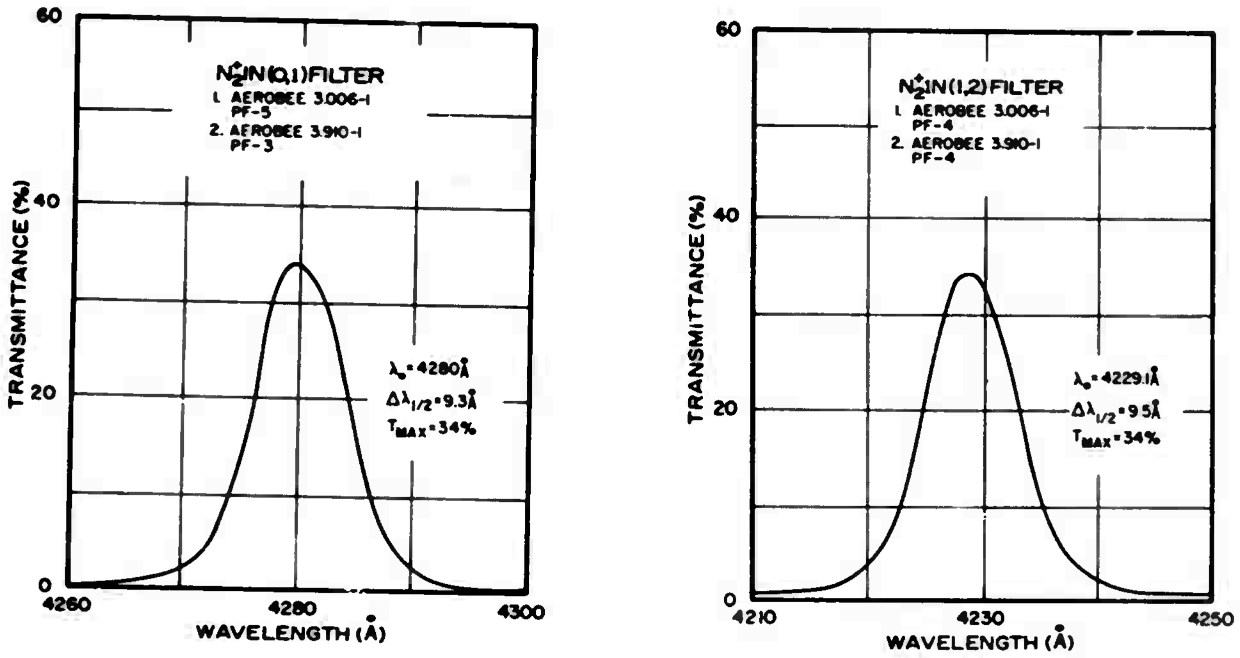

Figure C-1. Filter transmission curves: N_2^+ 1N (0,1) [left] and (1,2) [right] instruments.

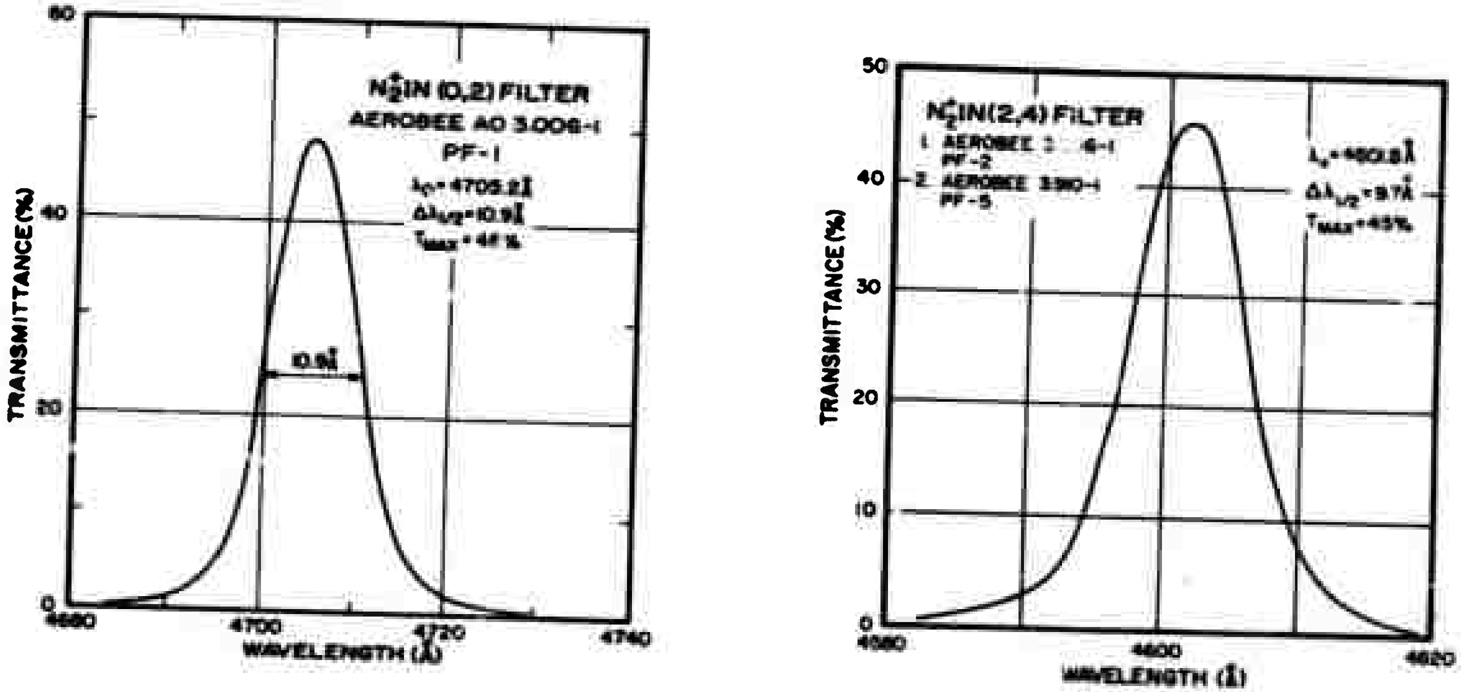

Figure C-2. Filter transmission curves: N_2^+ 1N (0,2) [left] and (2,4) [right] instruments.

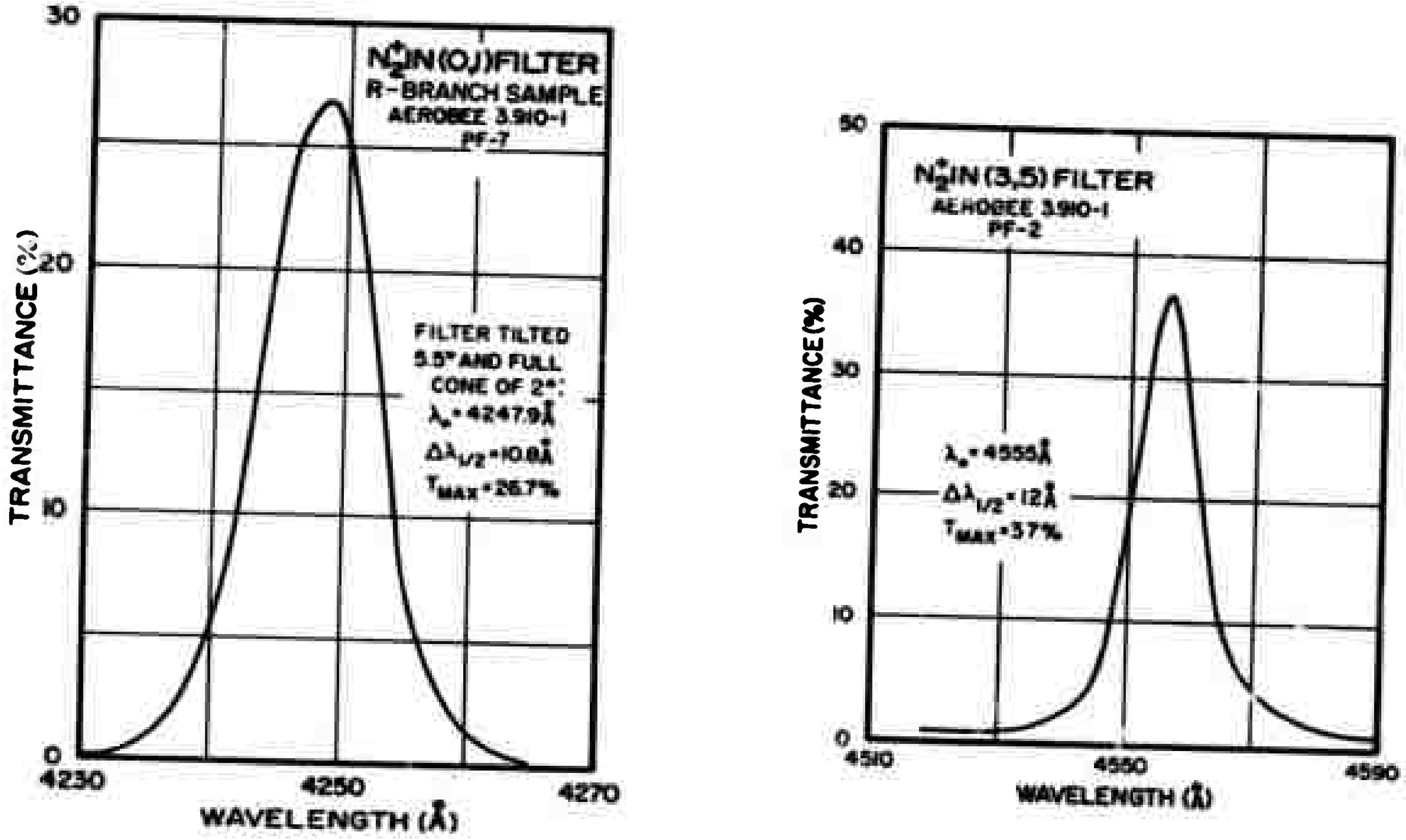

Figure C-3. Filter transmission curves: N_2^+ 1N (0,1) R-branch sample [left] and N_2^+ 1N (3,5) [right] instruments.

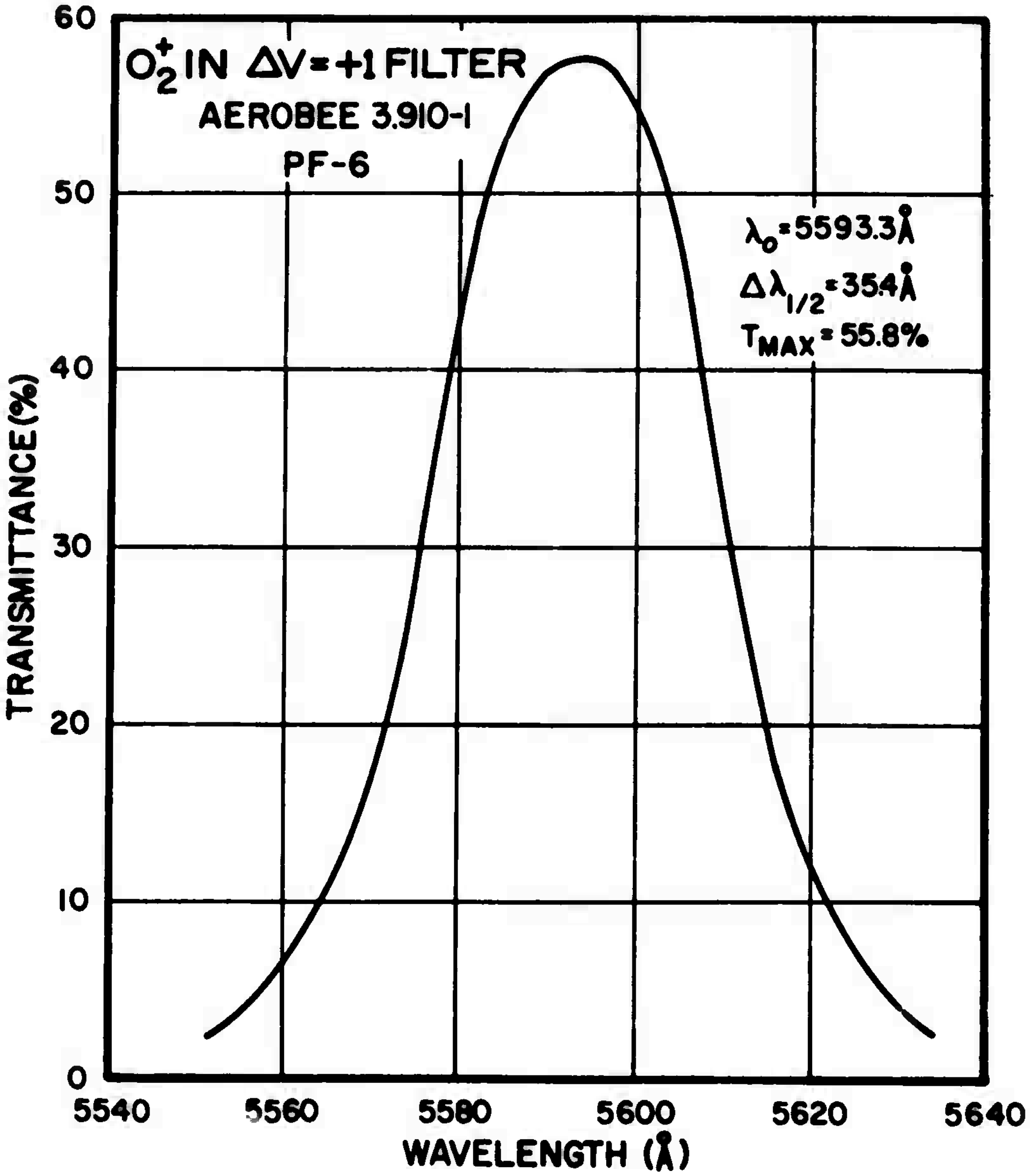

Figure C-4. Filter transmission curve: O_2^+ 1N ΔV = +1 instrument.

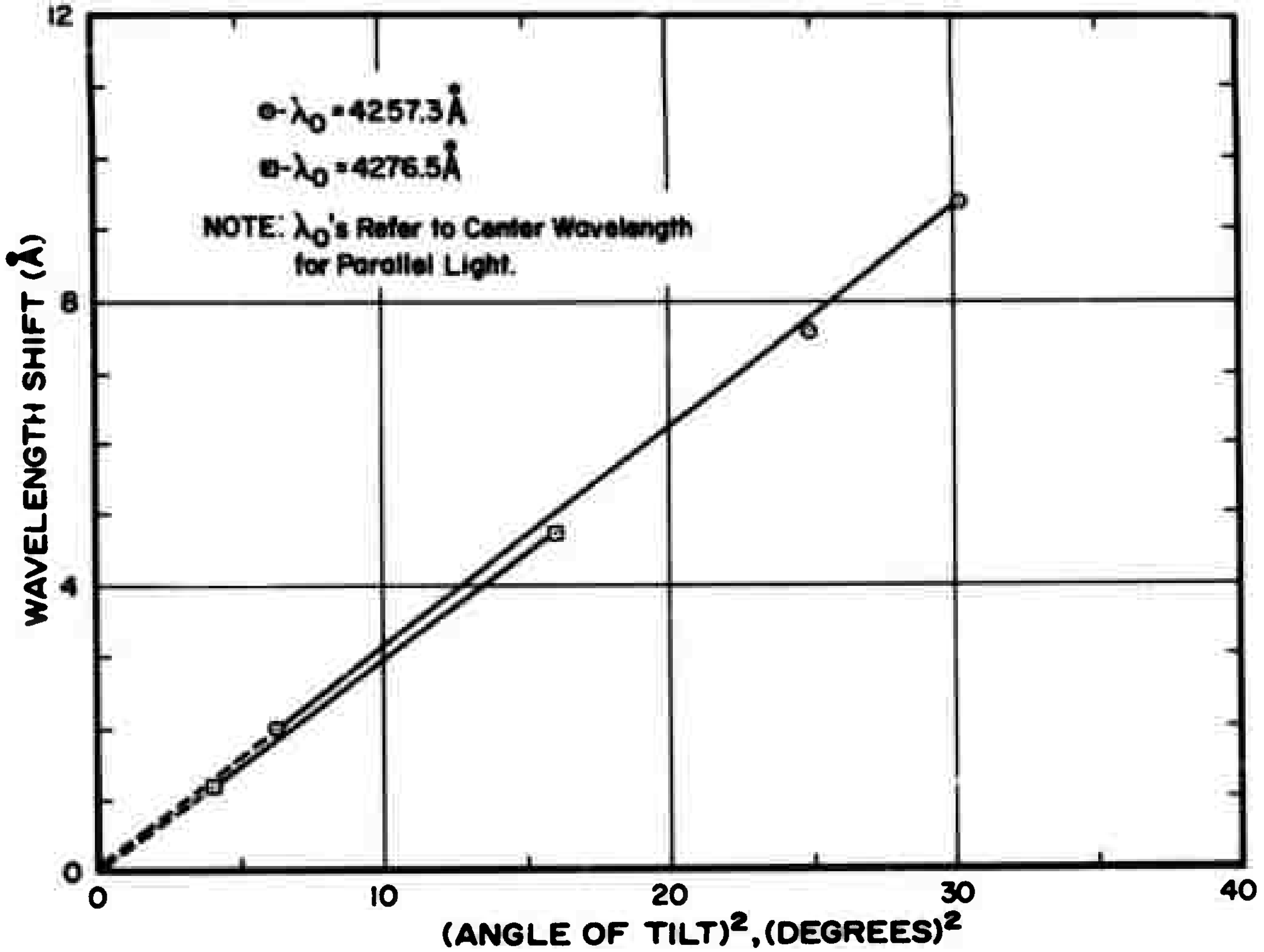

Figure C-5. Typical results for dependence of filter center wavelength on angle of tilt in nearly parallel light.

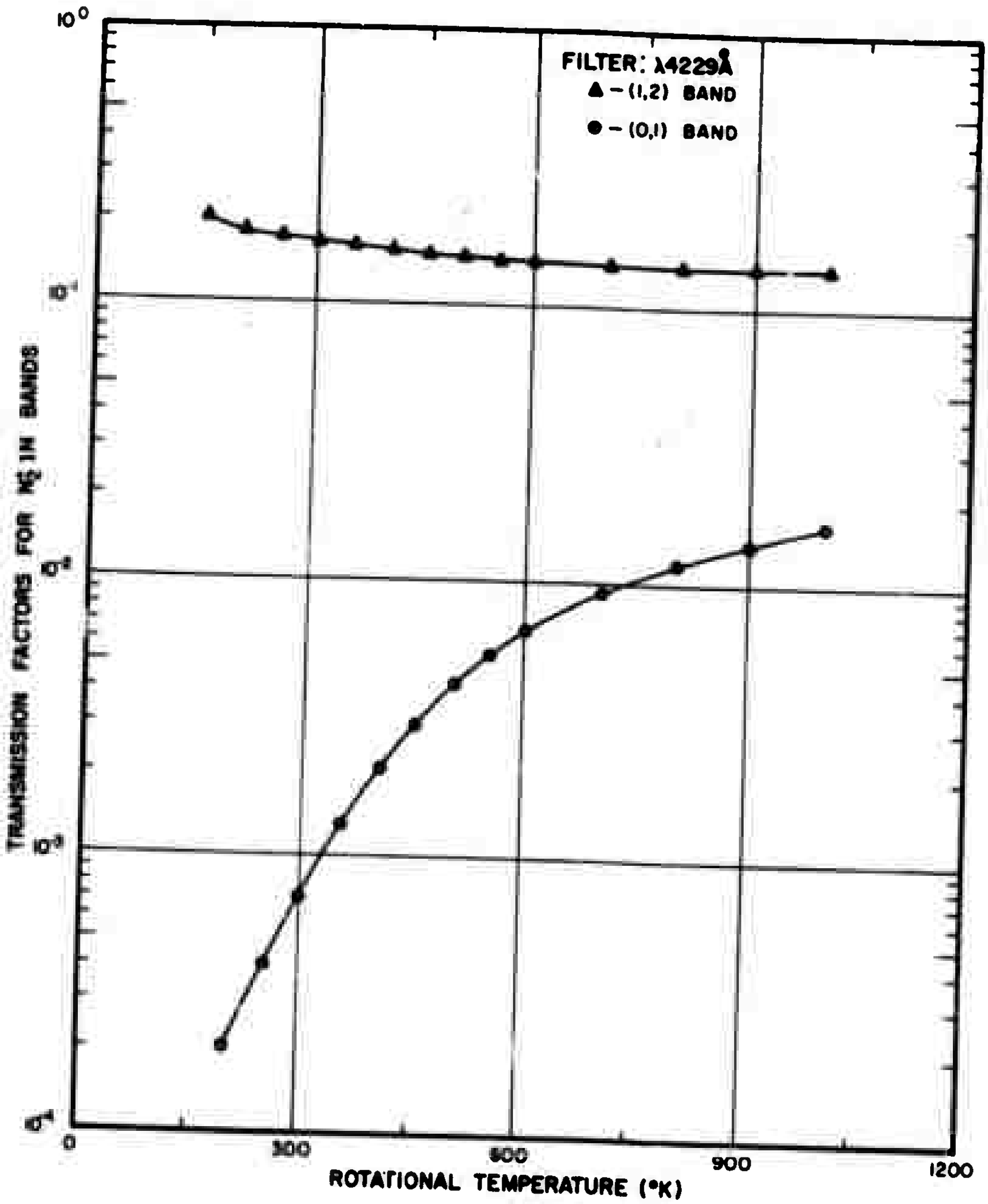

Figure C-6. Computed effective transmission factors for N_2^+ 1N (1,2) and (0,1) bands by λ_o 4229.1 Å filter at various rotational temperatures.

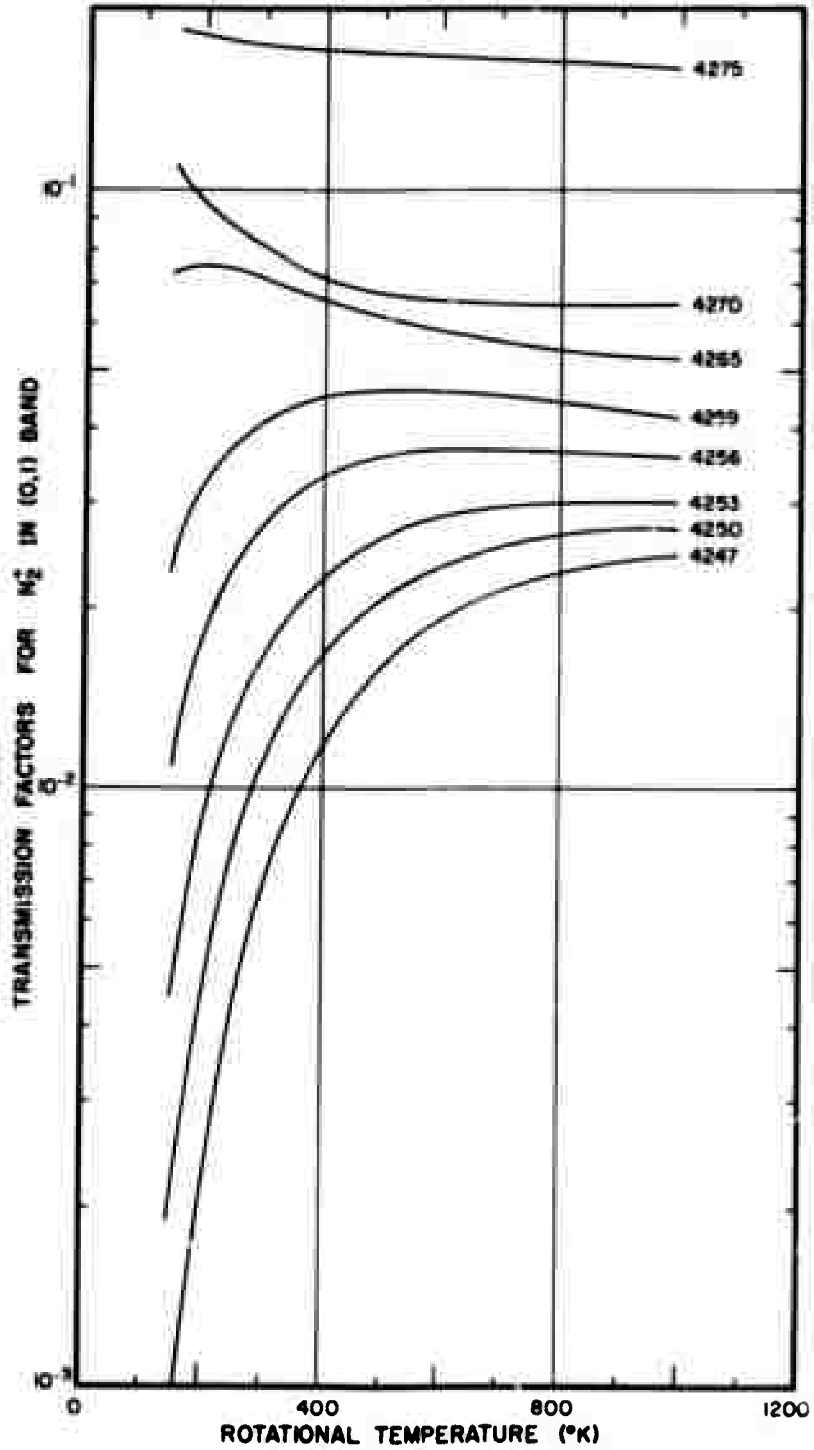

Figure C-7. Computed effective transmission factors for N_2^+ 1N (0,1) band [by a filter of $\Delta\lambda_{1/2}$ = 7 Å, "typical transmission profile," and the center wavelengths indicated by each curve] at various rotational temperatures.

C-8

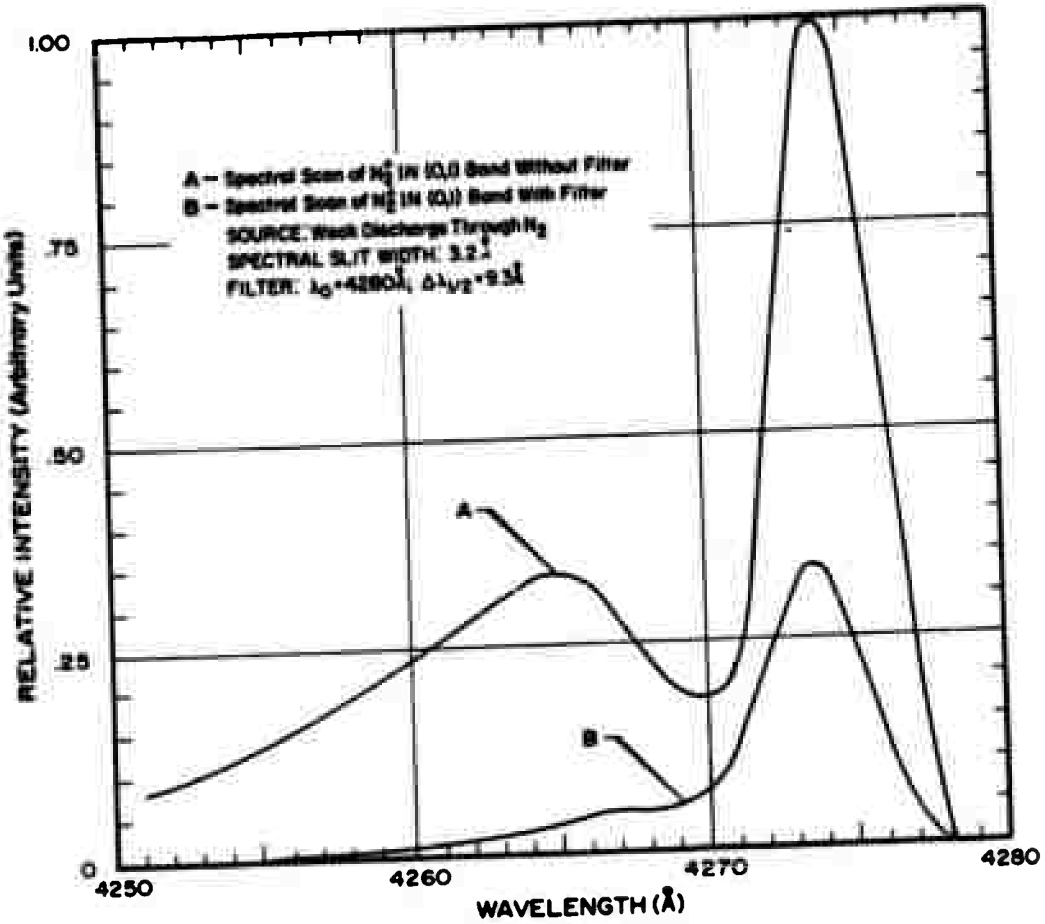

Figure C-8. Experimental results for effective transmission of N_2^+ 1N (0,1) band by λ_0 4280 Å filter ($T_r \approx 350°K$). Ratio of Areas = 0.20. Computed value assuming applicability of transmission curve of Figure C-1: 0.19.

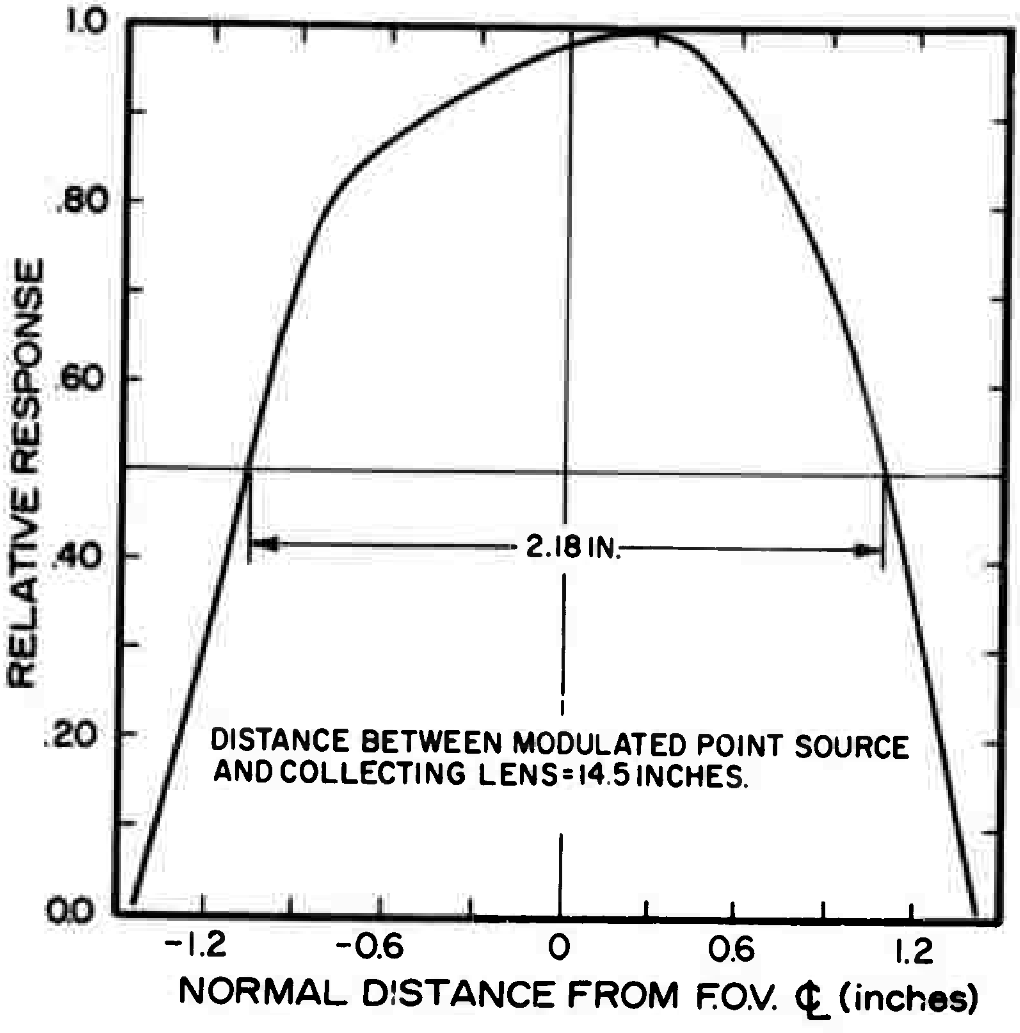

Figure C-9. Typical field-of-view curve for photometers.